DEEP-LEVEL IMPEDANCE SPECTROSCOPY OF ELECTRONIC MATERIALS

By

ANDREW NORBERT JANSEN

A DISSERTATION PRESENTED TO THE GRADUATE SCHOOL
OF THE UNIVERSITY OF FLORIDA IN PARTIAL FULFILLMENT
OF THE REQUIREMENTS FOR THE DEGREE OF
DOCTOR OF PHILOSOPHY

UNIVERSITY OF FLORIDA

1992

ACKNOWLEDGEMENTS

The author thanks the following individuals:

to my wife Rosalie for her love and encouragement since we first met,
to my parents Charles and Shirley for their love and guidance throughout the years,
to Professor Mark E. Orazem for his advice and support during my graduate studies,
to Pankaj Agarwal for his Indian recipes and numerical regression expertise,
to Matthew Esteban, Oliver Moghissi, and Paul Wojcik for their assistance and friendship,
to Professor Chih–Tang Sah for his discussions and reprints on semiconductor physics and,
to Professors Timothy J. Anderson, Oscar D. Crisalle, and Kevin S. Jones for their suggestions during the course of this work.

The author thanks Mr. Darwin Thusius of Sula Technologies for the GaAs sample and discussions on the DLTS instrumentation. The author also thanks Dr. David Morton and Dr. Robert Miller of the U.S. Army Electronics Technology and Device Laboratory for providing the ZnS:Mn TFEL panel and Dr. Gary Trost of the Raychem Corporation for providing the ZnO varistors. This work was supported by DARPA under the Optoelectronics program of the Florida Initiative in Advanced Microelectronics and Materials.

TABLE OF CONTENTS

ACKNOWLEDGEMENTS ii

LIST OF TABLES v

LIST OF FIGURES vi

ABSTRACT xiii

CHAPTERS

1 INTRODUCTION 1

2 BACKGROUND 3

3 EXPERIMENTAL METHOD AND INSTRUMENTATION 11

- 3.1 General Schematic 11
- 3.2 Electrochemical Impedance Spectroscopy 12
  - 3.2.1 Theory 12
  - 3.2.2 Signal Generation and Analysis 15
  - 3.2.3 Experimental Difficulties 25
- 3.3 Standard Characterization Techniques 26
  - 3.3.1 Mott–Schottky Profiling 26
  - 3.3.2 Deep–Level Transient Spectroscopy (DLTS) 27
  - 3.3.3 DLTS Equipment and Parameters 32
- 3.4 Optical Spectroscopy 36

4 DEVELOPMENT OF PROCESS MODEL 56

- 4.1 Shockley Read Hall Processes 56
  - 4.1.1 Equilibrium 61
  - 4.1.2 Non–equilibrium 64
  - 4.1.3 Small Signal Analysis 66
  - 4.1.4 Equivalent Circuit 71
- 4.2 Surface States 74
  - 4.2.1 Single Energy Level Surface State 74
  - 4.2.2 Surface Band 77
- 4.3 Complete Equivalent Circuit 82
  - 4.3.1 Simplifications of the Complete Circuit 84
  - 4.3.2 Analysis of the Recombination Circuit Components 87

5 SYSTEMS ANALYZED 96

- 5.1 Gallium Arsenide 96
- 5.2 ZnS:Mn Thin Film Electroluminescent (TFEL) Panel 97
- 5.3 ZnO Varistor 98

5.4 Cuprous Oxide in Alkaline–Chloride Solutions 99
  5.4.1 Background 100
  5.4.2 Experiment 103
6 RESULTS AND DISCUSSION 106
6.1 Gallium Arsenide 106
  6.1.1 Thermally Stimulated Deep–Level Impedance Spectroscopy . . 106
  6.1.2 Optically Stimulated Deep–Level Impedance Spectroscopy . . 112
6.2 Importance of Weighting on Regression Results 117
6.3 ZnS:Mn TFEL Panel 120
6.4 ZnO Varistors 122
6.5 Cuprous Oxide in Alkaline–Chloride Solution 126
6.6 Comparison of Impedance and Admittance 130
6.7 Three–Dimensional Representation 131
7 CONCLUSIONS 200
8 SUGGESTIONS FOR FUTURE WORK 202

APPENDIX

PROGRAM FOR DLTS INTERFACE 205
REFERENCES 212
BIOGRAPHICAL SKETCH 221

LIST OF TABLES

2.1 A comparison of methods used to identify deep–level states. 10

6.1 Comparison of values from DLZS, DLTS, and literature [71]. 143

6.2 Model variance weighting parameters used in regression of impedance data. Values were determined by Pankaj Agarwal. 162

LIST OF FIGURES

2.1 Energy band diagram of a n–type semiconductor with a deep–level state. 9

3.1 Experimental setup for Deep–Level Impedance Spectroscopy. 39

3.2 Basic inverting operational amplifier circuit (a) and overly simplified equivalent circuit of an operational amplifier (b). 40

3.3 Simplified block diagram for the Solartron 1286. 41

3.4 Simplified block diagram for the PAR 273. 42

3.5 Equivalent circuit from regression of (a) Solartron 1286 and (b) PAR 273 impedance data. 43

3.6 Comparison of Solartron cell data and equivalent circuit data for the Solartron and the PAR potentiostats in the form of an impedance plane plot. 44

3.7 Comparison of Solartron cell data and equivalent circuit data for the Solartron and the PAR potentiostats in the form of phase angle as a function of frequency. 45

3.8 Comparison of PAR cell data and equivalent circuit data for the Solartron and the PAR potentiostats in the form of an impedance plane plot. 46

3.9 Comparison of PAR cell data and equivalent circuit data for the Solartron and the PAR potentiostats in the form of phase angle as a function of frequency. 47

3.10 Frequency dependence of gain and phase shift for control op amp [27]. 48

3.11 Compensated (stable) and uncompensated gain and phase shift for control op amp [27]. 49

3.12 Energy levels as a function of distance for a n–type semiconductor under (a) equilibrium reverse bias, (b) equilibrium forward bias, and (c) transient reverse bias. 50

3.13 Capacitance decay as a function of time and temperature (left) and capacitance difference as a function of temperature (right). 51

3.14 Intensity of the focused light as a function of the wavelength for the 410–720 nm order sorting filter with 1200 and 600 grooves/mm diffraction gratings and the spectrometer exit/entrance slit width as parameters. 52

3.15 Intensity of the focused light as a function of the wavelength for the 720–1350 nm order sorting filter with the 600 grooves/mm diffraction grating and the spectrometer exit/entrance slit width as parameters. 53

3.16 Intensity of the focused light as a function of the wavelength for the 1200–2000 nm order sorting filter with the 300 grooves/mm diffraction grating and the spectrometer exit/entrance slit width as parameters. 54

3.17 Intensity of the focused light as a function of the wavelength for the 1800–3000 nm order sorting filter with the 300 grooves/mm diffraction grating and the spectrometer exit/entrance slit width as parameters. 55

4.1 Shockley Read Hall processes of a deep–level state. 89

4.2 Equivalent circuit corresponding to the small signal non–equilibrium case for a bulk deep–level state. Equations and notation are given in the text. 90

4.3 Equivalent circuit corresponding to the small signal non–equilibrium case for a surface state. Equations and notation are given in the text. 91

4.4 The complete non–equilibrium equivalent circuit with surface and bulk deep–level states for a Schottky barrier on the left side and an Ohmic contact on the right side with no DC leakage current. 92

4.5 The reduced equilibrium equivalent circuit with surface and bulk deep–level states for a Schottky barrier on the left side and an Ohmic contact on the right side. 93

4.6 Simplified equilibrium equivalent circuit with only surface states (a), and only bulk deep–level states (b) for a Schottky barrier on the left side and an Ohmic contact on the right side. 94

4.7 The reduced equilibrium equivalent circuit used in this work with a Schottky barrier on the left side and an Ohmic contact on the right side. 95

5.1 Cell configuration for the copper electrode experiments. 105

6.1 Imaginary component of the impedance as a function of the real component of the impedance for frequencies ranging from 65000 to 1 Hz with temperature as a parameter for n–type GaAs with Schottky contact. 132

6.2 Resistances from regression of simplified equivalent circuit to impedance data as a function of inverse temperature for n–type GaAs with Schottky contact. 133

6.3 Capacitances from regression of simplified equivalent circuit to impedance data as a function of inverse temperature for n–type GaAs with Schottky contact. 134

6.4 Energy diagram of a shallow donor state (E1), a midgap state (E2) slightly below the Fermi level (E_F), and a shallow acceptor state (E3) for negative half cycle (upper) and positive half cycle (lower) of sinusoid. 135

6.5 Inverse of resistances from regression of simplified equivalent circuit to impedance data as a function of inverse temperature for n–type GaAs with Schottky contact. 136

6.6 Equivalent circuit characteristic frequencies from regression of simplified equivalent circuit to impedance data as a function of inverse temperature for n–type GaAs with Schottky contact. 137

6.7 Product of temperature and equivalent circuit resistance as a function of inverse temperature for n–type GaAs with Schottky contact. 138

6.8 Product of temperature and equivalent circuit capacitance as a function of inverse temperature for n–type GaAs with Schottky contact. 139

6.9 Equivalent circuit characteristic frequencies divided by the square of temperature as a function of inverse temperature for n–type GaAs with Schottky contact. 140

6.10 DLTS emission rate divide by square of peak temperature as a function of inverse temperature for n–type GaAs with Schottky contact. 141

6.11 Mott–Schottky plot for n–type GaAs with Schottky contact. 142

6.12 Imaginary component of the impedance as a function of the real component of the impedance for frequencies ranging from 20000 to 4 Hz with optical energy as a parameter for n–type GaAs with Schottky contact. 144

6.13 Dimensionless real component of the impedance as a function of optical energy with electrical frequency as a parameter for n–type GaAs with Schottky contact. 145

6.14 Dimensionless imaginary component of the impedance as a function of optical energy with electrical frequency as a parameter for n–type GaAs with Schottky contact. 146

6.15 Dimensionless real component of the impedance as a function of light intensity at 1.1 eV with electrical frequency as a parameter for n–type GaAs with Schottky contact. 147

6.16 Dimensionless imaginary component of the impedance as a function of light intensity at 1.1 eV with electrical frequency as a parameter for n–type GaAs with Schottky contact. 148

6.17 Optical cross sections from DLOS experiments as a function of optical energy, from references [98, 99]. 149

6.18 Dimensionless total impedance as a function of optical energy with electrical frequency as a parameter for n–type GaAs with Schottky contact. 150

6.19 Dimensionless phase angle as a function of optical energy with electrical frequency as a parameter for n–type GaAs with Schottky contact. . . 151

6.20 Resistances from regression of impedance data to equivalent circuit as a function of optical energy for n–type GaAs with Schottky contact. . 152

6.21 Capacitances from regression of impedance data to equivalent circuit as a function of optical energy for n–type GaAs with Schottky contact. 153

6.22 Characteristic frequencies from regression of impedance data to equivalent circuit as a function of optical energy for n–type GaAs with Schottky contact. 154

6.23 Total system energy as a function of defect position. 155

6.24 Resistances from regression of impedance data to equivalent circuit with no weighting as a function of optical energy for n–type GaAs with Schottky contact. 156

6.25 Characteristic frequencies from regression of impedance data to equivalent circuit with no weighting as a function of optical energy for n–type GaAs with Schottky contact. 157

6.26 Resistances from regression of impedance data to equivalent circuit with proportional weighting as a function of optical energy for n–type GaAs with Schottky contact. 158

6.27 Characteristic frequencies from regression of impedance data to equivalent circuit with proportional weighting as a function of optical energy for n–type GaAs with Schottky contact. 159

6.28 Resistances from regression of impedance data to equivalent circuit with modulus weighting as a function of optical energy for n–type GaAs with Schottky contact. 160

6.29 Characteristic frequencies from regression of impedance data to equivalent circuit with modulus weighting as a function of optical energy for n–type GaAs with Schottky contact. 161

6.30 Imaginary component of the impedance as a function of the real component of the impedance for frequencies ranging from 0.2 to 100 Hz and with optical energy as a parameter for the ZnS:Mn TFEL panel. 163

6.31 Dimensionless real component of the impedance as a function of optical energy with electrical frequency as a parameter for the ZnS:MN TFEL panel. 164

6.32 Dimensionless imaginary component of the impedance as a function of optical energy with electrical frequency as a parameter for the ZnS:Mn TFEL panel. 165

6.33 Change in photon–released residual charge as a function of photon energy for a ZnS:Mn TFEL panel from reference [108]. 166

6.34 Total impedance as a function of frequency with optical energy as a parameter for the ZnS:Mn TFEL panel. 167

6.35 Phase angle as a function of frequency with optical energy as a parameter for the ZnS:Mn TFEL panel. 168

6.36 Resistances from regression of simplified equivalent circuit to impedance data as a function of inverse temperature for the ZnS:Mn TFEL panel. 169

6.37 Capacitances from regression of simplified equivalent circuit to impedance data as a function of inverse temperature for the ZnS:Mn TFEL panel. 170

6.38 Equivalent circuit characteristic frequencies from regression of simplified equivalent circuit to impedance data as a function of inverse temperature for the ZnS:Mn TFEL panel. 171

6.39 Imaginary component of the impedance as a function of the real component of the impedance for frequencies ranging from 20000 to 0.05 Hz with optical energy as a parameter for the unaged ZnO varistor. . . . 172

6.40 Imaginary component of the impedance as a function of the real component of the impedance for frequencies ranging from 1500 to 0.2 Hz with optical energy as a parameter for the aged ZnO varistor. 173

6.41 Dimensionless real component of the impedance as a function of optical energy with electrical frequency as a parameter for the aged ZnO varistor. 174

6.42 Dimensionless imaginary component of the impedance as a function of optical energy with electrical frequency as a parameter for the aged ZnO varistor. 175

6.43 Dimensionless real component of the impedance as a function of optical energy with electrical frequency as a parameter for the unaged ZnO varistor. 176

6.44 Dimensionless imaginary component of the impedance as a function of optical energy with electrical frequency as a parameter for the unaged ZnO varistor. 177

6.45 Resistances from regression of simplified equivalent circuit to impedance data as a function of inverse temperature for the unaged ZnO varistor. 178

6.46 Capacitances from regression of simplified equivalent circuit to impedance data as a function of inverse temperature for the unaged ZnO varistor. 179

6.47 Equivalent circuit characteristic frequencies from regression of simplified equivalent circuit to impedance data as a function of inverse temperature for the unaged ZnO varistor. 180

6.48 Imaginary component of the impedance as a function of the real component of the impedance for frequencies ranging from 1500 to 0.2 Hz with optical energy as a parameter for the unaged ZnO varistor annealed at 600°C. 181

6.49 Total impedance as a function of frequency under no illumination and illumination of 1.77 eV for the aged and unaged ZnO varistors annealed at 600°C. 182

6.50 Phase angle as a function of frequency under no illumination and illumination of 1.77 eV for the aged and unaged ZnO varistors annealed at 600°C. 183

6.51 Imaginary component of the impedance as a function of the real component of the impedance for frequencies ranging from 1500 to 0.2 Hz with optical energy near the bandgap as a parameter for the aged ZnO varistor. 184

6.52 Imaginary component of the impedance as a function of the real component of the impedance for frequencies ranging from 65000 to 0.1 Hz with optical energy as a parameter for cuprous oxide (aged in light) in alkaline–chloride solution. 185

6.53 Phase angle as a function of frequency with optical energy as a parameter for cuprous oxide (aged in light) in alkaline–chloride solution. . . 186

6.54 Dimensionless real component of the impedance as a function of optical energy with electrical frequency as a parameter for cuprous oxide (aged in light) in alkaline–chloride solution. 187

6.55 Dimensionless imaginary component of the impedance as a function of optical energy with electrical frequency as a parameter for cuprous oxide (aged in light) in alkaline–chloride solution. 188

6.56 Black body radiation intensity per wavelength as a function of wavelength with temperature as a parameter, from Planck distribution law. 189

6.57 Imaginary component of the impedance as a function of the real component of the impedance for frequencies ranging from 10000 to 0.2 Hz with optical energy as a parameter for cuprous oxide (aged in dark) in alkaline–chloride solution. 190

6.58 Phase angle as a function of frequency with optical energy as a parameter for cuprous oxide (aged in dark) in alkaline–chloride solution. . . 191

6.59 Dimensionless real component of the impedance as a function of optical energy with electrical frequency as a parameter for cuprous oxide (aged in dark) in alkaline–chloride solution. 192

6.60 Dimensionless imaginary component of the impedance as a function of optical energy with electrical frequency as a parameter for cuprous oxide (aged in dark) in alkaline–chloride solution. 193

6.61 Density of states as a function of energy for a disordered semiconductor (left) and a crystalline semiconductor with a discrete state (right). . . 194

6.62 Imaginary component of the impedance and of the admittance as a function of electrical frequency with optical energy as a parameter for the aged ZnO varistor. 195

6.63 Dimensionless real component of the impedance as a function of optical energy and electrical frequency for n–type GaAs with Schottky contact. 196

6.64 Dimensionless imaginary component of the impedance as a function of optical energy and electrical frequency for n–type GaAs with Schottky contact. 197

6.65 Dimensionless real component of the impedance as a function of optical energy and electrical frequency for the ZnS:Mn electroluminescent panel. 198

6.66 Dimensionless imaginary component of the impedance as a function of optical energy and electrical frequency for the ZnS:Mn electroluminescent panel. 199

Abstract of Dissertation Presented to the Graduate School
of the University of Florida in Partial Fulfillment of the
Requirements for the Degree of Doctor of Philosophy

DEEP-LEVEL IMPEDANCE SPECTROSCOPY
OF
ELECTRONIC MATERIALS

By

ANDREW NORBERT JANSEN

December, 1992

Chairman: Prof. Mark E. Orazem
Major Department: Chemical Engineering

Deep-Level Impedance Spectroscopy (DLZS) is suggested to be a new approach to analyze transitions of deep-level states in electronic materials. The technique is based on interpretation of both the real and imaginary components of the impedance response over a continuous range of electrical frequencies. The two parameters that were varied, temperature and optical energy, directly influenced the transition rate or occupancy of deep-level states.

Transition rates of the deep-level states were determined to have an Arrhenius relationship with temperature, indicating activation energy controlled reactions. Measurement of the impedance response as a function of temperature is termed Thermally Stimulated Deep-Level Impedance Spectroscopy (TS-DLZS).

Optical excitation had a marked effect on the real and imaginary components of the impedance when the optical energy matched the energy difference between the deep–level state and a carrier band. This variant of the technique is termed Optically Stimulated Deep–Level Impedance Spectroscopy (OS–DLZS).

A mathematical model was developed from mass balance equations and Poisson's equation to aid the analysis of the impedance data. For convenience during the regression, the model was posed in terms of an equivalent circuit of resistors and capacitors whose values were related to system properties such as reaction rate constants and concentrations. The data were regressed to the equivalent circuit through complex nonlinear regression. The influence of temperature, monochromatic light, and electrical frequency was evident in the impedance data and the regressed resistances and capacitances. The results from DLZS (data and regressed parameters) and the well–accepted Deep–Level Transient Spectroscopy (DLTS) for the EL2 state in GaAs were found to be in close agreement. This technique was also used to analyze semiconducting materials such as ZnS:Mn thin film electroluminescent panels, ZnO varistors, and cuprous oxide on copper in alkaline chloride solutions.

CHAPTER 1

INTRODUCTION

Deep–Level Impedance Spectroscopy (DLZS) is presented here as a new technique for characterization of electronic transitions in large band–gap semiconductor devices. This technique involves an analysis of the real and imaginary components of the impedance response over a continuous range of applied frequency under the influence of sub–bandgap illumination and/or temperature.

A history of impedance techniques is presented in Chapter 2. This chapter deals only with techniques that are relevant to the work presented in this manuscript. There are a considerable number of techniques and their variations used to analyze semiconductors that are described elsewhere in literature.

The experimental theory and application is discussed in Chapter 3. This discussion is designed to bring the next investigator up to speed on the experimentation and the details behind the impedance measurements. For those who have a good electronics background, much of this chapter may serve as a review.

In Chapter 4, some physical insight is provided as to the nature of electronic transitions between deep–level states and the carrier bands. The governing equations are developed and transformed into a simplified equivalent circuit.

A brief description of the samples used in this work is given in Chapter 5. The samples described are: n–type GaAs, a ZnS:Mn thin film electroluminescent panel, ZnO varistors, and Cu/Cu_2O in alkaline–chloride solution.

The results of this work are presented in Chapter 6 along with a discussion of its importance. This is intended to prove the validity of Deep–Level Impedance Spectroscopy, and hopefully, provide new insight to the semiconducting nature of these materials. Chapter 7 is a summary of the key points in this work, and suggestions for future work are presented in Chapter 8 . The computer program used to interface the DLTS equipment is included in the Appendix.

CHAPTER 2

BACKGROUND

In contrast to most spectroscopic techniques, Optically Stimulated Deep–Level Impedance Spectroscopy (OS–DLZS) can be regarded as encompassing two frequency domains, one that is electrical and one that is optical. The potential utility of employing a broad electrical frequency range is consistent with experimental observation that surface states have the largest influence on the impedance response at low frequencies [1, 2] and that the space charge capacitance is obtained most easily from high frequency measurements.

The application of sub-bandgap optical excitation of deep–level states was suggested by the body of work describing Electrochemical Photocapacitance Spectroscopy (EPS) [3–6].The emphasis on interpretation of both the real and imaginary components of the impedance was driven by the results of a mathematical model [7–10]that treated the influence of deep-level states on the impedance response of a semiconductor by solving the equations which govern the physics of the system, *e.g.,* Poisson's equation, conservation equations for electrons and holes, and homogeneous and heterogeneous rate expressions for generation and recombination. The modeling work suggested that, through use of monochromatic sub-bandgap optical excitation, the influence of even low concentrations of deep–level electronic states could be seen on the real part of the impedance measured at low electrical frequencies.

Deep–level states play an important role in solid state devices through their behavior as recombination centers. The electronic states of interest lie within the bandgap of the semiconductor. The goal is to determine that these states exist as well as to determine their concentration distribution and the associated rate constants for electronic transitions. Knowledge of these parameters is essential for the engineering of many electronic devices.

For example, deep–level states are undesirable when they facilitate electronic transitions which reduce the efficiency of photovoltaic cells. In other cases, the added reaction pathways for electrons result in desired effects. Electroluminescent panels, for example, rely on electronic transitions that result in emission of photons. The energy level of the states caused by introduction of dopants determines the color of the emitted light. Interfacial states are believed to play a key role in electroluminescence, and commercial development of this technology will hinge upon understanding the relationship between fabrication techniques and the formation of deep-level states. Deep–level states also influence the performance of solid–state varistors. While this technology is more established, development of new processing recipes will be facilitated by understanding how fabrication techniques, composition, and aging processes influence the energy and location of deep–level states. Copper in alkaline–chloride solutions (marine environment) does not suffer from stress corrosion cracking if its oxide film forms under illumination[11]. Deep–level states may be involved because cuprous oxide is a large band gap semiconductor.

The impact of deep–level states can be significant, even in concentrations that are very low by normal chemical standards. Several states can be associated with a chemical species, and such states may also appear as a result of vacancies or other crystalline defects. Traditional chemical means of detection, therefore, do not provide complete identification of deep–level electronic states. The techniques commonly employed to detect deep–level states tend to be electrical in nature since it is through their electronic behavior that these states influence device performance.

The electronic behavior of an electron donor deep–level state with energy E_T is illustrated in Figure 2.1. An electron can be emitted from the deep–level state to the conduction band if it acquires energy of $(E_C - E_T)$. Likewise, transfer of energy equal to $(E_T - E_V)$ can excite an electron from the valence band to an ionized deep–level state, *i.e.,* hole emission. An electron in the deep–level state that acquires energy $(E_D - E_T)$ can be excited to the donor state. Under equilibrium conditions, the occupancy of the state is governed by the Fermi-Dirac distribution function. In the absence of illumination, the deep–level state will influence the impedance response of the semiconductor only if the probability of occupancy of the state is close to 1/2, *i.e.,* if the state energy is close to the Fermi energy. If, for example, the probability of occupancy is essentially zero, the unfavorable energetics of the transition prevents the electrical excitation from moving electrons into the state. On the other hand, if the probability of occupancy is essentially unity, the need to satisfy Pauli exclusion prohibits transfer of electrons into the state. Similar arguments apply for transferring electrons out of the state.

At an interface with a dissimilar material, a redistribution of charged species occurs which results in the formation of a space charge region in the semiconductor. A space charge region can be formed at an interface with a metal, another semiconductor, or an electrolyte. In polycrystalline materials, a space charge region can also be formed at a grain boundary. Within the space charge region, the electron energy for the valence band, the conduction band, and the deep–level state can be described as varying with reference to a fixed Fermi energy. Thus the probability of occupancy of the deep–level state is a function of position, and, since the degree of band bending is determined by the potential applied to the system, the degree of occupancy is a function of applied potential. As discussed below, an anomalous change in the space charge capacitance with applied potential can be attributed to the influence of deep–

level states. The energy needed to excite deep–level electronic transitions can also be provided through illumination. Monochromatic illumination with energy less than the bandgap energy is preferred because band-to-band transitions can easily obscure the transitions involving deep–level states.

The distinguishing features of some electrical techniques used to characterize deep–level states are presented in Table 1. Anomalous changes in the space charge capacitance with applied potential have been attributed to the influence of deep–level states. In the absence of deep–level states, Mott–Schottky theory (see for example references [12, 13]) suggests that the inverse of the square of the space charge capacitance be a linear function of applied potential. The slope in this plot is proportional to the concentration of carriers and the intercept is related by a constant to the flat band potential. Changes in the slope of the Mott–Schottky plot can be related to nonuniform distribution of dopants or to potential–dependent ionization of deep–level states [8]. The presence of deep–level states is suggested if the capacitance is a function of the electrical frequency at which the capacitance is measured.

Development of electrochemical photocapacitance spectroscopy (EPS) [3–6]extended analyses based on Mott–Schottky theory by using monochromatic sub-bandgap illumination to change the occupancy of deep–level states. Changes in the space charge capacitance, measured at a fixed electrical frequency (usually around 1000 Hz) and applied potential, were observed as a function of photon energy. The energy at which a change in capacitance was observed was the energy of an allowed electronic transition. This approach can be used to map out the energy structure of an interface because transitions from the valence band to the deep–level state reduced the space charge capacitance, and transitions from the deep–level state to the conduction band increased the capacitance (assuming the deep–level state is a donor state in a n–type semiconductor). Since the charge held in the states may be very small as compared to that associated with doping species, the sensitivity of capacitance–based techniques requires precise measurement of the imaginary part of the impedance response.

Admittance Spectroscopy (AS) is a relatively new technique used to analyze deep–level states [14–18].In AS, the conductance (and the capacitance) of semiconductor samples are determined as a function of temperature at selected electrical frequencies. A plot of the conductance as a function of temperature is observed to have a peak. This peak temperature corresponds to a condition in which the emission rate of the trap equals the frequency of the perturbing sinusoid. An Arrhenius curve results if the frequency divided by the square of the peak temperature is plotted as a function of inverse temperature. The slope of this curve is proportional to the trap energy level from one of the carrier bands and the intercept is related to the capture cross–section and trap concentration. This technique is similar to DLTS (described below) in that the emission rate is varied via temperature sweeps. The difference is that the conductance is monitored in AS, whereas, a capacitance difference is monitored in DLTS. Results from AS and DLTS were found to be in close agreement [14–16].

Deep–Level Transient Spectroscopy (DLTS) [19] is, perhaps, the dominant capacitance–based technique used to detect deep–level electronic states. In DLTS, one monitors the space charge capacitance of the semiconductor in response to a pulse in potential. In addition, the temperature is changed in the experiment to vary the coefficient of the emission rate. The capacitance is measured at two different times following a pulse (in the forward direction); therefore, the transient change in occupation of a state in response to a step change in potential is observed as a change in measured capacitance. Interpretation of differences between the two values is based on assumption of an Arrhenius form for the rate constants.

The experimental part of the technique presented here bears closest resemblance to Optical Admittance Spectroscopy (OAS) [20, 21]. The major difference is that the complex impedance response is analyzed in DLZS; whereas, the complex admittance response is treated in OAS. The distinction between the two experimental techniques is, perhaps, subtle since impedance is simply the reciprocal of admittance. The main difference lies in the data analysis. As shown later, analysis in terms of impedance may be more sensitive to deep–level states at low frequencies.

This work addresses a light-enhanced form of electrochemical impedance spectroscopy. In this technique, the effect of photonic excitation of electronic transitions by light at selected wavelengths is detected by impedance spectroscopy applied over a broad frequency range. The photonic energy of the light used is less than the bandgap energy; therefore, any changes in the impedance spectrum with illumination can be attributed to transitions involving energy levels within the bandgap. This method differs from the more commonly used DLTS in that the wavelength of monochromatic sub-bandgap light is varied to excite electronic transitions at a fixed temperature (*e.g.*, room temperature); whereas, in DLTS, temperature is varied to change the occupancy of the states. A broad range of frequency (with emphasis on lower frequencies) for the impedance measurements is used instead of measuring an effective capacitance at a single high frequency. The use of a broad frequency range is the essential distinction between this approach and photocapacitance spectroscopy.

The effect of temperature on the impedance response is also analyzed in this work; this technique is referred to as Thermally Stimulated Deep–Level Impedance Spectroscopy (TS–DLZS). The rate of electronic transitions is dependent on the temperature in an Arrhenius manner, as in DLTS. Thermally Stimulated DLZS differs from DLTS in that a wide continuous range of frequencies is used and the real component of the impedance is also analyzed.

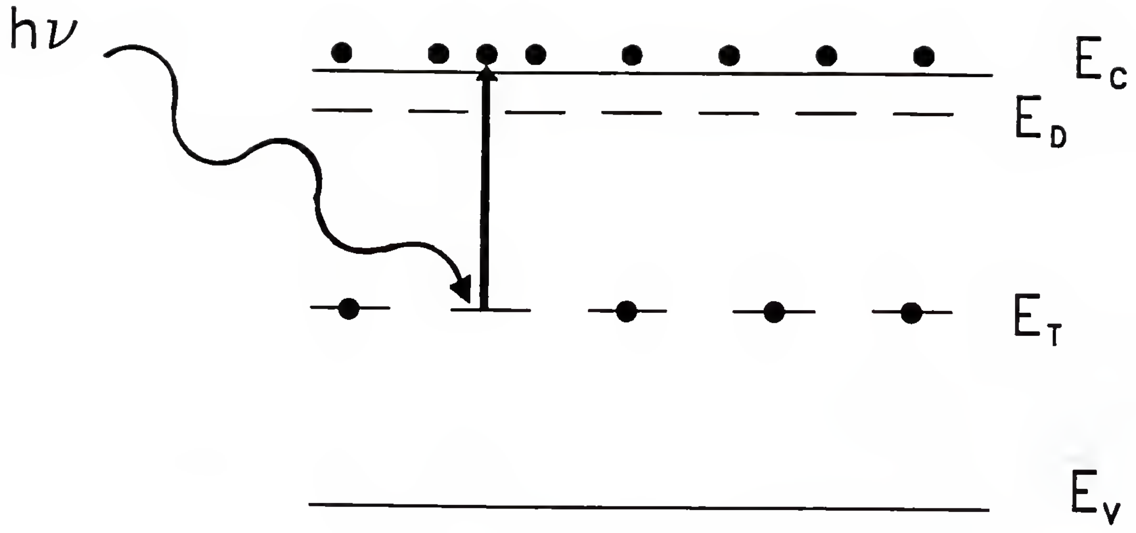

Figure 2.1: Energy band diagram of a n–type semiconductor with a deep–level state.

Table 2.1: A comparison of methods used to identify deep–level states.

Technique	Optical Excitation of Deep–Level States	Thermal Excitation of Deep–Level States	Electrical Frequency Range
MS[1]	No	No	single value about 1 kHz
PS[2]	Yes	No	single value about 1 kHz
DLTS[3]	No	Yes	rate windows (1 Hz to 5 kHz) capacitance measured at 1 MHz
AS[4]	No	Yes	single values (1 Hz to 1 MHz)
OAS[5]	Yes	No	0.1 Hz to 1 MHz
OS–DLZS[6]	Yes	No	0.05 Hz to 65 kHz
TS–DLZS[7]	No	Yes	1 Hz to 65 kHz

1. MS: Mott-Schottky Theory. Anomalous changes in differential capacitance are observed as a function of applied potential.
2. PS: Photocapacitance or Electrochemical Photocapacitance Spectroscopy (EPS). Changes in differential capacitance are observed as a function of photon energy.
3. DLTS: Deep-Level Transient Spectroscopy. Transient measurements of differential capacitance are made as a function of temperature.
4. AS: Admittance Spectroscopy. Changes in the admittance are observed as a function of frequency and temperature.
5. OAS: Optical Admittance Spectroscopy. Changes in the admittance spectrum are observed as a function of photon energy.
6. OS–DLZS: Optically Stimulated Deep–Level Impedance Spectroscopy: Changes in the impedance spectrum are observed as a function of photon energy and applied potential.
7. TS–DLZS: Thermally Stimulated Deep–Level Impedance Spectroscopy: Changes in the impedance spectrum are observed as a function of temperature and applied potential.

CHAPTER 3
EXPERIMENTAL METHOD AND INSTRUMENTATION

This chapter provides a detailed description of the equipment used throughout this work. The theoretical principles behind the techniques used are presented to help the reader understand the functions and limitations of the equipment. It is intended that this chapter supplement the operation manuals provided by the equipment distributors rather than replace them. A general description of the overall setup is given in the first section to provide an outline for the remainder of the chapter. The following sections describe the overall setup in greater detail.

3.1 General Schematic

A schematic of the experimental setup is given in Figure 3.1. The setup can be divided into two sections, one responsible for the optical frequency and the other for the electrical frequency. The light source was a 450 W Xenon lamp able to emit wavelengths of light greater than 300 nm. This light was diffracted in a SPEX Model 1681B Spectrometer to produce monochromatic light in accordance with Bragg's Law. The diffraction grating rulings were 1200, 600, 300 grooves/mm. The bandpass of the monochromatic light was set by means of an entrance and exit slit; the bandpass used was 18 nm unless otherwise noted. Harmonic frequencies were eliminated with order sorting filters and the light intensity was fixed with the use of neutral density filters at 15 ± 2 $\mathrm{mW/cm^2}$ unless otherwise noted. The samples were placed in a "dark box" to eliminate extraneous light sources and shielded with foil to prevent stray electric field interference, particularly at 60 Hz.

A potential bias was maintained across the sample by a PAR 273 potentiostat or a Solartron 1286 Electrochemical Interface (potentiostat). This was coupled with a Solartron 1250 Frequency Response Analyzer (FRA) which applied a sinusoidal voltage at select frequencies across the sample. The current was measured by the potentiostat and the phase relationship between the applied voltage and the measured current was analyzed by the FRA. The output of the FRA was the real and imaginary components of the impedance at each measured electrical frequency.

A Sula Technologies DLTS setup was used to perform the capacitance–voltage measurements and the DLTS experiments. The cryostatic chamber and temperature controller from this setup were also used to perform the temperature controlled impedance experiments.

3.2 Electrochemical Impedance Spectroscopy

The underlying principles behind impedance spectroscopy is presented first to better the understanding of the impedance equipment. A basic schematic of the electronics is then given.

3.2.1 Theory

The best single reference on the theory and application of impedance spectroscopy is a technical report written by Gabrielli [22]. This section provides a brief overview of some of the key concepts.

The principle behind impedance spectroscopy is to relate a physical model to experimental data in the form of real and imaginary components of the impedance. This is done by relating the physical model to an equivalent circuit by means of appropriate governing equations. The equivalent circuit is composed of resistors, capacitors, inductors, and/or constant phase elements. The physical model, transformed into an equivalent circuit with real and imaginary components, is in a form that can be directly compared to the impedance data.

The electrochemical cell, or sample, can be thought of as a black box with two terminals where the black box consists of a circuit of electronic components mentioned above. The impedance of this circuit is $Z(\omega) = a(\omega) + jb(\omega)$ where Z is the complex impedance that can be related to a real component, $a(\omega)$, and an imaginary component, $b(\omega)$, both being real numbers and having units of Ohms. The electrical frequency is given by ω with units of radians per second, and $j = \sqrt{-1}$. All three impedance values are a function of potential. The potential dependence is not written explicitly because in typical impedance analysis the potential is fixed as a parameter while the frequency is varied.

Let the voltage perturbation applied across the terminals be represented by a sinusoid,

$$V(t) = V_o \sin \omega t \tag{3.1}$$

where V_o is the amplitude of the voltage perturbation. The above equation assumes that the voltage perturbation is referenced to the steady state potential value. The measured current that flows through the cell as a result of the applied voltage perturbation can be represented by a sinusoid,

$$I(t) = \frac{V_o}{Z(\omega)} \sin(\omega t + \phi(\omega)) + \Sigma_m A_m \sin(m\omega t - \phi_m(\omega)) + n(t) \tag{3.2}$$

where $Z(\omega)$ is the total impedance of the cell and $\phi(\omega)$ is the phase shift between the applied voltage and the measured current. If the electrochemical cell was a resistor, the phase shift would be zero. If the cell was a capacitor, the phase shift would be $\frac{\pi}{2}$ (90°). Harmonics of order m are included in this expression as well as the contribution of random noise, $n(t)$. Harmonics are due to non–linear system response (see Cogger [23]).

The current expression above contains more information than is desired; only the impedance as a function of ω is sought, not $m\omega$, and noise decreases the confidence in the impedance data. The digital frequency response analyzer minimizes harmonic responses and noise through integration of equation (3.2) multiplied by either $\sin \omega t$ or $\cos \omega t$, *i.e.*,

$$I_r = \frac{1}{T} \int_0^T I(t) \sin \omega t dt = \frac{V_o}{Z(\omega)} \cos \phi(\omega) \quad \text{as} \quad T \longrightarrow \infty \tag{3.3}$$

and

$$I_j = \frac{1}{T} \int_0^T I(t) \cos \omega t dt = \frac{V_o}{Z(\omega)} \sin \phi(\omega) \quad \text{as} \quad T \longrightarrow \infty \tag{3.4}$$

where T is the integration time in integer multiples of the sinusoid period, $\frac{1}{2\pi\omega}$.

The integrals that contain the harmonic response are zero when the integration is over a complete cycle(s) because $\sin \omega t$, $\cos \omega t$, and $\sin m\omega t$ form an orthogonal set of functions (see Chapter 2 of Haberman [24]). The noise integral will tend towards zero as the integration time increases ($\frac{1}{T} \longrightarrow 0$). A trade off has to be made between "noise free" data ($T \longrightarrow \infty$) and a practical time length for the experiment (T is finite), particularly if the system is corroding. Non–stationary effects would not be eliminated in the noise integral even as $T \longrightarrow \infty$. The long integration time or short integration time in the FRA parameter menu refers to the integral time T.

The impedance is the voltage divided by the current which can be represented as a complex number, *i.e.*,

$$Z_{cell} = Z_{r,cell} + jZ_{j,cell} = \frac{V_r + jV_j}{I_r + jI_j} \tag{3.5}$$

where the subscript "cell" has been added to denote that this is the impedance of the cell (sample). Because the voltage is the applied signal, phase shift set to zero as a reference, the imaginary component of the voltage is zero ($V_j = 0$). The real part of the current is given by equation (3.3) and the imaginary part of the current is given by equation (3.4). These relations are easily derived with the aid of phasor diagrams used in introductory circuit books. A good reference is given by Smith [25].

The voltages and currents discussed so far occur across the sample. However, these values are modified by various gains in the potentiostat before reaching the frequency response analyzer. For instance, the voltage amplitude, V_o, from the signal generator will become KV_o where K is the transfer function of the potentiostat. The measured voltage passes through an amplifier of gain G_V before it reaches the FRA. The amplitude of the voltage signal at the FRA input becomes $G_V K V_o$. Likewise, the current signal becomes $G_I K V_o / Z_{cell}$ which is converted to a voltage signal by means of the measuring resistor, R. The current signal at the FRA input, in the form of a voltage, becomes $G_I R K V_o / Z_{cell}$.

The impedance that is actually measured by the FRA is

$$\begin{aligned} Z_{meas} = Z_{r,meas} + j Z_{j,meas} &= \frac{G_V K V_o}{G_I \frac{KV_o}{Z_{cell}} R \cos\phi + j G_I \frac{KV_o}{Z_{cell}} R \sin\phi} \\ &= \frac{G_V}{G_I} \frac{Z_{cell}}{R} \frac{1}{\cos\phi + j \sin\phi}. \end{aligned} \tag{3.6}$$

The relationship between the measured real and imaginary impedance and the cell real and imaginary impedance is

$$Z_{r,meas} = \frac{G_V}{G_I} \frac{1}{R} Z_{r,cell} \tag{3.7}$$

and

$$Z_{j,meas} = -\frac{G_V}{G_I} \frac{1}{R} Z_{j,cell}. \tag{3.8}$$

The ratio of the voltage and current gains in the potentiostat is designed to be unity over the frequency range used. Hence, the measuring resistor is the proportionality constant between the measured impedance and the cell impedance.

3.2.2 Signal Generation and Analysis

The potentiostat and frequency response analyzer are interfaced to the computer and controlled with the ZPLOT [26] software package. ZPLOT should not be used without first reading the ZPLOT manual and the operating manuals for the potentiostats [27, 28] and the frequency response analyzer [29]. The default parameters selected by ZPLOT are rarely appropriate to the system being studied.

3.2.2.1 Potentiostat

There are several parameters involved with each potentiostat (Solartron 1286 or PAR 273) that must be tailored to each experiment. The first is the desired cell configuration. All potentiostats allow at least three electrodes to be monitored or controlled; these are the working electrode, the counter electrode, and the reference electrode. The working electrode is the electrode of interest (*i.e.,* the sample electrode) and its potential is controlled relative to the reference electrode via the counter electrode. For instance, suppose that the working electrode is desired to be 0.5 volts more positive than the reference electrode, the potentiostat would adjust the potential of the counter electrode to maintain this desired potential drop.

The reference electrode potential versus the working electrode potential is measured with an operational amplifier, also referred to as an "op amp". It is worthwhile here to describe briefly the function of the operational amplifier (see for instance Malvino [30]). A basic inverting operational amplifier circuit is given in Figure 3.2(a) and the equivalent circuit for an operational amplifier is given in Figure 3.2(b). The minus sign is used to designate that the input is connected to the minus terminal of the op amp which means that the output has a phase shift of -180 degrees.

The overall voltage gain of the op amp circuit, G, is defined as the ratio of the output voltage, V_{out}, to the input voltage, V_{in}, ($G = V_{out}/V_{in}$). The differential voltage gain, A, is defined as the ratio of $V_{out}/(V_1 - V_2)$. A is large ($\approx 100,000$) and V_{out} is limited to the external driving voltage which is roughly 15 volts, therefore $V_1 - V_2$ is very small ($\approx 10^{-6}$ volts).

The op amp varies the output voltage V_{out} in response to the input voltage V_{in}. The output voltage is feedback through the resistor, R_f, and thus affects the potential at the input terminal such that $V_1 - V_2$ is small. R_{in} is the input impedance of the op amp and is typically 2 MΩ, large enough that essentially no current flows through the op amp. There are two main features of an ideal op amp; no potential drop or current flow across the input terminals. Thus, a potential or current measurement can be made without affecting the system being measured.

The overall voltage gain can be determined from the differential gain equation ($A(V_1 - V_2) = V_{out}$) and the fact that the currents through the two external resistors, R_f and R_s, must be equal because no current flows through the op amp ($I_s = I_f = I$). With these two assumptions, the voltage across the op amp can be expressed as

$$V_2 - V_1 = V_{in} - IR_s \tag{3.9}$$

or

$$V_2 - V_1 = V_{out} + IR_f. \tag{3.10}$$

Equation (3.9) can be related to the differential voltage gain, A, in order to derive an explicit current expression, *i.e.*,

$$-A(V_{in} - IR_s) = V_{out} \Longrightarrow I = \frac{V_{out} + AV_{in}}{AR_s}. \tag{3.11}$$

This current expression is substituted into equation (3.10) to eliminate I, *i.e.*,

$$-AV_{out} - A\frac{V_{out} + AV_{in}}{AR_s}R_f = V_{out}. \tag{3.12}$$

The last expression is rearranged to yield the overall voltage gain,

$$G = \frac{V_{out}}{V_{in}} = \frac{-AR_f/R_s}{1 + A + R_f/R_s}. \tag{3.13}$$

For $A \gg R_f/R_s$, the overall voltage gain reduces to $-R_f/R_s$. This result could have been derived from the start with the assumption that $V_2 = V_1 = 0$, *i.e.*,

$$I = \frac{V_{in} - 0}{R_s} = \frac{0 - V_{out}}{R_f} \quad \text{or} \quad \frac{V_{out}}{V_{in}} = -\frac{R_f}{R_s} = G. \tag{3.14}$$

This information will be used later in analyzing the current measurement capabilities of each potentiostat and in determining the proper bandwidth selection to ensure stability in potentiostatic control of the system.

The PAR 273 potentiostat is capable of applying ±100 volts between the counter and working electrodes just to maintain a fraction of a volt difference between the reference and working electrodes. As a safety precaution, the PAR 273 is installed with a cell enable/disable switch so that the electrode leads can be adjusted without fear of electrocution. The Solartron 1286 is capable of applying ±20 volts between the counter and working electrodes and does not have such a safety switch.

Three electrode configurations are used primarily in electrochemical experiments. For example, one of the systems studied here had a 0.5 M NaCl (pH 10) electrolytic solution with a cuprous oxide working electrode, a saturated calomel reference electrode (SCE), and a platinum counter electrode. The two cell configuration is used primarily in solid state systems such as semiconductor devices with either metal Schottky barriers or Ohmic contacts. It is extremely important to be mindful of the correct lead connections when using the two electrode cell configuration; the reference electrode lead is connected (shorted) to the counter electrode lead. This permits the measurement of the working electrode versus the reference electrode and control of this potential difference via the counter electrode. Never use just the reference or counter electrode alone versus the working electrode. This would not allow potentiostatic control of the system because the reference electrode can only measure the potential between the reference and the working electrodes and the counter electrode can only control the potential between the reference and the working electrodes by passing current between the counter electrode and the working electrode.

Simplified block diagrams that include only the options relevant to the impedance work done in this work are presented for the Solartron 1286 (Figure 3.3) and the PAR 273 (Figure 3.4). Not surprisingly, both block diagrams have the same general features, with the exception of the current measurement circuit and the second reference electrode capability of the Solartron 1286. The second reference electrode permits measurement of the potential difference between two sections of the electrolytic solution. The counter electrode maintains this potential difference. Note that the potential of the working electrode is not measured in this four electrode configuration. Thus, all two and three electrode cell configurations require that the second reference electrode lead be shorted to the working electrode.

3.2.2.2 Current measurement

There are differences in the current measurement circuits of the two potentiostats that are worth discussing here. Both potentiostats determine the current passing through the working electrode with the aid of a high quality measuring resistor in series with the working electrode. The current flows through the resistor which creates a potential drop across the resistor equal to IR_m. This potential drop is measured with an op amp as shown in the block diagrams.

Two differences in the current measuring circuits become evident from a closer look at the block diagrams. The first is that the resistors in the Solartron range from 0.1 Ω to 100 $k\Omega$ and those of the PAR range from 1 Ω to 10 $M\Omega$. The second difference is that the Solartron uses an additional op amp to boost the low current signal (1, 10, and 100 $k\Omega$ resistors). A possible disadvantage of the latter point is the introduction of the additional op amp circuit in the Solartron. This circuit might impart some of its own impedance versus frequency response into the cell data being measured.

The larger measuring resistors in the PAR 273 permit low current measurements with less noise. This statement is based on the simple relation $V = IR$; small I requires a large R to maintain the same potential drop and, hence, potential sensitivity. Currents in the nanoamp range are observed when the impedance of the cell is large ($10^8\Omega$), as was the case for most of the devices analyzed in this work. This brings up an important point–how to be certain that the signal being measured actually reflects the cell alone or the electronic system of the potentiostat as well, especially if the impedance of the cell is near the limits of detection. The majority of systems analyzed can be represented as passive circuit elements such as resistors, capacitors, and inductors; some of the very same components used to apply and measure the voltage and current.

A solution to this dilemma was suggested by Dr. Ron Haak of the ALZA Corporation. He proposed that the impedance data of the cell being analyzed be regressed to a suitable equivalent circuit and to build this circuit with resistors and capacitors on a breadboard. The same impedance scan would be performed on this equivalent circuit and the result compared with the original cell data. This test proved to be very fruitful in the case of the ZnS:Mn thin film electroluminescent panel. Both potentiostats gave reproducible results; however, these results depended on the potentiostat used. The Solartron showed a change in phase angle from around -90 degrees to around -20 degrees at low frequencies ($\approx$ 0.2 Hz); whereas, the PAR indicated that the phase angle remained relatively constant around -90 degrees in the same frequency range.

The Solartron cell data was regressed with ZFIT [31] to a resistor in series with a resistor and capacitor parallel to each other as shown in Figure 3.5(a). This equivalent circuit was built with resistors and capacitors, measured to three significant figures with an Ohm meter and a capacitance meter. The PAR impedance scan of this circuit was identical to the predicted results (see Figures 3.6 and 3.7). The Solartron could only predict the qualitative features of the equivalent circuit, even though the original cell data was obtained with the Solartron.

The PAR 273 cell data was regressed in a like manner to yield the equivalent circuit shown in Figure 3.5(b). Note that the capacitor is roughly the same as for the equivalent circuit above but that the parallel resistor is about 40 times greater. This resistor was considered to be so large that it could be assumed to have an infinite resistance, thus reducing the circuit to a resistor and capacitor in series. This circuit would have a -90 degree phase shift at low frequencies. It was not expected that the resistor and capacitor in series was a good fit to the original data; however, it was adequate to test the behavior of each potentiostat to such a highly capacitive system such as the ZnS:Mn panel. The results from both potentiostats on the resistor–capacitor series are presented in Figures 3.8 and 3.9. The PAR was able to predict the capacitive nature much better than was the Solartron at low frequencies. Based on these series of experiments, it was decided that the PAR 273 was the appropriate choice in potentiostats to analyze the ZnS:Mn panel. Similar checks were performed for the other systems.

3.2.2.3 Stability and bandwidth

This subsection is a brief review of Chapter 9 of the Solartron 1286 operating manual [27]. A system is considered to be stable if its output is a direct response to an applied input signal. An unstable system can exhibit spontaneous undriven output or an output due to a previous input signal. Such a system could result in oscillations in the potentiostatic control of the system. In terms of operational amplifier theory, a system becomes unstable when the loop gain is greater than or equal to unity and the phase shift is 0 or ± 360 degrees.

The loop gain is defined as the product of all the gains that incorporate the loop. There are four gains in Figures 3.3 and 3.4:

1) G_1 – differential voltage gain of potential control amplifier, A_1,

2) G_c – cell gain,

3) G_2 – differential voltage gain of potential measurement amplifier, A_2, and

4) G_r – gain due to resistors R_1 and R_2 (not shown in Figure 3.4).

The last gain, G_r, is composed of resistors and hence will not impart a phase shift. It will only attenuate the signal. G_2 has been designed to be frequency independent with a gain of unity except at very high frequencies. The cell gain varies from cell to cell and the gain of the control op amp, G_1 is the parameter that can be varied to ensure stability.

The input signal to amplifier A_1 is connected to the minus terminal which means that the output will experience a phase shift of -180 degrees. If the cell being analyzed is capacitive, it will also impart a phase shift of -90 degrees for a total of -270 degrees. The differential voltage gain, G_1, is constant at low frequencies. However, the gain decreases at some frequency with an additional phase shift of -90 degrees as shown in Figure 3.10. The total phase shift becomes -360 degrees which means that the feedback signal is in phase with the input drive signal. The two signals add together at the minus terminal to form a larger amplitude input signal which the op amp amplifies with gain A_1 to form the output signal. The output signal is feedback to the minus terminal where it is added to the in phase input signal and again amplified. This cyclic behavior will lead to instability if the loop gain is greater than or equal to unity. For loop gains less than unity, the feedback signal would be attenuated upon each pass and the system would be stable.

The differential voltage gain of A_1 can be varied such that the unity loop gain occurs away from the -360 degree phase shift. This point can be graphically demonstrated with the aid of Figure 3.11 where two G_1 gains are shown. The uncompensated loop gain has unity gain at -360 degrees, and hence, is unstable. With the selection of a lower bandwidth gain (compensated) for the amplifier A_1, the phase shift at unity loop gain becomes -270 degrees and the system is stable.

The Solartron 1286 has ten ranges (labelled A to J) of bandwidths to choose from and the PAR 273 has two (labelled "high speed" and "high stability"). Bandwidths C, D, and "high stability" have high and low pass frequency filters and, due to the extra electronic circuits, should only be selected if none of the other bandwidths are appropriate. An oscilloscope is used to determine the proper bandwidth with a potential square wave form applied across the cell. If the bandwidth is too wide, the square wave will exhibit 'ringing' which indicates that the differential voltage gain is too large. Too narrow of a bandwidth means that the gain is too small and the resulting wave form will be overdamped. A correct bandwidth choice will yield a square wave form on the oscilloscope with perhaps a slight overshoot.

3.2.2.4 Frequency response analyzer

The Solartron 1250 Frequency Response Analyzer (FRA) performs two duties: 1) generates an output wave form and 2) analyzes up to two input wave forms. The generated wave form can be a sine, square, or triangle wave at frequencies from 10 μ Hz to 65,500 Hz. These wave forms are synthesized with a 10 MHz crystal oscillator along with digital processing to provide a frequency accuracy of 1 part in 10,000 [32]. This method is reported to be better than the previous phase–lock methods. The FRA generator has the added advantage that it protects itself from both short–circuiting of its HI and LO terminals as well as excessive external voltage (> ±18 volts).

The analyzer section of the FRA can simultaneously measure two input channels which in the work presented here is the voltage and current (converted to a voltage signal) from the potentiostat. The analyzer displays the ratio of the two channels in either rectangular $(a + jb)$, polar (r, θ), or log polar $(\log r, \theta)$ coordinates. Integration time on the analyzer menu specifies the maximum number of cycles to be integrated if the convergence criteria is not meet. At least 1 cycle is integrated below frequencies of 655 Hz and 61 cycles above 655 Hz regardless of the number of cycles specified in the ZPLOT parameter menu. Only one integration over a cycle is necessary to eliminate the D.C. and harmonic frequencies of the fundamental frequency desired. However, integration over more cycles reduces the amount of noise in each channel.

Two convergence criteria are available in the auto integration mode. The first is labelled "short integration time" which means that the channel measurement is continued and averaged until the standard deviation of the average does not vary by more than ±10 percent of the average or until the maximum integration time has been reached as specified above. An "Error 82" message will occur when the latter case has occurred; this does not imply that the data point should be discarded, only that the convergence criteria has not been met. The second option is labelled "long integration time" and is similar to the short integration time except that the convergence criteria is ±1 percent. The convergence criteria can be applied to either input channel. The current channel (Channel 1) should be chosen since this channel is the response of the voltage signal from the generator and is expected to have the most noise. The voltage channel is the controlled channel in the potentiostat and hence is not expected to be as noisy.

There are five voltage range selections for the channel input (30 mV, 300 mV, 3 V, 30 V, and 300 V) as well as an Auto selection feature. Before making a selection, other than the Auto selection, the Channel 1 and 2 signals from the potentiostat should be measured on the oscilloscope to determine the peak voltage. Note that the voltage channel (Channel 2) can be fixed because the applied sine wave remains relatively constant when the Solartron 1286 or the PAR 273 is used as a potentiostat. However, the current channel (Channel 1) is best left in the Auto selection because the current varies several orders of magnitude as the impedance of the cell changes with frequency. The reverse is true when in galvanostatic (current) control.

3.2.3 Experimental Difficulties

The large impedance of the materials used in this study made collection of accurate impedance data difficult at low frequencies. The experimental frequency range was constrained by an unfavorable signal to noise ratio. The currents measured at low frequencies were extremely small (in the nanoamp range), and currents smaller than this were beyond the range of the potentiostat used. This problem was addressed in this work by increasing the amplitude for the potential perturbation from the 10 mV characteristic of electrochemical studies to 1 to 3 V for the ZnS:Mn panel and the ZnO varistors. Reproducibility of the impedance response for different magnitudes suggested that the system response was linear at even these large amplitudes.

The signal to noise ratio was further improved, when possible, by increasing the area of the device tested. For example, the current output of the electroluminescent panel was increased by 2 orders of magnitude by electrically coupling 100 pixels. The electronic transitions involving deep–level states have time constants that are large in comparison to the inverse of the lowest measured frequency. In other words, the imaginary impedance did not tend toward zero at the lowest frequency used. The large time constant for these systems was also apparent in the hysteresis observed for these systems. In order to obtain reproducible data, it was necessary to wait between each run to allow the electronic states to equilibrate. Approximately 24 hours was required between runs for the ZnS:Mn TFEL panel and the unaged varistor; whereas, a wait time of 1 hour was sufficient for the aged varistor, and a few minutes for the GaAs semiconductor and the copper/cuprous oxide electrode. The problem of memory effects in electroluminescent panels is discussed in references [33, 34, 35].

3.3 Standard Characterization Techniques

Two standard techniques were used in this work to provide a comparison to electrochemical impedance spectroscopy. These are Mott–Schottky or C-V profiling and Deep–Level Transient Spectroscopy (DLTS).

3.3.1 Mott–Schottky Profiling

The Mott–Schottky relationship is used to determine the concentration of shallow level states in the bulk of a semiconductor. This relationship can be represented as [36]

$$\frac{1}{C^2} = \frac{2(V_{bi} - V - \frac{kT}{q})}{A^2 q K \varepsilon_o (N_D - N_A)} \tag{3.15}$$

where C is the measured capacitance, V_{bi} is the built in potential, V is the applied potential, A is the surface area, $K\varepsilon_o$ is the permittivity of the semiconductor, N_D is the donor concentration, and N_A is the acceptor concentration. Deep–level states can be incorporated into this expression by considering them to be either donor–like or acceptor–like in nature. Assume, for example, that the deep–level state is acceptor–like in nature in that it becomes negative when ionized. Equation (3.15) then becomes

$$\frac{1}{C^2} = \frac{2(V_{bi} - V - \frac{kT}{q})}{A^2 q K \varepsilon_o (N_D - N_A - N_T)} \tag{3.16}$$

where N_T the concentration of deep–level states that are ionized, occupied by an electron.

The above equation can be expressed explicitly in terms of the net donor concentration through the derivative of equation (3.16) with respect to the applied potential. The result is

$$N_D - N_A - N_T = -\frac{2}{A^2 qK\varepsilon_o}\frac{1}{d(\frac{1}{C^2})/dV}. \tag{3.17}$$

Equations (3.16) and (3.17) are implemented easily by plotting the inverse of the square of the measured capacitance ($\frac{1}{C^2}$) versus the applied voltage, V. The slope of this curve is referred to as the Mott–Schottky slope and is used in equation (3.17) to calculate the net donor or acceptor concentration. If the semiconductor is n–type the slope will be negative, and for p–type semiconductors the slope is positive.

The capacitance is measured by applying a high frequency sinusoidal voltage perturbation about the set applied voltage bias. This frequency is typically in the MHz range, values too high to change the occupation of most deep–level states. Changes in the Mott–Schottky slope with frequency as a parameter have been attributed to interface states or bulk deep–level states in the literature [1,2,37–39].

3.3.2 Deep–Level Transient Spectroscopy (DLTS)

Yau and Sah [40] first demonstrated the influence of deep–level states on the capacitance decay of a pulsed semiconductor as a function of temperature in 1971. This concept was further refined by Lang [19] in 1974 into the present day technique known as Deep–Level Transient Spectroscopy (DLTS). DLTS has become the most widely used technique to determine the energy and concentration of deep–level states. The theory behind DLTS is briefly outlined in this section for a n–type Schottky barrier, a more involved presentation for other situations is given by Lang [19].

A Schottky barrier is required on one side of the semiconductor and an Ohmic contact on the other side. The semiconductor is held at a steady state reverse bias and periodically pulsed in the forward bias direction. The reverse bias creates a space charge region of width W_r which is a region void of majority carriers (electrons). All deep–level states with energy greater than the Fermi energy level, E_F, will emit their electron into the conduction band. Steady state equilibrium is reached when all such states are empty. This is shown in an energy versus distance diagram in Figure 3.12 (a).

The semiconductor is forward biased for approximately 1 msec. The majority carriers are swept into the space charge region at a rate that can be considered to be instantaneous. The width of the space charge region decreases to W_f and the energy level of the deep–level state falls below the Fermi energy level in a portion of the region $W_r - W_f$. All the states in this portion capture electrons to reach a forward biased equilibrium. This situation is shown in Figure 3.12 (b). These states will not have time to capture electrons, reach equilibrium, if the pulse is too short in duration.

The semiconductor is again reverse biased which creates a transient space charge region of width $W_{r'}$ that decays to the reverse biased equilibrium value, W_r. $W_{r'} > W_r$ because the trapped electrons are neutral species, and hence, more conduction band electrons vacate in order to maintain the same reverse bias level as before. The deep–level state energy level is above the Fermi energy level in a portion of the newly acquired space charge region. The trapped electrons in this region will be emitted into the conduction band to reach the reverse biased equilibrium. The space charge width will decrease towards the equilibrium width W_r as these trapped electrons are emitted into the conduction band. This transient case is shown in Figure 3.12 (c). It is this transient decay of the space charge region that is monitored in DLTS experiments by observing the time dependence of capacitance.

The emission rate constant can be extracted from the transient capacitance from the capacitance–voltage relationship of a space charge region, equation (3.16), and an Arrhenius expression for the emission rate of electrons from the deep–level state.

Equation (3.16) can be rearranged into a more appropriate form,

$$C(t) = \sqrt{\frac{A^2 qK\varepsilon_o(N_D - N_A - n_T(t))}{2(V_{bi} - V - \frac{kT}{q})}} \tag{3.18}$$

where it is noted that the capacitance and deep–level state concentration are a function of time. It is convenient here to define a capacitance difference, *i.e.*,

$$\Delta C(t) = C(t) - C_{ss} = \sqrt{\frac{A^2 qK\varepsilon_o}{2(V_{bi} - V - \frac{kT}{q})}}\left(\sqrt{N_D - N_A - n_T(t)} - \sqrt{N_D - N_A - n_{T_s}}\right) \tag{3.19}$$

where C_{ss} and n_{T_s} are the steady state reverse bias capacitance and deep–level concentration, respectively. This equation is made dimensionless upon division by C_{ss},

$$\frac{\Delta C(t)}{C_{ss}} = \frac{\sqrt{N_D - N_A - n_T(t)} - \sqrt{N_D - N_A - n_{T_s}}}{\sqrt{N_D - N_A - n_{T_s}}} = \sqrt{\frac{N_D - N_A - n_T(t)}{N_D - N_A - n_{T_s}}} - 1. \tag{3.20}$$

Equation (3.20) relates the measured transient capacitance to the transient concentration of ionized deep–level states. This is not of the form typically used in DLTS analysis to estimate the total concentration of states. Two additional assumptions are needed; the steady state (reverse bias) concentration of deep–level states is several orders of magnitude smaller than the net donor concentration, and the forward bias pulse is long enough that all of the deep–level states are occupied. The former assumption can be expressed as

$$\frac{\Delta C(t)}{C_{ss}} = \sqrt{1 - \frac{n_T(t)}{N_D - N_A}} - 1. \tag{3.21}$$

A Taylor's series approximation of equation (3.21) about $\frac{n_T(t)}{N_D - N_A} \approx 0$ yields

$$\frac{\Delta C(t)}{C_{ss}} = -\frac{1}{2}\frac{n_T(t)}{N_D - N_A}. \tag{3.22}$$

The latter assumption means that the total concentration of states is proportional to the capacitance difference immediately following the forward bias, *i.e.*,

$$\frac{\Delta C(t = 0)}{C_{ss}} = -\frac{1}{2}\frac{N_{TT}}{N_D - N_A} \tag{3.23}$$

where N_{TT} is the total trap concentration. This is the relationship used in most DLTS analysis.

The kinetic expression for the rate of change of trap occupancy is used to link the concentration, and hence, the measured capacitance to the desired emission rate constant. The transient concentration of trapped electrons can be expressed as

$$\frac{dn_T}{dt} = -e_n N_T + e_p(N_{TT} - N_T) + c_n N(N_{TT} - N_T) + c_p P N_T \tag{3.24}$$

where e_n is the emission rate constant for electrons, e_p is the emission rate constant for holes, c_n is the capture rate constant for electrons, and c_p is the capture rate constant for holes. The concentration of electrons and holes in the space charge region can be neglected when the reverse bias is applied. Hence, there are no electrons or holes to be captured by the deep–level state and equation (3.24) is simplified to

$$\frac{dn_T}{dt} = -N_T(e_n + e_p) + e_p N_{TT}. \tag{3.25}$$

Under steady state reverse bias conditions,

$$\frac{N_{Ts}}{N_{TT}} = \frac{e_p}{e_n + e_p}. \tag{3.26}$$

An electron trap under reverse bias with energy greater than the Fermi energy will tend to be empty of electrons at steady state, or in other words, $N_{Ts} \approx 0$. This implies from equation (3.26) that $e_n \gg e_p$. Equation (3.25) can be solved easily with the neglect of the hole emission rate constant, the result being

$$n_T(t) = N_{TT} \exp(-e_n t). \tag{3.27}$$

Equations (3.22) and (3.27) are combined to provide the necessary link between the measured capacitance and the electron emission rate,

$$\Delta C(t) = -\frac{1}{2}\frac{N_{TT} C_{ss}}{N_D - N_A} \exp(-e_n t) \propto \exp(-e_n t). \tag{3.28}$$

As can be seen from this relation, the capacitance decay following the forward bias to reverse bias step change is a simple exponential in time. Lang [41], in a preceding paper, also addresses the case in which non–exponential transient decays are present. He indicated that this case is likely for intermediate and shallow level states. DLTS can still be applied to non–exponential transients, however, the concentration of states cannot be determined *via* equation (3.23) because an extrapolation to $\Delta C(t = 0)$ is required [41].

The emission rate constant is given by

$$e_n = \sigma_n \gamma_n \frac{1}{g} T^2 \exp(\frac{E_T - E_C}{kT}) \tag{3.29}$$

where σ_n is the capture cross–section of the trap, g is the trap spin degeneracy, and $E_T - E_C$ is the energy difference between the deep–level state and the conduction band. γ_n is a temperature independent quantity that is derived in Section 4.3.2 along with equation (3.29).

The procedure of DLTS can be best illustrated with the aid of Figure 3.13 where capacitance is shown as a function of both temperature and time. In the actual DLTS experiment, the complete capacitance decay is not monitored but rather, it is only determined at two points in time as shown in Figure 3.13. The difference between these two capacitance readings is the output signal that is typically connected to the y–terminal of an x–y plotter (the x–terminal is connected to the temperature output signal). Time t_1 is referred to as the initial delay, *i.e.*, the time between the start of the reverse bias (end of the forward bias) and the time of the first capacitance measurement. The ratio of t_1 and t_2 is designed to be a constant. It is convenient to consider the emission rate, e_n, as the inverse of a time constant, τ.

The capacitance difference, $C(t_1) - C(t_2)$, will have a peak value when the selection of the two correlation times (t_1 and t_2) occur as near as possible to the beginning and end of the transient decay, respectively. These two times are constant throughout each DLTS experiment, and hence, the peak capacitance difference is found by varying the emission rate via the temperature (see equation (3.29)). The relationship between the emission rate and the two correlation times can be easily derived. From equation (3.28) we have

$$C(t_1) - C(t_2) \propto \exp(-e_n t_1) - \exp(-e_n t_2). \tag{3.30}$$

The derivative of equation (3.30) with respect to e_n is zero at the peak capacitance difference. Setting the derivative of equation (3.30) to zero yields

$$e_n = \ln(\frac{t_1}{t_2})/(t_1 - t_2). \tag{3.31}$$

The goal is to find the temperature at which equation (3.31) is true, *i.e.,* the temperature at which $C(t_1) - C(t_2)$ has its maximum value. A plot of the natural log of e_n/T^2 versus the inverse of the peak temperature will be a straight line of slope $(E_T - E_C)/k$ and the intercept is proportional to σ_n.

3.3.3 DLTS Equipment and Parameters

The DLTS equipment was purchased through Sula Technologies (Palo Alto, CA) and consisted of a cryostatic chamber, a Sula Technologies Deep Level Spectrometer, a Lake Shore Model 805 Temperature Controller (Lake Shore Cryotronics, Inc. of Westerville, OH), a 7-liter Dewar flask to hold liquid nitrogen, and a variable speed circulation pump to draw the liquid nitrogen through the cryostatic chamber, along with various tubing and electrical connectors. A roughing pump was supplied by Pete Axson, a technician for Dr. Timothy J. Anderson's research group located in this department. The roughing pump is used to evacuate the cryostatic chamber to prevent condensation from forming on the semiconductor sample at low temperatures and also to minimize heat loss to the environment due to convection.

Inside the cryostatic chamber was a thermal block connected to a heater element, controlled by the temperature controller, and a stainless steel tube through which liquid nitrogen is drawn. The combination provides a wide range of controllable temperatures. The lowest temperature possible is 78K to 84K and the highest practical temperature is around 420K. A rather large brass block (0.25 inch thick × 3 inch diameter) was attached to the thermal block by teflon screws with a thin teflon spacer in between the thermal block and the brass block to provide electrical insulation. The anode and cathode leads were loose wires; there was no sample mount provided. It was left to the purchaser to design his or her own sample mount.

Pat Watson, while at Cornell University, suggested that the brass block be replaced because of a severe temperature lag between the thermal block and the sample due to the block's large mass. He recommended replacing the brass block with a sapphire disk (1mm thick × 2 cm diameter) that has a thin layer of gold deposited on it. The sapphire has good thermal conductivity and is also an electrical insulator. One of the leads was connected to the gold with silver paste and the other lead was soldered to a needle. Silver paste was used to improve the connection between the gold layer and the semiconductor metal backing. However, the gold layer became damaged after repeated pasting and removal of the samples.

It was decided to replace the sapphire disk with a 304 stainless steel plate of similar dimensions. The original teflon sheet was placed between the steel and the thermal block. Stainless steel was chosen because it does not form an electrically insulating oxide layer as do iron and most brasses particularly at higher temperatures. However, it is near impossible to solder to stainless steel. It was necessary to attach one of the leads to the steel plate by drilling a small hole at one corner of the plate, bending this corner up away from the thermal block, twisting a wire through the hole, and caking the wire and hole with silver paste. The other lead was connected to a blunted needle. The needle was blunted with a honing stone to prevent it from gouging into the semiconductor. Vacuum grease was used on both sides of the teflon spacer to improve the thermal contact. The needle was mechanically fastened to the thermal support with a cut and heat–formed plexi–glass sheet in the shape of a 'T'. The stainless steel plate was also fixed in place with a plexi–glass block screwed into the thermal block.

A small copper shell was "riveted" to the stainless steel plate to house the 100Ω platinum temperature sensor used to measure the sample temperature, the other temperature sensor (sensor A) is in the thermal block and is used as the control sensor by the temperature controller. With this configuration, the thermal block sensor temperature reached 78K at its lowest and the sample sensor temperature reached 84K at its lowest. Although the temperature controller can maintain a temperature as high as 800K, it was found from experience that at temperatures above 420K problems arose due to the coaxial cables shorting out near the stainless steel plate. This problem was minimized by keeping the cables as far from the thermal block as possible.

The Sula Technologies Deep Level Spectrometer did not have an IEEE–488 computer interface although the temperature controller did. Initially, a Metrabyte Corporation (Taunton, MA) analog-to-digital converter was used but was later overloaded in a non–related experiment. However, a Hewlett–Packard 7090A x–y plotter was available in our lab capable of analog–to–digital data acquisition with 12 bit resolution. The interface programs for both the Metrabyte converter and the HP 7090A [42, 43] were written in Microsoft QuickBASIC 4.5 computer language. The program for the HP 7090A is included in the appendix.

The operating instructions for the deep level spectrometer [44] are a concise description of the front panel controls. It is expected in the manual that the user has a thorough understanding of Lang's [19] paper before using the spectrometer. Several important relationships will be stressed here. The manual lists two heuristics that should be obeyed in the choice of front panel parameters. These are:

> The period (time between pulses) is greater than or equal to the length of the pulse plus ten times the initial delay (time t_1). This guarantees that enough time has been allowed for completion of the correlation process, *i.e.*, measurement of $C(t_1)$ and $C(t_2)$.
>
> The period is less than or equal to one hundred times the initial delay. This guarantees that the electronics of the spectrometer have time to respond to the pulsing in order to make an accurate capacitance measurement.

The ratio of times t_1 and t_2 is designed to be constant in the spectrometer as recommended by Lang [19]. For this spectrometer, the rate window, or time constant, at the peak capacitance difference is

$$\tau = \frac{1}{e_n} = 4.3 \times t_1 \tag{3.32}$$

where t_1 is also referred to as the initial delay. Another important relationship used to estimated the state concentration is the capacitance difference at the start of the reverse bias,

$$\Delta C(t=0) = 3[C(t_1) - C(t_2)] \text{ evaluated at its peak value.} \tag{3.33}$$

The steady state capacitance or background capacitance, C_{ss}, is determined with a 150 mV peak to peak voltage sinusoid at a frequency of 1 MHz applied across the semiconductor sample. Deep–level states are not expected to influence the signal at such a high frequency. The resulting current is converted to a voltage signal which is applied across a phase sensitive detector. The steady state capacitance is also used in the Mott–Schottky plots described in an earlier section, however, the forward bias pulse should be off during these measurements.

3.4 Optical Spectroscopy

A SPEX Model 1681B Spectrometer was used to create the monochromatic light. The spectrometer was chosen over lasers because of the greater range of wavelengths available (the bandgap of the semiconductors analyzed ranged from 1.4 to 3.6 eV). Three diffraction gratings were used with rulings of 1200, 600, and 300 grooves/mm for visible light, near infrared, and infrared, respectively. The light source was a 450 W Xenon lamp that emits wavelengths of light greater than 300 nm. The light beam exiting the spectrometer passed through: (1) a order sorting filter to eliminate higher energy harmonics of the fundamental wavelength, (2) a collimating lens to convert the divergent rays of light to parallel rays, (3) neutral density filters to control the light intensity, and (4) a focusing lens to focus the beam onto the sample. The intensity of the focused light spot was typically 5 to 20 mW/cm^2 and the dimensions were 8×6 mm.

The intensity of the monochromatic beam was dependent on the wavelength of the light. This was due to the Xenon light source and the diffraction gratings. The intensity of the focused light as a function of the wavelength are shown for each order sorting filter in Figures 3.14 to 3.17 with the diffraction grating and the spectrometer exit/entrance slit width as parameters. Curves are shown for two diffraction gratings in Figure 3.14 because the intensity with the 600 grooves/mm grating was larger than that of the 1200 grooves/mm grating for wavelengths greater than 660 nm.

The intensity was not measured for each experiment. Instead, the intensity of the light exiting the spectrometer was determined for each selected wavelength from Figures 3.14 to 3.17. The intensity was reduced to the desired value with neutral density filters and, in some cases, small variations of the exit slit width. Checks were made periodically on the accuracy of this method. There were some indications that the intensity spectrum is changing as the Xenon lamp ages. An estimate was made during the last month of experiments of the error in the intensity value by comparing the desired intensity with the intensity measured after the appropriate neutral density filters. It was found that the intensity varied by approximately 22 percent of the desired value. The error should be less for experiments that were conducted earlier. The order of experiments was: cuprous oxide in alkaline–chloride solution, ZnS:Mn electroluminescent panel, n–type GaAs, and ZnO varistors. For the GaAs sample, the intensity was measured before the impedance experiments for each wavelength to be used and, thus, should have a much lower error in intensity.

The bandpass of the spectrometer is the band of wavelengths that pass through the exit slit and is determined from the dispersion (wavelength in nanometers divided by the slit width in millimeters) and the exit slit width in millimeters. For instance, the 1200 grooves/mm grating (dispersion of 3.7 nm/mm) set at a wavelength of 500 nm and an exist slit width of 5 mm will have a bandpass of 18.5 nm, or in other words, light of wavelength 490.75 to 509.25 nm will pass through the exit slit. The dispersion value is considered constant for each diffraction grating and harmonic order of the wavelength that is selected [45]. The dispersion is 3.7 nm/mm for the 1200 grooves/mm grating, 7.2 nm/mm for the 600 grooves/mm grating, and 14.4 nm/mm for the 300 grooves/mm grating all at the fundamental wavelength of the grating.

The bandpass is one disadvantage of the spectrometer over a laser. The exact location of an optical transition is obscured by the range of wavelengths that exit the spectrometer. A small bandpass minimizes this uncertainty, but also reduces the spot size and the intensity of the beam. It is also necessary to check if the range of wavelengths exceeds the range of the order sorting filter. For instance, if the spectrometer is set at 720 nm, light of wavelength 730 nm and its harmonic wavelength at 365 nm will also pass if the bandpass is large. The harmonic at 365 nm is the wavelength of concern because the 410–720 nm order sorting filter begins to pass light of this wavelength as can be seen from an inspection of Figure 3.14.

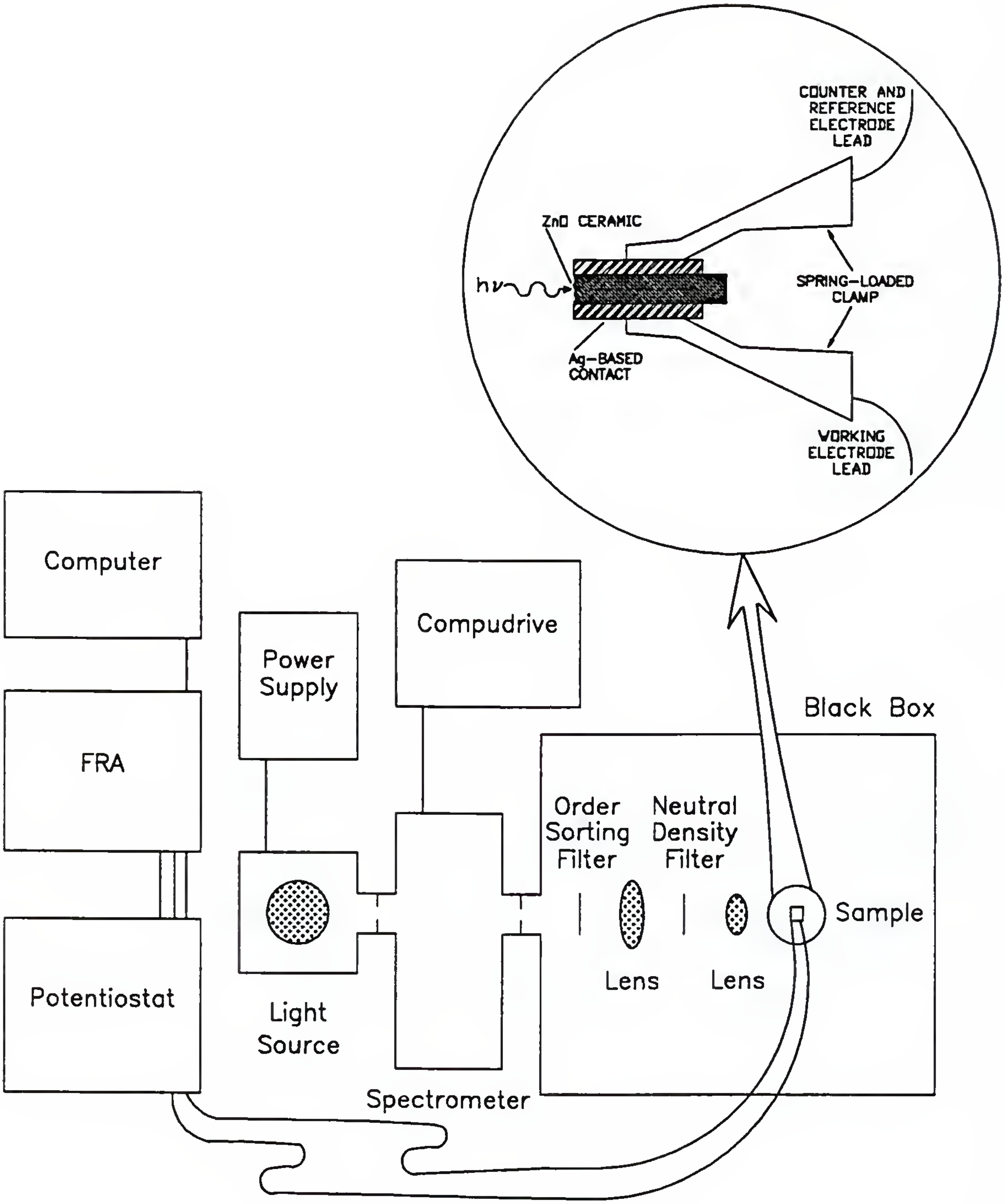

Figure 3.1: Experimental setup for Deep–Level Impedance Spectroscopy.

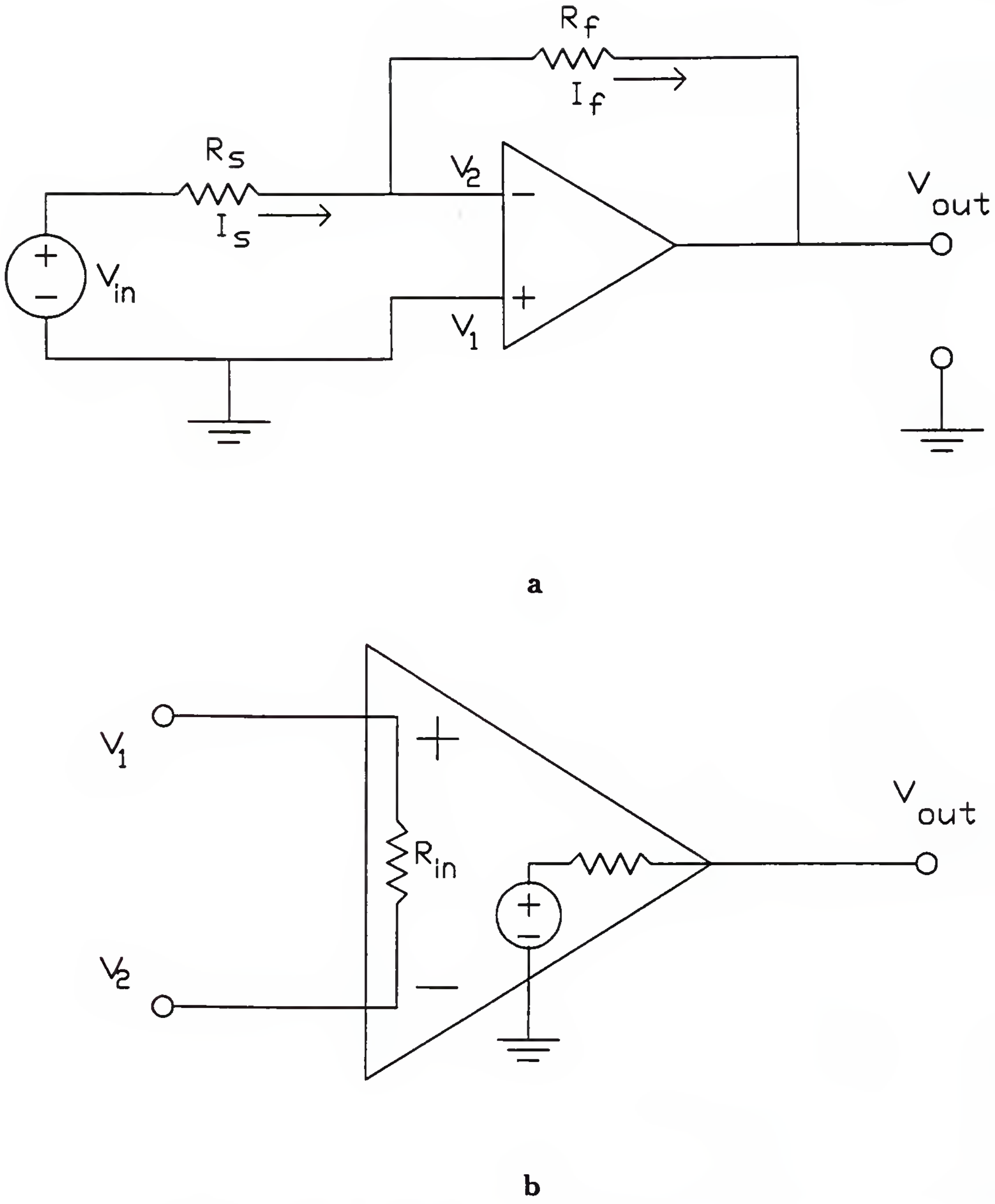

Figure 3.2: Basic inverting operational amplifier circuit (a) and overly simplified equivalent circuit of an operational amplifier (b).

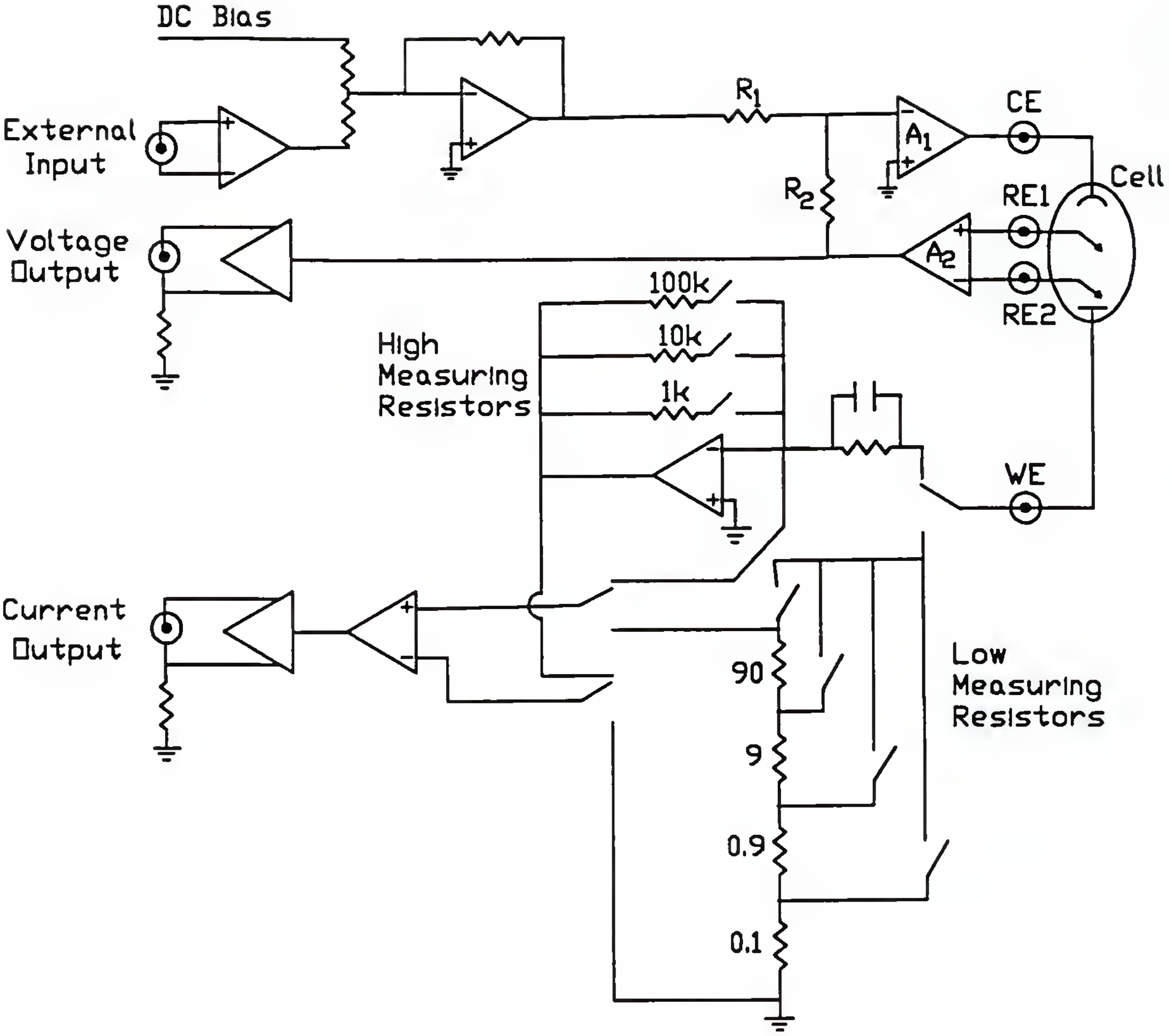

Figure 3.3: Simplified block diagram for the Solartron 1286.

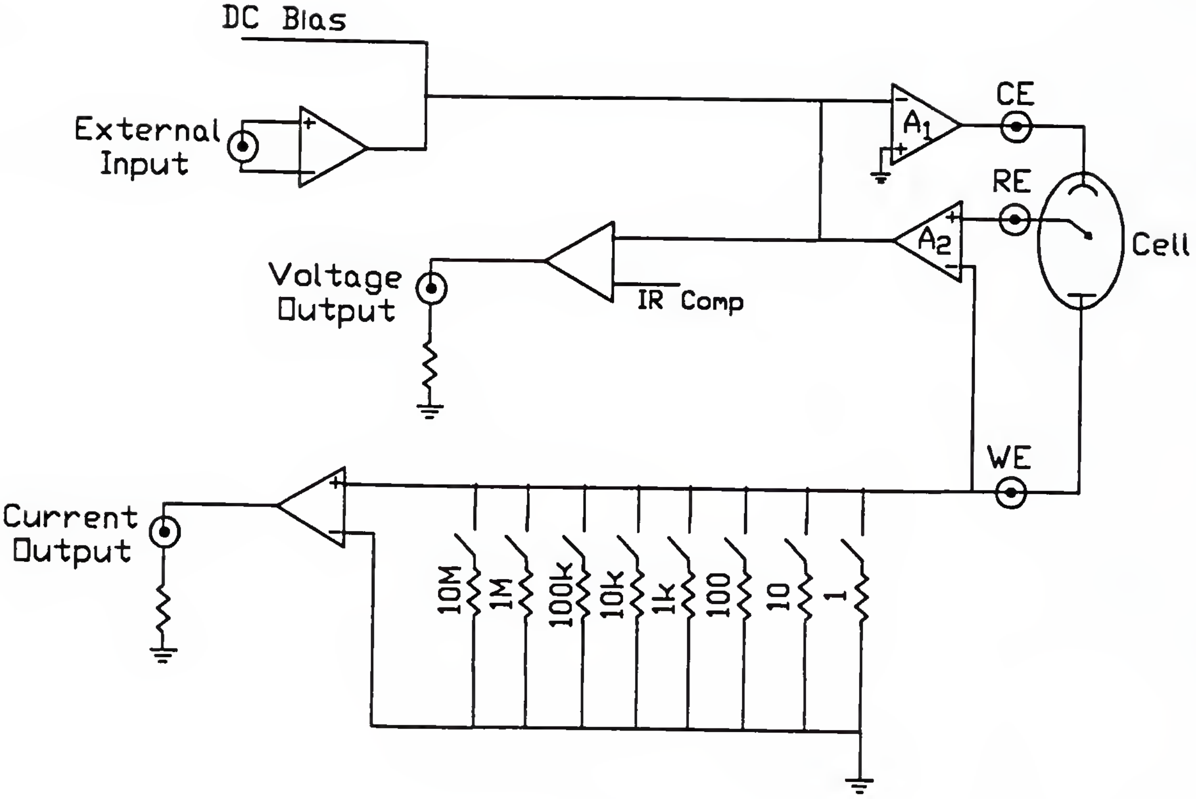

Figure 3.4: Simplified block diagram for the PAR 273.

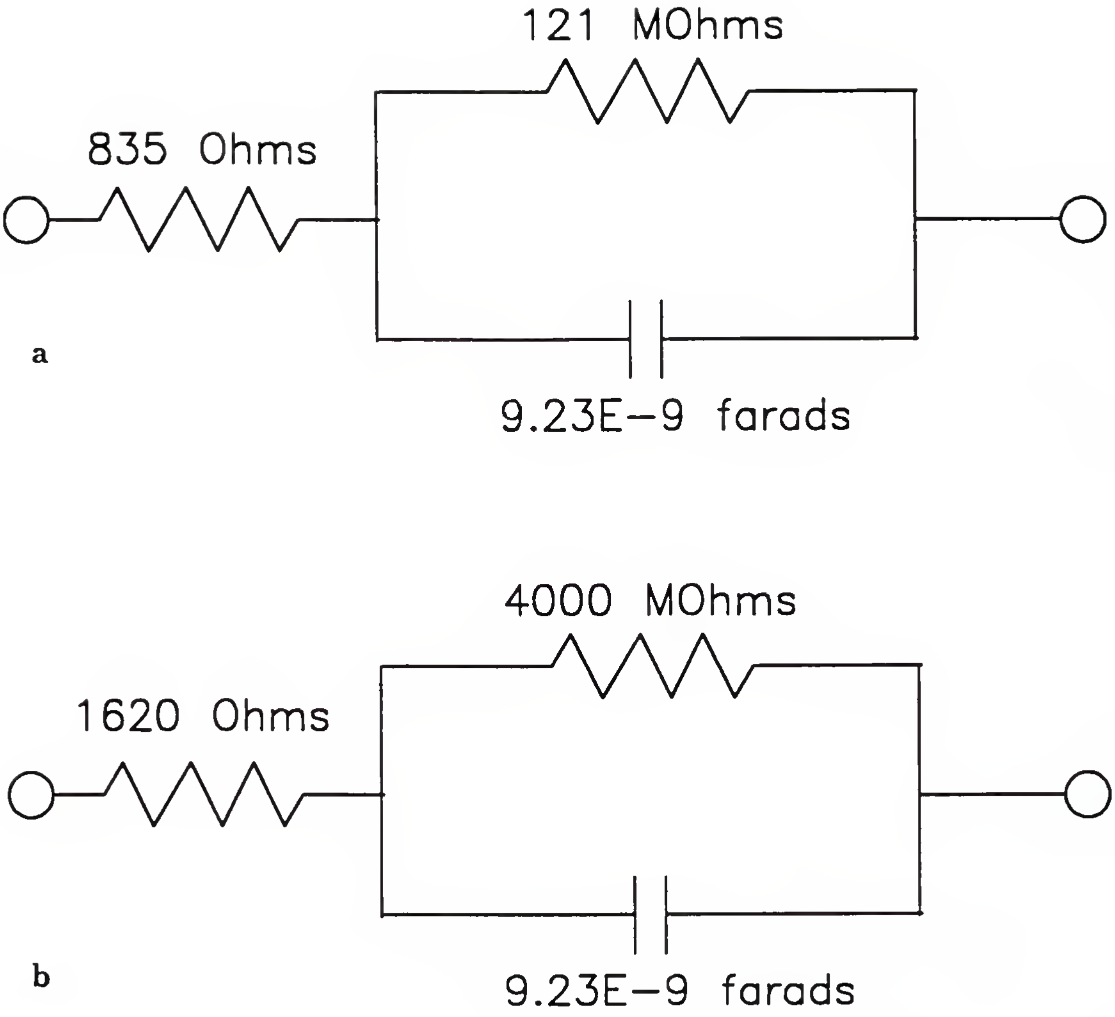

Figure 3.5: Equivalent circuit from regression of (a) Solartron 1286 and (b) PAR 273 impedance data.

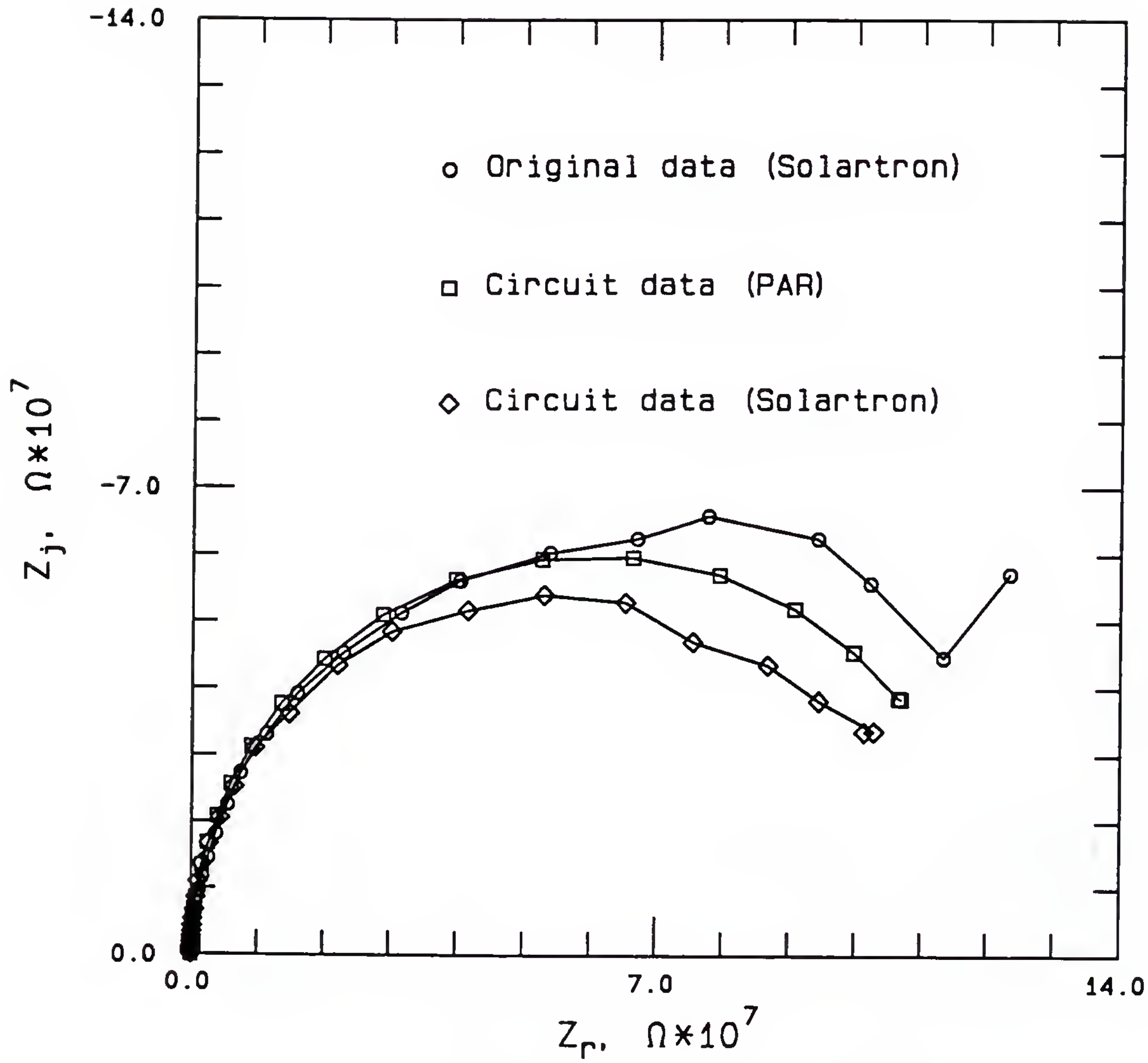

Figure 3.6: Comparison of Solartron cell data and equivalent circuit data for the Solartron and the PAR potentiostats in the form of an impedance plane plot.

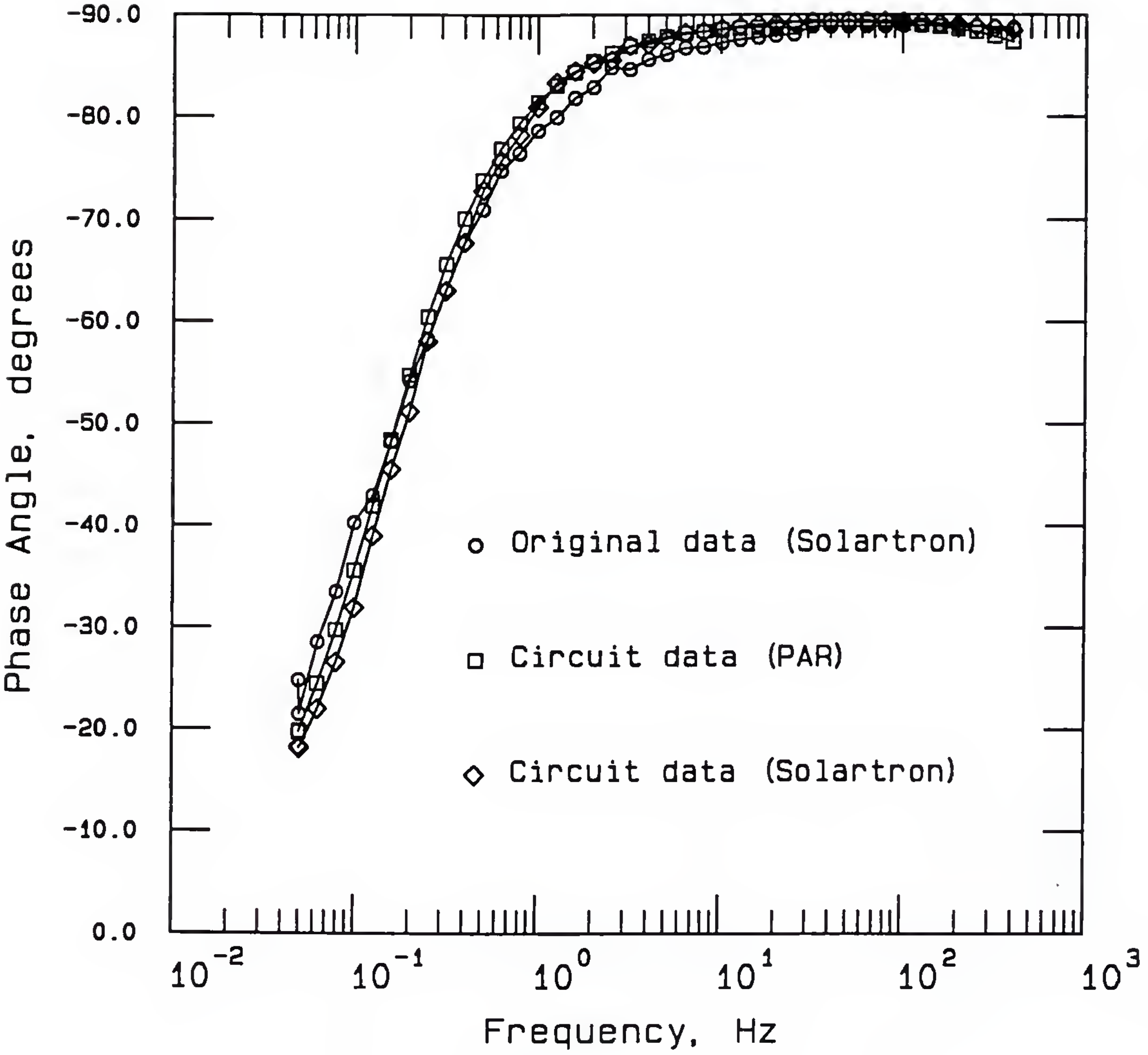

Figure 3.7: Comparison of Solartron cell data and equivalent circuit data for the Solartron and the PAR potentiostats in the form of phase angle as a function of frequency.

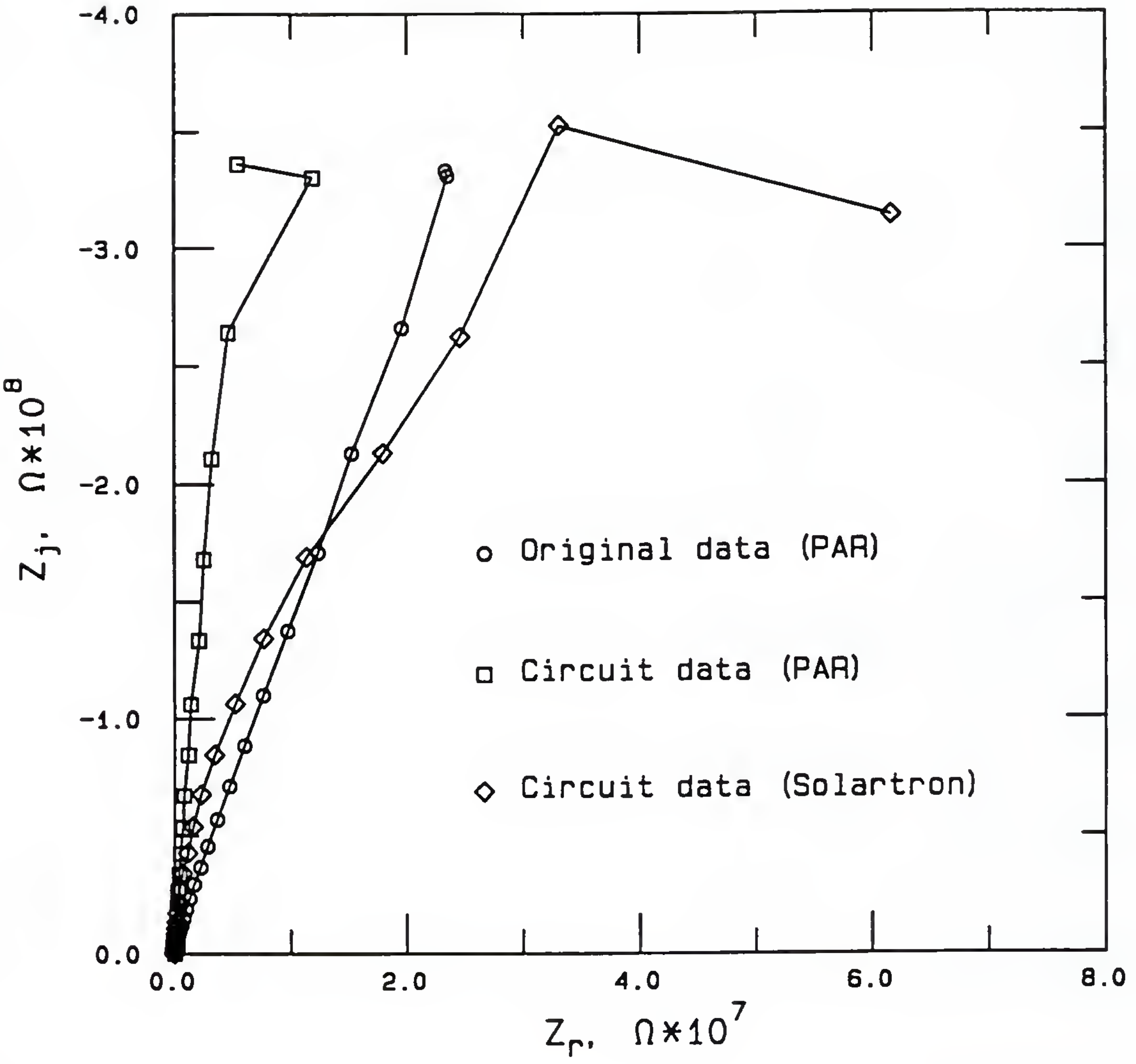

Figure 3.8: Comparison of PAR cell data and equivalent circuit data for the Solartron and the PAR potentiostats in the form of an impedance plane plot.

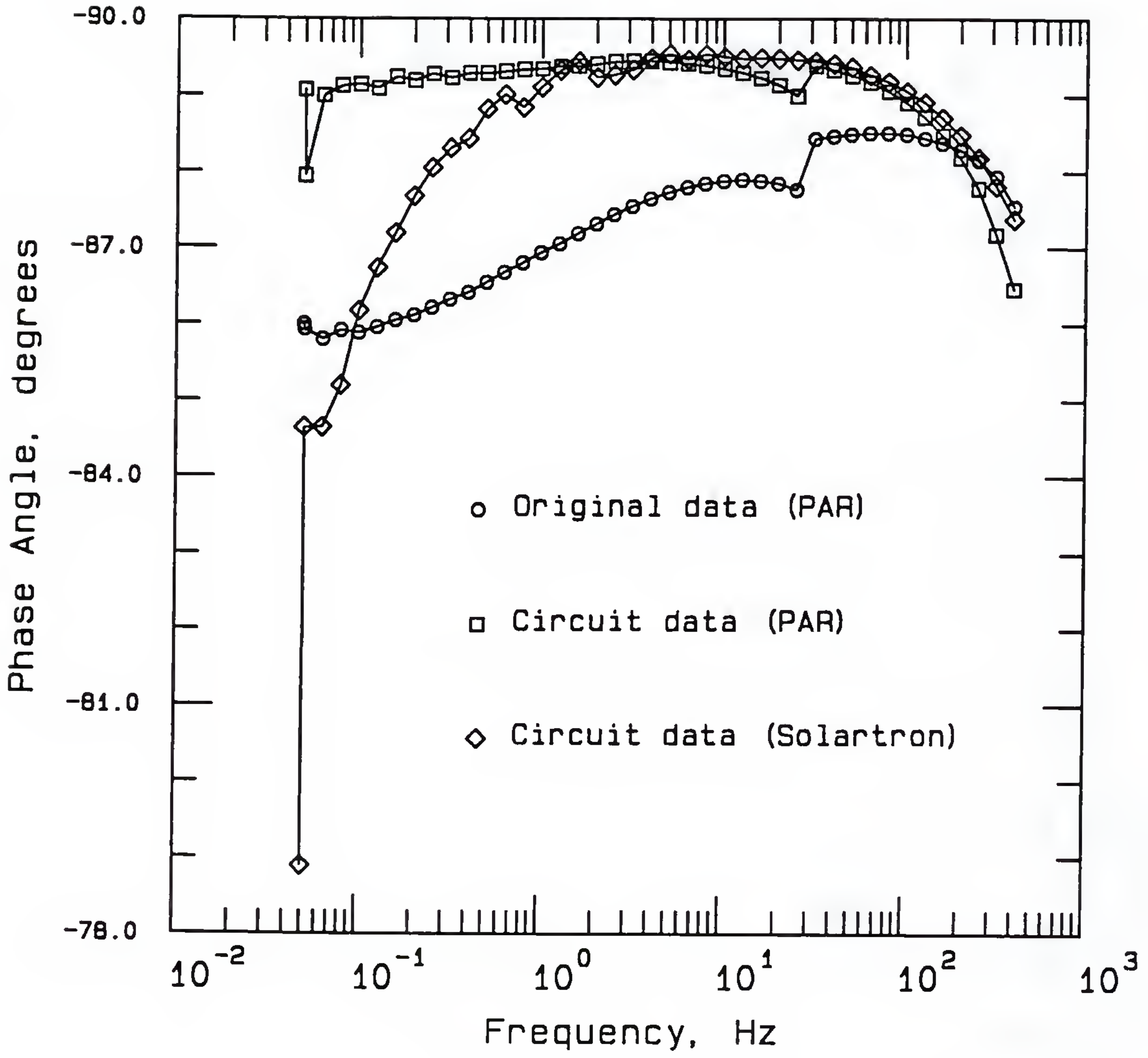

Figure 3.9: Comparison of PAR cell data and equivalent circuit data for the Solartron and the PAR potentiostats in the form of phase angle as a function of frequency.

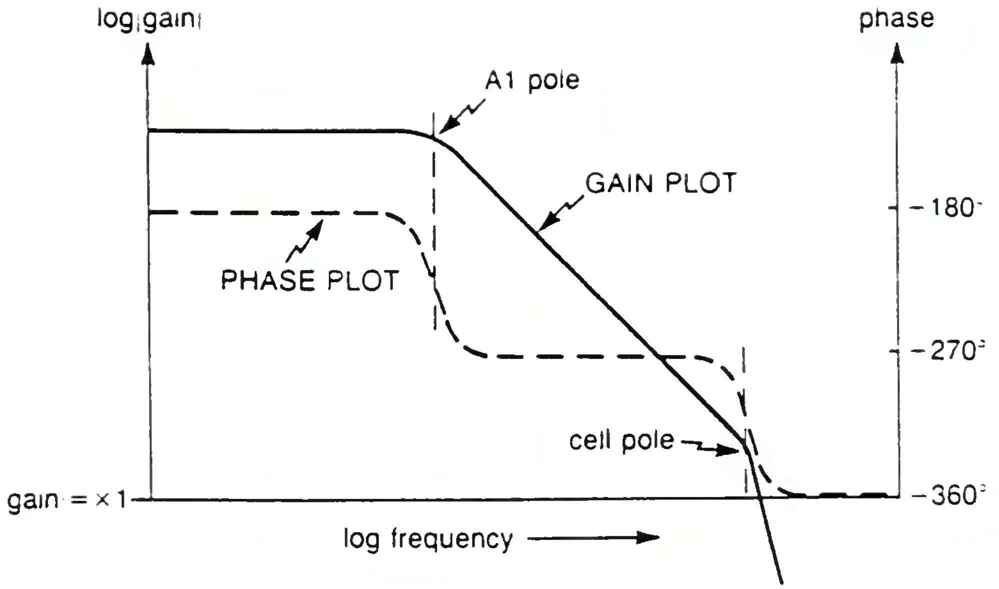

Figure 3.10: Frequency dependence of gain and phase shift for control op amp [27].

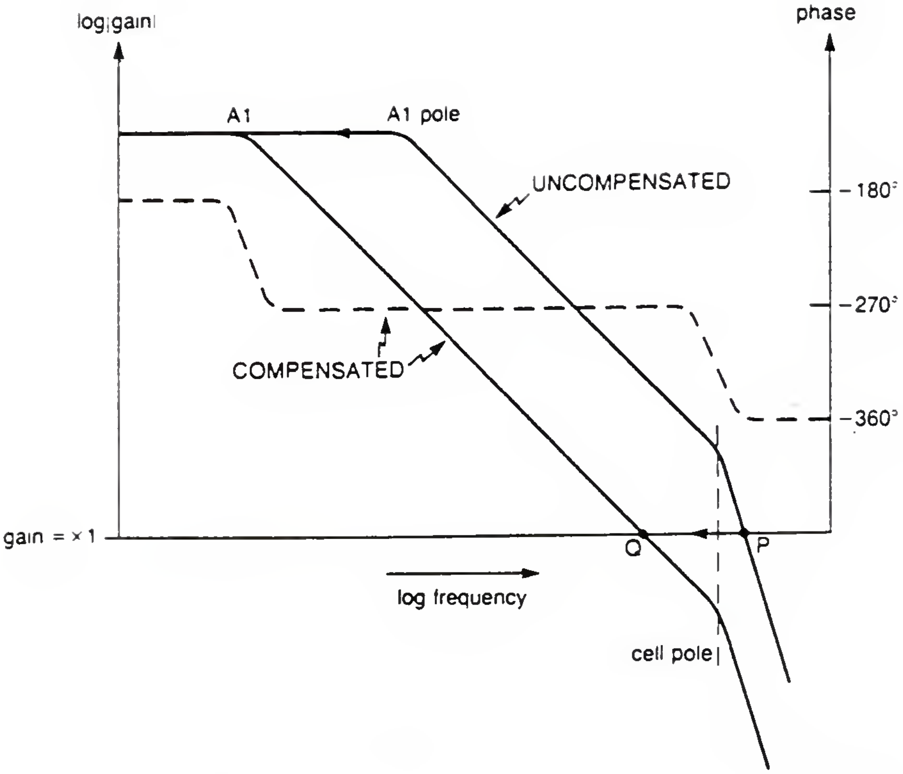

Figure 3.11: Compensated (stable) and uncompensated gain and phase shift for control op amp [27].

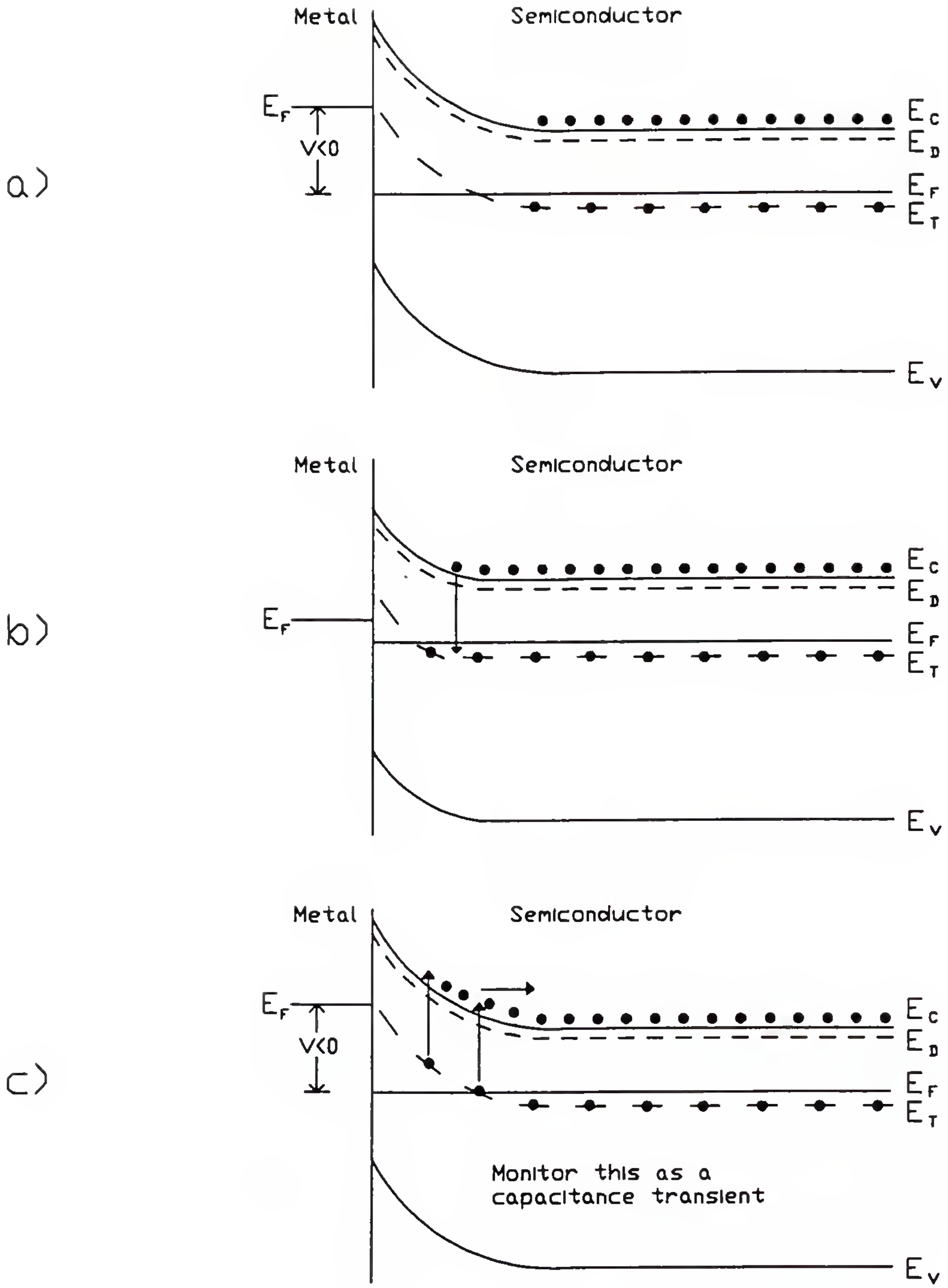

Figure 3.12: Energy levels as a function of distance for a n–type semiconductor under (a) equilibrium reverse bias, (b) equilibrium forward bias, and (c) transient reverse bias.

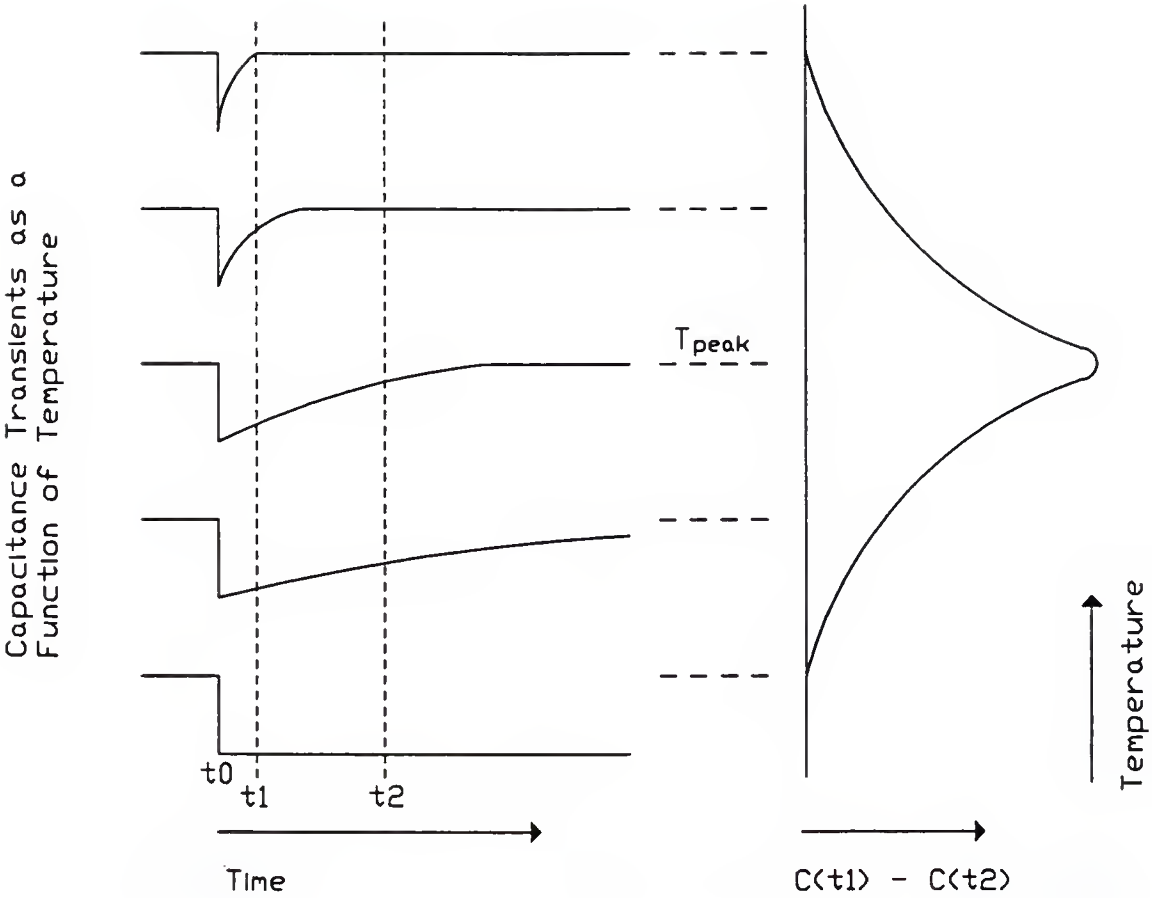

Figure 3.13: Capacitance decay as a function of time and temperature (left) and capacitance difference as a function of temperature (right).

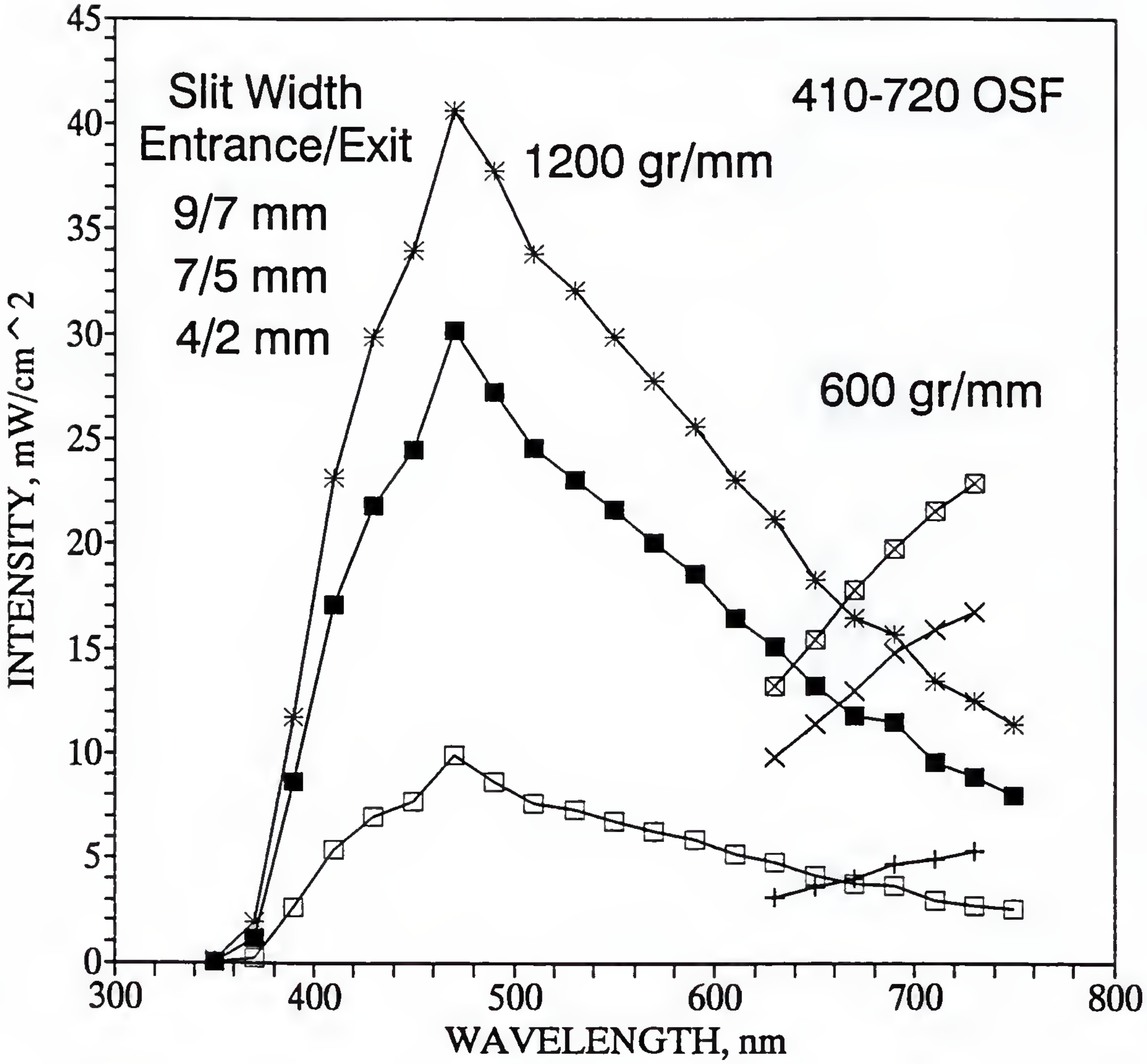

Figure 3.14: Intensity of the focused light as a function of the wavelength for the 410–720 nm order sorting filter with 1200 and 600 grooves/mm diffraction gratings and the spectrometer exit/entrance slit width as parameters.

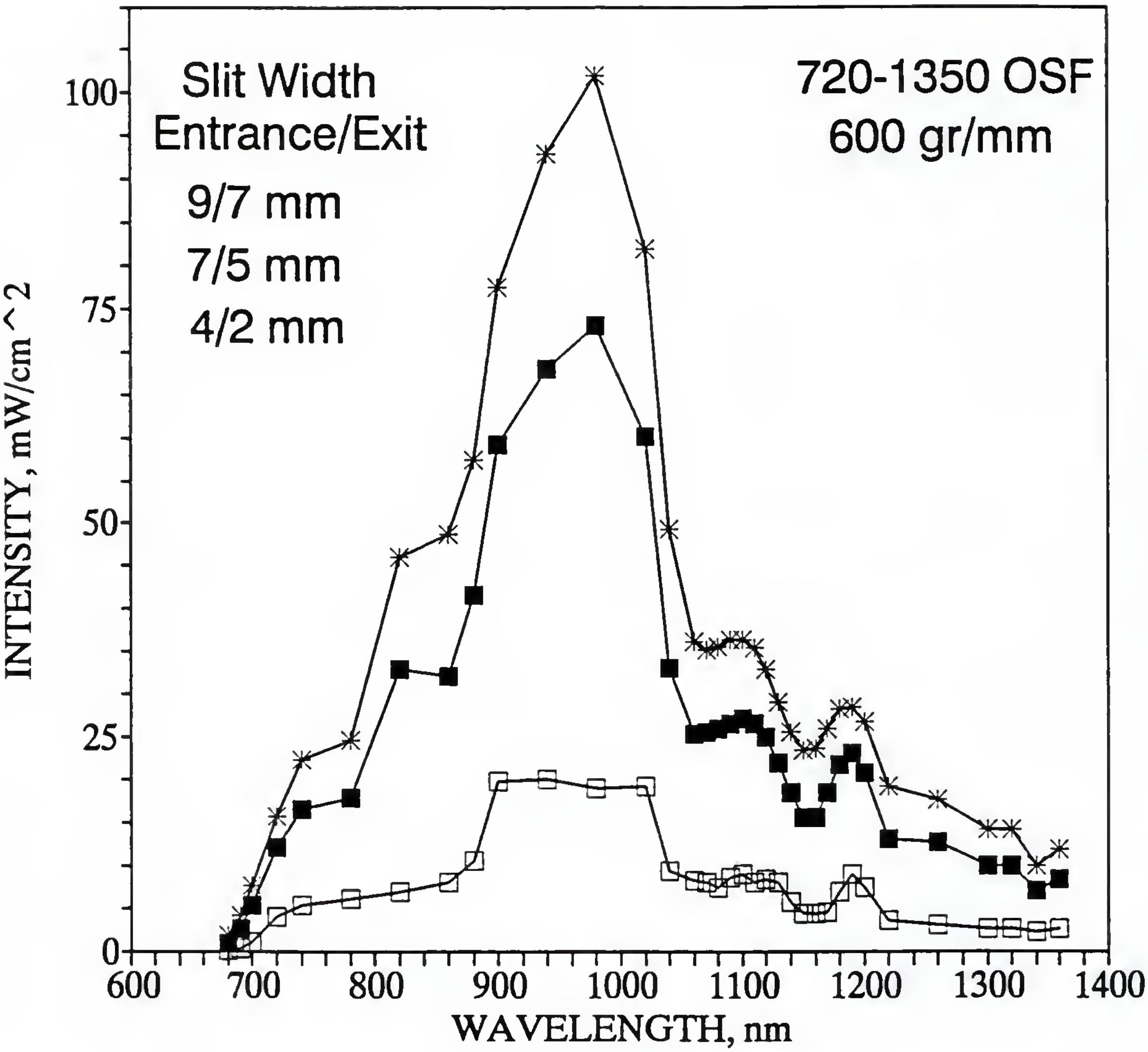

Figure 3.15: Intensity of the focused light as a function of the wavelength for the 720–1350 nm order sorting filter with the 600 grooves/mm diffraction grating and the spectrometer exit/entrance slit width as parameters.

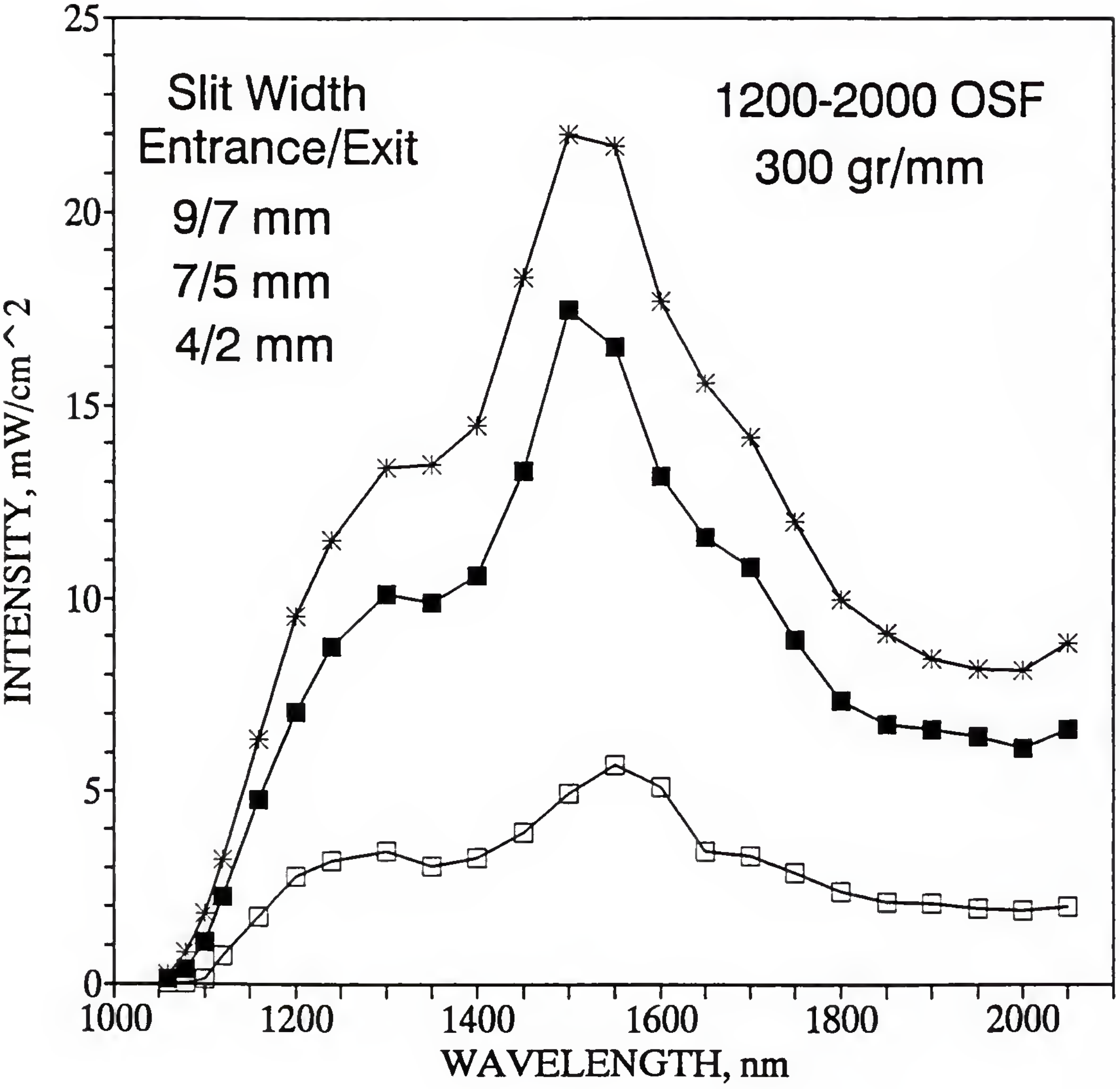

Figure 3.16: Intensity of the focused light as a function of the wavelength for the 1200–2000 nm order sorting filter with the 300 grooves/mm diffraction grating and the spectrometer exit/entrance slit width as parameters.

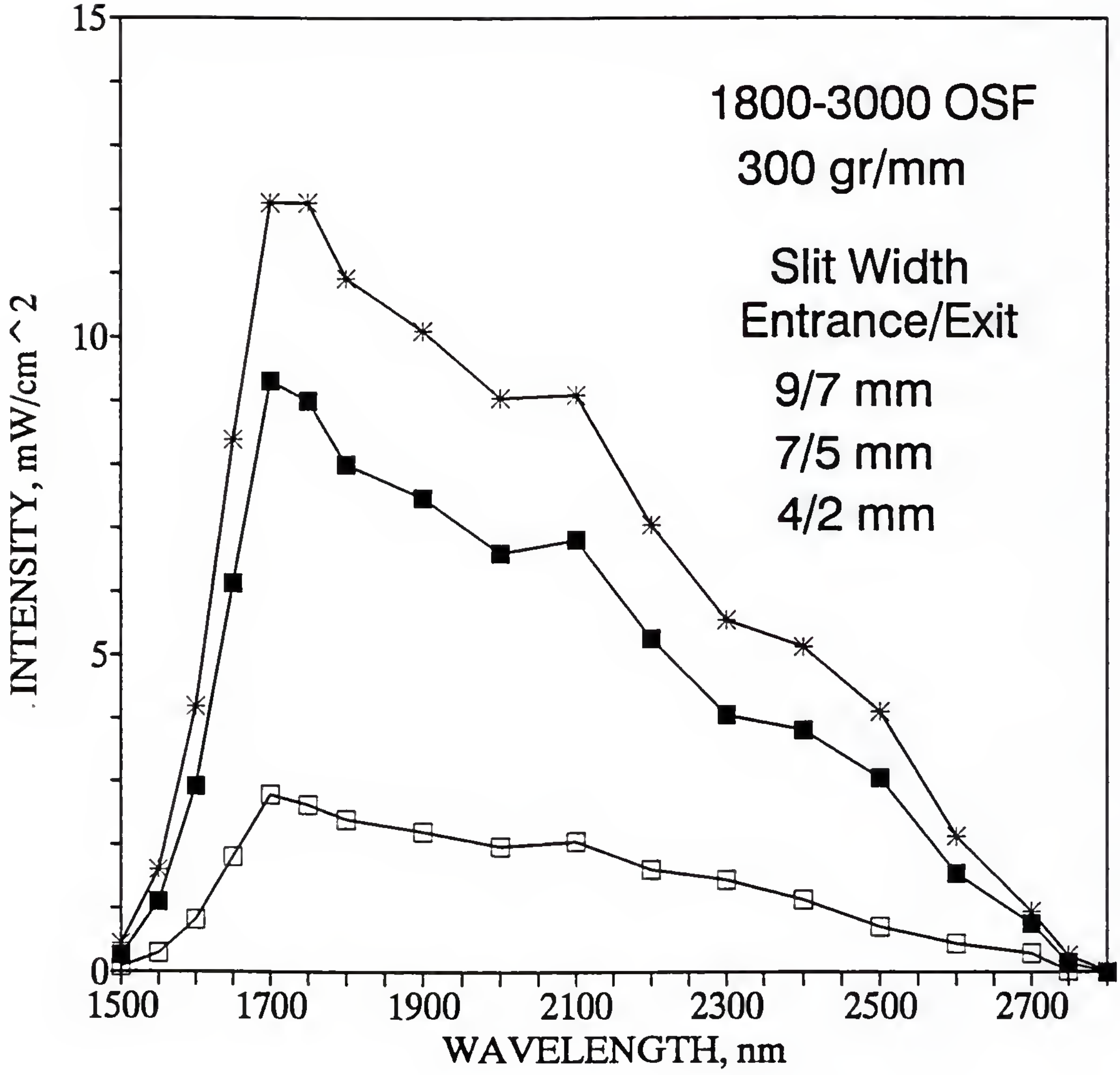

Figure 3.17: Intensity of the focused light as a function of the wavelength for the 1800–3000 nm order sorting filter with the 300 grooves/mm diffraction grating and the spectrometer exit/entrance slit width as parameters.

CHAPTER 4

DEVELOPMENT OF PROCESS MODEL

The objective of this chapter is to develop a mathematical model that describes transport and reaction processes involving deep–level states. Some physical insight into the electronic processes of these states is provided in the first section. In the following sections, the governing equations for both bulk and surface states are developed, and the model is posed in terms of an equivalent circuit composed of resistors, capacitors, and current generators. Finally, various assumptions are made to obtain a usable circuit.

4.1 Shockley Read Hall Processes

The influence of deep-level states or traps on the statistics of electron–hole recombination was first described by Shockley and Read [46] and Hall [47]. Deep–level states, as their name implies, lie close to the middle of the energy band gap of the semiconductor. Due to the large energy separation from the valence band and conduction band edges, deep–level states are not fully ionized at room temperature. In contrast, shallow–level states are those considered to be fully ionized at room temperature due to thermal excitation.

The interaction between a deep–level state and electrons and holes can be described by four processes represented in Figure 4.1. Process (a) involves a conduction band electron that comes in the vicinity of a deep–level state and is "trapped" by it. In order for this electron to be trapped, it must lose an amount of energy equal to $(E_C - E_T)$ by either radiative (photon) or non–radiative (phonon) processes, or a combination of both. Process (b) involves a trapped electron being emitted to the conduction band after receiving an amount of energy equal to $(E_C - E_T)$ from either optical or thermal excitation for instance.

Process (c) is the capture of a deep–level state electron by the valence band. Valence band electrons are more tightly held to the crystal atom than are the conduction band electrons, which have a much larger radius of travel (of several lattice constants). This allows the analogy that conduction band electrons can be considered to be negative charges floating in a sea of fixed positive nuclei (lattice sites) as in a metal. Valence band electrons are held in a tight sphere about a nucleus and can move only if the neighboring nucleus has an electron vacant site that it can jump into. Once the electron moves into this vacant site, it leaves a net positive charge behind. This positive charge will appear to be an entity, a hole, moving opposite that of the valence band electron. Thus, it is feasible to consider process (c) as being the capture of a valence band hole. For a deep–level state electron to be captured by the valence band, it must lose an amount of energy equal to $(E_T - E_V)$, or likewise, for a valence band hole to be captured by the trap, it must lose the same amount of energy.

Process (d) involves the emission of a valence band electron to the deep–level state after receiving energy $(E_T - E_V)$. This can also be thought of as hole emission from the deep–level state to the valence band since an electron vacant deep–level state has been filled by a valence band electron, thus leaving a hole in the valence band.

The four processes involving deep–level states can be described in terms of chemical reactions between two species, holes and electrons. Elementary reactions proceed at a rate that is directly proportional to the concentration of each reactant. Thus for process (a), the rate of conduction band electron capture is proportional to the concentration of conduction band electrons and the concentration of electron–vacant deep–level states. The concentration of conduction band electrons per energy increment can be expressed as $f(E)D(E)dE$ where f(E) is the probability that a state at energy E will be occupied by an electron and $D(E)$ is the density of states at energy E. The concentration of electron–vacant deep–level states can be expressed as $[1 - f_T(\mathbf{r},t)]N_{TT}(\mathbf{r})$ where $f_T(\mathbf{r},t)$ is the probability that a deep–level state will be occupied by an electron and is a function of position and time. $[1 - f_T(\mathbf{r},t)]$ is the probability that this state will be vacant or occupied by a hole. The total concentration of deep–level states is given by $N_{TT}(\mathbf{r})$ which is a function of position only.

Process (a) becomes $dr_a = c_n(E)[1 - f_T(\mathbf{r},t)]N_{TT}(\mathbf{r})f(E)D(E)dE$ where $c_n(E)$ is called the capture coefficient and is a function of energy. $c_n(E)$ can be thought of as a reaction rate constant. This expression is integrated over the energy range of the conduction band ($E_C \rightarrow \infty$),

$$r_a = [1 - f_T(\mathbf{r},t)]N_{TT}(\mathbf{r}) \int_{E_C}^{\infty} c_n(E)f(E)D(E)dE. \tag{4.1}$$

Here, it is convenient to use a mean capture coefficient defined as

$$< c_n >= \frac{\int_{E_C}^{\infty} c_n(E)f(E)D(E)dE}{\int_{E_C}^{\infty} f(E)D(E)dE}. \tag{4.2}$$

Process (a) becomes

$$r_a =< c_n > [1 - f_T(\mathbf{r},t)]N_{TT}(\mathbf{r})n =< c_n > p_T n \tag{4.3}$$

where it is noted that the denominator of equation(4.2) is equal to n, the total concentration of conduction band electrons, and p_T is the concentration of holes occupying deep–level states.

The mean capture coefficient is often described as the product of the mean thermal velocity of conduction band electrons, $\bar{v_n}$ and a capture cross–section, σ_n,

($< c_n >= \bar{v}_n\sigma_n$). Blakemore [48] suggests that this definition is a carry over from atomic physics where it was hoped that the capture cross–section would be proportional to the cross–section of an atom ($\sim 10^{-16}$ cm^{-2}). However, he points out that the capture cross–section can range anywhere from 10^{-25} to 10^{-12}cm^{-2}. Despite this apparent discrepancy, the term capture cross–section remains in common use. Grove [49] considers σ_n to be a measure of how close a carrier has to come to a trap center in order to be captured. Hence, a deep–level state can easily capture an electron if it has a large capture cross–section and/or if the mean thermal velocity of the electron is increased, by an increase in the temperature, for example.

Electron emission from the deep–level state, process (b), can be represented as a reaction between an electron–occupied deep–level state and an electron–vacant conduction band site. The concentration of electrons occupying a deep–level state is given by $f_T(\mathbf{r},t)N_{TT}(\mathbf{r})$ and the concentration of vacant conduction band sites is given by $[1-f(E)]D(E)dE$ at an energy increment dE. These symbols are defined above; note that $[1-f(E)]$ is the probability that a conduction band site is vacant. An incremental expression for process (b) becomes: $dr_b = e_n(E)f_T(\mathbf{r},t)N_{TT}(\mathbf{r})[1-f(E)]D(E)dE$ where $e_n(E)$ is the reaction rate constant or the emission constant. This expression is integrated over the conduction band energy range,

$$r_b = f_T(\mathbf{r},t)N_{TT}(\mathbf{r}) \int_{E_C}^{\infty} e_n(E)[1-f(E)]D(E)dE. \tag{4.4}$$

This rate expression is typically redefined as

$$r_b = e_n f_T(\mathbf{r},t)N_{TT}(\mathbf{r}) = e_n n_T \tag{4.5}$$

where n_T is the concentration of electrons occupying deep–level states and e_n is defined as

$$e_n = \int_{E_C}^{\infty} e_n(E)[1-f(E)]D(E)dE. \tag{4.6}$$

For low concentrations of conduction band electrons or the non–degenerate case, a majority of the conduction band sites will be vacant (*i.e.*, $f(E) \approx 0$), in which case

e_n can be approximated by

$$e_n \approx \int_{E_C}^{\infty} e_n(E)D(E)dE. \tag{4.7}$$

Note that as the concentration of free electrons increases, $f(E)$ increases, and therefore, the emission rate constant decreases. Or in other words, the emission rate decreases as the number of free electrons increases because there are fewer vacant conduction band sites for the deep–level state to emit its electron into.

Hole capture by the deep–level state can by treated as a reaction between an electron occupying a deep–level state and a free hole in the valence band. The concentration of trapped electrons is given by $f_T(\mathbf{r},t)N_{TT}(\mathbf{r})$ and the concentration of holes in the valence band is given by $[1 - f(E)]D(E)dE$. The incremental rate of process (c) is $dr_c = c_p(E)f_T(\mathbf{r},t)N_{TT}(\mathbf{r})[1 - f(E)]D(E)dE$ which can be integrated over the energy range of the valence band to yield

$$r_c = f_T(\mathbf{r},t)N_{TT}(\mathbf{r}) \int_{-\infty}^{E_V} c_p(E)[1 - f(E)]D(E)dE. \tag{4.8}$$

The hole capture coefficient is averaged similar to the electron capture coefficient,

$$< c_p >= \frac{\int_{-\infty}^{E_V} c_p(E)[1 - f(E)]D(E)dE}{\int_{-\infty}^{E_V}[1 - f(E)]D(E)dE} \tag{4.9}$$

in which case

$$r_c =< c_p > f_T(\mathbf{r},t)N_{TT}(\mathbf{r})p =< c_p > n_{TP} \tag{4.10}$$

where it is noted that the denominator of equation(4.9) is the concentration of holes in the valence band. $< c_p >$ is traditionally defined as the product of a hole capture cross–section, σ_p, and the mean thermal velocity of a hole, $\bar{v_p}$.

Hole emission by the deep–level state is a reaction between an electron–vacant (hole occupied) deep–level state and a hole–vacant (electron occupied) valence band site. The concentration of trapped holes is given as $[1 - f_T(\mathbf{r},t)]N_{TT}(\mathbf{r})$ and the concentration of valence band electrons is given as $f(E)D(E)dE$. The incremental rate of hole emission is given as: $dr_d = e_p(E)[1 - f_T(\mathbf{r},t)]N_{TT}(\mathbf{r})f(E)D(E)dE$ where $e_p(E)$ is the hole emission constant. This expression is integrated over the valence band energy range to yield

$$r_d = [1 - f_T(\mathbf{r},t)]N_{TT}(\mathbf{r}) \int_{-\infty}^{E_V} e_p(E)f(E)D(E)dE. \tag{4.11}$$

This rate expression is redefined as

$$r_d = e_p[1 - f_T(\mathbf{r},t)]N_{TT}(\mathbf{r}) = e_p p_T \tag{4.12}$$

where

$$e_p = \int_{-\infty}^{E_V} e_p(E)f(E)D(E)dE \approx \int_{-\infty}^{E_V} e_p(E)D(E)dE \tag{4.13}$$

because $f(E) \approx 1$ in the valence band for the non–degenerate case.

4.1.1 Equilibrium

The above formulations are general in that no equilibrium constraints were placed on them. Here, relationships are derived based on the conditions of thermal equilibrium. The "principle of detailed balance" will be used. Shockley [50] quotes John C. Slater's description of this principle: "When a system has reached thermal equilibrium, it has run down and is no longer changing. Past and future are alike to it. Now imagine that a motion picture is made of the system, showing atoms and electrons in detail. This film can be projected backwards in time and since past and future are alike, the observer will not be able to tell the difference. Now suppose, for example, the forward–running picture shows on the average (Cap. n) electrons being captured per unit volume per unit time on traps giving up the energy in the form of heat waves (phonons), and suppose it shows (Em. n) electrons being emitted per unit volume per unit time, acquiring the energy from heat waves. Then, if the picture is run backwards, each actual emission process will appear to be a capture, and there will appear thus to be (Em. n) captures per unit time. Thus, if (Em. n) is not equal to (Cap. n), forward and backwards running of the film can be distinguished, contrary to the assumption that the system is run down. Thus, the principle of detailed balance requires that each process and its reverse proceed at equal rates."

With this in mind, process (a) must proceed at the same rate as its reverse, process (b). On average, a conduction band electron loses energy and is captured by a trap at the same time a trapped electron gains the same unit of energy and is emitted to the conduction band. Likewise, process (c) proceeds at the same rate as process (d). A valence band hole loses energy and is captured by a trap at the same time a trapped hole gains energy and is emitted to the valence band. These rate expressions are related as follows:

$$r_a = r_b \Longrightarrow < c_{ne} > p_{Te} n_e = e_{ne} n_{Te} \tag{4.14}$$

and

$$r_c = r_d \Longrightarrow < c_{pe} > n_{Te} p_e = e_{pe} p_{Te} \tag{4.15}$$

where the subscript e has been added to denote equilibrium conditions. These equations can be solved in terms of ratios by equating $\frac{n_{Te}}{p_{Te}}$ of each relation,

$$\frac{n_{Te}}{p_{Te}} = \frac{< c_{ne} > n_e}{e_{ne}} = \frac{e_{pe}}{< c_{pe} > p_e}. \tag{4.16}$$

The ratio of the third term to the second term is equal to unity, *i.e.*,

$$\frac{e_{pe} e_{ne}}{< c_{pe} >< c_{ne} > n_e p_e} = 1. \tag{4.17}$$

The mass–action law states that the product of the electron and hole concentration is equal to the intrinsic concentration squared ($n_e p_e = n_i^2$) under thermal equilibrium. This relationship combined with equation(4.17) yields "the detailed–balance relationship" [50]:

$$e_{ne} e_{pe} =< c_{ne} >< c_{pe} > n_i^2. \tag{4.18}$$

The rate coefficients can be expressed in terms of an Arrhenius activation energy through the use of the principle of detailed balance. We have from the equality of rates (a) and (b) at thermal equilibrium [46, 51],

$$\frac{e_{ne}}{< c_{ne} >} = \frac{n_e p_{Te}}{n_{Te}} = \frac{[1 - f_{Te}]n_e}{f_{Te}}. \tag{4.19}$$

Under the assumption of non–degeneracy, the equilibrium concentration of electrons in the conduction band is given as (Boltzmann's approximation)

$$n_e = n_i \exp(\frac{E_F - E_i}{kT}) \tag{4.20}$$

where E_F is the Fermi level of the semiconductor, E_i is the intrinsic energy level, and $k = 8.6173 \times 10^{-5} \frac{eV}{K}$ is the Boltzmann's constant.

The probability of the deep–level state at energy level E_T being occupied by an electron can be described by a Fermi–Dirac distribution function at equilibrium,

$$f_{Te} = \frac{1}{1 + \frac{1}{g} \exp(\frac{E_T - E_F}{kT})} \tag{4.21}$$

where g is the impurity level spin degeneracy [48] which refers to the number of states having the same energy level E_T. The subscript e has been added to the distribution function to indicate that this is an equilibrium expression. The ratio of hole occupancy to electron occupancy in equation (4.19) becomes

$$\frac{[1 - f_{Te}]}{f_{Te}} = \frac{1}{g} \exp(\frac{E_T - E_F}{kT}). \tag{4.22}$$

Equations (4.20) and (4.22) are substituted into equation (4.19) to yield

$$\frac{e_{ne}}{< c_{ne} >} = n_i \frac{1}{g} \exp(\frac{E_T - E_i}{kT}) \equiv n_1, \tag{4.23}$$

where n_1 is defined as the concentration of conduction band electrons if the Fermi level coincides with the energy level of the deep–level state. This definition was first used by Shockley [46]. Note that the Fermi level will be modified by the spin degeneracy, g.

The ratio $e_{pe}/ < c_{pe} >$ can be described in a similar manner when process (c) proceeds at the same rate as process (d) (thermal equilibrium),

$$\frac{e_{pe}}{< c_{pe} >} = \frac{f_{Te}}{[1 - f_{Te}]} p_e = g \exp(\frac{E_F - E_T}{kT}) n_i \exp(\frac{E_i - E_F}{kT}) \qquad (4.24)$$

or

$$\frac{e_{pe}}{< c_{pe} >} = g n_i \exp(\frac{E_i - E_T}{kT}) \equiv p_1. \qquad (4.25)$$

p_1 is defined as the equilibrium concentration of valence band holes if the Fermi level coincides with the energy level of the deep–level state, modified by g.

4.1.2 Non–equilibrium

This section considers the carrier concentrations and the deep–level states under non–equilibrium conditions as developed by Sah [51, 52, 53]. The following transport equations are of the form

$$Accumulation = Flux \;\; Gradient + Net \;\; Rate \;\; of \;\; Production$$

on a unit volume basis. The rate of change of the conduction band electrons can be represented as

$$\frac{\partial n(\mathbf{r},t)}{\partial t} = q^{-1} \nabla \cdot \mathbf{j}_n - < c_n > n(\mathbf{r},t) p_T(\mathbf{r},t) + e_n n_T(\mathbf{r},t) + G_n(\mathbf{r}) + g_n(\mathbf{r},t). \qquad (4.26)$$

The rate of change of the valence band holes can be represented as

$$\frac{\partial p(\mathbf{r},t)}{\partial t} = -q^{-1} \nabla \cdot \mathbf{j}_p - < c_p > p(\mathbf{r},t) n_T(\mathbf{r},t) + e_p p_T(\mathbf{r},t) + G_p(\mathbf{r}) + g_p(\mathbf{r},t). \qquad (4.27)$$

The rate of change of the concentration of deep–level state electrons can be represented as

$$\frac{\partial n_T(\mathbf{r},t)}{\partial t} =< c_n > n(\mathbf{r},t) p_T(\mathbf{r},t) - e_n n_T(\mathbf{r},t) \qquad (4.28)$$
$$- < c_p > p(\mathbf{r},t) n_T(\mathbf{r},t) + e_p p_T(\mathbf{r},t) + G_T(\mathbf{r}) + g_t(\mathbf{r},t).$$

The notation in parenthesis has been added to indicate the dependence on position and time. The terms $G_n(\mathbf{r}), g_n(\mathbf{r},t), G_p(\mathbf{r})$, and $g_p(\mathbf{r},t)$ have been introduced to account for other net generation processes which are separated into steady state and dynamic terms. These net generation processes include such contributions as the influence of other deep–level states, and conduction band to valence band generations and recombinations. $G_T(\mathbf{r})$ and $g_t(\mathbf{r},t)$ have been added to allow for optical excitation of the deep–level states [51]. The carrier flux can be attributed to contributions of drift (migration) and diffusion processes [52] *i.e.,*

$$\mathbf{j}_n = q\mu_n n\mathbf{E} + qD_n\nabla n, \text{ and} \tag{4.29}$$

$$\mathbf{j}_p = q\mu_p p\mathbf{E} - qD_p\nabla p. \tag{4.30}$$

These carrier flux expressions would have an additional term to treat any DC leakage current. For the present development, it is assumed that DC leakage current is not present.

The above equations are related to the electrostatic potential via Poisson's equation:

$$\begin{aligned}\rho &= q[p(\mathbf{r},t) - n(\mathbf{r},t) + (N_D(\mathbf{r},t) - n_D(\mathbf{r},t)) - (N_A(\mathbf{r},t) - n_A(\mathbf{r},t)) - n_T(\mathbf{r},t)] \\ &= K\varepsilon_o\nabla\cdot\mathbf{E} = -K\varepsilon_o\nabla^2\psi \end{aligned} \tag{4.31}$$

where ρ is the concentration of charged species, $q = 1.602 \times 10^{-19}$ C is the electronic charge, K is the dielectric constant, $\varepsilon_o = 8.85419 \times 10^{-12}\frac{\mathrm{C}}{\mathrm{V\cdot m}}$ is the permittivity of vacuum, $\mathbf{E}$ is the electric field, ψ is the electrostatic potential, $N_D(\mathbf{r},t)$ is the donor concentration, $n_D(\mathbf{r},t)$ is the concentration of un–ionized donors, $N_A(\mathbf{r},t)$ is the concentration of acceptors, $n_A(\mathbf{r},t)$ is the concentration of un– ionized acceptors, $(N_D(\mathbf{r},t) - n_D(\mathbf{r},t))$ is the concentration of ionized donors, and $(N_A(\mathbf{r},t) - n_A(\mathbf{r},t))$ is the concentration of ionized acceptors. $n_T(\mathbf{r},t)$ is the concentration of ionized deep–level states where it is assumed that the state is negative when ionized.

4.1.3 Small Signal Analysis

The above non–equilibrium equations will be analyzed here with the small signal approach. There are several assumptions made in the present development which are: the perturbation from equilibrium ($np \neq n_i^2$) is small such that only the first two terms of the Taylor series are sufficient, the shallow–level donors and acceptors are fully ionized ($n_D, n_A = 0$) at the temperatures analyzed, the semiconductor remains non–degenerate such that the non–equilibrium concentration of electrons, holes, and trapped electrons can be expressed with a quasi–Fermi energy level for each (F_n, F_p, F_T), and the system is one–dimensional.

The four rate constants are assumed to be equal to their equilibrium values ($e_n = e_{ne}$, $e_p = e_{pe}$, $< c_n > = < c_{ne} >$, $< c_p > = < c_{pe} >$). This implies that the ratios $e_n / < c_n >$ and $e_p / < c_p >$ are constant and, in light of equations (4.23) and (4.25),

$$E_T - E_i = \text{ constant.} \tag{4.32}$$

The quasi–Fermi energy level assumption, valid for a non–degenerate semiconductor, permits the use of the Einstein relation in the flux equations. The Einstein relation is

$$D_i = \frac{kT}{q}\mu_i. \tag{4.33}$$

The one–dimensional electron and hole flux equations become

$$\dot{\mathbf{j}}_n = \mu_n n \frac{\partial F_n}{\partial x}, \quad \text{and} \tag{4.34}$$

$$\dot{\mathbf{j}}_p = \mu_p p \frac{\partial F_p}{\partial x}. \tag{4.35}$$

The concentrations can be approximated by the first two terms of the Taylor series. The electron concentration becomes

$$n(\mathbf{r}, t) \doteq N(\mathbf{r}) + \frac{\partial n(\mathbf{r}, t)}{\partial t} \mid_t \partial t = N(\mathbf{r}) + \partial n(\mathbf{r}, t) \tag{4.36}$$

where

$$n(\mathbf{r},t) = n_i \exp(\frac{F_n - E_i}{kT}). \tag{4.37}$$

The partial derivative with respect to time can be expressed as

$$\frac{\partial n(\mathbf{r},t)}{\partial t}\mid_t = \frac{n_i}{kT}\exp(\frac{F_n - E_i}{kT})(\frac{\partial F_n}{\partial t} - \frac{\partial E_i}{\partial t}) = \frac{N(\mathbf{r})}{kT}(\frac{\partial F_n}{\partial t} - \frac{\partial E_i}{\partial t}). \tag{4.38}$$

The hole concentration can be represented as

$$p(\mathbf{r},t) \doteq P(\mathbf{r}) + \frac{\partial p(\mathbf{r},t)}{\partial t}\mid_t \partial t = P(\mathbf{r}) + \partial p(\mathbf{r},t) \tag{4.39}$$

where

$$p(\mathbf{r},t) = n_i \exp(\frac{E_i - F_p}{kT}) \tag{4.40}$$

and

$$\frac{\partial p(\mathbf{r},t)}{\partial t}\mid_t = \frac{n_i}{kT}\exp(\frac{E_i - F_p}{kT})(\frac{\partial E_i}{\partial t} - \frac{\partial F_p}{\partial t}) = \frac{P(\mathbf{r})}{kT}(\frac{\partial E_i}{\partial t} - \frac{\partial F_p}{\partial t}). \tag{4.41}$$

The trapped electron concentration can be represented as

$$n_T(\mathbf{r},t) \doteq N_T(\mathbf{r}) + \frac{\partial n_T(\mathbf{r},t)}{\partial t}\mid_t \partial t = N_T(\mathbf{r}) + n_t(\mathbf{r},t) \tag{4.42}$$

where

$$n_T(\mathbf{r},t) = \frac{N_{TT}(\mathbf{r})}{1 + \frac{1}{g}\exp(\frac{E_T - F_T}{kT})} \tag{4.43}$$

and

$$\begin{aligned}\frac{\partial n_T(\mathbf{r},t)}{\partial t}\mid_t &= -\frac{N_{TT}(\mathbf{r})}{[1 + \frac{1}{g}\exp(\frac{E_T - F_T}{kT})]^2}\frac{1}{gkT}\exp(\frac{E_T - F_T}{kT})(\frac{\partial E_t}{\partial t} - \frac{\partial F_t}{\partial t}) \\ &= -\frac{N_T(\mathbf{r})}{kT}\frac{P_T(\mathbf{r})}{N_{TT}(\mathbf{r})}(\frac{\partial E_t}{\partial t} - \frac{\partial F_t}{\partial t}).\end{aligned} \tag{4.44}$$

The trapped hole concentration can be represented as

$$p_T(\mathbf{r},t) \doteq P_T(\mathbf{r}) + \frac{\partial p_T(\mathbf{r},t)}{\partial t}\mid_t \partial t = P_T(\mathbf{r}) + p_t(\mathbf{r},t) \tag{4.45}$$

where

$$p_T(\mathbf{r},t) = \frac{N_{TT}(\mathbf{r})\frac{1}{g}\exp(\frac{E_T - F_T}{kT})}{1 + \frac{1}{g}\exp(\frac{E_T - F_T}{kT})} \tag{4.46}$$

and

$$\frac{\partial p_T(\mathbf{r},t)}{\partial t}\Big|_t =$$

$$\left[\frac{N_{TT}(\mathbf{r})\frac{1}{gkT}\exp(\frac{E_T-F_T}{kT})}{1+\frac{1}{g}\exp(\frac{E_T-F_T}{kT})} - \frac{N_{TT}(\mathbf{r})}{[1+\frac{1}{g}\exp(\frac{E_T-F_T}{kT})]^2}\frac{1}{kT}(\frac{1}{g}\exp(\frac{E_T-F_T}{kT}))^2\right](\frac{\partial E_t}{\partial t} - \frac{\partial F_t}{\partial t})$$

$$= \frac{P_T(\mathbf{r})}{kT}[1 - \frac{P_T(\mathbf{r})}{N_{TT}(\mathbf{r})}](\frac{\partial E_t}{\partial t} - \frac{\partial F_t}{\partial t}) = \frac{P_T(\mathbf{r})}{kT}\frac{N_T(\mathbf{r})}{N_{TT}(\mathbf{r})}(\frac{\partial E_t}{\partial t} - \frac{\partial F_t}{\partial t}). \qquad (4.47)$$

The results of the above derivations with the substitution of $\partial E_t = \partial E_i$ are reproduced here for clarity

$$n(\mathbf{r},t) = N(\mathbf{r}) + \frac{N(\mathbf{r})}{kT}(\partial F_n - \partial E_i), \qquad (4.48)$$

$$p(\mathbf{r},t) = P(\mathbf{r}) + \frac{P(\mathbf{r})}{kT}(\partial E_i - \partial F_p), \qquad (4.49)$$

$$n_T(\mathbf{r},t) = N_T(\mathbf{r}) - \frac{N_T(\mathbf{r})}{kT}\frac{P_T(\mathbf{r})}{N_{TT}(\mathbf{r})}(\partial E_i - \partial F_t), \quad \text{and} \qquad (4.50)$$

$$p_T(\mathbf{r},t) = P_T(\mathbf{r}) + \frac{P_T(\mathbf{r})}{kT}\frac{N_T(\mathbf{r})}{N_{TT}(\mathbf{r})}(\partial E_i - \partial F_t). \qquad (4.51)$$

Equations (4.48) to (4.51) are substituted in the non-equilibrium equation (4.26) to yield

$$\frac{N(\mathbf{r})}{kT}(\frac{\partial F_n}{\partial t} - \frac{\partial E_i}{\partial t}) = \nabla\cdot\left(\frac{\mu_n}{q}[N(\mathbf{r}) + \frac{N(\mathbf{r})}{kT}(\partial F_n - \partial E_i)][\nabla(F_n + \partial F_n)]\right)$$

$$- < c_n > [N(\mathbf{r}) + \frac{N(\mathbf{r})}{kT}(\partial F_n - \partial E_i)][P_T(\mathbf{r}) + \frac{P_T(\mathbf{r})}{kT}\frac{N_T(\mathbf{r})}{N_{TT}(\mathbf{r})}(\partial E_i - \partial F_t)]$$

$$+ e_n[N_T(\mathbf{r}) - \frac{N_T(\mathbf{r})}{kT}\frac{P_T(\mathbf{r})}{N_{TT}(\mathbf{r})}(\partial E_i - \partial F_t)] + G_n(\mathbf{r}) + g_n(\mathbf{r},t)$$

$$= \left\{\frac{\mu_n}{q}\nabla\cdot(N(\mathbf{r})\nabla F_n) - < c_n > N(\mathbf{r})P_T(\mathbf{r}) + e_n N_T(\mathbf{r}) + G_n(\mathbf{r})\right\} \qquad (4.52)$$

$$+\nabla\cdot\left(\frac{\mu_n}{q}N(\mathbf{r})\nabla\partial F_n + \frac{N(\mathbf{r})\nabla F_n}{kT}(\partial F_n - \partial E_i)\right) + g_n(\mathbf{r},t)$$

$$-\left[< c_n > N(\mathbf{r})P_T(\mathbf{r})\frac{N_T(\mathbf{r})}{N_{TT}(\mathbf{r})} + e_n N_T(\mathbf{r})\frac{P_T(\mathbf{r})}{N_{TT}(\mathbf{r})}\right](\frac{\partial E_i - \partial F_t}{kT})$$

$$- < c_n > N(\mathbf{r})P_T(\mathbf{r})(\frac{\partial F_n - \partial E_i}{kT}) + \nabla\cdot\left(\frac{\mu_n}{q}\frac{N(\mathbf{r})}{kT}(\partial F_n - \partial E_i)\nabla\partial F_n\right)$$

$$- < c_n > N(\mathbf{r})P_T(\mathbf{r})\frac{N_T(\mathbf{r})}{N_{TT}(\mathbf{r})}(\frac{\partial F_n - \partial E_i}{kT})(\frac{\partial E_i - \partial F_t}{kT}).$$

The terms in the curly bracket is the steady state equation and hence can be set equal to zero, and the last two terms are second order terms which can be dropped since the Taylor series included only first order terms.

It is advantageous to divide the semiconductor into elements and to assume that in each element the static quasi–Fermi potentials and the static electron, hole, and trap concentrations are independent of position. The dynamic generation terms are also assumed to be independent of position within each element. However, these properties can vary from element to element but are constant within each element. Equation (4.52) reduces to

$$\frac{N}{kT}(\frac{\partial F_n}{\partial t} - \frac{\partial E_i}{\partial t}) - \frac{\mu_n}{q}N\frac{\partial^2 \partial F_n}{\partial x^2} + < c_n > NP_T(\frac{\partial F_n - \partial E_i}{kT}) \tag{4.53}$$

$$-[< c_n > NP_T\frac{N_T}{N_{TT}} + e_n N_T\frac{P_T}{N_{TT}}](\frac{\partial F_t - \partial E_i}{kT}) = g_n(t).$$

Substitution of equations (4.48) to (4.51) into equation (4.27) yields

$$\frac{P(\mathbf{r})}{kT}(\frac{\partial E_i}{\partial t} - \frac{\partial F_p}{\partial t}) = -\nabla \cdot \left(\frac{\mu_p}{q}[P(\mathbf{r}) + \frac{P(\mathbf{r})}{kT}(\partial E_i - \partial F_p)][\nabla(F_p + \partial F_p)]\right)$$

$$- < c_p > [P(\mathbf{r}) + \frac{P(\mathbf{r})}{kT}(\partial E_i - \partial F_p)][N_T(\mathbf{r}) - \frac{N_T(\mathbf{r})}{kT}\frac{P_T(\mathbf{r})}{N_{TT}(\mathbf{r})}(\partial E_i - \partial F_t)]$$

$$+ e_p[P_T(\mathbf{r}) + \frac{P_T(\mathbf{r})}{kT}\frac{N_T(\mathbf{r})}{N_{TT}(\mathbf{r})}(\partial E_i - \partial F_t)] + G_p(\mathbf{r}) + g_p(\mathbf{r}, t). \tag{4.54}$$

This equation can be reduced with the subtraction of the steady state equation, the elimination of second order terms, and with the assumption of position independent static properties within each element as well as the dynamic generation term to yield

$$\frac{P}{kT}(\frac{\partial F_p}{\partial t} - \frac{\partial E_i}{\partial t}) - \frac{\mu_p}{q}P\frac{\partial^2 \partial F_p}{\partial x^2} + < c_p > PN_T(\frac{\partial F_p - \partial E_i}{kT}) \tag{4.55}$$

$$-[< c_p > PN_T\frac{P_T}{N_{TT}} + e_p P_T\frac{N_T}{N_{TT}}](\frac{\partial F_t - \partial E_i}{kT}) = -g_p(t).$$

Substitution of equations (4.48) to (4.51) into equation (4.28) yields

$$\begin{aligned}
\frac{N_T(\mathbf{r})P_T(\mathbf{r})}{kTN_{TT}(\mathbf{r})}\left(\frac{\partial F_t}{\partial t}-\frac{\partial E_i}{\partial t}\right) &=< c_n > [N(\mathbf{r})+N(\mathbf{r})(\frac{\partial F_n-\partial E_i}{kT})] \qquad (4.56)\\
&[P_T(\mathbf{r})+P_T(\mathbf{r})\frac{N_T(\mathbf{r})}{N_{TT}(\mathbf{r})}(\frac{\partial E_i-\partial F_t}{kT})]-e_n[N_T(\mathbf{r})-N_T(\mathbf{r})\frac{P_T(\mathbf{r})}{N_{TT}(\mathbf{r})}(\frac{\partial E_i-\partial F_t}{kT})]\\
&-< c_p > [P(\mathbf{r})+P(\mathbf{r})(\frac{\partial E_i-\partial F_p}{kT})][N_T(\mathbf{r})-N_T(\mathbf{r})\frac{P_T(\mathbf{r})}{N_{TT}(\mathbf{r})}(\frac{\partial E_i-\partial F_t}{kT})]\\
&+e_p[P_T(\mathbf{r})+P_T(\mathbf{r})\frac{N_T(\mathbf{r})}{N_{TT}(\mathbf{r})}(\frac{\partial E_i-\partial F_t}{kT})]+G_T(\mathbf{r})+g_t(\mathbf{r},t).
\end{aligned}$$

This equation is reduced by subtraction of the steady state equation, elimination of second order terms, and with the assumption of position independent element properties to yield

$$\begin{aligned}
&\frac{N_TP_T}{kTN_{TT}}\left(\frac{\partial F_t}{\partial t}-\frac{\partial E_i}{\partial t}\right)=\\
&-\left[< c_n > NP_T\frac{N_T}{N_{TT}}+e_nN_T\frac{P_T}{N_{TT}}+< c_p > PN_T\frac{P_T}{N_{TT}}+e_pP_T\frac{N_T}{N_{TT}}\right]\left(\frac{\partial F_t-\partial E_i}{kT}\right)\\
&+< c_p > PN_T\left(\frac{\partial F_p-\partial E_i}{kT}\right)+< c_n > NP_T\left(\frac{\partial F_n-\partial E_i}{kT}\right)+g_t(t). \qquad (4.57)
\end{aligned}$$

Poisson's equation becomes

$$\begin{aligned}
\frac{1}{q}K\varepsilon_o\nabla^2(E_i+\partial E_i) &= q\Big[P(\mathbf{r})+P(\mathbf{r})(\frac{\partial E_i-\partial F_p}{kT})-N(\mathbf{r})-N(\mathbf{r})(\frac{\partial F_n-\partial E_i}{kT})\\
&+N_D(\mathbf{r})-N_A(\mathbf{r})-N_T(\mathbf{r})+N_T(\mathbf{r})\frac{P_T(\mathbf{r})}{N_{TT}(\mathbf{r})}(\frac{\partial E_i-\partial F_t}{kT})\Big] \qquad (4.58)
\end{aligned}$$

where it was assumed that the electrostatic potential is equal to the intrinsic energy level divided by the electronic charge, $q\psi=-E_i$. The derivative with respect to time of this equation is more useful here,

$$\frac{1}{q^2}K\varepsilon_o\frac{\partial}{\partial t}\nabla^2\partial E_i=\frac{P}{kT}\left(\frac{\partial E_i-\partial F_p}{\partial t}\right)-\frac{N}{kT}\left(\frac{\partial F_n-\partial E_i}{\partial t}\right)+\frac{N_TP_T}{kTN_{TT}}\left(\frac{\partial E_i-\partial F_t}{\partial t}\right). \qquad (4.59)$$

4.1.4 Equivalent Circuit

The small signal non–equilibrium equations derived above can be related to an equivalent circuit composed of common circuit elements such as resistors and capacitors. To do this, the partial quasi–Fermi and the partial intrinsic energy levels have to be related to a voltage [51, 52]. This can be done by dividing the energy levels by the electronic charge,

$$v_n = -\frac{\partial F_n}{q}, \quad v_p = -\frac{\partial F_p}{q}, \quad v_t = -\frac{\partial F_t}{q}, \quad \text{and} \quad v_i = -\frac{\partial E_i}{q}. \tag{4.60}$$

Kirchhoff's current law is applied to each small signal equation. This law states that the sum of all the currents entering and exiting a circuit node must be zero. At this point it is useful to remember that the current through a capacitor is equal to the capacitance multiplied by the time derivative of the voltage across the capacitor and the current through a conductor is the conductance multiplied by the voltage drop across the conductor. The small signal equation derived above are reproduced below for clarity,

$$\begin{aligned}\frac{N}{kT}(\frac{\partial F_n}{\partial t} - \frac{\partial E_i}{\partial t}) - \frac{\mu_n}{q}N\frac{\partial^2 \partial F_n}{\partial x^2} + < c_n > NP_T(\frac{\partial F_n - \partial E_i}{kT}) \\ -[< c_n > NP_T\frac{N_T}{N_{TT}} + e_n N_T\frac{P_T}{N_{TT}}](\frac{\partial F_t - \partial E_i}{kT}) = g_n,\end{aligned} \tag{4.61}$$

$$\begin{aligned}\frac{P}{kT}(\frac{\partial F_p}{\partial t} - \frac{\partial E_i}{\partial t}) - \frac{\mu_p}{q}P\frac{\partial^2 \partial F_p}{\partial x^2} + < c_p > PN_T(\frac{\partial F_p - \partial E_i}{kT}) \\ -[< c_p > PN_T\frac{P_T}{N_{TT}} + e_p P_T\frac{N_T}{N_{TT}}](\frac{\partial F_t - \partial E_i}{kT}) = -g_p,\end{aligned} \tag{4.62}$$

$$\begin{aligned}\frac{N_T P_T}{kTN_{TT}}(\frac{\partial F_t}{\partial t} - \frac{\partial E_i}{\partial t}) = \\ -\left[< c_n > NP_T\frac{N_T}{N_{TT}} + e_n N_T\frac{P_T}{N_{TT}} + < c_p > PN_T\frac{P_T}{N_{TT}} + e_p P_T\frac{N_T}{N_{TT}}\right](\frac{\partial F_t - \partial E_i}{kT}) \\ + < c_p > PN_T(\frac{\partial F_p - \partial E_i}{kT}) + < c_n > NP_T(\frac{\partial F_n - \partial E_i}{kT}) + g_t,\end{aligned} \tag{4.63}$$

and

$$-\frac{1}{q^2}K\varepsilon_o\frac{\partial}{\partial t}\nabla^2\partial E_i = \frac{P}{kT}(\frac{\partial F_p - \partial E_i}{\partial t}) + \frac{N}{kT}(\frac{\partial F_n - \partial E_i}{\partial t}) + \frac{N_T P_T}{kTN_{TT}}(\frac{\partial F_t - \partial E_i}{\partial t}). \tag{4.64}$$

The next step is to replace the quasi–Fermi energy level perturbations, ∂F, with the corresponding voltages, $-qv$, and multiply the above equations by the electronic charge, q. This changes the voltage coefficients into capacitances and conductances. There are four voltage parameters in equations (4.61) to (4.64), v_n, v_p, v_t, and v_i. These equations are re–arranged into voltage drops across circuit elements, *i.e.*, $v_n - v_i$, $v_p - v_i$, $v_t - v_i$, $v_n - v_t$, and $v_p - v_t$. It is assumed that direct band to band processes are included in g_n and g_p and hence, $v_n - v_p$ need not be considered here. To find the coefficients of the these voltage drops, it is best to collect all the coefficients of like voltage and then regroup the voltages with common coefficient for each equation. The relationship, $N_{TT} = N_T + P_T$ is used several times.

Upon doing the above, the equations can be expressed as

$$\frac{q^2 N}{kT}\frac{\partial(v_n - v_i)}{\partial t} - q\mu_n N\frac{\partial^2 v_n}{\partial x^2} + \frac{q^2 < c_n > NP_T}{kT}(v_n - v_t)$$

$$+ \frac{q^2 P_T}{kTN_{TT}}[< c_n > NP_T - e_n N_T](v_t - v_i) = -qg_n, \tag{4.65}$$

$$\frac{q^2 P}{kT}\frac{\partial(v_p - v_i)}{\partial t} - q\mu_p P\frac{\partial^2 v_p}{\partial x^2} + \frac{q^2 < c_p > PN_T}{kT}(v_p - v_t)$$

$$+ \frac{q^2 N_T}{kTN_{TT}}[< c_p > PN_T - e_p P_T](v_t - v_i) = qg_p, \tag{4.66}$$

$$\frac{q^2 N_T P_T}{kTN_{TT}}\frac{\partial(v_t - v_i)}{\partial t} - \frac{q^2}{kTN_{TT}}\left[< c_n > NP_T^2 - e_n P_T N_T + < c_p > PN_T^2 - e_p P_T N_T\right](v_t - v_i)$$

$$- \frac{q^2 < c_p > PN_T}{kT}(v_p - v_t) - \frac{q^2 < c_n > NP_T}{kT}(v_n - v_t) = qg_t, \tag{4.67}$$

and

$$\frac{q^2 P}{kT}\frac{\partial(v_p - v_i)}{\partial t} + \frac{q^2 N}{kT}\frac{\partial(v_n - v_i)}{\partial t} + \frac{q^2 N_T P_T}{kTN_{TT}}\frac{\partial(v_t - v_i)}{\partial t} = -K\varepsilon_o\frac{\partial}{\partial t}\frac{\partial^2 v_i}{\partial x^2}. \tag{4.68}$$

At this point, the semiconductor is divided into equally spaced elements in order to treat the second order derivatives. The second order derivatives are discretized with the central finite difference method applied to three elements. The second order derivatives of each potential in the above governing equations can be expressed as

$$\frac{\partial^2 v_k}{\partial x^2} \approx \frac{v_{k+1} - 2v_k + v_{k-1}}{(\Delta x)^2} = \frac{v_{k+1} - v_k}{(\Delta x)^2} - \frac{v_k - v_{k-1}}{(\Delta x)^2} \tag{4.69}$$

where the subscript k is used to indicate the element number. It is apparent that the second derivative in potential can be thought of as a potential drop across a circuit component at the beginning of the element minus the potential drop across a circuit component at the end of the element.

We now let

$$C_n = \frac{q^2 N}{kT}, \tag{4.70}$$

$$C_p = \frac{q^2 P}{kT}, \tag{4.71}$$

$$C_T = \frac{q^2 N_T P_T}{kT N_{TT}}, \tag{4.72}$$

$$G_n = \frac{q \mu_n N}{(\Delta x)^2}, \tag{4.73}$$

$$G_p = \frac{q \mu_p P}{(\Delta x)^2}, \tag{4.74}$$

$$C_K = \frac{K \varepsilon_o}{(\Delta x)^2}, \tag{4.75}$$

$$G_{nT} = \frac{q^2 < c_n > N P_T}{kT}, \tag{4.76}$$

$$G_{pT} = \frac{q^2 < c_p > P N_T}{kT}, \tag{4.77}$$

$$G_{nTi} = \frac{q^2 P_T}{kT N_{TT}} [< c_n > N P_T - e_n N_T], \tag{4.78}$$

$$G_{pTi} = \frac{q^2 N_T}{kT N_{TT}} [< c_p > P N_T - e_p P_T], \tag{4.79}$$

$$i_n = -q g_n, \tag{4.80}$$

$$i_p = q g_p, \quad \text{and} \tag{4.81}$$

$$i_T = qg_t. \tag{4.82}$$

The above conductances have units of current per volt per volume and the capacitances have units of charge per volt per volume.

These conductances and capacitances are substituted in the above equations to yield

$$C_n\frac{\partial(v_n - v_i)}{\partial t} - G_{n,k}(v_{n,k-1} - v_{n,k}) + G_{n,k+1}(v_{n,k} - v_{n,k+1}) + G_{nT}(v_n - v_t) + G_{nTi}(v_t - v_i) = i_n, \tag{4.83}$$

$$C_p\frac{\partial(v_p - v_i)}{\partial t} - G_{p,k}(v_{p,k-1} - v_{p,k}) + G_{p,k+1}(v_{p,k} - v_{p,k+1}) + G_{pT}(v_p - v_t) + G_{pTi}(v_t - v_i) = i_p, \tag{4.84}$$

$$C_T\frac{\partial(v_t - v_i)}{\partial t} - (G_{nTi} + G_{pTi})(v_t - v_i) - G_{pT}(v_p - v_t) - G_{nT}(v_n - v_t) = i_T, \tag{4.85}$$

and

$$\begin{aligned} & C_p\frac{\partial(v_p - v_i)}{\partial t} + C_n\frac{\partial(v_n - v_i)}{\partial t} + C_T\frac{\partial(v_t - v_i)}{\partial t} \\ &= -C_{K,k}\frac{\partial(v_{i,k-1} - v_{i,k})}{\partial t} + C_{K,k+1}\frac{\partial(v_{i,k} - v_{i,k+1})}{\partial t}. \end{aligned} \tag{4.86}$$

The corresponding equivalent circuit is given in Figure 4.2. Equations (4.70) to (4.86) and Figure 4.2 are consistent with that derived by Sah [51, 52].

4.2 Surface States

The treatment of surface states presented here follows that of Sah [54]. Surface states can be a discrete single energy level defect or a distributed energy level defect (surface band). The single energy level surface state is treated first.

4.2.1 Single Energy Level Surface State

A single energy level surface state can be treated like a bulk state except that the surface state is limited to a two–dimensional plane. The appropriate equations in this case are Gauss' Law and the kinetic expression of the surface state charge. Gauss' Law is a boundary condition to Poisson's Equation in that it relates the first derivative of the potential to the charge located at the surface. The surface concentrations can be expressed in terms of quasi–Fermi energy levels that are either bulk values evaluated at the surface (F_{ns}, F_{ps}) or newly defined levels associated with the surface state (F_{Ts}). The concentration of electrons evaluated at the surface is given by

$$n_s(t) = n_i \exp(\frac{F_{ns} - E_{is}}{kT}), \tag{4.87}$$

and of holes,

$$p_s(t) = n_i \exp(\frac{E_{is} - F_{ps}}{kT}). \tag{4.88}$$

The concentration of electrons trapped by the surface state can be expressed as

$$n_{Ts}(t) = \frac{N_{TTs}}{1 + \frac{1}{g}\exp(\frac{E_{Ts} - F_{Ts}}{kT})}. \tag{4.89}$$

The concentration of surface states that are electron vacant is given by

$$p_{Ts}(t) = \frac{N_{TTs}\frac{1}{g}\exp(\frac{E_{Ts} - F_{Ts}}{kT})}{1 + \frac{1}{g}\exp(\frac{E_{Ts} - F_{Ts}}{kT})} \tag{4.90}$$

where N_{TTs} is the total concentration of surface states, E_{is} is the intrinsic energy level evaluated at the surface, E_{Ts} is the surface state energy level, and the subscript s denotes that these are either surface properties or parameters associated with the surface state.

The Taylor series approximations of the surface concentrations are

$$n_s(t) = N_s + \frac{N_s}{kT}(\partial F_{ns} - \partial E_{is}), \tag{4.91}$$

$$p_s(t) = P_s + \frac{P_s}{kT}(\partial E_{is} - \partial F_{ps}), \tag{4.92}$$

$$n_{Ts}(t) = N_{Ts} - \frac{N_{Ts}}{kT}\frac{P_{Ts}}{N_{TTs}}(\partial E_{is} - \partial F_{ts}), \quad \text{and} \tag{4.93}$$

$$p_{Ts}(t) = P_{Ts} + \frac{P_{Ts}}{kT}\frac{N_{Ts}}{N_{TTs}}(\partial E_{is} - \partial F_{ts}). \tag{4.94}$$

where the substitution $\partial E_{ts} = \partial E_{is}$ has been used. This substitution can be derived in the same manner as equation (4.32).

The non–equilibrium equations that describe the rate processes between the carrier bands and the surface state are the time rate of change of surface state occupancy

$$\frac{\partial n_{Ts}(t)}{\partial t} = < c_{ns} > n_s(t)p_{Ts}(t) - e_{ns}n_{Ts}(t) - < c_{ps} > p_s(t)n_{Ts}(t) + e_{ps}p_{Ts}(t) + G_{Ts} + g_{ts}(t) \tag{4.95}$$

and Gauss' Law

$$-K\varepsilon_o\frac{\partial\psi}{\partial x} = qn_{Ts}(t) \tag{4.96}$$

where it is assumed that the potential gradient on the metal contact is zero.

These equations apply to a two–dimensional plane and hence, are based per unit of area, cm^2. The surface state electron occupancy equation is two–dimensional throughout because n_{Ts} is per surface area, not volume. The emission rate coefficients have units of inverse time. The product of the capture rate coefficients and the respective carrier concentration have units of time. Both of these expressions are multiplied by a concentration of surface state, the product of such has units of per time per area.

Upon substitution of the Taylor series approximations of the surface concentrations, the above governing equations become

$$\begin{aligned}\frac{N_{Ts}P_{Ts}}{kTN_{TTs}}\left(\frac{\partial F_{ts}}{\partial t} - \frac{\partial E_{is}}{\partial t}\right) - < c_{ps} > P_sN_{Ts}\left(\frac{\partial F_{ps} - \partial E_{is}}{kT}\right) - < c_{ns} > N_sP_{Ts}\left(\frac{\partial F_{ns} - \partial E_{is}}{kT}\right)\\ + \Big[< c_{ns} > N_sP_{Ts}\frac{N_{Ts}}{N_{TTs}} + e_{ns}N_{Ts}\frac{P_{Ts}}{N_{TTs}} + < c_{ps} > P_sN_{Ts}\frac{P_{Ts}}{N_{TTs}}\\ + e_{ps}P_{Ts}\frac{N_{Ts}}{N_{TTs}}\Big]\left(\frac{\partial F_{ts} - \partial E_{is}}{kT}\right) = g_{ts}(t)\end{aligned} \tag{4.97}$$

and the time derivative of Gauss' Law becomes

$$\frac{1}{q}\varepsilon_o\frac{\partial}{\partial t} - K\frac{\partial\partial E_{is}}{\partial x} = \frac{qN_{Ts}P_{Ts}}{kTN_{TTs}}\left(\frac{\partial E_{is} - \partial F_{ts}}{\partial t}\right) \tag{4.98}$$

where the steady state equation has been eliminated as well as the second order terms.

These equations are in a form that can be related to equivalent circuit elements. The quasi Fermi levels are related to potentials through the electronic charge as done for the bulk governing equations. The coefficients of the governing potential equations can then be considered as simple resistors and capacitors with units of current and charge per volt per square area.

The governing equations can be expressed as

$$C_{Ts}\frac{\partial(v_{ts}-v_{is})}{\partial t} - (G_{nTis}+G_{pTis})(v_{ts}-v_{is}) - G_{pTs}(v_{ps}-v_{ts}) - G_{nTs}(v_{ns}-v_{ts}) = i_{Ts} \tag{4.99}$$

and

$$C_{Ts}\frac{\partial(v_{ts}-v_{is})}{\partial t} = C_{Ks}\frac{\partial(v_{is}-v_{i1})}{\partial t} \tag{4.100}$$

where

$$C_{Ts} = \frac{q^2 N_{Ts} P_{Ts}}{kT N_{TTs}}, \tag{4.101}$$

$$C_{Ks} = \frac{K\varepsilon_o}{\Delta x} \tag{4.102}$$

$$G_{nTs} = \frac{q^2 < c_{ns} > N_s P_{Ts}}{kT}, \tag{4.103}$$

$$G_{pTs} = \frac{q^2 < c_{ps} > P_s N_{Ts}}{kT}, \tag{4.104}$$

$$G_{nTis} = \frac{q^2 P_{Ts}}{kT N_{TTs}}[< c_{ns} > N_s P_{Ts} - e_{ns} N_{Ts}], \tag{4.105}$$

$$G_{pTis} = \frac{q^2 N_{Ts}}{kT N_{TTs}}[< c_{ps} > P_s N_{Ts} - e_{ps} P_{Ts}], \tag{4.106}$$

$$\text{and} \quad i_{ts} = q g_{ts}. \tag{4.107}$$

The corresponding equivalent circuit is given in Figure 4.3. Equations (4.99) to (4.107) and Figure 4.3 are consistent with that derived by Sah [54].

4.2.2 Surface Band

An equivalent circuit is developed in this section to incorporate a surface deep-level state that is distributed over an energy range. Silicon has been observed [55] to have such a surface band. The four rate processes depicted in Figure 4.1 are assumed to occur at the surface as in the bulk. The development here differs slightly from before in that the capture and emission rate coefficients are a function of the carrier band energy level and also the energy between the carrier band and surface band. Each incremental process is developed first, then the small signal analysis is applied, and the equivalent circuit is deduced.

Process (asb) is the rate of electron capture by the surface band and can be expressed as

$$d^2r_{asb} = c_{nsb}(E, E_{sb})f(E)D(E)[1 - f_{sb}(E_{sb})]D_{sb}(E_{sb})dEdE_{sb} \tag{4.108}$$

where E_{sb} is the energy level of the surface band increment dE_{sb}, and the subscript sb is used to indicate a surface band property. All other symbols are consistent with earlier definitions. This equation becomes upon integration over the conduction band

$$dr_{asb} =< c_{nsb}(E_{sb}) > n_s[1 - f_{sb}(E_{sb})]D_{sb}(E_{sb})dE_{sb} \tag{4.109}$$

where

$$< c_{nsb}(E_{sb}) >=< c_{nsb} >= \frac{1}{n_s}\int_{E_C}^{\infty} c_{nsb}(E, E_{sb})f(E)D(E)dE. \tag{4.110}$$

Process (bsb) is the rate of electron emission from the surface band and is given by

$$d^2r_{bsb} = e_{nsb}(E, E_{sb})[1 - f(E)]D(E)f_{sb}(E_{sb})D_{sb}(E_{sb})dEdE_{sb}. \tag{4.111}$$

This equation becomes upon integration over the conduction band

$$dr_{bsb} = e_{nsb}(E_{sb})f_{sb}(E_{sb})D_{sb}(E_{sb})dE_{sb} \tag{4.112}$$

where

$$e_{nsb}(E_{sb}) = e_{nsb} = \int_{E_C}^{\infty} e_{nsb}(E, E_{sb})[1 - f(E)]D(E)dE. \tag{4.113}$$

The principle of detailed balance applies to the surface band states at each increment of energy, *i.e.*, $dr_{asb} = dr_{bsb}$. This yields the following relation:

$$\frac{e_{nsb}}{< c_{nsb} >} = \frac{n_e[1 - f_{sb}]}{f_{sb}} = n_i\frac{1}{g}\exp(\frac{E_{sb} - E_i}{kT}) \tag{4.114}$$

where the distribution function was assumed to have the same form as equation (4.20) and equation (4.22) was used to relate the equilibrium electron concentration to the intrinsic concentration. This relation will be used in the derivation of the equivalent circuit.

Process (csb), the rate of hole capture can be expressed as

$$d^2r_{csb} = c_{psb}(E, E_{sb})[1 - f(E)]D(E)f_{sb}(E_{sb})D_{sb}(E_{sb})dEdE_{sb} \tag{4.115}$$

and upon integration over the valence band becomes

$$dr_{csb} =< c_{psb}(E_{sb}) > p_s f_{sb}(E_{sb})D_{sb}(E_{sb})dE_{sb} \tag{4.116}$$

where

$$< c_{psb}(E_{sb}) >=< c_{psb} >= \frac{1}{p_s}\int_{-\infty}^{E_V} c_{psb}(E, E_{sb})[1 - f(E)]D(E)dE. \tag{4.117}$$

Process (dsb) is the rate of hole emission from the surface band and is given by

$$d^2r_{dsb} = e_{psb}(E, E_{sb})f(E)D(E)[1 - f_{sb}(E_{sb})]D_{sb}(E_{sb})dEdE_{sb}. \tag{4.118}$$

This equation becomes upon integration over the valence band

$$dr_{dsb} = e_{psb}(E_{sb})[1 - f_{sb}(E_{sb})]D_{sb}(E_{sb})dE_{sb} \tag{4.119}$$

where

$$e_{psb}(E_{sb}) = e_{psb} = \int_{-\infty}^{E_V} e_{psb}(E, E_{sb})f(E)D(E)dE. \tag{4.120}$$

The rate of process (csb) equals the rate of process (dsb) at each increment of surface band energy under thermal equilibrium. This yields the equilibrium relation between rate constants,

$$\frac{e_{psb}}{< c_{psb} >} = gn_i\exp(\frac{E_i - E_{sb}}{kT}) \tag{4.121}$$

which was derived in the same manner as equation (4.114).

The governing equations at the surface are similar to those of the single energy level surface state. The rate of surface band state concentration must be addressed at a particular energy level and not as an integrated sum of reactions because equilibrium conditions only apply to individual states at a particular energy level. Thus the rate of change of surface band concentration is given by

$$\frac{\partial n_{sb}(E_s)}{\partial t} = [dr_{asb} - dr_{bsb} - dr_{csb} + dr_{dsb} + g_{sb}(E_{sb}, t)]\,|_{E_{sb}}\,. \tag{4.122}$$

Gauss' Law can be expressed as

$$-\frac{K\varepsilon_o}{q}\frac{\partial\psi}{\partial x} = q\int_{E_l}^{E_u} f_{sb}(E_{sb})D_{sb}(E_{sb})dE_{sb} \tag{4.123}$$

where E_u and E_l are the upper and lower energy bounds of the surface band, respectively.

The concentrations of electrons and holes, and the surface band distribution function can be approximated with the first two terms of the Taylor series expansion. These expressions are

$$n_s = N_s + \frac{N_s}{kT}(\partial F_{ns} - \partial E_{is}), \tag{4.124}$$

$$p_s = P_s + \frac{P_s}{kT}(\partial E_{is} - \partial F_{ps}), \tag{4.125}$$

$$f_{sb}(E_{sb}) = f_{sb} - \frac{1}{kT}f_{sb}(1 - f_{sb})(\partial E_{is} - \partial F_{sb}), \text{ and} \tag{4.126}$$

$$1 - f_{sb}(E_{sb}) = 1 - f_{sb} + \frac{1}{kT}f_{sb}(1 - f_{sb})(\partial E_{is} - \partial F_{sb}) \tag{4.127}$$

where f_{sb} (without the energy notation) denotes the static distribution function which is a function of E_{sb}.

An additional assumption is necessary in the present case due to the distributed nature of the surface band; small perturbations in potential are independent of the surface band energy level. The above Taylor series approximations are substituted into the governing equations to yield

$$\int_{E_l}^{E_u} \frac{1}{kT}f_{sb}(1 - f_{sb})D_{sb}(E_{sb})dE_{sb}\left(\frac{\partial F_{ns}}{\partial t} - \frac{\partial E_{is}}{\partial t}\right) = \int_{E_l}^{E_u} [< c_{nsb}(E_{sb}) > [N_s +$$

$$\frac{N_s}{kT}(\partial F_{ns} - \partial E_{is})][1 - f_{sb} + \frac{1}{kT}f_{sb}(1 - f_{sb})(\partial E_{is} - \partial F_{sb})]D_{sb}(E_{sb})$$

$$- e_{nsb}(E_{sb})[f_{sb} - \frac{1}{kT}f_{sb}(1 - f_{sb})(\partial E_{is} - \partial F_{sb})]D_{sb}(E_{sb}) \tag{4.128}$$

$$- < c_{psb}(E_{sb}) > [P_s + \frac{P_s}{kT}(\partial E_{is} - \partial F_{ps})][f_{sb} - \frac{1}{kT}f_{sb}(1 - f_{sb})(\partial E_{is} - \partial F_{sb})]D_{sb}(E_{sb})$$

$$+e_{psb}(E_{sb})[1 - f_{sb} + \frac{1}{kT}f_{sb}(1 - f_{sb})(\partial E_{is} - \partial F_{sb})]D_{sb}(E_{sb}) + g_{sb}(E_{sb}, t)\Big] dE_{sb}.$$

The time derivative of Gauss' Law can be expressed as

$$-\frac{K\varepsilon_o}{q}\frac{\partial}{\partial t}\frac{\partial \psi}{\partial x} = q\int_{E_l}^{E_u} \frac{1}{kT}f_{sb}(1 - f_{sb})(\frac{\partial E_{is}}{\partial t} - \frac{\partial F_{sb}}{\partial t})D_{sb}(E_{sb})dE_{sb}. \tag{4.129}$$

The steady state equation is subtracted from the above equations and second order terms are neglected. The governing equations become, upon regrouping the dynamic energy terms,

$$\int_{E_l}^{E_u} \frac{1}{kT}f_{sb}(1 - f_{sb})D_{sb}(E_{sb})dE_{sb}(\frac{\partial F_{sb}}{\partial t} - \frac{\partial E_{is}}{\partial t}) = \tag{4.130}$$

$$\int_{E_l}^{E_u} < c_{nsb}(E_{sb}) > \frac{N_s(1 - f_{sb})D_{sb}(E_{sb})}{kT}dE_{sb}(\partial F_{ns} - \partial F_{sb})$$

$$+\int_{E_l}^{E_u} \Bigg[< c_{nsb}(E_{sb}) > \frac{N_s(1 - f_{sb})^2 D_{sb}(E_{sb})}{kT}$$

$$-e_{nsb}(E_{sb})\frac{f_{sb}(1 - f_{sb})D_{sb}(E_{sb})}{kT}\Bigg] dE_{sb}(\partial F_{sb} - \partial E_{is})$$

$$+\int_{E_l}^{E_u} \left[< c_{psb}(E_{sb}) > \frac{P_s f_{sb} D_{sb}(E_{sb})}{kT} - e_{psb}(E_{sb})\frac{f_{sb}(1 - f_{sb})D_{sb}(E_{sb})}{kT}\right] dE_{sb}(\partial F_{sb} - \partial E_{is})$$

$$+\int_{E_l}^{E_u} < c_{psb}(E_{sb}) > \frac{P_s f_{sb} D_{sb}(E_{sb})}{kT}dE_{sb}(\partial F_{ps} - \partial F_{sb}) + \int_{E_l}^{E_u} g_{sb}(E_{sb}, t)dE_{sb}$$

and

$$-\frac{K\varepsilon_o}{q}\frac{\partial}{\partial t}\frac{\partial \partial E_{is}}{\partial x} = q\int_{E_l}^{E_u} \frac{1}{kT}f_{sb}(1 - f_{sb})(\frac{\partial E_{is}}{\partial t} - \frac{\partial F_{sb}}{\partial t})D_{sb}(E_{sb})dE_{sb}. \tag{4.131}$$

These governing equations are related to common circuit components through the substitution of $-qv$ in place of the quasi Fermi energies and multiplication of each equation by the electronic charge, q. The governing equations can be expressed as

$$C_{sb}\frac{\partial(v_{sb} - v_{is})}{\partial t} - (G_{nisb} + G_{pisb})(v_{sb} - v_{is}) - G_{psb}(v_{ps} - v_{sb}) - G_{nsb}(v_{ns} - v_{sb}) = i_{sb} \tag{4.132}$$

and

$$C_{sb}\frac{\partial(v_{sb}-v_{is})}{\partial t}=C_{Ks}\frac{\partial(v_{is}-v_{i1})}{\partial t} \tag{4.133}$$

where the conductances have units of current per volt per area and the capacitances have units of charge per volt per area. These circuit components are defined as

$$C_{sb}=q^2\int_{E_l}^{E_u}\frac{1}{kT}f_{sb}(1-f_{sb})D_{sb}(E_{sb})dE_{sb} \tag{4.134}$$

$$C_{Ks}=\frac{K\varepsilon_o}{\Delta x} \tag{4.135}$$

$$G_{nsb}=\int_{E_l}^{E_u}<c_{nsb}(E_{sb})>\frac{N_s(1-f_{sb})D_{sb}(E_{sb})}{kT}dE_{sb} \tag{4.136}$$

$$G_{psb}=\int_{E_l}^{E_u}<c_{psb}(E_{sb})>\frac{P_sf_{sb}D_{sb}(E_{sb})}{kT}dE_{sb} \tag{4.137}$$

$$G_{nisb}=\int_{E_l}^{E_u}\left[<c_{nsb}(E_{sb})>\frac{N_s(1-f_{sb})^2D_{sb}(E_{sb})}{kT}-e_{nsb}(E_{sb})\frac{f_{sb}(1-f_{sb})D_{sb}(E_{sb})}{kT}\right]dE_{sb} \tag{4.138}$$

$$G_{pisb}=\int_{E_l}^{E_u}\left[<c_{psb}(E_{sb})>\frac{P_sf_{sb}D_{sb}(E_{sb})}{kT}-e_{psb}(E_{sb})\frac{f_{sb}(1-f_{sb})D_{sb}(E_{sb})}{kT}\right]dE_{sb} \tag{4.139}$$

$$\text{and}\quad i_{sb}=q\int_{E_l}^{E_u}g_{sb}(E_{sb},t)dE_{sb}. \tag{4.140}$$

The corresponding equivalent circuit is identical to the equivalent circuit for the single energy level surface state given in Figure 4.3. This circuit and its related equations are consistent with that of Sah [54].

4.3 Complete Equivalent Circuit

The surface state equivalent circuit can be coupled to the bulk state equivalent circuit by converting the bulk state capacitances and conductances from a volume basis to a surface area basis. This is done by multiplying these terms by the width of the element, W, which is identical to the Δx term in the dielectric capacitance. The two circuits can be linked by this step because $C_{Ks}=WC_K=K\varepsilon_o/W$. The complete equivalent circuit is shown in Figure 4.4 for a Schottky barrier with no DC leakage current. The Schottky contact can be treated as a capacitance, C_o, connected only to the intrinsic energy line because electrons and holes cannot flow across a Schottky contact; only charging and discharging is allowed in an ideal case. The Ohmic contact on the right side of the circuit can be treated as a short of all three energy lines because a potential difference cannot be maintained in a metal contact.

The circuit shown in Figure 4.4 represents the minimum number of elements needed to model a Schottky contact (one element) with surface states (one element). In the case of a pn junction, at least two bulk state elements are needed. It can be assumed that surface states at the Ohmic contacts can be neglected because the contacts would appear as a short across the surface states. One of the bulk state elements would represent a semiconductor with p–type behavior and the other element would represent n–type behavior.

The use of only one element can be rationalized from an analysis of the deep–level state terms at various locations in the semiconductor. The trap capacitance, C_t, is proportional to the product of the trapped electron concentration, N_T, and the trapped hole concentration, P_T. The trap can be assumed to be completely full or empty in the bulk of the semiconductor depending on the location of the trap energy level in relation to the Fermi level. Therefore the product $N_T P_T$ is zero and, hence, the trap capacitance is zero. Likewise, band bending at the surface will make either N_T or P_T zero and the trap capacitance zero. The maximum in the trap capacitance will occur at the point where the trap energy level, E_T, crosses the Fermi energy level at which point $N_T = P_T$. The product of the trapped electron probability and the trapped hole probability, $f_T[1 - f_T]$ is its maximum value of one fourth at this point. It is this region of the semiconductor that this equivalent circuit addresses. The point at which the two energy levels cross is not the width of the depletion layer but is of the same order of magnitude [56]. It is also worth noting that in the absence of either a Schottky contact or pn junction, the equivalent circuit would be represented by a single conductance term, G_n or G_p. (Replace the Schottky capacitance, C_o in Figure 4.4 with a short between v_{ps}, v_{is}, and v_{ns}). No space charge region would form and, hence, the filling and emptying of traps would not take place. Although surface and/or bulk states may be present, neither would influence the electrical response.

4.3.1 Simplifications of the Complete Circuit

It was assumed that the experiments performed in this work do not perturb the semiconductor far from equilibrium such that the steady state quasi–Fermi levels equal the equilibrium Fermi level, E_F. The steady state concentrations are equal to their equilibrium concentrations with this assumption. As a direct result of this equilibrium assumption, the transconductance terms, G_{nTi}, G_{pTi}, *etc.*, are zero (rate of emission equals rate of capture) and can be removed from the circuit.

Additional assumptions can be made if the semiconductor is n–type or p–type. All of the semiconductor devices studied in this work can be treated as n–type semiconductors with Schottky contacts. The concentration of electrons is many orders of magnitude greater than the concentration of electrons for this case ($p_e n_e = n_i^2$, $n_e \approx 10^{17}, n_i \approx 10^{10}$). This permits the removal of the hole conductance (G_p), the hole capacitance (C_p), and the hole recombination conductance (G_{pTi}) terms in Figure 4.4. This also has the effect of removing the hole surface state recombination term (G_{pTis}) from the circuit even though the concentration of holes at the surface might be of the same order of magnitude as the bulk concentration of electrons [57]. The resulting equivalent circuit is presented in Figure 4.5.

The circuit in Figure 4.5 can be further simplified if there is only a surface state and no bulk states (Figure 4.6(a)) or only a bulk state and no surface state (Figure 4.6(b)). Note the general features of Figures 4.5 and 4.6. A trap conductance and capacitance series is in parallel to a capacitance. The conductance–capacitance series can be thought of as a recombination arm and the capacitance as a space charge capacitance. The space charge capacitance is composed of either the dielectric capacitance and the electron capacitance in series for the surface state case, or, only the electron capacitance for a bulk state. This space charge capacitance will remain constant in either case so long as the concentration of deep–level states is several orders of magnitude smaller than the concentration of electrons due to shallow–level states.

It was assumed throughout the derivation of this circuit that the two dielectric capacitances were identical because in the finite difference approximation of the second derivative of potential, the element width, Δx, was assumed to be constant. This is certainly true for the case of a large number of bulk elements. However, in the present case only one bulk state element was used and the assumption of equal sized element widths is not appropriate. The element width that comprises the space charge region is very small and of the same order of magnitude as the depletion width, W. Whereas, the element width near the Ohmic contact incorporates the bulk of the semiconductor and is on the order of a millimeter. This implies that the dielectric capacitance terms, which are inversely proportional to the element width, differ by several orders of magnitude. The dielectric capacitance near the Schottky contact is much larger than the dielectric capacitance near the Ohmic contact to the extent that the latter term can be treated as an open circuit.

The governing equations in this chapter have been developed for the case of one bulk deep–level state and one surface state. There will be one additional governing equation that resembles the kinetic trap equation for each additional state present. These will appear as recombination arms in parallel to those depicted in Figures 4.4 to 4.6 with similar definitions. (Multiple energy level states were also treated by Sah [58].)

Based on the above discussion, the final simplified equivalent circuit used to regress the experimental data is given in Figure 4.7. This circuit has all the essential features that were mentioned above, namely, the equivalent circuit for a surface state is identical to that of a bulk state. It is possible to distinguish the two types of states by means of a Mott–Schottky plot (C^2 versus applied bias) as discussed in Chapter 2. A leakage resistor has been added to the equivalent circuit of Figure 4.7 to account for the non–ideal behavior of the Schottky contact (DC leakage current). This term is proportional to the exponential of an activation energy. The activation energy can be the barrier height of the Schottky barrier or the energy difference between the conduction band and a surface state energy level. Leakage resistance was addressed for a p-n junction in the literature [59, 60]. The leakage resistor may also be the internal resistor, R_{in}, of the measuring op amp, especially in cases in which the sample impedance is of the same order of magnitude as R_{in}[61]

A similar circuit was derived by van der Ziel [62] in 1959 to account for generation–recombination noise due to traps in semiconductors. Van der Ziel [63] also determined trap activation energies by measuring noise resistance as a function of frequency and temperature (similar to Admittance Spectroscopy). Dare–Edwards *et al.* [64] developed a similar circuit by eliminating terms from the governing equations before developing an equivalent circuit. Nicollian and Goetzberger [55] developed this circuit (without leakage resistance) to analyze interface states of metal–insulator–semiconductor (MIS) capacitors.

The impedance data was regressed to the simplified equivalent circuit by complex nonlinear regression [65, 66]. This regression method is based on the Levenberg–Marquardt algorithm [67]. An alternative is to use the nonlinear regression package by Macdonald [68]. Various weighting schemes were used in the data regression; this will be discussed in the Results and Discussion chapter.

4.3.2 Analysis of the Recombination Circuit Components

This section explores the information that can be obtained from the equivalent circuit presented in Figure 4.7. The terms of interest in relation to deep–level states are the conductance and capacitance in the recombination arm. These terms are for a bulk trap

$$C_T = \frac{q^2 N_T P_T}{kT N_{TT}} \tag{4.141}$$

and

$$R_{nT} = \frac{1}{G_{nT}} = \frac{kT}{q^2 < c_n > N P_T}. \tag{4.142}$$

It is necessary to determine the temperature dependence of these terms.

The concentration of conduction band electrons for a non–degenerate semiconductor is given by [36]

$$N = N_c \exp(\frac{E_F - E_C}{kT}) \tag{4.143}$$

where

$$N_c = 2(\frac{2\pi m_e kT}{h^2})^{1.5} M_c \tag{4.144}$$

and m_e is the effective mass of the electron, h is the Planck constant, and M_c is the number of equivalent conduction band minima. The concentration of empty traps is given by $P_T = (1 - f_T)N_{TT}$. The product NP_T can be represented as

$$N P_T = N_c N_{TT} \frac{\frac{1}{g}\exp(\frac{E_T - E_C}{kT})}{1 + \frac{1}{g}\exp(\frac{E_T - E_F}{kT})}. \tag{4.145}$$

The electron capture coefficient is defined as the capture cross–section multiplied by the thermal velocity of the electron, *i.e.*,

$$< c_n > = \sigma_n \bar{v_n} = \sigma_n \sqrt{3kT/m_e}. \tag{4.146}$$

The last two expressions are substituted into equation (4.142),

$$R_{nT} = \frac{kT}{q^2 \sigma_n \bar{v_n} N_c N_{TT}} [g + \exp(\frac{E_T - E_F}{kT})] \exp(\frac{E_C - E_T}{kT}), \tag{4.147}$$

or

$$R_{nT} = \frac{k}{q^2 \sigma_n \gamma_n T N_{TT}} [g + \exp(\frac{E_T - E_F}{kT})] \exp(\frac{E_C - E_T}{kT}) \tag{4.148}$$

where

$$\gamma_n = 2(\frac{2\pi m_e k}{h^2})^{1.5} M_c \sqrt{3k/m_e}. \tag{4.149}$$

Note that $N_c \bar{v_n} = \gamma_n T^2$.

The recombination capacitance or trap capacitance can be expressed as

$$C_T = \frac{q^2 N_{TT}}{gkT} \exp(\frac{E_T - E_F}{kT})[1 + \frac{1}{g} \exp(\frac{E_T - E_F}{kT})]^{-2}. \tag{4.150}$$

The product of the recombination resistance and the recombination capacitance is the time constant of the recombination arm. The inverse of this time constant can be thought of as a characteristic frequency. The equivalent circuit characteristic frequency can be expressed as

$$\frac{1}{R_{nT} C_T} = \sigma_n \gamma_n T^2 [\exp(\frac{E_F - E_C}{kT}) + \frac{1}{g} \exp(\frac{E_T - E_C}{kT})]. \tag{4.151}$$

The emission rate used in DLTS analysis can be derived here with the principle of detailed balance, equation (4.14), *i.e.*,

$$e_n N_T = < c_n > P_T N = \sigma_n \bar{v_n} N_c P_T \exp(\frac{E_F - E_C}{kT}), \tag{4.152}$$

or

$$e_n = \sigma_n \bar{v_n} N_c \frac{1 - f_T}{f_T} \exp(\frac{E_F - E_C}{kT}) = \sigma_n \bar{v_n} N_c \frac{1}{g} \exp(\frac{E_T - E_C}{kT}). \tag{4.153}$$

This equation is rearranged such that the temperature dependence is shown explicitly,

$$e_n = \sigma_n \gamma_n T^2 \frac{1}{g} \exp(\frac{E_T - E_C}{kT}). \tag{4.154}$$

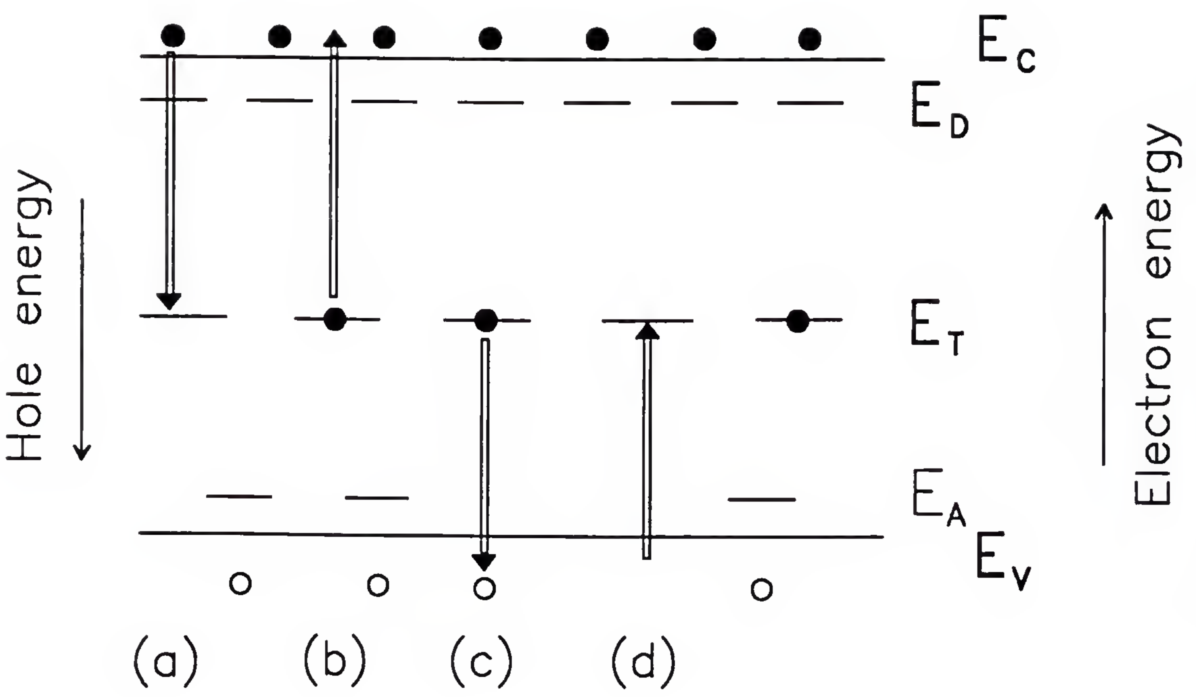

Figure 4.1: Shockley Read Hall processes of a deep-level state.

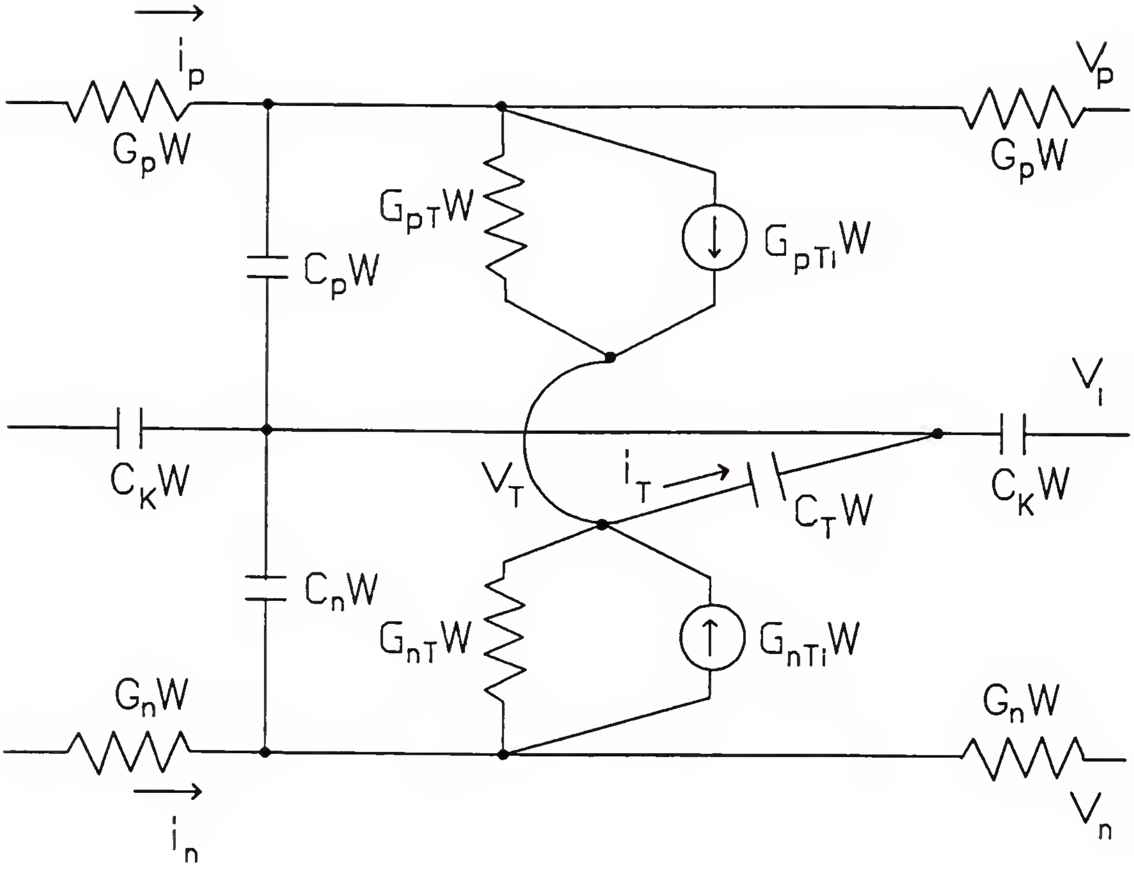

Figure 4.2: Equivalent circuit corresponding to the small signal non–equilibrium case for a bulk deep–level state. Equations and notation are given in the text.

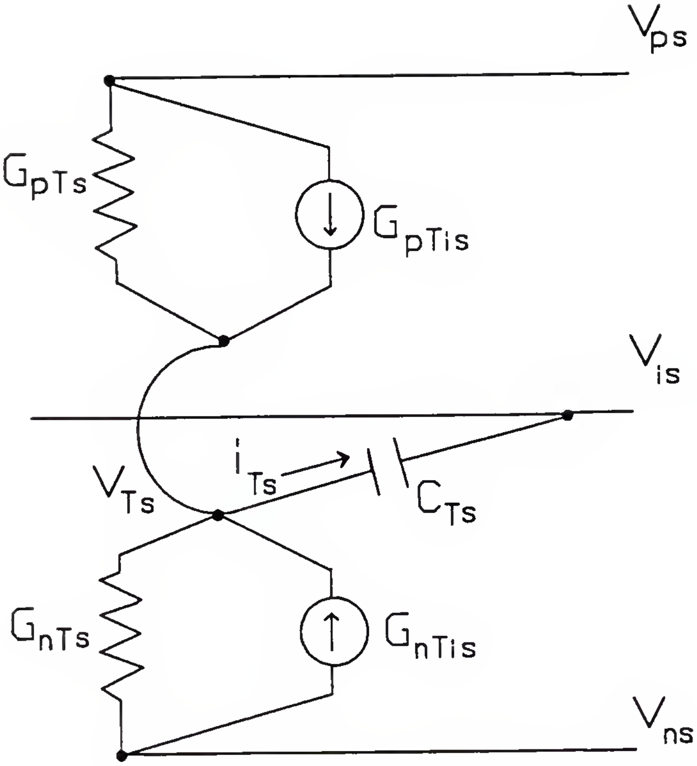

Figure 4.3: Equivalent circuit corresponding to the small signal non–equilibrium case for a surface state. Equations and notation are given in the text.

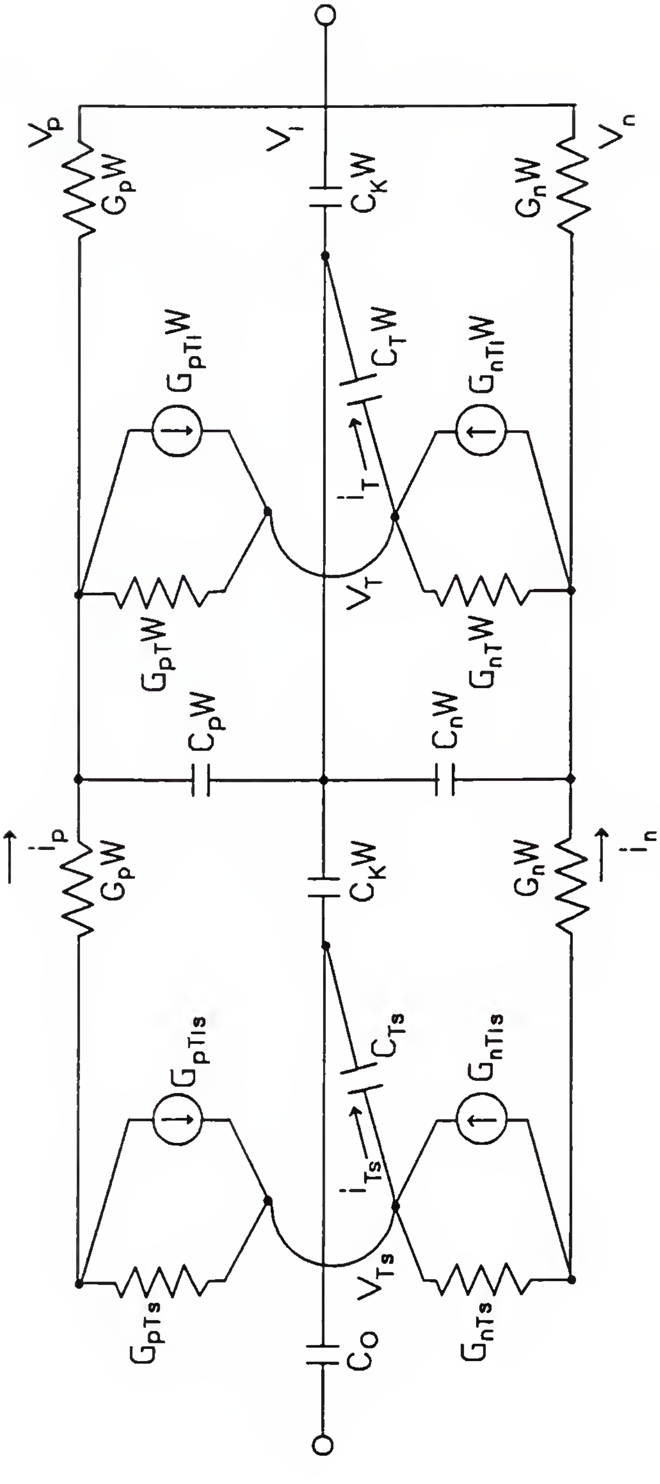

Figure 4.4: The complete non–equilibrium equivalent circuit with surface and bulk deep–level states for a Schottky barrier on the left side and an Ohmic contact on the right side with no DC leakage current.

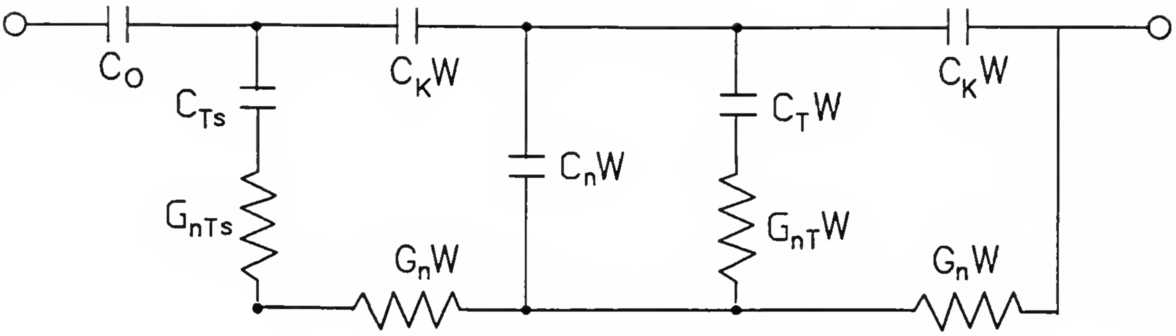

Figure 4.5: The reduced equilibrium equivalent circuit with surface and bulk deep-level states for a Schottky barrier on the left side and an Ohmic contact on the right side.

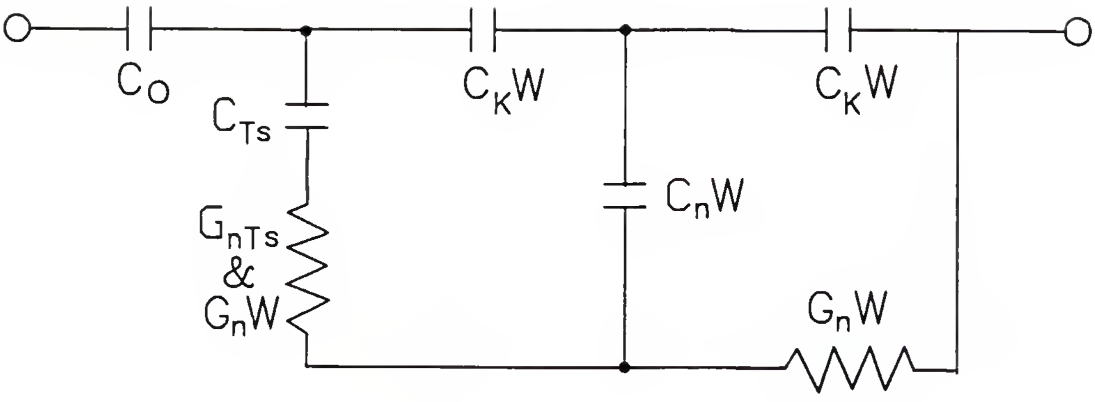

a

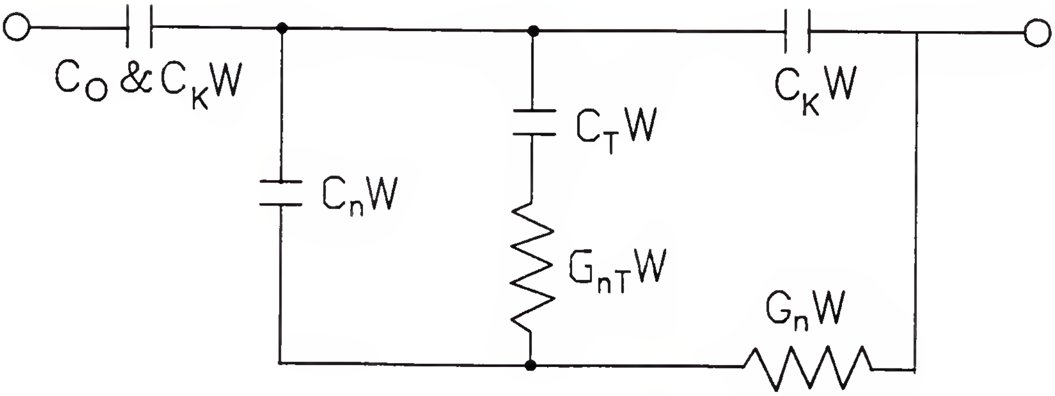

b

Figure 4.6: Simplified equilibrium equivalent circuit with only surface states (a), and only bulk deep-level states (b) for a Schottky barrier on the left side and an Ohmic contact on the right side.

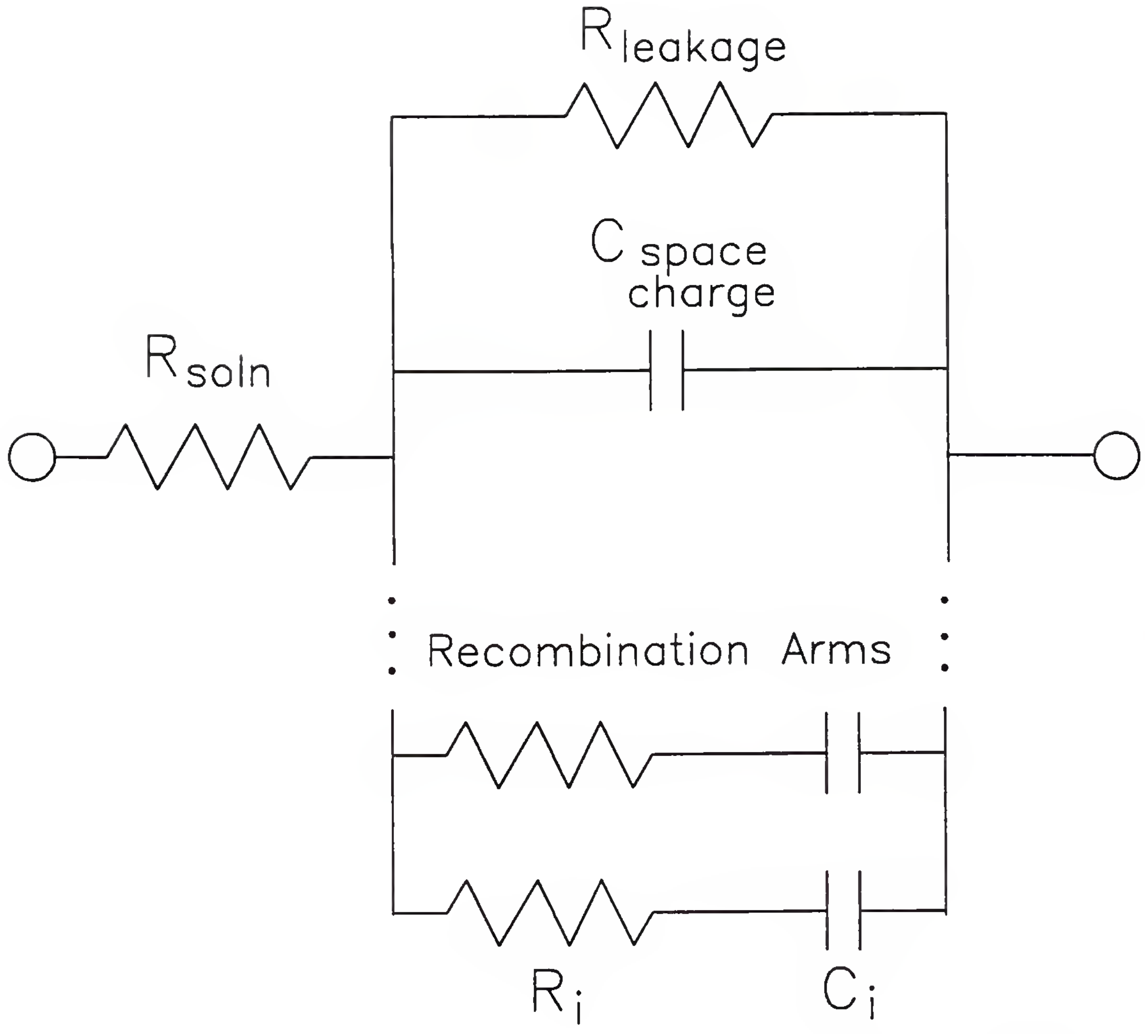

Figure 4.7: The reduced equilibrium equivalent circuit used in this work with a Schottky barrier on the left side and an Ohmic contact on the right side.

CHAPTER 5

SYSTEMS ANALYZED

An n–type gallium arsenide sample was used to calibrate the technique presented here against the well–known Deep–Level Transient Spectroscopy (DLTS) technique. The other samples analyzed in this work have large bandgaps and were known to have at least one deep–level state. The large bandgap guaranteed that the states near the mid–bandgap would not be ionized at room temperature and were thus susceptible to excitation by optical energy in the range of energies available with the present equipment.

5.1 Gallium Arsenide

The interest in single–crystal gallium arsenide in the past couple decades has led to the generation of vast amounts of literature on its properties. One of the best sources on GaAs is the collection of reprints edited by John S. Blakemore [69]. Many of the references on GaAs cited in this work were found in this source but the original publication is reported in the bibliography.

Several characteristic deep–level states were found to exist. The state referred to as EL2 is of particular interest to this work because its energy band lies approximately 0.83 eV below the conduction band and it is a majority trap. Thus, an n–type single gallium arsenide crystal with a Schottky barrier on one side and an Ohmic contact on the other is sufficient to demonstrate the validity of the DLZS technique. This state lies within the available range of optical energy with the present equipment (0.5 to

3.2 eV) and is a well studied state due to its presence in all bulk grown and vapor phase epitaxy grown samples [70, 71] (it is not present in samples grown by molecular beam epitaxy). The EL2 state is believed to be associated with an arsenic antisite, As_{Ga} (an arsenic atom occupying a gallium lattice site) [72].

The EL2 state is also labeled as ET1, ES1, and EB2 to denote the location of the various laboratories that analyzed this state (EL = Laboratoires d'Electronique et de Physique Appliquée (LEP), ET = University of Tokyo, ES = University of Sheffield, EB = Bell Telephone Laboratories, EF = University of Florida, EI = Institut für Angewandte Festkörperphysik).

An n–type gallium arsenide sample with a Schottky contact was provided by Mr. Darwin Thusius of Sula Technologies. The sample was grown by the horizontal Bridgmann technique (bulk grown) with silicon as the dopant ($N_D \approx 10^{17}$ cm^{-3}). The surface was reactively ion etched prior to deposition of titanium Schottky contacts (Ti, Pt, Au) on the top and a gold Ohmic contact (Au, Ge, Ni) on the bottom. The Schottky contacts were circular dots with a diameter of 1 mm.

5.2 ZnS:Mn Thin Film Electroluminescent (TFEL) Panel

"It is one of the ultimate dreams of mankind to create a TV display by using the flat panel display, that is, 'TV–on–the–wall"' [73]. Three display technologies are in competition to this end; liquid crystal, plasma, and electroluminescence [73]. Color liquid crystal displays are, as of 1989, limited to a maximum diagonal size of 14 inches. Monochromatic plasma displays have been made with a diagonal as large as 1.5 meters, however, color plasma displays suffer from low brightness and luminous efficiency. Electroluminescent displays have the highest resolution of the three technologies, however, the red, green, and blue color phosphors suffer from low luminance. Monochromatic (yellow) ZnS:Mn electroluminescent panel has the best performance in terms of luminous efficiency, longevity, and luminance [73]. For a review of the physics of electroluminescence see references [74–76].

The manganese atom (ion) in ZnS:Mn A.C. thin film electroluminescent (TFEL) panels is responsible for the emission of yellow light. The electronic transition occurs within the 3d–shell of the manganese ion, Mn^{2+}, ($1s^2 2s^2 2p^6 3s^2 3p^6 3d^5 4s^2$). An electron in an excited state, ${}^4T_1({}^4G)$, radiatively relaxes to the ground state, ${}^6A_1({}^6S)$ [77]. The energy of the emitted photon is centered at 2.12 eV (wavelength at 585 nm), yellow light. Various other radiative and non–radiative processes also take place within the 3d–shell [78–80].These energy transitions are within the range of the present equipment and an optical–impedance analysis of them should prove fruitful.

The sample tested was a thin film electroluminescent (TFEL) panel that consisted of a ZnS:Mn (1 wt. %) active layer sandwiched between two Y_2O_3 insulating layers. This sample was provided by Dr. David C. Morton, Department of the Army, Electronics Technology and Devices Laboratory at Fort Monmouth, NJ. The active layer was electron–beam deposited to a thickness of 5000 Å. The insulating layers were 2000 Å thick and deposited by the radio–frequency method. Aluminum was deposited on one of the insulating layers and indium–tin oxide (ITO) on the other. The bandgap of this polycrystalline device is around 3.6 eV.

5.3 ZnO Varistor

Varistors are used to protect parallel electronic components from voltage spikes. The most common are metal oxides which are typically greater than 80 mole% ZnO [81]. Potentiodynamic scans show that varistors behave as insulators at low applied potentials but allow a large current to pass when the applied voltage exceeds the breakdown potential. The breakdown potential is generally defined to be the applied potential at which the current density passed by the varistor is 1 mA/cm^2. ZnO varistors are polycrystalline, and the nonlinear electrical response has been attributed to formation of back-to-back diodes at the grain boundaries [82–84].The space charge regions associated with the grain boundaries are influenced by deep–level states which could arise from the ceramic sintering process or from dopant species.

Two ZnO varistors were tested in this work. One was tested in an "unaged" condition, and the other was tested after being subjected to a duty cycle to simulate the effect of "aging." The composition of both ZnO varistors was 1.0% (atomic) Bi, 0.9% Co, 0.25% Cr, 0.2% Mn, 0.5% Sb, 0.001% Al, with the remainder Zn on an oxygen free basis. Both varistors were fired at 1060 °C in air for 4 hours and then annealed. A silver based ink was fired onto the ZnO ceramic to form the electrical contact. The varistors were annealed for 4 hours at 800 °C. The recipe for fabrication of these varistors is given in reference [85]. The duty cycle used to simulate the aging process subjected the varistor to a positive square wave potential with an amplitude such that a current of 1 A/cm^2 passed for a period of 60 μs. This was followed by a 0 V bias for 15ms, a negative potential necessary to pass a current of 1 A/cm^2 for 60 μs, and another 15 ms of 0 V bias. This procedure was repeated for 575 hours.

The nominal bandgap of ZnO is approximately 3.2 eV. The measured breakdown potential for the device fabricated was 100 V. The main effect of aging apparent in the current–potential curves was that the current passed at low potentials (*e.g.,* 1 V) increased by several orders of magnitude. The breakdown potential was comparatively unaffected by aging.

5.4 Cuprous Oxide in Alkaline–Chloride Solutions

A brief history is presented first to highlight the semiconducting nature of cuprous oxide and its response to illumination.. A detailed account of the copper electrode manufacturing is also given.

5.4.1 Background

Copper and copper alloys have found a wide use in the marine environment. Copper sheathing was originally used on wooden vessels to mechanically protect the wood and also to prevent marine growth and barnacles. These advantages are provided by copper's low rate of dissolution. It is noble enough to prevent noticeable corrosion in sea water, but corrodes uniformly enough to prevent marine growth from becoming permanently attached. Copper corrodes at a slow uniform rate of approximately 0.002 ipy (inches per year) in low velocity sea water [86]. The corrosion products formed on the copper surface in sea water are a mixture of cupric oxychlorides, cupric hydroxide, basic cupric carbonate, and calcium sulfates. A protective layer of cuprous oxide also forms on the surface as a distinct layer [86].

The electrode potential of copper ($\mathrm{Cu} \rightleftharpoons \mathrm{Cu}^{++} + 2e^-$ or $\mathrm{Cu} \rightleftharpoons \mathrm{Cu}^{+} + e^-$) is cathodic to the standard hydrogen electrode ($\frac{1}{2}\mathrm{H}_2 \rightleftharpoons \mathrm{H}^+ + e^-$) except in extremely acidic solutions (greater than 5N) [86]. Hence, the oxidation of Cu metal to Cu^{++} and the complimentary half cell reaction of H^+ reduction to H_2 gas will not occur, but rather, copper ions would plate out of solution onto the metal. The only other possible cathodic (reduction) reaction that could cause the anodic (oxidation) reaction of copper is O_2 reduction. The two half cell reactions of interest are:

$$2\mathrm{Cu} \rightleftharpoons 2\mathrm{Cu}^{++} + 4e^- \tag{5.1}$$

and

$$2\mathrm{H}_2\mathrm{O} + \mathrm{O}_2 + 4e^- \rightleftharpoons 4\mathrm{OH}^-. \tag{5.2}$$

The O_2 reduction reaction holds for alkaline solutions (sea water is alkaline). Oxygen has a dual role in that it causes copper corrosion but also forms an adherent cuprous oxide layer on the surface that hinders further corrosion [86].

Uhlig [87] suggested that the corrosion rate was limited at the metal–oxide interface rather than oxygen diffusion through the oxide layer or oxygen reduction at the oxygen–oxide interface (see also Fromhold [88] for a critique). However, diffusion through the oxide would control the corrosion rate for very thick oxide layers. Uhlig presented three observations (from other authors) to support his claim. The first observation was that the corrosion rate is dependent on the crystal orientation but, the oxides of iron and copper have a cubic lattice in which diffusion is isotropic. (Corrosion is dependent on the crystal orientation of the metal, not the oxide.) The second observation was that the corrosion rate activation energy is discontinuous at the lattice transformation for iron (α(bcc) to γ(fcc)). The third observation was that the corrosion rate changed at the Curie temperature for nickel metal, and iron–nickel and chromium–iron alloys. Metals undergo a magnetic transition at the Curie temperature. The last two observations are relevant because it can be inferred that the corrosion rate changes upon a transition in the metal, and not, in the oxide layer or the solution.

Cuprous oxide is a semiconductor and was used as a crystal rectifier before the advent of transistors [89]. It is therefore advisable to investigate the semiconducting properties of the copper oxide layer on the corroding copper metal. Deep–level states could also be present in the cuprous oxide layer as in any semiconductor. Ives and Rawson [90] suggested that chloride ions (Cl^-) replace oxide ions (O^{2-}) in the cuprous oxide layer. They determined that chloride ions were present in the oxide layer by chemical analysis. This would make the semiconductor deficient in negative charge (one less for each chloride ion) and thus promote the vacancy of a copper ion site. Vacancies are typically deep–level states.

Nagasubramanian *et al.* [91] used both the photoacoustic spectrum and the photocurrent action spectrum to determine the bandgap of p–type cuprous oxide in acetonitrile solutions with various redox couples. (The cuprous oxide layer was formed through anodization of copper in NaOH solutions.) They determined the bandgap to be 2.0 eV with a flatband potential of +0.16 V versus a saturated calomel electrode (SCE) and indicated that it was a direct band to band transition. Collisi and Strehblow [92] investigated the cuprous oxide layer on copper in alkaline solution with various redox couples using photocurrent spectroscopy. They determined the layer to be p–type with an indirect bandgap of 2.3 eV and a flatband potential of -0.52 eV versus SCE.

Bertocci [93] investigated the influence of white light on the Cu_2O film on copper through the measurement of photopotentials. He noted that the oxide film was photoconductive and demonstrated that light decreased the charge transfer resistance, rather than the resistivity of the oxide film. Varying the nickel and aluminum content of the copper alloy affected the corrosion resistance of the alloy but did not change the semiconducting properties of the oxide film. However, Bertocci found that the type of majority carrier (n–type or p–type) within the oxide layer depended on the method of preparation of the oxide layer. He also noted that illumination can lower the electrode potential (due to the photopotential) below the cuprous oxide/copper equilibrium which would lead to the destruction of the oxide film [93].

Escalante and Kruger [11] demonstrated that copper did not suffer from stress corrosion cracking under illumination for periods as long as five days, but did in the dark within twenty–four hours. Kruger and Calvert [94] used ellipsometry to study the formation of cuprous oxide on a single crystal of copper. They described the formation as a competition between growth and dissolution, *i.e.*,

$$2\mathrm{Cu} + \frac{1}{2}\mathrm{O}_2 \rightleftharpoons \mathrm{Cu}_2\mathrm{O} \tag{5.3}$$

and

$$\frac{1}{2}\mathrm{Cu}_2\mathrm{O} + \frac{1}{4}\mathrm{O}_2 + 2\mathrm{H}^+ \rightleftharpoons \mathrm{Cu}^{++} + \mathrm{H}_2\mathrm{O}, \tag{5.4}$$

respectively, where illumination promotes the dissolution reaction because it is essentially a Cu/Cu_2O photocell as described by Mott [95].

5.4.2 Experiment

A copper rod (99.99%) with a diameter of 6 mm was cut to a length of approximately 1 cm. One of the ends was shaped with a file to form a flat protrusion that extended 4 mm from the circular portion of the sample. A hole was drilled through the flat protrusion to facilitate the connection of a copper wire with a brass nut and bolt. The copper sample was then cleaned in an ultrasonic cleaner with the following solutions: 0.1 M HCl acid for five minutes; acetone for five minutes; and deionized water for five minutes. After this cleaning process, the sample was annealed in a radio frequency heater (Thermolyne Type 21100 Tube Furnace) by the following process: the heater, with sample, was purged with industrial grade argon gas for thirty minutes; the sample was heated to $1000°F$ over approximately thirty minutes time; the sample was maintained at $1000°F$ for one hour [96]; and then cooled to room temperature (in the argon environment) over a four hour period of time.

A purplish tarnish was present on the sample even though the argon gas was filtered through Ascarite II and Drierite to remove carbon dioxide and water, respectively. This tarnish was removed by repeating the ultrasonic cleaning process used above. The tarnish may be due to other impurities in the argon gas, to impurities in the copper sample that diffused to the surface during the annealing, to thermal decay of the rubber stoppers at the ends of the four foot long tube (although no visible signs of decay were present), or to back diffusion of the oil used in the air lock (a constant flow of argon should have presented this). The rubber stoppers should be replaced with some other material like teflon–the rubber stoppers initially melted when a two foot long tube was used by Oliver C. Moghissi.

A copper wire was bolted to the sample and the wire was strung through a glass tube bent into the shape of a "U". The wire was pulled tight to hold the copper sample against the end of the glass tube. The copper sample and the tube end were encased in epoxy to form a water tight seal between the sample and the glass tube. This guaranteed that only the polished surface of the sample would be exposed to the electrolyte. The epoxy used was a two–component laminating resin system (HEXCEL Epolite 2410 & Safe-T-Poxy from HEXCEL Corporation, Chatsworth, CA). This epoxy was used because it is water resistant. After the epoxy hardened (one day), the excess epoxy was filed off to expose the surface of the copper. The electrode was polished sequentially with 600 grit paper, 4000 grit paper, and then alumina powder (1 micron) suspended in water.

Two electrodes were made in the above manner. One of the electrodes was aged in ambient light conditions for approximately three weeks. The other electrode was aged in a dark environment for approximately five weeks. The solution used to age both samples was 0.5 M sodium chloride at pH 10. The solution that each electrode aged in was also used in the impedance experiments.

A schematic of the cell configuration used in the deep–level impedance spectroscopy experiments is presented in Figure 5.1. The copper electrode was 1 cm below the solution surface. A platinum sheet was used as the counter electrode and a saturated calomel electrode (SCE) was used as the reference electrode.

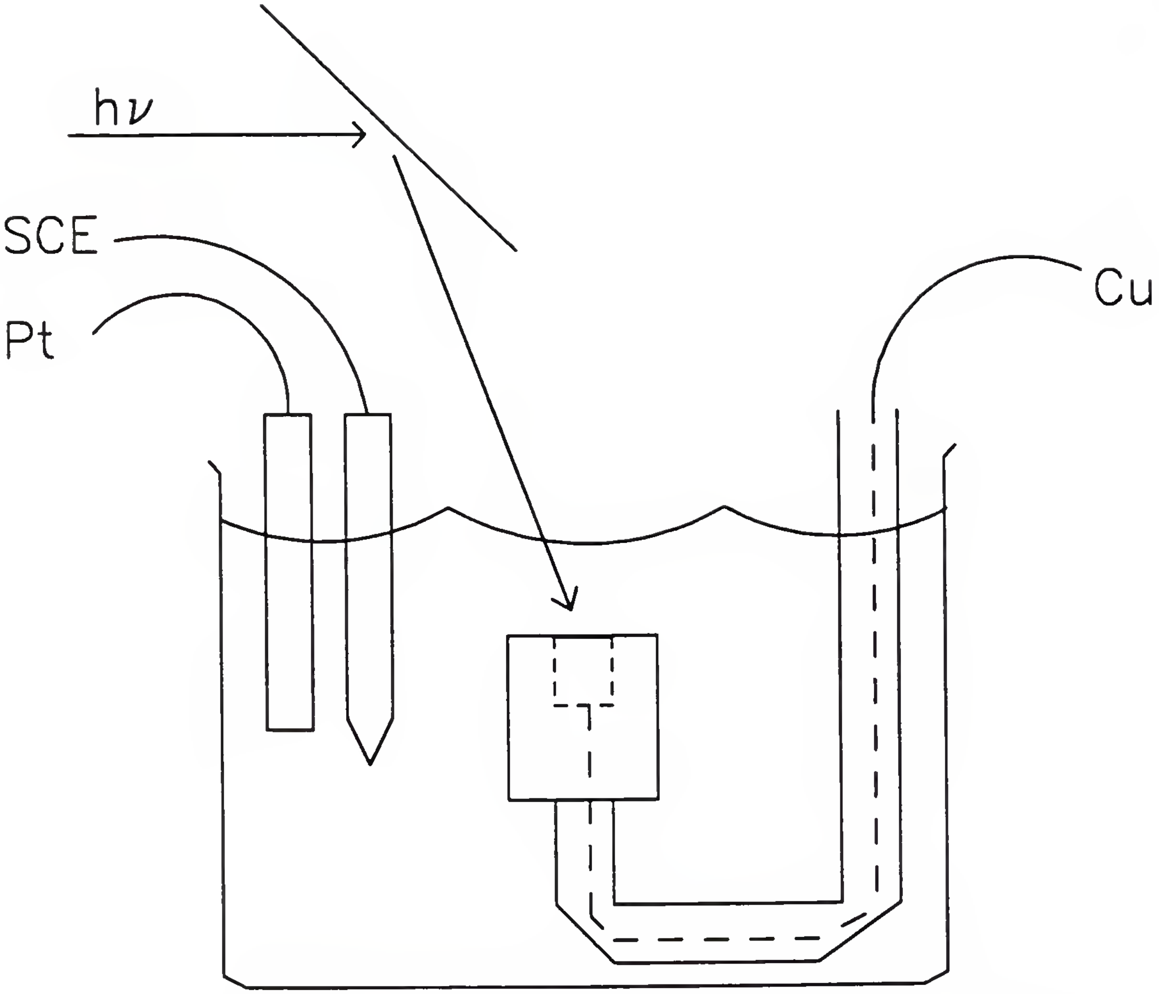

Figure 5.1: Cell configuration for the copper electrode experiments.

CHAPTER 6
RESULTS AND DISCUSSION

The first section in this chapter is based on the results of the n–type GaAs sample (Schottky contact) to demonstrate the validity of the equivalent circuit derived in a previous chapter and the usefulness of a combined optical and electrical frequency spectrum. The second section is devoted to the influence of data weighting in numerical regression. Results are presented for the ZnS:Mn electroluminescent panel and the ZnO varistors in the next two sections. Cuprous oxide on copper in alkaline–chloride solution is also discussed.

6.1 Gallium Arsenide

Results will be presented first for GaAs at six temperatures between 320 K and 420 K under dark conditions. These results are used to evaluate the equivalent circuit model because a direct comparison can be made to Deep–Level Transient Spectroscopy (DLTS) results which is also a thermal based technique. Optical excitation results are presented in the next subsection. These two methods are referred to here as Thermally Stimulated Deep–Level Impedance Spectroscopy (TS–DLZS) and Optically Stimulated Deep–Level Impedance Spectroscopy (OS–DLZS), respectively.

6.1.1 Thermally Stimulated Deep–Level Impedance Spectroscopy

The thermal impedance data for the GaAs sampled presented in this section was collected by Paul T. Wojcik and used in his masters' thesis. Figure 6.1 is a plot of the imaginary component of the impedance versus the real component of the impedance at 300 K and 340 K. Five replicate runs were made at each temperature (except at 300 K) to demonstrate the reproducibility of the experiment and also to determine the variance of the data to be used to weight the data in the numerical regression. (this will be discussed in the next section). The frequency ranged from 65,000 Hz to 1 Hz where the high frequency data resides at the plot origin. This type of plot is correctly referred to as an impedance plane plot. The potential bias was 0 Volts and the applied sinusoidal perturbation was 3 mV. The Solartron 1286 (potentiostat) was used with bandwidth C.

The impedance data were regressed to the equivalent circuit given in Figure 4.7. The regression was a complex fit with model variance weighting; this will be discussed in a later section. Four resistor–capacitor pairs were regressed to the impedance data taken at 300 K, 320 K, and 340 K; three pairs at 360 K, 380 K, and 400 K; and two pairs at 420 K. The resistances and capacitances are plotted on a log plot as a function of the inverse temperature in Figures 6.2 and 6.3, respectively. In these plots, the filled squares represent the leakage resistor and the space charge capacitance. The other symbols refer to the recombination arm resistances and capacitances. The lines in Figures 6.2 represent the linear regression of log resistances to inverse temperature. The resulting activation energy (proportional to the slope) for each line is shown.

An analysis of Figures 6.2 and 6.3 in relation to equations (4.147) and (4.150) confirms the validity of the equivalent circuit. In particular, the resistances obey an Arrhenius relationship with the temperature, and the capacitances are relatively temperature independent. This statement can be proven with a closer look at the physical processes that take place as a result of a sinusoidal perturbation.

Deep–level states influence the impedance response only if they are partially occupied. States that are completely full or completely empty will not emit or capture electrons in response to the sinusoidal perturbation. The influence of a state on the impedance response can be explained with the aid of an energy diagram, Figure 6.4. Three states are depicted in this figure, state E1 is close to the conduction band (shallow donor), state E2 is near the midgap (deep–level donor), and state E3 is close to the valence band (shallow acceptor). The Fermi level is also shown (E_F). States that reside at energies greater than approximately kT electron volts below the Fermi level (state E3) are filled with electrons and states that reside at energies greater than kT above the Fermi level (E1) are vacant. State E1 has emitted its electrons into the conduction band where they are mobile, leaving behind fixed (in space) positive charges. State E3 has been filled with electrons from the valence band. These electrons are fixed (in space) negative charges but, the electron vacancies in the valence band, or holes, are free to migrate and diffuse similar to the electrons in the conduction band.

State E2 lies below the Fermi level in the bulk of the sample, and thus, remains filled with electrons. However, the energy level rises and falls below the Fermi level in the space charge region in response to the rise and fall nature of the sinusoid. An E2 electron near the space charge region that rises above the Fermi level is thermodynamically favored in the conduction band and will thus be emitted into it as shown in Figure 6.4. Likewise, an E2 vacancies is thermodynamically favored to have an electron as its energy falls below the Fermi level. (Kinetics are also important–the frequency of the sinusoid and/or temperature dictates the kinetics of emission and capture processes.) The Fermi level remains constant because the system is assumed to remain at equilibrium–no carriers are injected into the semiconductor ($np = n_i^2$).

From the above discussion it can be inferred that only the states that are close to the Fermi level, or brought close through biasing, will influence the impedance response. (Optical excitation is a way these states can influence the impedance response without being close to the Fermi level.) In the portion of the space charge region that influences the impedance, the energy of the deep-level state approximately equals the Fermi level. Thus, in equations (4.147) to (4.151) $E_T \approx E_F$, and these equations become

$$R_{nT} \approx \frac{k}{q^2 \sigma_n \gamma_n T N_{TT}} (g+1) \exp(\frac{E_c - E_t}{kT}), \tag{6.1}$$

$$C_T \approx \frac{q^2 N_{TT}}{kT} \frac{g}{(g+1)^2}, \tag{6.2}$$

and

$$\frac{1}{R_{nT} C_T} \approx \sigma_n \gamma_n T^2 (1 + \frac{1}{g}) \exp(\frac{E_t - E_c}{kT}). \tag{6.3}$$

The regressed parameters were used to prove that the equivalent circuit model developed in Chapter 4 is appropriate. In particular, the equation for the resistance includes an Arrhenius relationship with temperature, as was observed for the regressed resistances (Figure 6.2). Also, the capacitance expression does not include an Arrhenius dependence with temperature, as was observed for the regressed capacitances (Figure 6.3). Figure 6.5 is the traditional plot of an Arrhenius relationship (negative slopes) where the inverse of the resistance is plotted as a function of the inverse temperature on a semilog plot. The equivalent circuit characteristic frequencies (equation (4.151)) are plotted in Figure 6.6 as a function of the inverse temperature. These characteristic frequencies also obey an Arrhenius relationship to temperature as predicted by equation (6.3).

The filled squares in all figures of regressed circuit elements represent either the leakage resistor (R_{leak}), the space charge capacitance (C_n), or some product of the two ($R_{leak} C_n$). The space charge capacitance is expected to have a slight Arrhenius dependence on temperature with an activation energy of $E_C - E_F$. No assumption of $E_T \approx E_F$ was necessary here, because C_n does not depend on the concentration of deep-level states. The regressed space charge capacitance also has a slight Arrhenius relationship with temperature as can be seen from an inspection of Figure 6.3. These capacitances are more uniform than the deep-level state capacitances. This could be due to the fact that the space charge capacitance is the dominant capacitance in the equivalent circuit and, thus, would have a higher confidence in the numerical regression. The leakage resistance is not a well defined term in this work at present, however, as mentioned during the development of the simplified circuit, this term is expected to also have an Arrhenius dependence where the activation energy is either a surface state or the height of the Schottky barrier. This dependence is apparent upon inspection of Figure 6.2. The leakage resistance would be independent of the temperature if the leakage resistance was due to the measuring op amp.

Four states can be inferred from plots of the regressed resistances and characteristic frequencies, Figures 6.2, 6.5, and 6.6. The activation energy of the leakage resistances is 0.802 eV. The activation energy of the remaining three recombination resistances are 0.482, 0.277, and 0.295 eV. The last state (resistance) appeared only at the three lowest temperatures. This state may be a doublet of the state at 0.277 eV because both the activation energies and the intercept are relatively close to each other.

These activation energies are not quite correct because the temperature dependence of the pre-exponentials was not treated. The correct method, in keeping with equations (6.1) to (6.3), is to plot temperature multiplied by the resistance, temperature multiplied by the capacitance, and the characteristic frequency divided by the square of temperature, as a function of inverse temperature. These plots are presented in Figures 6.7 to 6.9, respectively. Activation energies were derived from the slopes of the curves and capture cross–sections were derived from the intercepts. These values are presented in Table 6.1 along with the results from DLTS and literature. An effective value of $\gamma_n = g 1.9 \times 10^{24} \mathrm{m}^{-2}\mathrm{K}^{-2}\mathrm{s}^{-1}$ for GaAs was found in the literature [97]. The spin degeneracy (g) was assumed for the present to be equal to one.

Deep-Level Transient Spectroscopy (DLTS) was performed on this same sample as a comparison. The emission rate divided by the square of the peak temperature is plotted as a function of the inverse temperature in Figure 6.10. Three states were found with activation energies of 0.83, 0.48, and 0.32 eV. The capacitance was measured as a function of reverse bias with the DLTS spectrometer. This data was plotted in the form of a Mott–Schottky plot (Figure 6.11); the shallow-level dopant concentration was determined from the slope to be $N_D = 1.1 \times 10^{17}\text{cm}^{-3}$. The state at energy 0.48 eV below the conduction band was not tabulated in the literature. However, Weber *et al.*, [72] point out that a group V atom on a group III site (proposed for EL2) is expected to be a double donor. They also observed from Photo–EPR (Electron Paramagnetic Resonance) results that the EL2 state was a double donor with an energy level at $E_V + 0.75$ eV and another at $E_V + 0.52$ eV.

The activation energies from DLTS are in agreement with those determined from numerical regression of the impedance data given in Table 6.1. The capture cross-sections, determined from the intercepts of the curves in Figure 6.9, differ by several orders of magnitude from the DLTS values. The difference could be due to the narrow range of temperatures used (300 K to 420 K) which necessitates extrapolation over a very large temperature range. The intercept would be strongly influenced by small deviations in the regressed slope. These intercepts are not dependent on volume, unlike the intercepts of Figures 6.7 and 6.8. Trap concentrations and the shallow-level dopant concentration (from the space charge capacitance) were determined from the intercepts of the curves in Figure 6.8. These intercepts are dependent on an estimate of the volume as well as small deviations in the slopes (extrapolation over a very large temperature range).

The donor concentration was determined from the intercept of the space charge capacitance and is given in Table 6.1. Evaluation of the slope of this curve determined that the Fermi level was 0.041 eV below the conduction band. The donor concentration was also determined from the slope of the Mott–Schottky plot and is given in the same table. This value was one order of magnitude greater than the value determined from the space charge capacitance. The Mott–Schottky value for the donor concentration was used to calculate the Fermi level from the equation listed in the bottom right corner of Table 6.1. The Fermi level was calculated to be 0.038 eV below the conduction band (comparable to 0.041 eV). If the Fermi energy determined from the slope of the space charge capacitance is used in the same equation, the resulting donor concentration is in close agreement with the Mott–Schottky value. This suggests that evaluations dependent on the slope are much more reliable than those dependent on the intercept.

The appropriate volume estimate to use in the calculation of shallow and deep-level concentrations was assumed to be the volume near or within the Schottky depletion region where the concentration of holes and electrons fluctuate with the perturbing signal. Bonham and Orazem [7] used a numerical model to determine the width of this region. They obtained a value of approximately 6 to 8 times the Debye length. The Debye length for a GaAs sample with $N_D = 1.1 \times 10^{17}$ cm^{-3} at room temperature is 1.2×10^{-6} cm. The volume used in deriving Table 6.1 was 6 times the Debye length multiplied by the surface area of the Ti contact (1 mm diameter) or, 5.6×10^{-8} cm^3.

6.1.2 Optically Stimulated Deep–Level Impedance Spectroscopy

The influence of temperature as a parameter (under dark conditions) on the impedance response was discussed in the previous subsection. The influence of optical energy as a parameter (at room temperature) is discussed here. Figure 6.12 is a plot of the imaginary component of the impedance as a function of the real component of the impedance with optical energy as a parameter. The frequency ranged from 20,000 Hz to 4 Hz where the high frequency data resides at the plot origin. The intensity was set at approximately 6 mW/cm^2 for each wavelength used. The potential bias was 0 Volts and the applied sinusoidal perturbation was 20 mV. The PAR 273 potentiostat was used with the high speed bandwidth selection. Not much information can be gained from data plotted in this format because the high frequency data is compressed at the origin as well as the impedance data at high optical energies (large decrease in impedance due to emitted carriers). A more appropriate plot consists of making the impedance dimensionless by dividing the impedance component under optical stimulation at each electrical frequency by the impedance component in the dark at that same electrical frequency. Optical energy is the independent variable and electrical frequency is the parameter. These plots are presented in Figures 6.13 and 6.14.

The real component of the impedance divided by the real component in the dark is plotted as a function of optical energy in Figure 6.13 at three select electrical frequencies, 10000, 200, and 5.02 Hz. The dimensionless real impedance remains at unity for optical energy less than 0.8 eV for the three frequencies depicted. For optical energy greater than 0.8 eV, the real impedance decreased for 5.02 Hz and actually increased for 200 Hz. This is the energy difference $E_C - E_{EL2}$ for the EL2 state in GaAs. For the case of 10000 Hz, the real impedance increased for optical energy greater than 1.3 eV.

The imaginary component of the impedance in the dark divided by the imaginary component under illumination is plotted as a function of optical energy in Figure 6.14 at three select electrical frequencies. This ratio can be thought of as being a dimensionless capacitance (capacitance divided by capacitance in the dark). The imaginary impedance decreased for optical energy greater than 0.8 eV for 5.02 Hz and decreased for optical energy greater than 1.3 eV for 200 Hz. The dimensionless imaginary impedance remained at unity for the case of 10000 Hz. These two plots can be used to further emphasize the importance of electrical frequency in characterizing deep–level states.

The effect of light intensity on the impedance response was investigated to estimate the uncertainty of the data presented in Figures 6.13 and 6.14. The dimensionless real and imaginary component of the impedance are presented in Figures 6.15 and 6.16, respectively, as a function of light intensity for three electrical frequencies and optical energy of 1.1 eV (1130 nm). As mentioned in Chapter 3, the uncertainty of the light intensity was approximately 22 percent. This corresponds to an intensity range of 4.7 to 7.3 mW/cm^2. The variation in the dimensionless impedance in this intensity range was determined, from Figures 6.15 and 6.16, to be within the physical size of the symbols in Figures 6.13 and 6.14.

The two transitions at 0.8 eV and 1.3 eV might involve the same deep–level state in which the state is emitting its electron into successively higher conduction bands. Chantre *et al.,* [98] (see also [99]) used Deep–Level Optical Spectroscopy (DLOS) to investigate the optical excitation of the EL2 state. (They refer to this state as an oxygen state which was the current belief at that time, 1981). At a temperature of 85 K they observed the EL2 state emitting its electron into the Γ conduction band for $h\nu > 0.8$ eV, into the L conduction band for $h\nu > 1.05$ eV, and into the X conduction band for $h\nu > 1.25$ eV. Their results are presented in Figure 6.17 as a plot of optical cross sections as a function of optical energy. It is interesting to note that in 1962, Sturge [100] observed similar features in a plot of the absorption coefficient for GaAs as a function of optical energy at low temperatures. He attributed this to impurities.

Figure 6.18 and 6.19 are dimensionless plots of the total impedance and the phase angle, respectively. These two sets of data have the same characteristics as the dimensionless capacitance, Figure 6.14. Namely, optical excitation has little influence at frequencies around 10000 Hz, the impedance and phase angle decrease at optical energy greater than 0.8 eV for 5.02 Hz and at optical energy greater than 1.3 eV for 200 Hz. This result is rather surprising because it suggests that the real component of the impedance has little influence on the total impedance and phase angle even though $Z_{tot} = Z_r + Z_j$ and $\phi = \arctan(Z_j/Z_r)$. However, it was demonstrated in Figure 6.13 that optical energy greater than 0.8 eV influenced the real impedance at both 5.02 Hz and 200 Hz and that this influence was in opposite directions (decreased for 5.02 Hz and increased for 200 Hz). Also, optical energy greater than 1.3 eV increased the real impedance for the 10000 Hz case unlike the capacitance, total impedance, and phase angle.

The observations just mentioned suggest that the real and imaginary components of the impedance are a more sensitive representation of impedance data. Consider the case where $|Z_j| \gg Z_r$. For such cases $Z_{tot} = Z_j$; changes in the real component of the impedance are masked by the imaginary component. The phase angle approaches an asymptotic limit of -90 degrees as $|Z_j|$ becomes larger than Z_r (for negative Z_j). For $|Z_j| > 57Z_r$, the phase angle ranges from -89 degrees to -90 degrees. Here too, the real component of the impedance is masked by the imaginary component.

The optical impedance data was regressed to the simplified equivalent circuit in the same manner as was the thermal impedance data in the previous subsection. Figure 6.20 is a plot of the resistances that resulted from the numerical regression of the impedance data to the equivalent circuit as a function of optical energy. As before, the filled squares represent the leakage resistance and the other symbols represent the recombination resistances. Two observations can be made from this plot; the leakage resistance decreases the most with optical stimulation, and one set of recombination resistances disappears at approximately 0.85 eV and another set at approximately 1.25 eV. It is at these optical energies that the impedance data also change.

Figure 6.21 is a plot of the capacitances that resulted from the numerical regression of the impedance data to the equivalent circuit (filled squares represent the space charge capacitance) as a function of optical energy. Optical stimulation had little influence on the space charge capacitance. This would suggest that the number of carrier created due to optical excitation was much less than the number of carriers due to shallow level states because the space charge capacitance is proportional to the total number of free carriers. At optical energies of approximately 0.85 eV and 1.25 eV, one set of recombination capacitances disappeared in the same manner as the recombination resistances in the previous figure. The characteristic frequencies of these electronic transitions ($\frac{1}{RC}$) is plotted in Figure 6.22 as a function of optical energy. Here too, one set of characteristic frequencies disappear at energies of 0.85 eV and 1.25 eV.

Three deep–level states were found in the DLTS experiments and three recombination pairs were found in the numerical regression of the optical impedance data. The raw optical data indicated one transition at approximately 0.8 eV which would correspond to the EL2 state and another transition at 1.3 eV. This higher energy transition might also involve the EL2 state in which the EL2 state is emitting its electron into the next higher conduction band. The two lower energy states found in the DLTS experiments were not evident in the raw optical impedance data, *i.e.,* no appreciable shift in impedance data was observed between dark conditions and the lowest optical energy of 0.59 eV. This could be due to low concentrations of these two states as observed in the DLTS analysis. However, some shift in the regressed recombination terms should have been observed between the dark regressed parameters and those at 0.59 eV.

It is possible that these two states experienced a large lattice relaxation upon excitation, referred to as a Frank–Condon energy shift (see references [101–105]).For such a case, the optical energy necessary to excite a state is larger than the thermal energy. This is shown qualitatively in Figure 6.23 in the form of a configurational–coordinate diagram [98,103–105].The curve labeled “C” corresponds to the total system energy of an unoccupied deep–level with its electron delocalized in the conduction band, as a function of distance. The curve labeled “V” corresponds to the total system energy of an unoccupied deep–level with its electron delocalized in the valence band. Curve “D” is the total system energy with an electron localized at the deep–level state. This lattice relaxation configuration diagram was proposed for the EL2 state [98, 99, 106]. The difference between thermal and optical excitation energy is approximately 0.1 eV.

Chantre *et al.,* [98] determined that the EL6 state has a large lattice relaxation associated with it. They determined a thermal activation energy of 0.31 eV and an optical excitation energy of 0.86 eV. Hence, the change in the impedance response for optical energies greater than 0.8 eV may be due to emission from both the EL2 state and the EL6 state.

6.2 Importance of Weighting on Regression Results

Much of the regression work used in this manuscript was made possible by my colleague, Pankaj Agarwal, in his attempt to find an appropriate generalizable regression technique for impedance data. Four different weighting schemes were tried in the regression of the impedance data to the simplified equivalent circuit [107]. The first scheme was to not weight the data which meant that larger values of the impedance would have the strongest influence. The function to be minimized in this case is

$$J = \sum_k (Z_{r,k} - \hat{Z}_{r,k})^2 + \sum_k (Z_{j,k} - \hat{Z}_{j,k})^2 \tag{6.4}$$

where $\hat{Z}$ is the model (equivalent circuit) impedance and Z is the experimental impedance. Resistances and characteristic frequencies from regression with no weighting are presented in Figures 6.24 and 6.25, respectively. Only one Arrhenius type curve can be inferred from this plot; the leakage resistance (and leakage characteristic frequency) at 0.8 eV. The other recombination values do not clearly indicate another Arrhenius type transition.

The second type of weighting scheme was proportional weighting which makes each data point have equal influence in the regression. The function that is minimized in proportional weighting regression is given by

$$J = \sum_k \frac{(Z_{r,k} - \hat{Z}_{r,k})^2}{Z_{r,k}^2} + \sum_k \frac{(Z_{j,k} - \hat{Z}_{j,k})^2}{Z_{j,k}^2}. \tag{6.5}$$

Resistances and characteristic frequencies from regression with proportional weighting are presented in Figures 6.26 and 6.27, respectively. As with the no weighting scheme, only the leakage resistance (and leakage characteristic frequencies) at 0.8 eV is apparent in this plot. The other recombination values are even more scattered than with no weighting. This is rather surprising because proportional weighting would be expected intuitively to be better than no weighting because more data points would play an effective role in the regression.

The third type of weighting scheme was modulus weighting which weights each data point against a percentage of the total impedance (modulus). The function that is minimized in modulus weighting regression is given by

$$J = \sum_k \frac{(Z_{r,k} - \hat{Z}_{r,k})^2}{\alpha |Z|_k^2} + \sum_k \frac{(Z_{j,k} - \hat{Z}_{j,k})^2}{\alpha |Z|_k^2}. \tag{6.6}$$

Resistances and characteristic frequencies from regression with modulus weighting are presented in Figures 6.28 and 6.29, respectively.

The ideal weighting scheme would be to weight the data based on the actual confidence in the experimental data. The variance of the data reflects this, σ^2. In fact, the proportional and modulus weighting schemes are approximations of the variance weighting scheme where the standard deviation is assumed to be proportional to the magnitude of the impedance components and the total impedance, respectively (variance is the square of the standard deviation). However, large numbers of experiments need to be repeated to accurately determine the variance. Between five and ten experiments were repeated for several types of electrochemical systems, *i.e.*, n–type gallium arsenide (solid state), zinc oxide (solid state), and cuprous oxide in alkaline–saline solution. The standard deviation was determined for the real and imaginary components of the impedance data. The standard deviation was found to be the same for the real and imaginary components.

The error was assumed to be proportional to the real and imaginary components of the impedance. The error was also observed to increase as the impedance became much larger than the measuring resistor. A semi–empirically derivation was made for the error structure [107]. The resulting form can be expressed as

$$\sigma_\epsilon = \alpha|Z_j| + \beta|Z_r| + \gamma\frac{|Z|^2}{R_m} \tag{6.7}$$

where σ_ϵ is the standard deviation of the real or imaginary error, R_m is the measuring resistance, and α, β, and γ are constants that are determined through regression of the experimentally determined standard deviation to equation (6.7).

The error structure constants were observed to be dependent on the nature of system (electrochemical or solid state) and on the type of potentiostat (Solartron 1286 or PAR 273). The values used in this work are tabulated in Table 6.2. The error structure is assumed to equal the standard deviation, and thus, the model of the variance is the square of the error, *i.e.*, $\hat{\sigma}^2 = \sigma_\epsilon^2$. The function that is minimized in the regression with model variance weighting is given by

$$J = \sum_k \frac{(Z_{r,k} - \hat{Z}_{r,k})^2}{\hat{\sigma}^2} + \sum_k \frac{(Z_{j,k} - \hat{Z}_{j,k})^2}{\hat{\sigma}^2}. \tag{6.8}$$

6.3 ZnS:Mn TFEL Panel

Impedance data obtained for the ZnS:Mn thin film electroluminescent (TFEL) panel are presented as an impedance plane plot in Figure 6.30. The imaginary component of the impedance is plotted against the real component of the impedance with optical energy and electrical frequency as parameters. The electrical frequency range was 0.2 to 100 Hz. The right end of each curve corresponds to the start of the frequency sweep at 0.2 Hz with the origin as the end of the sweep at 100 Hz. The experimental results presented in Figure 6.30 were reproducible as indicated by the two data sets presented for an optical energy of 2.07 eV. The experimental procedure necessary to achieve this degree of reproducibility were mentioned in Chapter 3. The changes in the impedance spectra attributed to electronic excitation were much larger than those observed for variation of light intensity. The light intensity in these experiments was held at 15±2 mW/cm^2. As shown in Figure 6.30 for an incident light energy of 2.48 eV, the changes in the impedance spectra caused by variation of intensity from 14 to 20 mW/cm^2 was small as compared to those caused by variation of optical energy.

Within experimental error, the results obtained in the dark and under monochromatic illumination with optical energies of 1.04, 1.55, and 1.24 were identical. Thus, no electronic transitions were observed for energies less than or equal to 1.55 eV. The effect of at least one electronic transition was observed between 1.55 eV and 2.07 eV. Transitions were also observed between 2.07 eV and 2.48 eV, and between 2.48 eV and 3.10 eV. Smaller increments in wavelength were used to isolate these transitions. These results are presented in Figures 6.31 and 6.32. The dimensionless real component of the impedance is plotted in Figure 6.31 as a function of optical energy with electrical frequency as a parameter. Likewise, the dimensionless imaginary component of the impedance is plotted in Figure 6.32.

Six transitions, labeled C through H, can be observed from these two plots. The advantage of using both the real and imaginary components of the impedance is that transitions which have little influence on one component may affect the other component significantly. This can be seen by comparing the large signal response of transitions H and G in Figure 6.31 with the relatively small response in Figure 6.32.

The transitions observed in this work are consistent with those of Uchiike *et al.* [108] who used a photon–released residual charge technique (see Figure 6.33). The transitions in Figures 6.31 and 6.32 were labelled such that a direct comparison can be made with the results of Uchiike *et al.* [108]. Comparison of Figures 6.31 and 6.32 with Figure 6.33 reveals the greater sensitivity of the technique presented here, OS–DLZS, to the electronic transitions "G" and "F". Transition "H" is not even visible in Figure 6.33.

The transitions of the 3d^n levels of the Mn ion in the ZnS crystal have been investigated by optical absorption measurements [77] and by Excited State Absorption (ESA) [79]. Five transitions were observed by optical absorption. The first transition is $^6A_1 \leftrightarrow {}^4T_1$ at 2.22 eV, the second is $^6A_1 \leftrightarrow {}^4T_2$ at 2.44 eV, and the third is $^6A_1 \leftrightarrow {}^4E$ and/or $^6A_1 \leftrightarrow {}^4A_1$ at 2.64 eV where $^6A_1$ is the ground state. The two additional transitions had energy–level differences of 2.81 and 3.14 eV. The emission of yellow light is due to $^4T_1 \leftrightarrow {}^6A_1$ transition. The first three transitions might correspond to the transitions F, E, and D observed by Uchiike *et al.* [108] and in the work presented here.

The magnitude of the impedance and the phase angle are given as a function of frequency in Figures 6.34 and 6.35, respectively, for four values of optical energy. The linear dependence (on a log–log scale) of the impedance magnitude on frequency (Figure 6.34) is typical of highly capacitive systems. The horizontal region at high frequency might be attributed to the stray capacitance of the measuring resistor in the potentiostat. The phase angle, presented in Figure 6.35, increased as the optical energy increased. Here too, the capacitive nature of the device is evident; purely capacitive systems have a phase angle of -90 degrees.

The impedance data was regressed to the simplified equivalent circuit in the same manner as the GaAs sample. Three recombination resistance–capacitance pairs were found to exist in addition to the leakage resistor and space charge capacitance. The regressed resistances and capacitances are presented in Figure 6.36 and 6.37, respectively, as a function of optical energy. The characteristic frequencies ($\frac{1}{RC}$) are presented in Figure 6.38 as a function of optical energy. Transitions H (1.7 eV), G (1.9 eV), and F (2.2 eV) have a distinct influence on both the regressed resistances and capacitances as can be seen from the discontinuities in Figures 6.36 and 6.37 at these energies. Transition D (2.7 eV) is apparent in Figure 6.36 and transition E (2.5 eV) is apparent in Figure 6.37, but not *vice versa.* Note that transitions D and E are pronounced in one or the other of these plots, unlike the real and imaginary components of the raw impedance data presented in Figures 6.31 and 6.32. However, all the transitions except H and G are less pronounce upon multiplication of the resistances with their corresponding capacitances as can be seen from an inspection of Figure 6.38.

6.4 ZnO Varistors

A comparison was made in this work between aged and unaged ZnO varistors. The impedance plane plots (imaginary component of the impedance as a function of the real component of the impedance for frequencies ranging from 1500 to 0.2 Hz with optical energy as a parameter) are presented in Figure 6.39 for the unaged ZnO varistor and in Figure 6.40 for the aged ZnO varistor. The most apparent effect of aging was the decrease in the low frequency impedance corresponding to a lower resistance to current flow. This difference was observed, even though the applied potential was 0 V. Use of impedance techniques to evaluate the effect of aging would not require driving the device to the breakdown potential.

As shown in Figures 6.39 and 6.40, no electronic transitions were excited by illumination at optical energies below 1.55 eV. The imaginary and the real component of the impedance decreased significantly around 1.75 eV for both the aged and unaged varistors. The decrease in the imaginary component suggests that the corresponding electronic transition between 1.55 and 1.75 eV was from the deep–level state to the conduction band. The imaginary part of the impedance increased when the optical energy was increased to 2.03 eV for the unaged varistor which suggests an electronic transition from the valence band to the deep–level state. The shift in the impedance response under illumination at 2.07 eV was much more dramatic for the aged varistor than that observed for the unaged varistor at 2.03 eV. These results suggest that the electronic state(s) undergo a shift in energy level and/or concentration upon aging. However, the impedance response at 3.1 eV matches the impedance response under no illumination for the aged and unaged varistor.

The electronic state near the middle of the bandgap for the aged ZnO varistor was investigated further by measuring the impedance spectrum at light wavelength increments of 20 nm from 800 nm (1.55 eV) to 600 nm (2.07 eV). The resulting real component of the impedance divided by its value at dark conditions is presented in Figure 6.41 as a function of the optical energy of incident light at four electrical frequencies selected from the impedance data. The imaginary component of the impedance at dark conditions divided by imaginary component under illumination is presented in Figure 6.42. The term $Z_{\mathrm{j,dark}}/Z_{\mathrm{j}}$ can be regarded as a dimensionless capacitance, assuming that the data can be represented by a resistor and capacitor in series. The electrical frequencies selected span four orders of magnitude. The first electronic transition was observed for photon energies ranging from 1.67 eV to 1.77 eV, at which point the second electronic transition became important. Figures 6.41 and 6.42 illustrate the greater sensitivity of the impedance response to deep–level states at low electrical frequencies.

Smaller increments in wavelength were used to isolate the transitions in the unaged ZnO varistor. These results are presented in Figures 6.43 and 6.44 as plots of the dimensionless real and imaginary component of the impedance, respectively, versus optical energy. Four electrical frequencies were chosen as parameters. From an inspection of these two figures, it is observed that the dimensionless real and imaginary components of the impedance at 10000 Hz are not influenced by illumination to any appreciable extent. The dimensionless imaginary impedance increased at 1.6 eV for 0.05 Hz and also for 2.0 Hz, but to a much lesser extent. Both curves exhibit maximums around 1.8 eV. The dimensionless real impedance increased at 1.6 eV for 2.0 Hz and decreased at 1.6 eV for 0.05 Hz. Both curves also exhibit a maximum or minimum at around 1.8 eV. This behavior was observed for the n–type GaAs.

Two broad bands were observed in electroluminescence spectra [109] at 1.31 eV and at 1.78 eV. Both bands were related to the Cobalt ion. These transitions were observed to occur at 1.16 eV and 1.31 eV in the photoluminescence spectra [109]. Pöppl and Völkel [110] suggest, from Photo–Electron Spin Resonance (ESR) experiments, that an unknown defect exists in ZnO ceramics and single crystals which can be ionized with optical energy greater than 1.6 eV. They also discussed zinc and oxygen defects that can be excited with energy between 1.6 eV and 2.4 eV. Simpson and Cordaro [111] used photocapacitance and photoconductance measurements to identify two interface states at 2.49 eV and 2.79 eV below the conduction band.

The unaged ZnO varistor impedance data was regressed to the simplified equivalent circuit. Seven recombination resistance–capacitance pairs were found to exist in addition to the leakage resistance and space charge capacitance. The regressed resistances and capacitances are presented in Figures 6.45 and 6.46, respectively, as a function of optical energy. The characteristic frequencies ($\frac{1}{RC}$) are presented in Figure 6.47 as a function of optical energy. The large number of recombination pairs might be attributed to the polycrystalline–ceramic nature of the varistor. Ceramic varistors are composed of various organic binders and metals.

It is difficult to analyze the regressed parameters because almost each recombination term was influenced by illumination. Some general features can be discerned, namely, the space charge capacitance remains constant under illumination, and, the recombination resistances and capacitances exhibited a change at approximately 1.5 eV with a maximum at approximately 1.7 eV. This is qualitatively the same behavior exhibited by the aged ZnO varistor (see Figures 6.41 and 6.42).

Deep–Level Transient Spectroscopy (DLTS) experiments were performed on the aged and unaged varistors. Two states were found in each. The aged varistor has one donor–type state at 0.318 eV and another at 0.206 eV (from the conduction band). The unaged varistor has two similar states at 0.326 eV and 0.241 eV. No other states were observed for either varistor. These two states may be the states that are optically excited (see Figure 6.23), in which case the difference between optical excitation energy and thermal excitation is approximately 1.4 eV. However, a thermal excitation energy of approximately 1.7 eV would most likely not be seen with the present DLTS equipment because of the high temperatures needed to thermally emit trapped electrons to the conduction band. Two deep–level states, one at approximately 0.2 eV and another at approximately 0.3 eV (from the conduction band), were also observed by others in the literature [112–115].

Preliminary experiments were also performed on an unaged ZnO varistor that was annealed at 600°C instead of 800°C. As shown in Figure 6.48, no electronic transitions were excited by illumination at optical energies below 1.55 eV. The imaginary component of the impedance decreased significantly at 1.77 eV, as was observed for the aged and unaged (800°C) varistors mentioned above. The impedance response at 2.07 eV was similar to the response at 1.77 eV, likewise, for the impedance responses at 2.48 eV and 3.11 eV. These discrete changes in the impedance response were not observed for the varistors annealed at 800°C. Note also that the impedance response at 3.11 eV does not match the dark impedance response. These preliminary results suggest that the energy–level distribution of the electronic state(s) are dependent on the annealing temperature. The results obtained for the aged and unaged (annealed at 600°C) varistors, in the dark and under illumination (1.77 eV), are compared directly in Figures 6.49 (magnitude) and 6.50 (phase angle).

The OS–DLZS technique was also used to determine the effective optical bandgap of the aged ZnO varistor, and the results are presented in impedance plane format in Figure 6.51. A bandpass of 9 nm was used with an illumination intensity of 4.4 ± 0.5 mW/cm^2, and the electrical frequency range was 1500 to 0.2 Hz. The optical energy levels used were 3.11, 3.27, 3.36, 3.45, and 3.55 eV. An order sorting filter was not available for this energy range, however, higher energy harmonics were not expected to exist since the light source was incapable of emitting wavelengths below 300 nm (4.14 eV). The large separation between the impedance curves at 3.27 eV and 3.36 eV and again between 3.36 eV and 3.45 eV in Figure 6.51 suggest that the optical bandgap is a distributed state that lies between 3.27 and 3.45 eV.

6.5 Cuprous Oxide in Alkaline–Chloride Solution

The cuprous oxide electrode that was aged in ambient light conditions for approximately three weeks was analyzed first. A reddish–brown film developed on the copper electrode. This film was much darker in shade in a quarter section of the electrode.

Both electrodes were observed to have a loose outer film layer and an inner adherent layer. The inner layer was a bright yellow for both electrodes. The Solartron 1286 was used with a 10 mV perturbation from the FRA. The applied bias was 0 Volts. Mononchromatic light intensity was fixed at 10 mW/cm^2 for each wavelength used.

In Figure 6.52, the imaginary component of the impedance is plotted as a function of the real component of the impedance with optical energy and electrical frequency as parameters. The electrical frequency ranged from 0.1 Hz (high impedance) to 65000 Hz (low impedance). The phase angle is plotted as a function of the frequency in Figure 6.53 with optical energy as a parameter. The imaginary and real components of the impedance increased upon illumination as can be seen from an inspection of Figure 6.52. For optical energy greater than approximately 1.85 eV, the imaginary component of the impedance decreased. This decrease in impedance could be due to band–to–band transitions. An additional characteristic frequency centered at 200 Hz is observed in Figure 6.53 for optical energy greater than 1.85 eV. This may also be related to band–to–band transitions because, as noted in the previous chapter, the bandgap of cuprous oxide is approximately 2 eV depending on the system.

Additional impedance scans were performed at smaller increments in wavelength. These results are plotted in Figures 6.54 and 6.55 as dimensionless real and imaginary components of the impedance, respectively, as functions of optical energy with electrical frequency as a parameter. It is observed from these plots that the real and imaginary components of the impedance data increased to a relatively constant value under illumination for energy less than 1.8 eV. This could be due to a discrete electronic transition within either the bulk of the semiconductor, such as a bulk deep–level state, or at the surface such as a surface state and/or surface reaction. This discrete transition exists between 0.5 eV (lowest optical energy used) and approximately 0.25 eV which is the maximum thermal energy due to black body radiation at room temperature. A plot of Planck's distribution law for black body radiation (see for example [116]) is given in Figure 6.56. Because the impedance increased under illumination, and the cuprous oxide is a p–type semiconductor, the net effect of illumination below 1.8 eV is the consumption of holes. For optical energy greater than 1.8 eV the impedance components either decreased or increased depending on the electrical frequency as can be seen in Figures 6.54 and 6.55.

The cuprous oxide electrode that was aged in dark conditions for approximately five weeks was observed to have a uniform film with a reddish–purple color. The PAR 273 potentiostat was used because the impedance was much larger than that of the previous electrode. The applied bias was 0 Volts and the sinusoidal perturbation was 5 mV. Mononchromatic light intensity was fixed at 15 mW/cm^2 for each wavelength used.

The imaginary component of the impedance is plotted as a function of the real component of the impedance with optical energy and electrical frequency as parameters in Figure 6.57. The electrical frequency ranged from 0.2 Hz (high impedance) to 10000 Hz (low impedance). In Figure 6.58, the phase angle is plotted as a function of the frequency with optical energy as a parameter. The imaginary component of the impedance decreased upon illumination as can be seen from an inspection of Figure 6.57. An additional characteristic frequency centered at 10 Hz is observed in Figure 6.58 for optical energy greater than 1.9 eV, as was the case in Figure 6.53. This too may be related to band–to–band transitions.

The dimensionless real and imaginary components of the impedance are plotted as functions of optical energy in Figures 6.59 and 6.60, respectively. Three electrical frequencies were chosen as parameters. The imaginary component of the impedance data decreased as optical energy increased for each of the electrical frequencies. This decrease became stronger for optical energy greater than 1.8 eV. The change in the imaginary component of the impedance was over several orders of magnitude, unlike the change observed from Figure 6.55 for the electrode aged in the light. This could be due to a disordered band structure because no discrete change in impedance was observed. The net effect of illumination is the creation of holes because the imaginary component of the impedance decreased (cuprous oxide is a p–type semiconductor). The real component of the impedance increased for high electrical frequencies and decreased for relatively low electrical frequencies as optical energy increased (see Figure 6.59).

The impedance data was fit to the simplified equivalent circuit used in the previous section. The residual errors of this fit were not random, but instead, oscillated over the frequency spectrum. Error oscillation is an indication that the equivalent circuit is not an appropriate circuit [66]. Such a result is not surprising because diffusion of oxygen and cuprous ions in the electrolyte have not been incorporated into the equivalent circuit. The equivalent circuit used in this work only treated deep–level states in semiconductors. Mass transport limited diffusion of oxygen could, under certain conditions, be represented by a Warburg element ($Z_W \propto (j\omega)^{-0.5}$) [22]. An appropriate equivalent circuit should incorporate reaction and transport processes in the electrolyte as well as in the semiconducting oxide layer.

Danzfuss and Stimming [117] investigated the photoelectrochemical properties of iron–tin oxides. They point out that many metal oxides are amorphous (non-crystalline) semiconductors, or, disordered semiconductors. In a disordered semiconductor, the band edge extends into the band gap. This is also referred to as a band tail. The band edge in crystalline semiconductors is represented by a sharp increase in the density of states between the forbidden (band) gap and the carrier bands. A qualitative schematic of the density of states as a function of energy is given in Figure 6.61 for a disordered semiconductor and a crystalline semiconductor with a discrete (localized) state. Monochromatic illumination would excite band–to–band transitions over a range of optical energy for the disordered semiconductor as shown in Figure 6.61. Whereas, the same illumination of a crystalline system would not excite band–to–band transitions with energy less than the band gap. Localized (discrete) states that exist within the band gap would be emptied (or filled) at a particular energy. The electron or hole liberated by the illumination is free to participate in redox reactions at the surface such as oxygen reduction (indicated in Figure 6.61).

The steady decrease in the imaginary component of the impedance with optical energy for the cuprous oxide aged in the dark is an indication that this system could be a disordered semiconductor. Whereas, the impedance data for the electrode aged in ambient light is an indication of a more crystalline system with a discrete transition between 0.25 eV and 0.5 eV.

6.6 Comparison of Impedance and Admittance

The impedance is inversely related to the admittance. Presentation of results in the form of admittance spectra is popular in the analysis of electronic devices since the behavior at high frequencies is emphasized. The deep–level states analyzed here, however, were shown to be sensitive to low electrical frequencies. Presentation of the results in the form of impedance spectra emphasizes deviations at low frequency. The comparison of impedance and admittance spectra is demonstrated in Figure 6.62. Three data sets of the aged ZnO varistor were chosen for this comparison; data obtained in the dark where no states were activated by light, data obtained at 1.77 eV where an electronic transition has occurred, and data obtained at 2.07 eV where another transition has shifted the impedance back towards the dark conditions. The imaginary component of the impedance was plotted against the electrical frequency with optical energy as the parameter. This data was converted to admittance, and the imaginary component of the admittance was also plotted as a function of the electrical frequency in Figure 6.62. Similar results are obtained when the real component of the impedance and admittance are presented in the same format. The impedance spectrum is much more sensitive to optical excitation of deep–level states at low frequencies.

6.7 Three–Dimensional Representation

The influence of the two frequency domains, electrical and optical, on the impedance response can be demonstrated with the aid of three–dimensional plots. The log of the dimensionless real and imaginary components of the impedance are presented in Figures 6.63 and 6.64, respectively, for the n–type GaAs sample as a function of electrical frequency (log) and optical energy. Similar three–dimensional plots are presented for the ZnS:Mn electroluminescent panel in Figures 6.65 and 6.66.

The most important observation that can be made from these plots is that deep-level states have the strongest influence on the impedance response only if the applied electrical frequency and optical energy match the same conditions of the electronic transition involving the deep–level state. For high values of the electrical frequency and/or low values of optical energy, the dimensionless impedance remains constant, as can be seen from an inspection of each of the four 3–D plots. At high frequencies, the kinetics of the deep–level state are too slow to influence the response, and optical energy less than the activation energy will not result in emission of a trapped electron or hole.

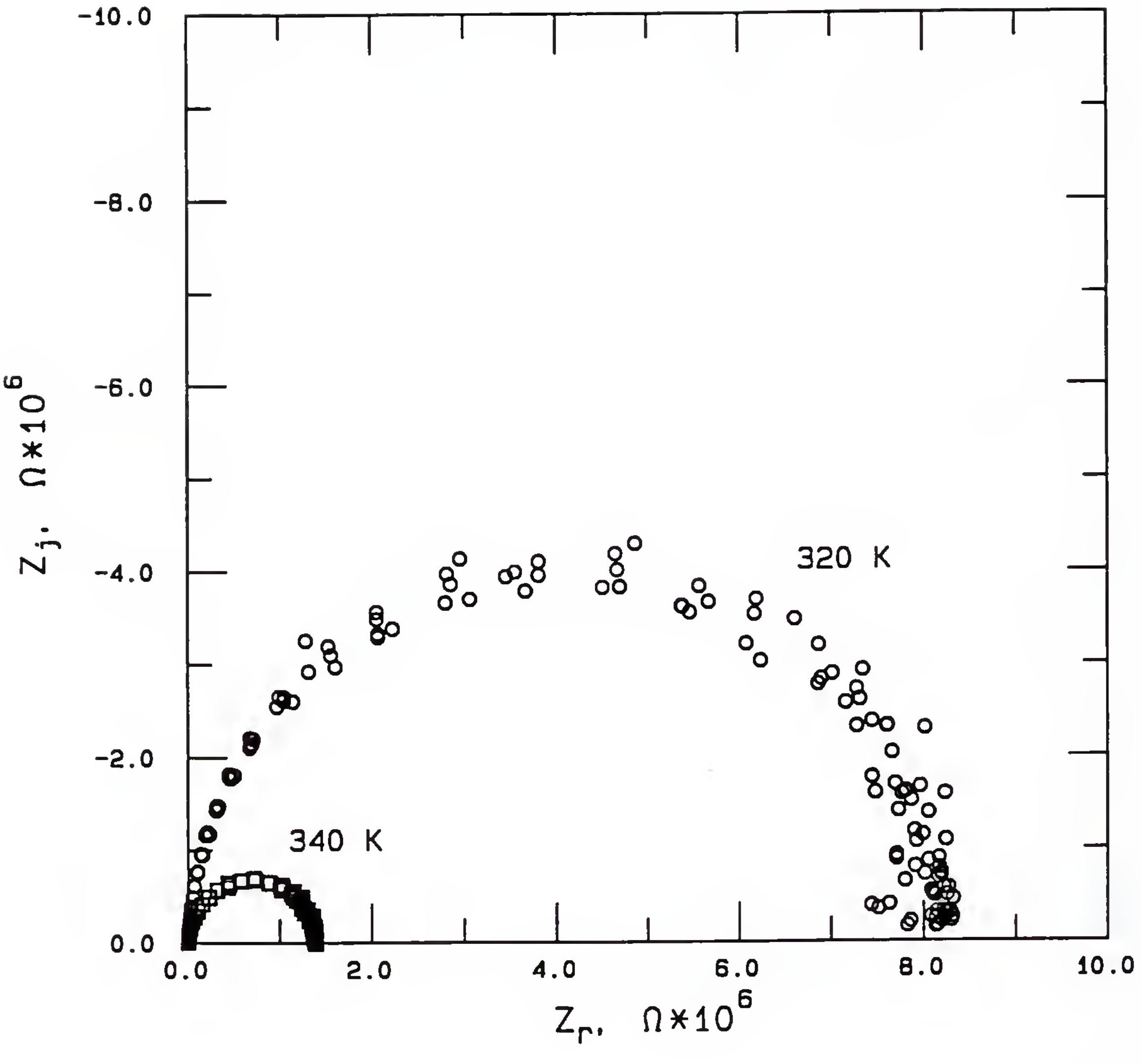

Figure 6.1: Imaginary component of the impedance as a function of the real component of the impedance for frequencies ranging from 65000 to 1 Hz with temperature as a parameter for n–type GaAs with Schottky contact.

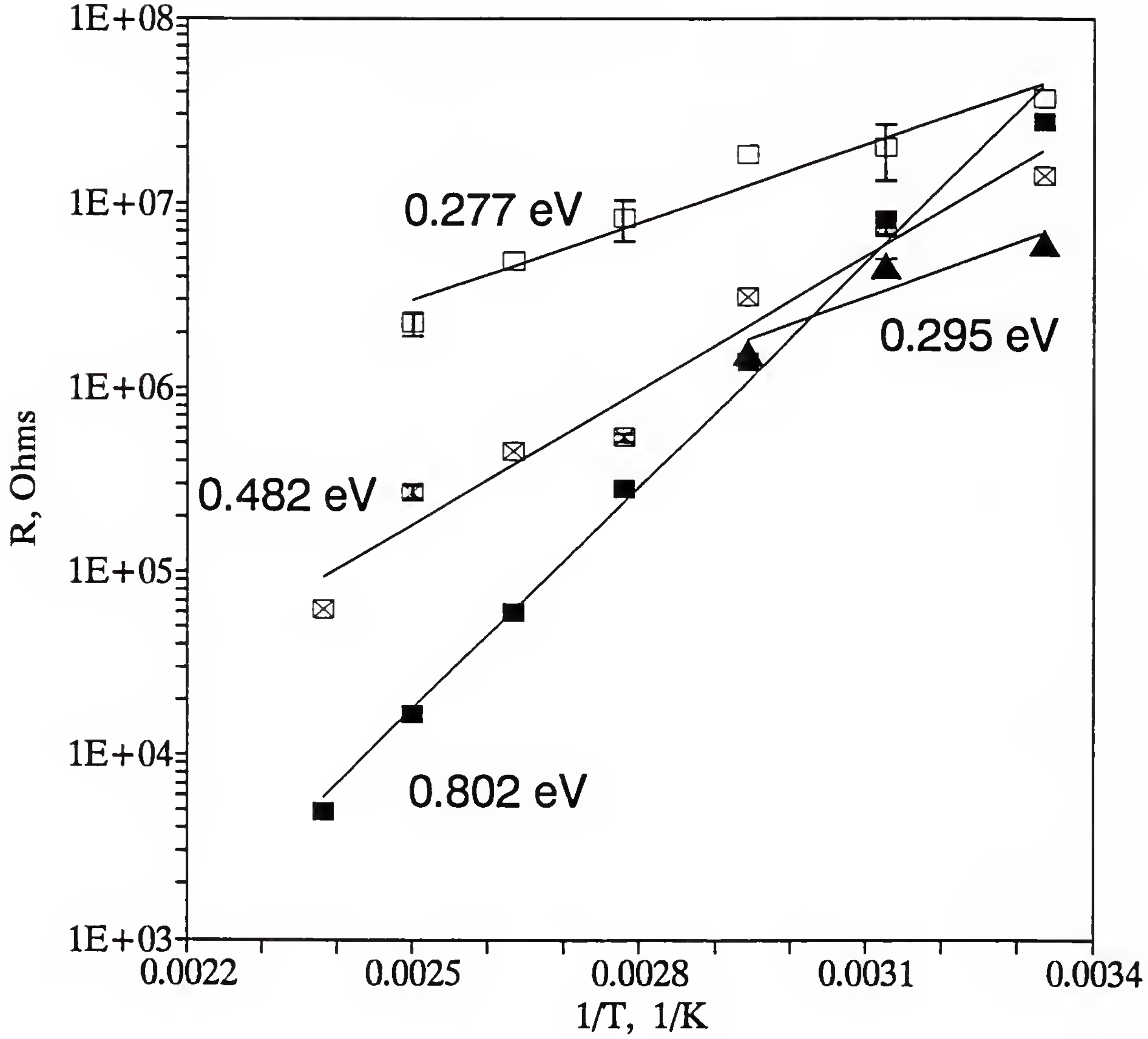

Figure 6.2: Resistances from regression of simplified equivalent circuit to impedance data as a function of inverse temperature for n-type GaAs with Schottky contact.

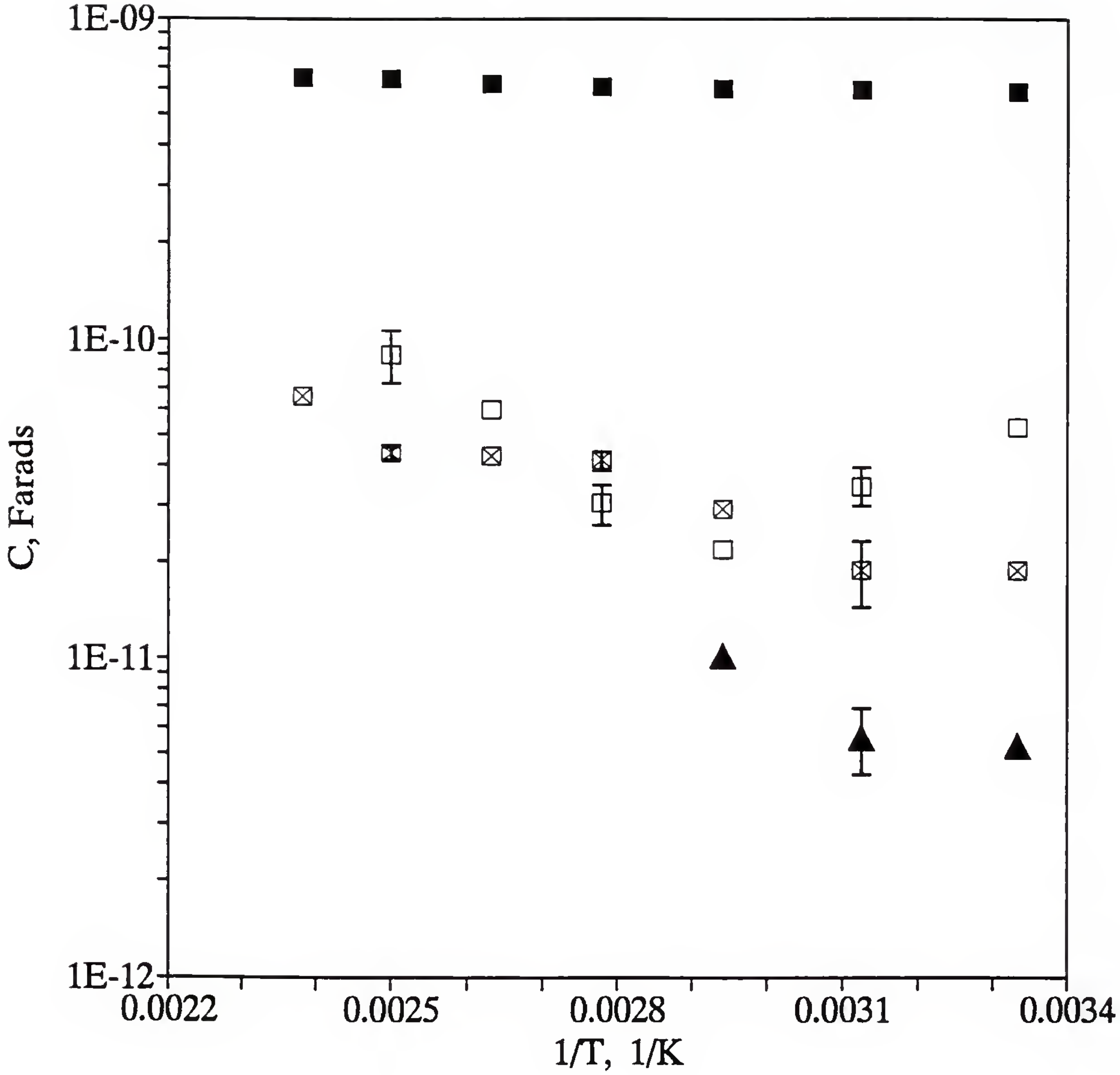

Figure 6.3: Capacitances from regression of simplified equivalent circuit to impedance data as a function of inverse temperature for n–type GaAs with Schottky contact.

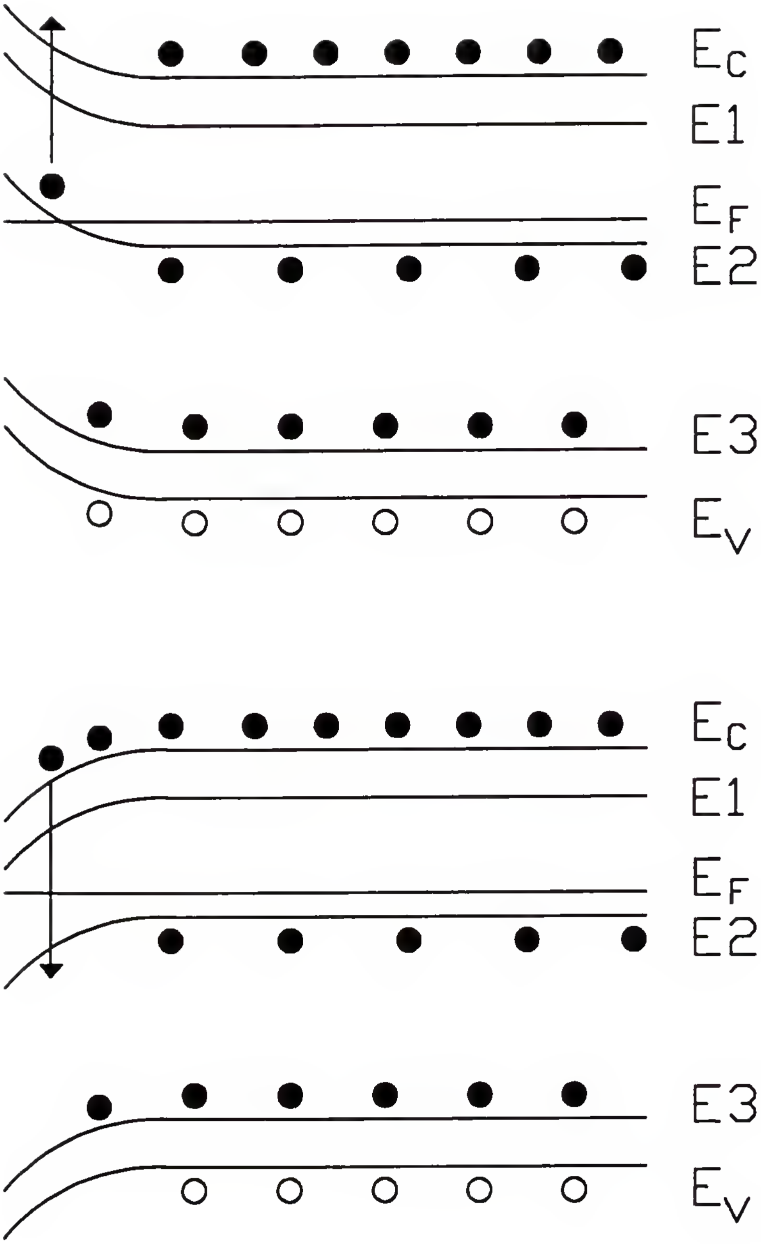

Figure 6.4: Energy diagram of a shallow donor state (E1), a midgap state (E2) slightly below the Fermi level (E_F), and a shallow acceptor state (E3) for negative half cycle (upper) and positive half cycle (lower) of sinusoid.

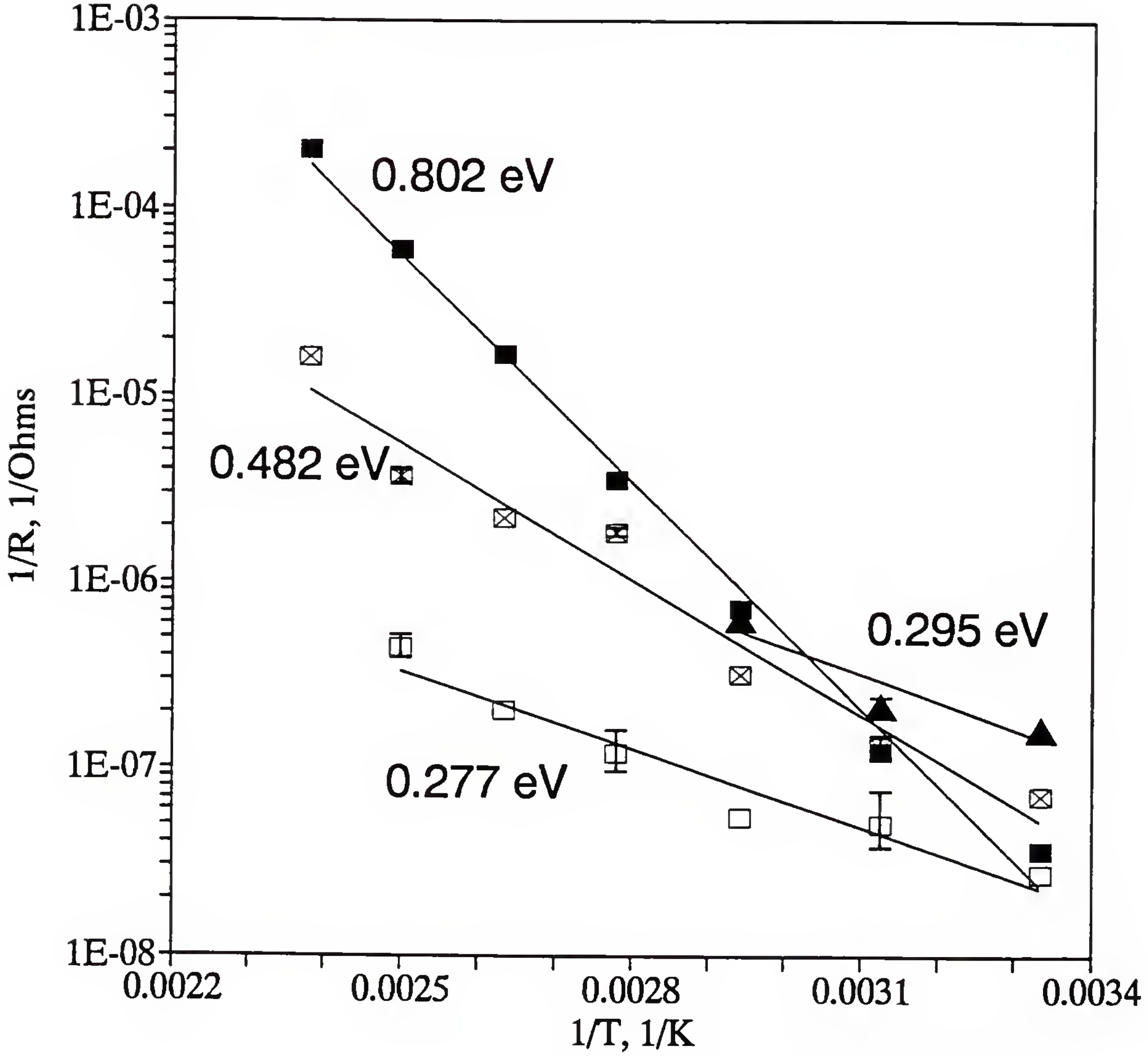

Figure 6.5: Inverse of resistances from regression of simplified equivalent circuit to impedance data as a function of inverse temperature for n–type GaAs with Schottky contact.

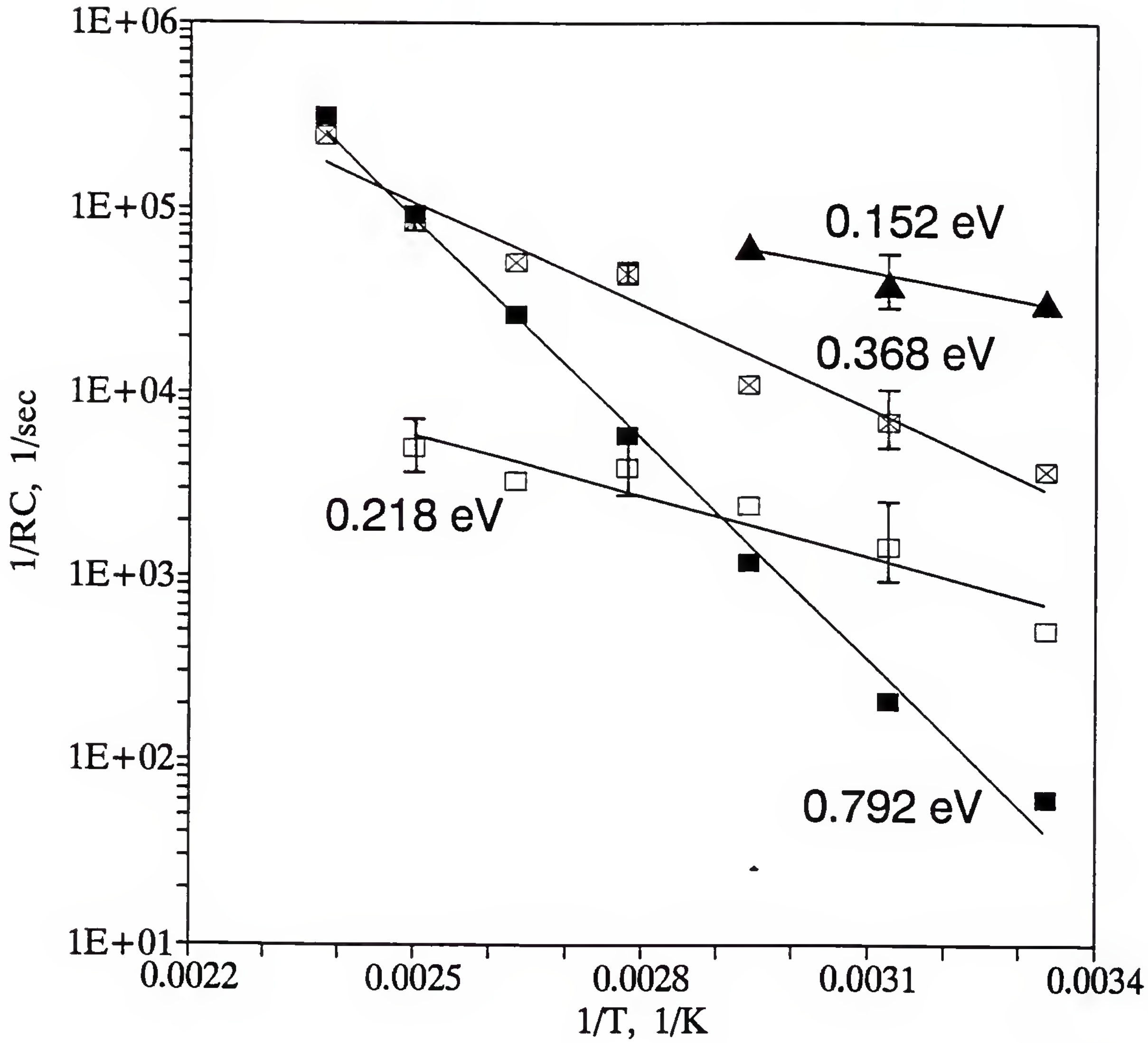

Figure 6.6: Equivalent circuit characteristic frequencies from regression of simplified equivalent circuit to impedance data as a function of inverse temperature for n–type GaAs with Schottky contact.

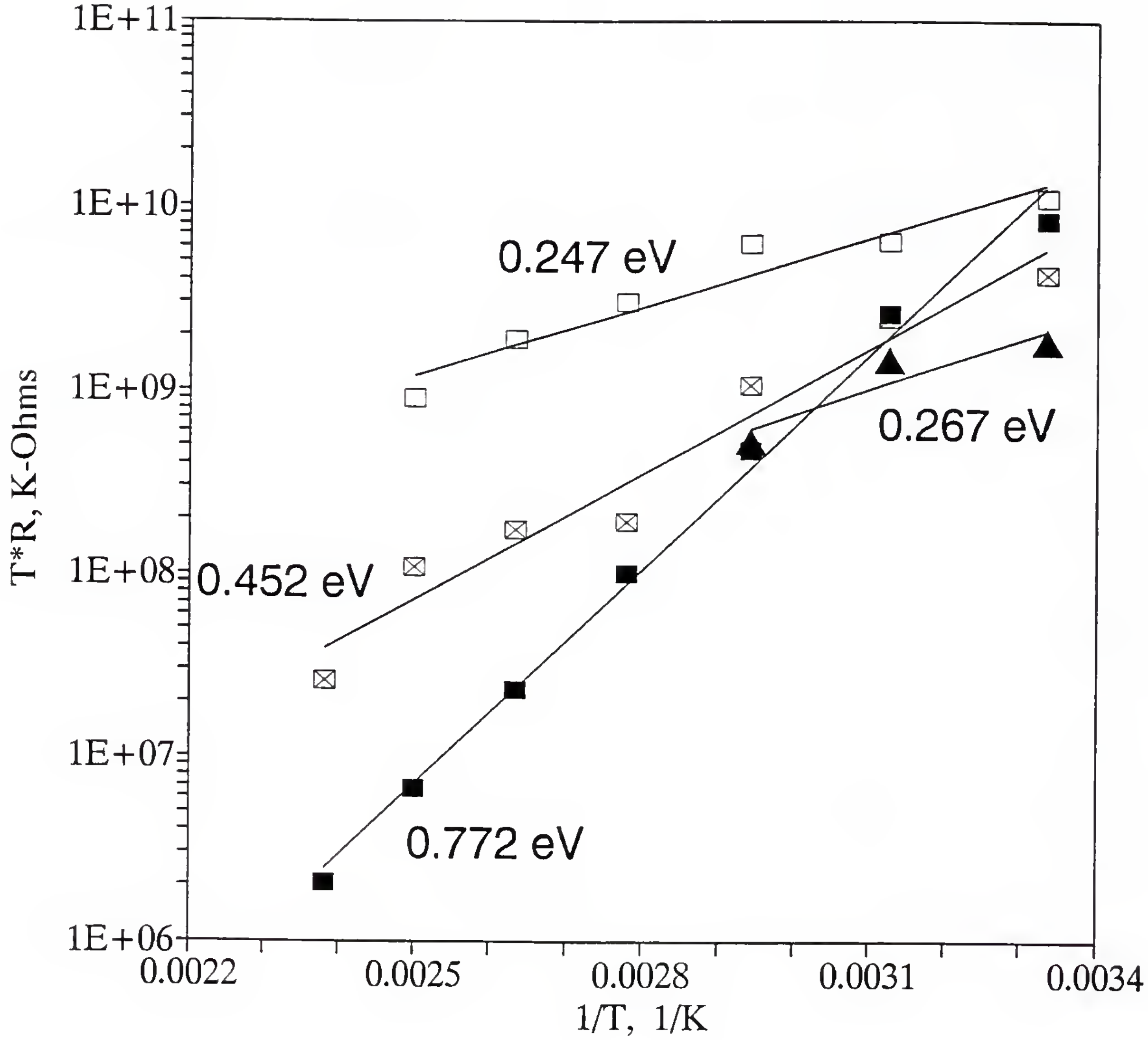

Figure 6.7: Product of temperature and equivalent circuit resistance as a function of inverse temperature for n–type GaAs with Schottky contact.

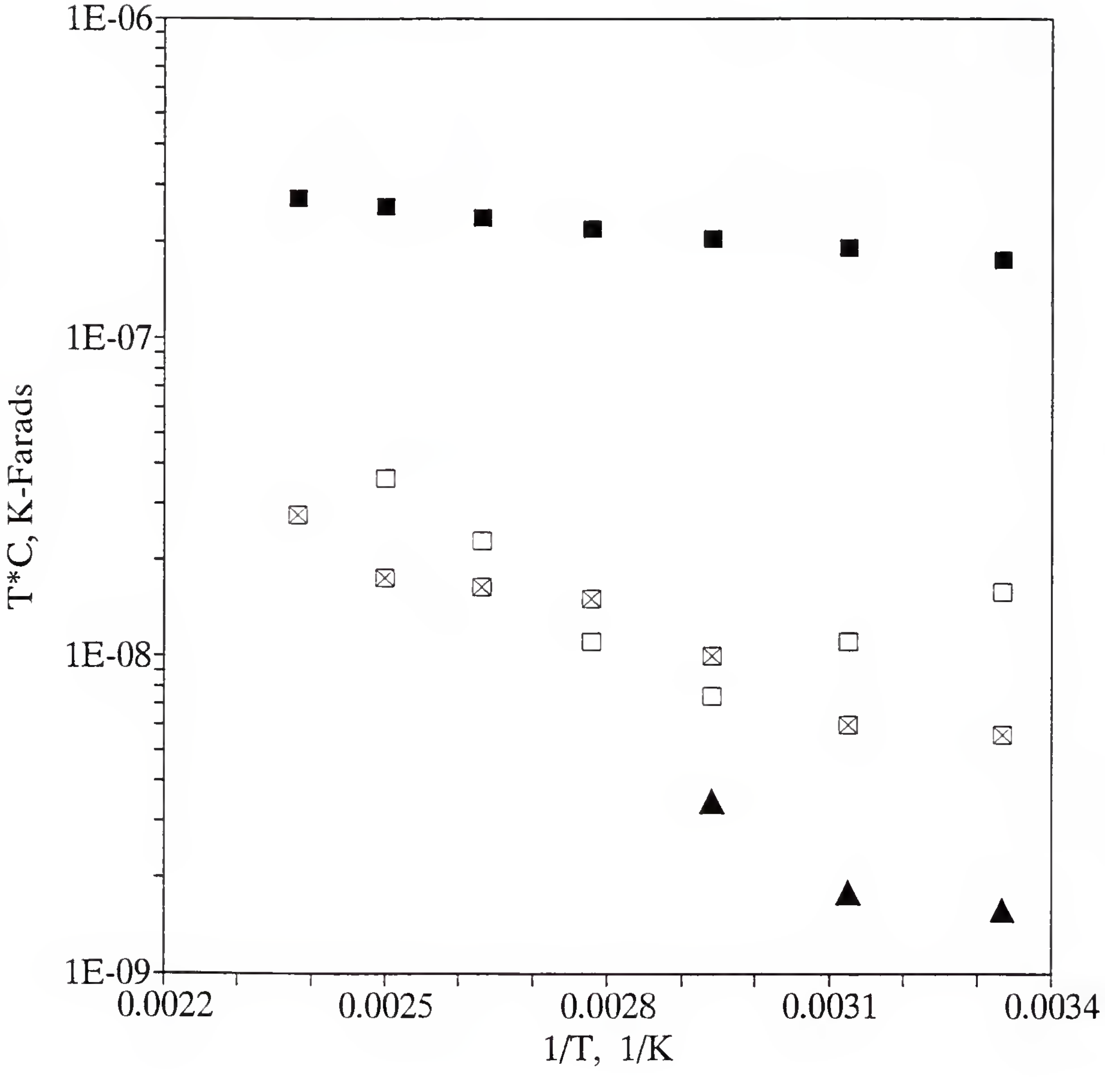

Figure 6.8: Product of temperature and equivalent circuit capacitance as a function of inverse temperature for n–type GaAs with Schottky contact.

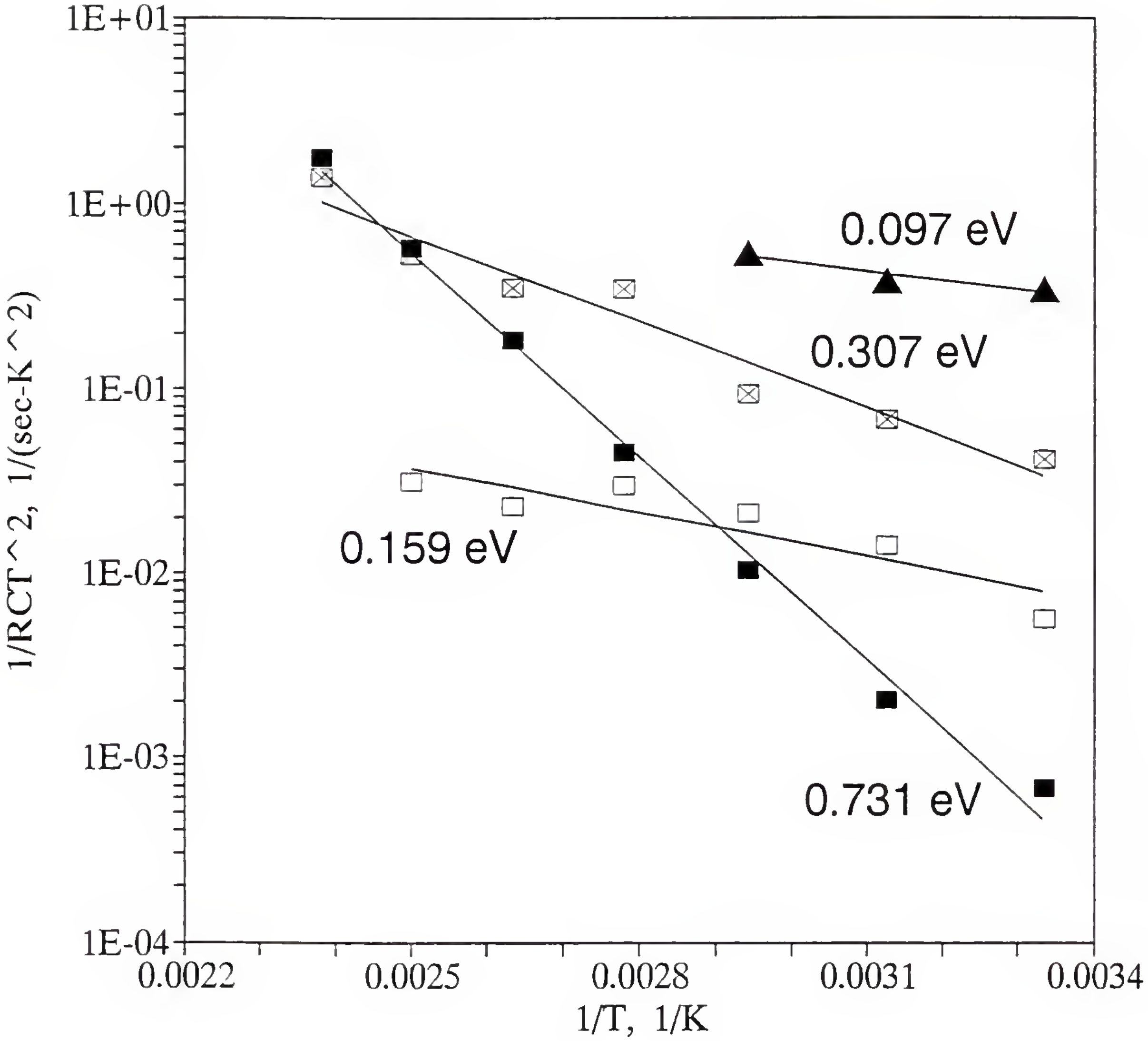

Figure 6.9: Equivalent circuit characteristic frequencies divided by the square of temperature as a function of inverse temperature for n–type GaAs with Schottky contact.

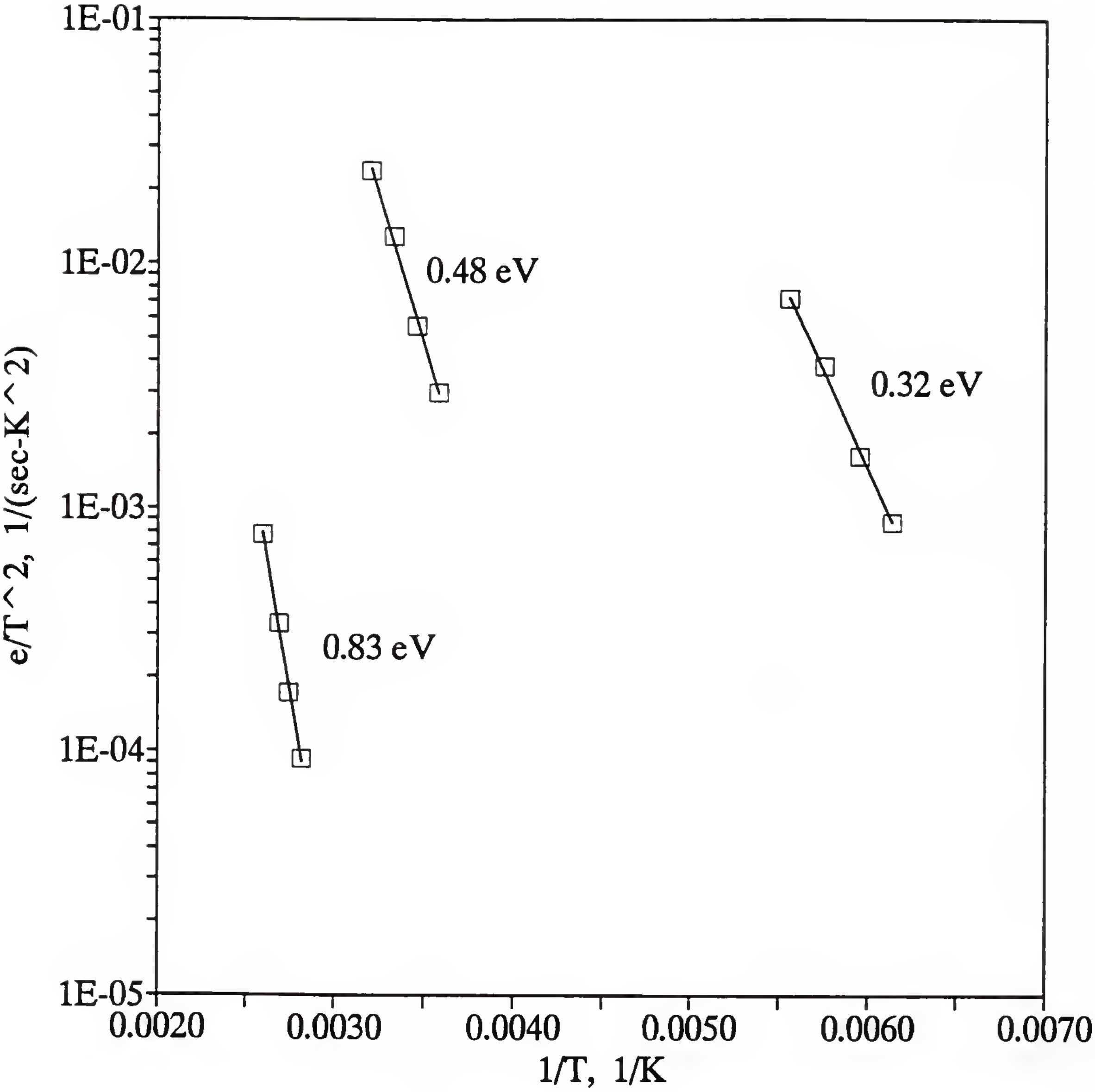

Figure 6.10: DLTS emission rate divide by square of peak temperature as a function of inverse temperature for n-type GaAs with Schottky contact.

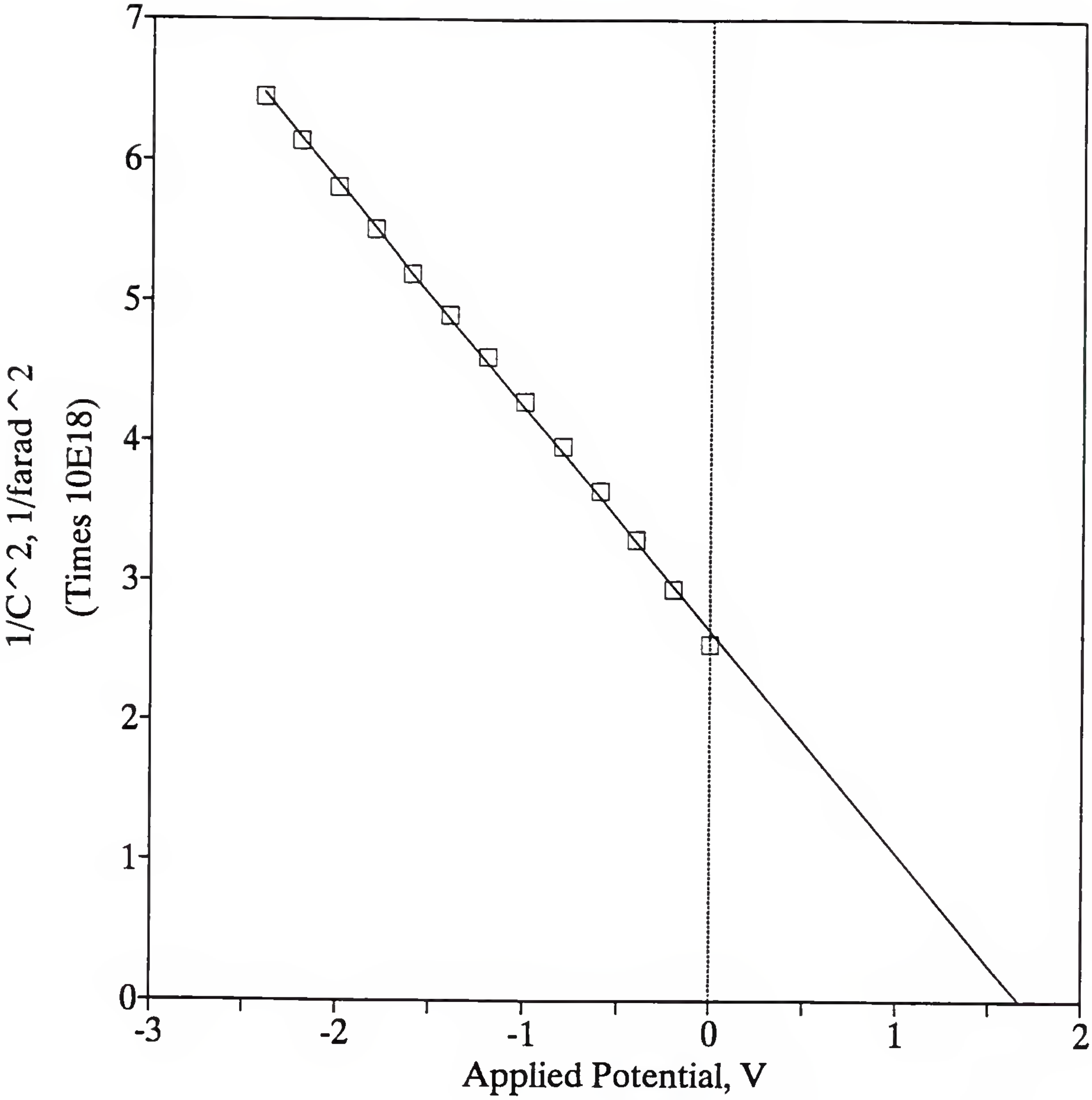

Figure 6.11: Mott–Schottky plot for n–type GaAs with Schottky contact.

	Activation Energy Capture Cross–Section Concentration	
DLZS	DLTS	Literature
Leakage Resistance 0.772 ± 0.028 eV — —	0.827 ± 0.043 eV $2.7 \pm 0.3 \times 10^{-13}$ cm^2 7.8×10^{15} cm^{-3}	ET1 = ES1 = EL2 0.83—0.85 eV 1.0—6.5$\times 10^{-13}$ cm^2 —
Recombination 0.452 ± 0.043 eV 1.3×10^{-17} cm^2 1×10^{15} cm^{-3}	0.483 ± 0.021 eV $8.1 \pm 0.6 \times 10^{-15}$ cm^2 6.4×10^{14} cm^{-3}	— — —
Recombination 0.247 ± 0.034 eV 9.8×10^{-21} cm^2 1×10^{15} cm^{-3}	0.318 ± 0.010 eV $3.0 \pm 0.2 \times 10^{-14}$ cm^2 8.7×10^{14} cm^{-3}	ET2, EL6 (bulk) 0.30–0.35 eV 0.25–15 $\times 10^{-14}$ cm^2 —
	Donor Concentration $E_C - E_F$	
Capacitance C_n 8×10^{15} cm^{-3} (intercept) 0.041 ± 0.002 eV (slope)	Mott–Schottky Plot 1.1×10^{17} cm^{-3} —	$E_C - E_F = kT \ln \frac{N_C}{N_D}$ — 0.038 eV at 300 K

Table 6.1: Comparison of values from DLZS, DLTS, and literature [71].

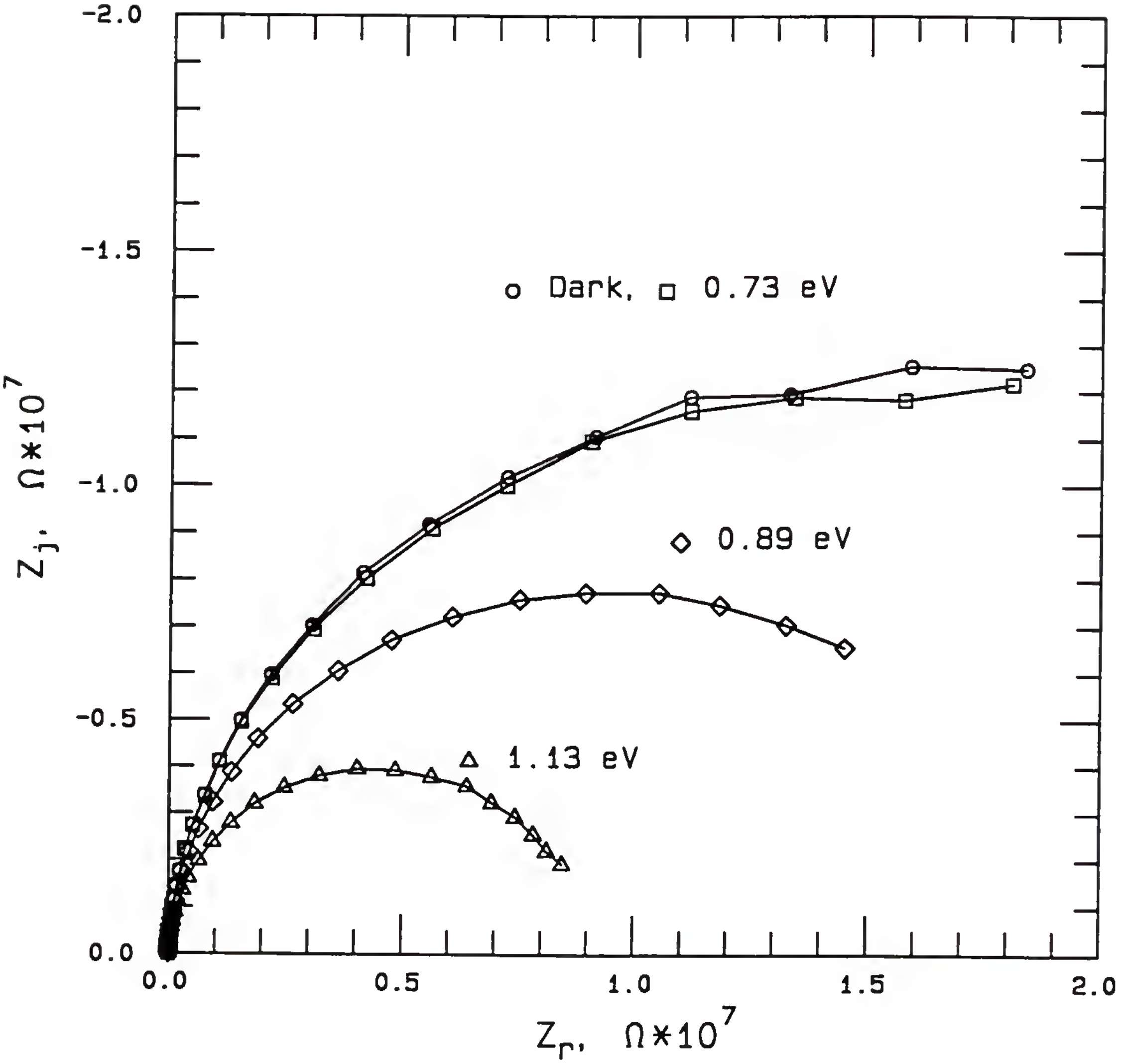

Figure 6.12: Imaginary component of the impedance as a function of the real component of the impedance for frequencies ranging from 20000 to 4 Hz with optical energy as a parameter for n–type GaAs with Schottky contact.

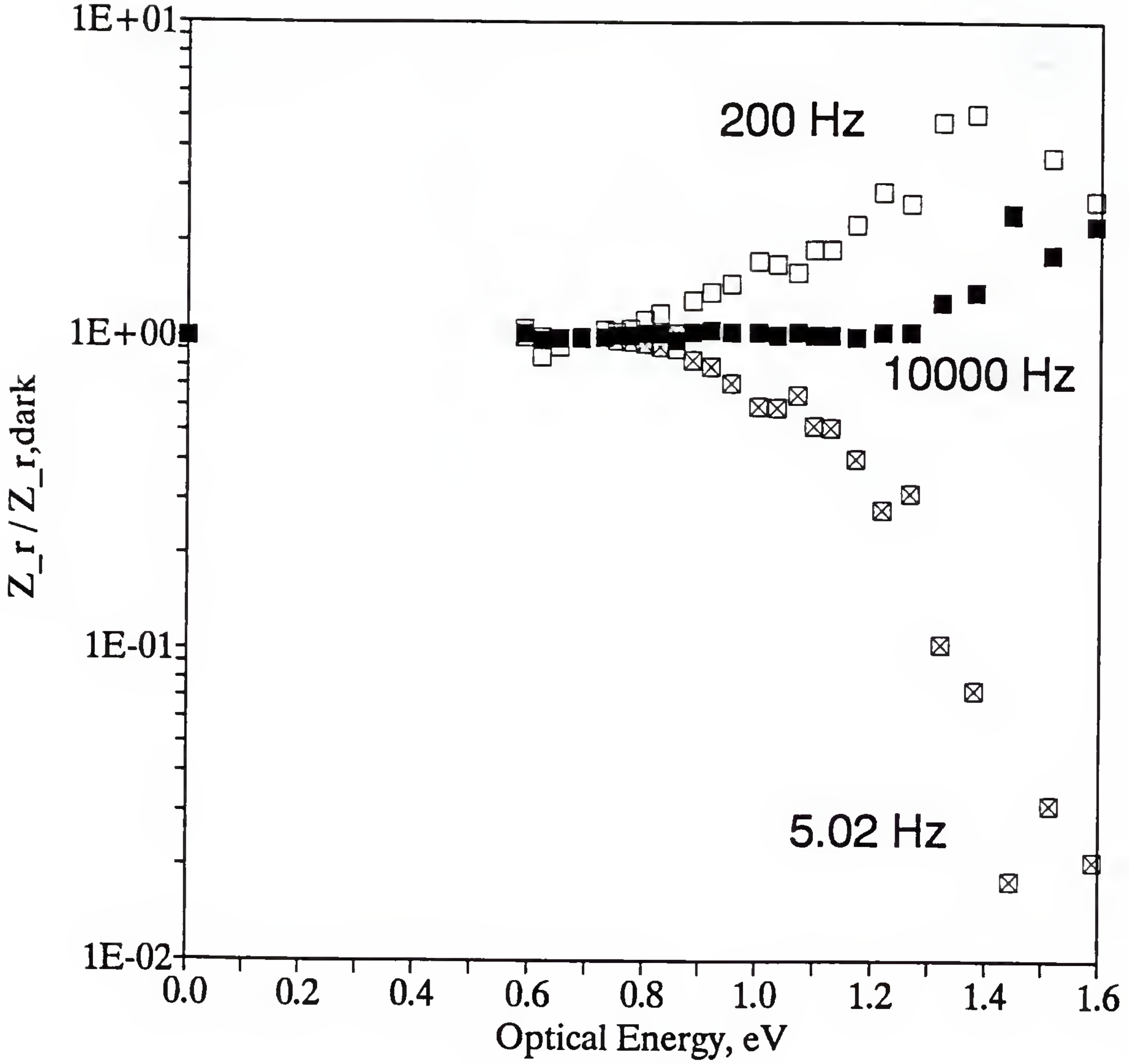

Figure 6.13: Dimensionless real component of the impedance as a function of optical energy with electrical frequency as a parameter for n–type GaAs with Schottky contact.

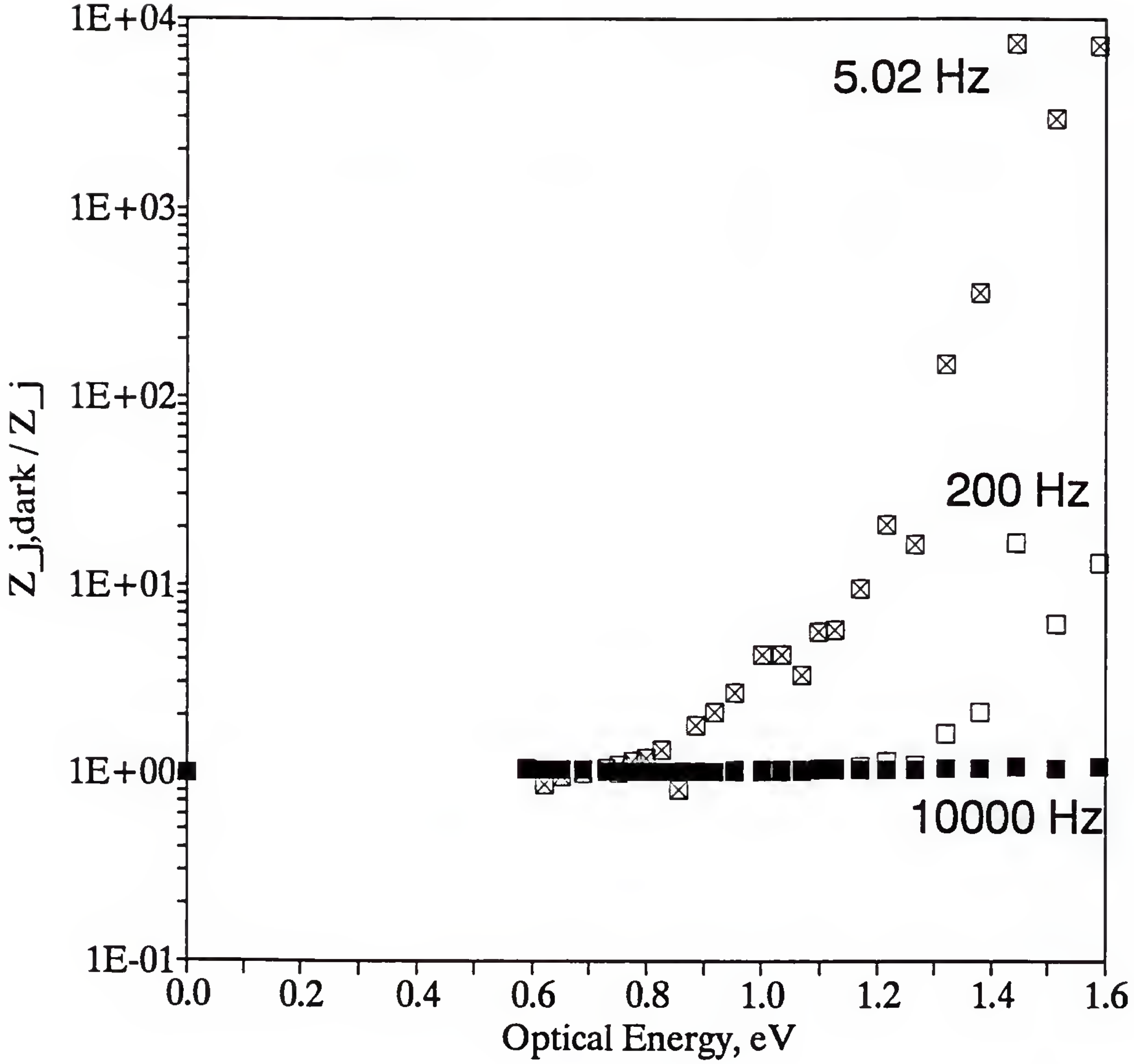

Figure 6.14: Dimensionless imaginary component of the impedance as a function of optical energy with electrical frequency as a parameter for n–type GaAs with Schottky contact.

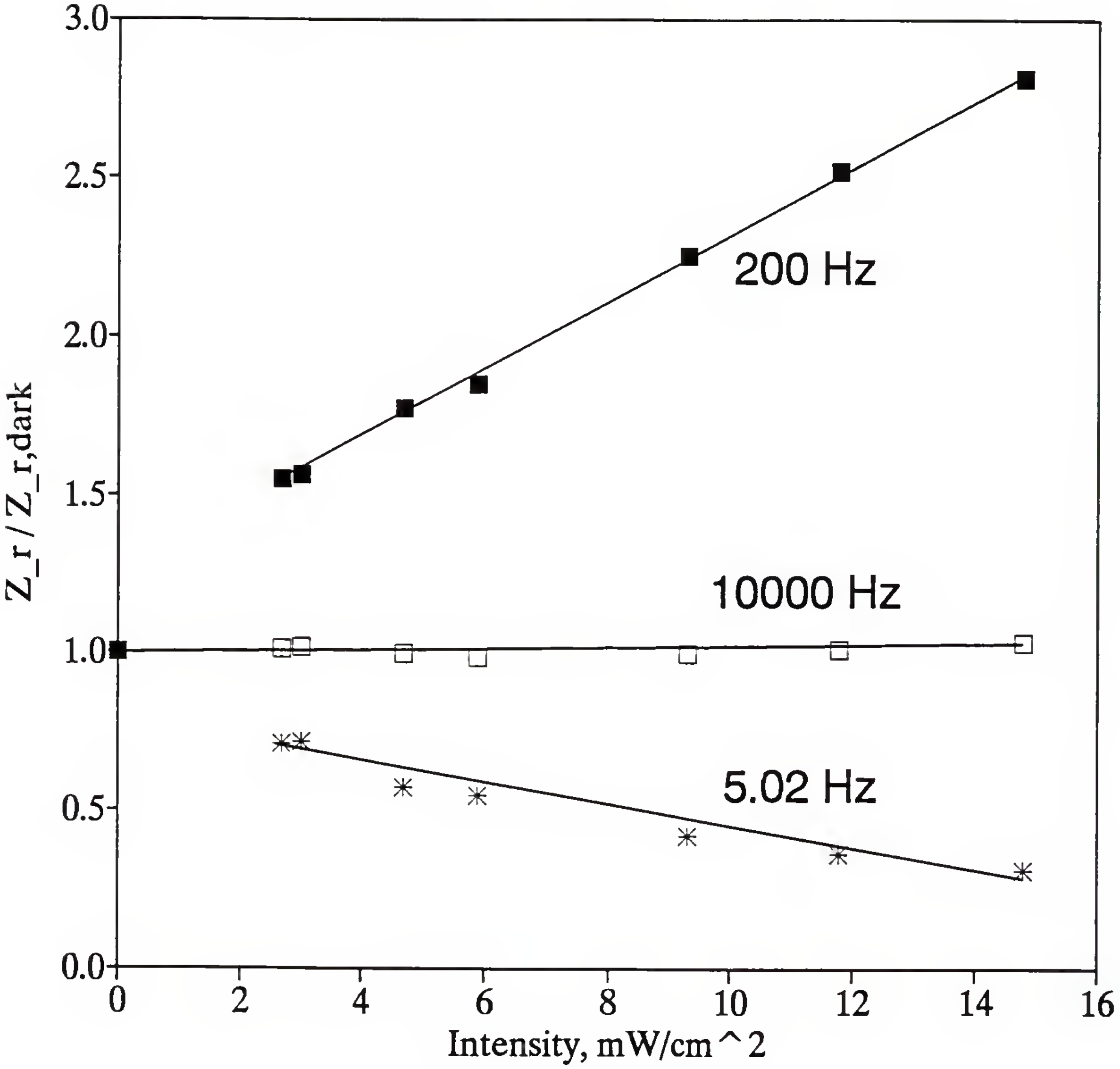

Figure 6.15: Dimensionless real component of the impedance as a function of light intensity at 1.1 eV with electrical frequency as a parameter for n-type GaAs with Schottky contact.

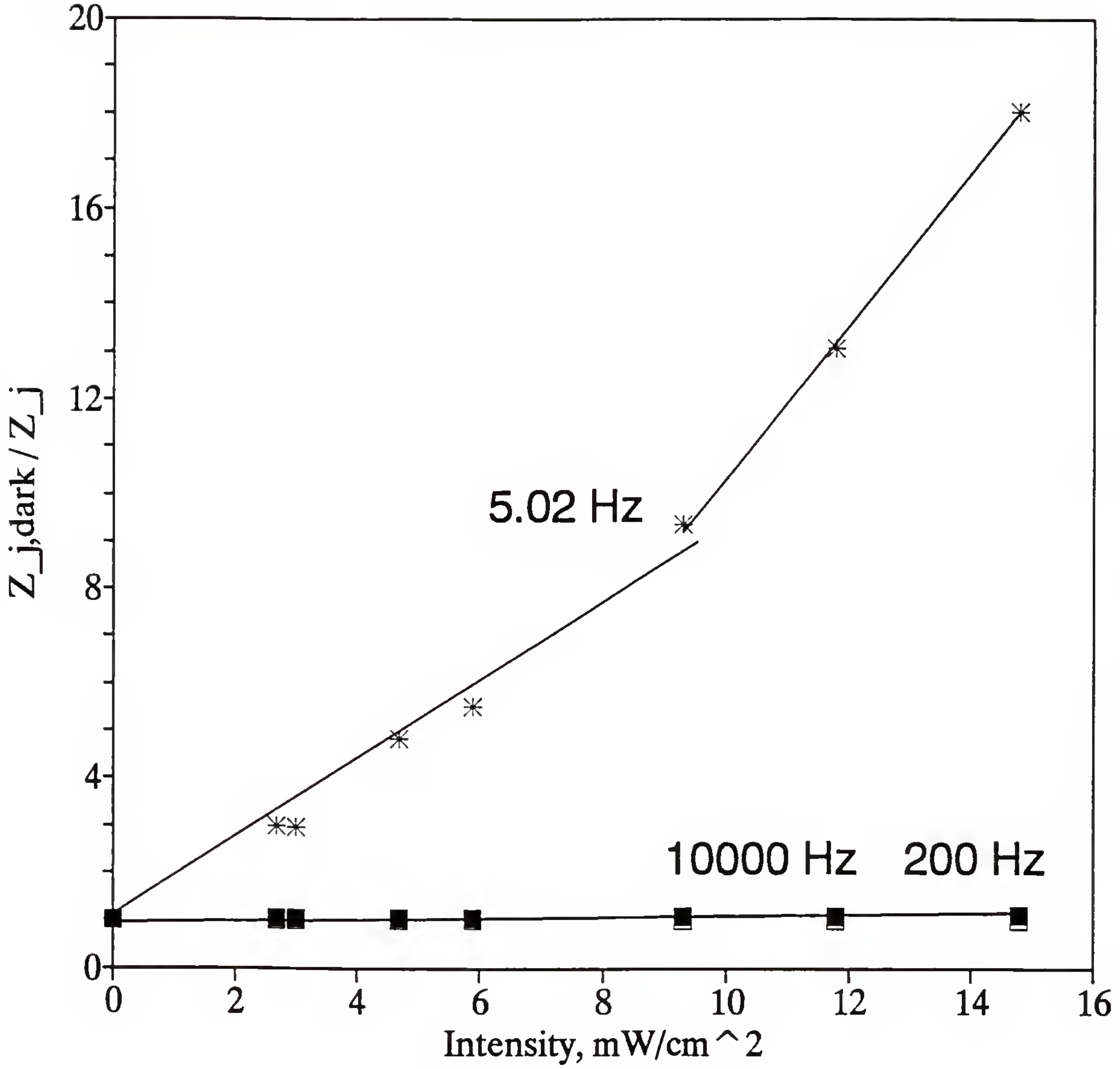

Figure 6.16: Dimensionless imaginary component of the impedance as a function of light intensity at 1.1 eV with electrical frequency as a parameter for n-type GaAs with Schottky contact.

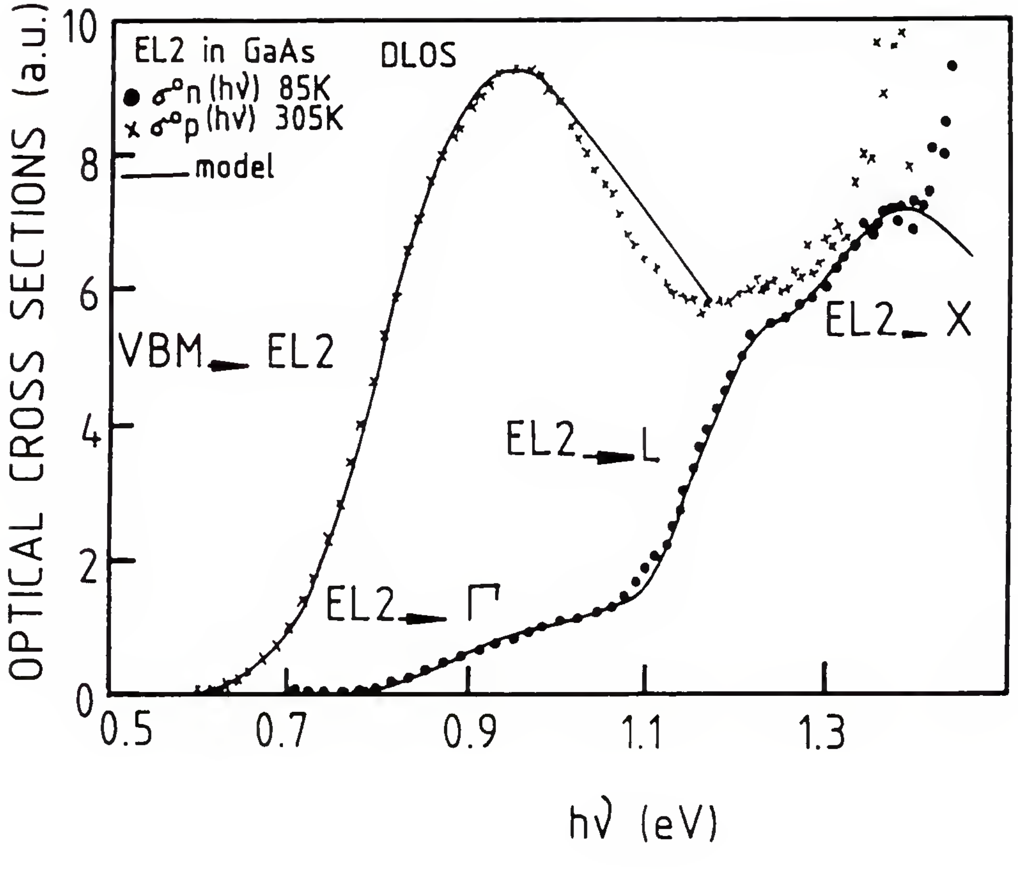

Figure 6.17: Optical cross sections from DLOS experiments as a function of optical energy, from references [98, 99].

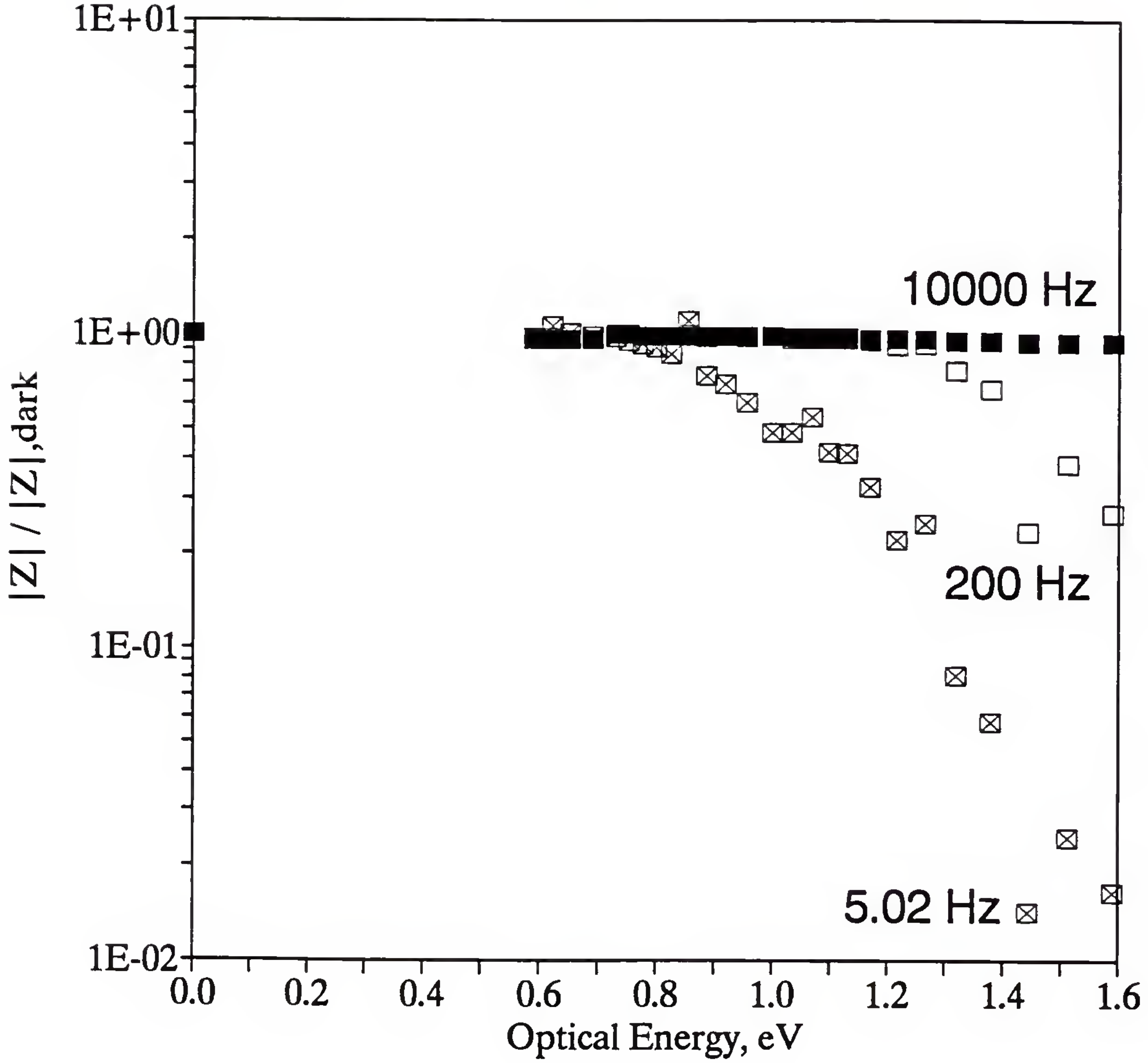

Figure 6.18: Dimensionless total impedance as a function of optical energy with electrical frequency as a parameter for n-type GaAs with Schottky contact.

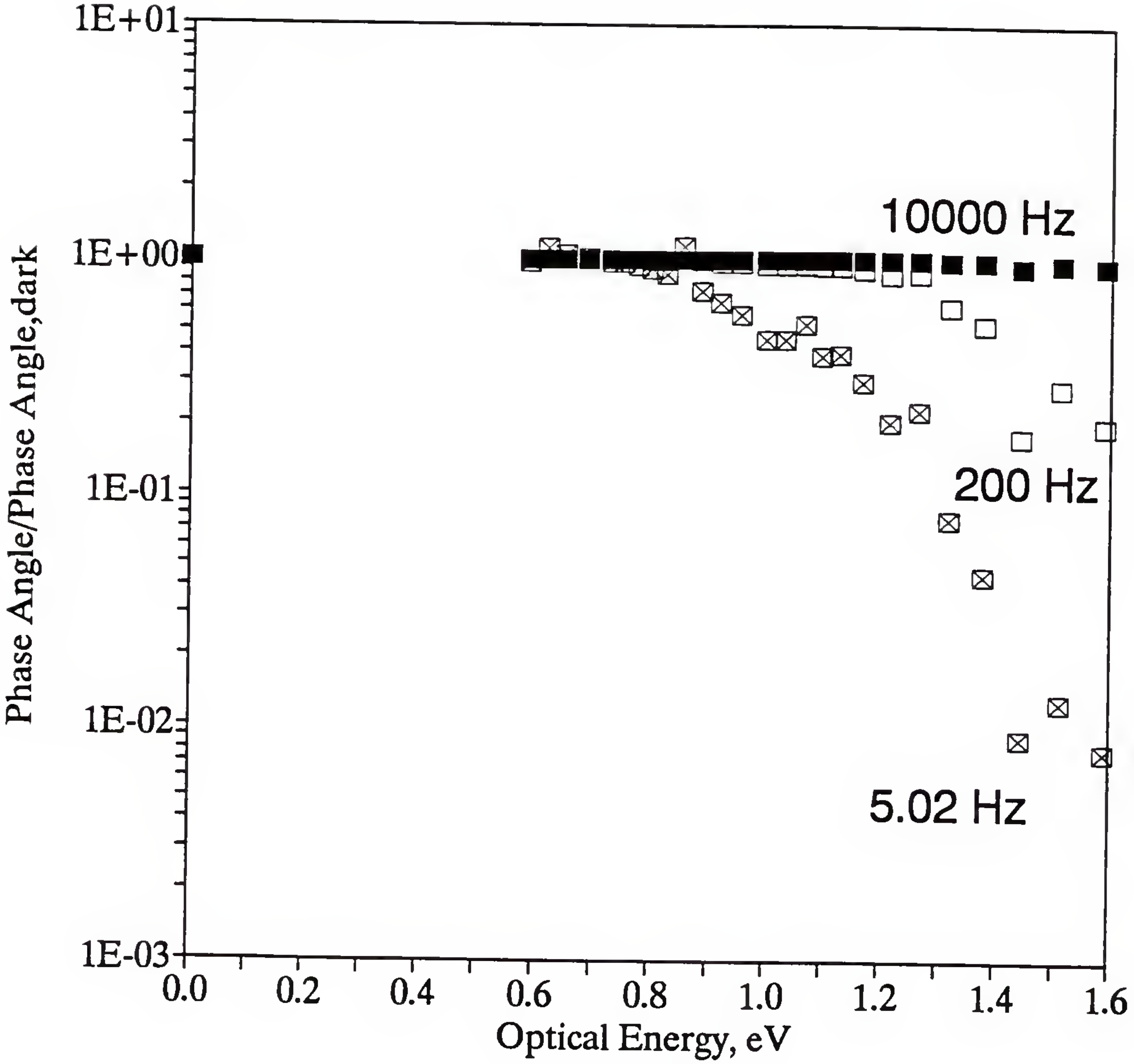

Figure 6.19: Dimensionless phase angle as a function of optical energy with electrical frequency as a parameter for n-type GaAs with Schottky contact.

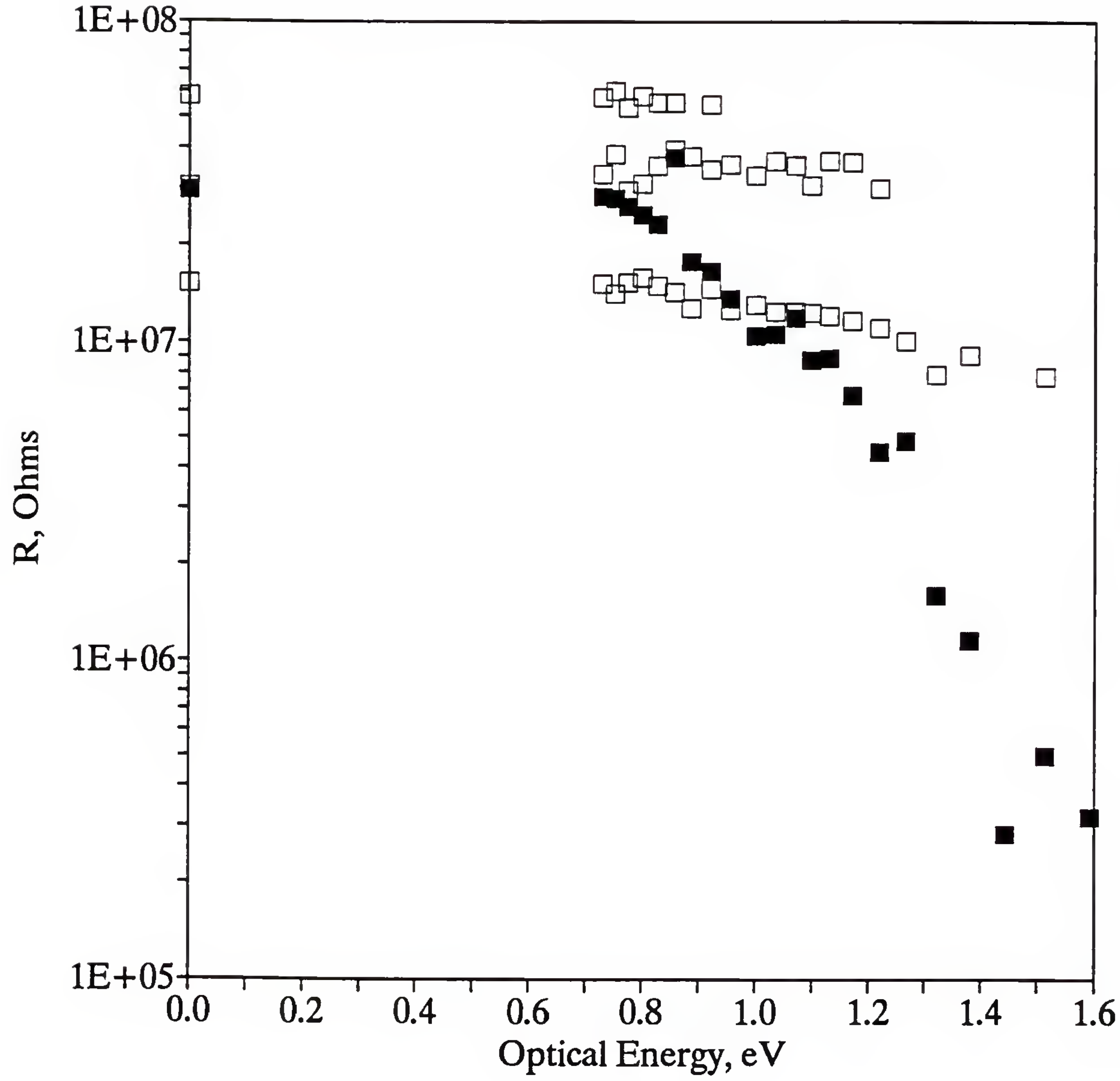

Figure 6.20: Resistances from regression of impedance data to equivalent circuit as a function of optical energy for n-type GaAs with Schottky contact.

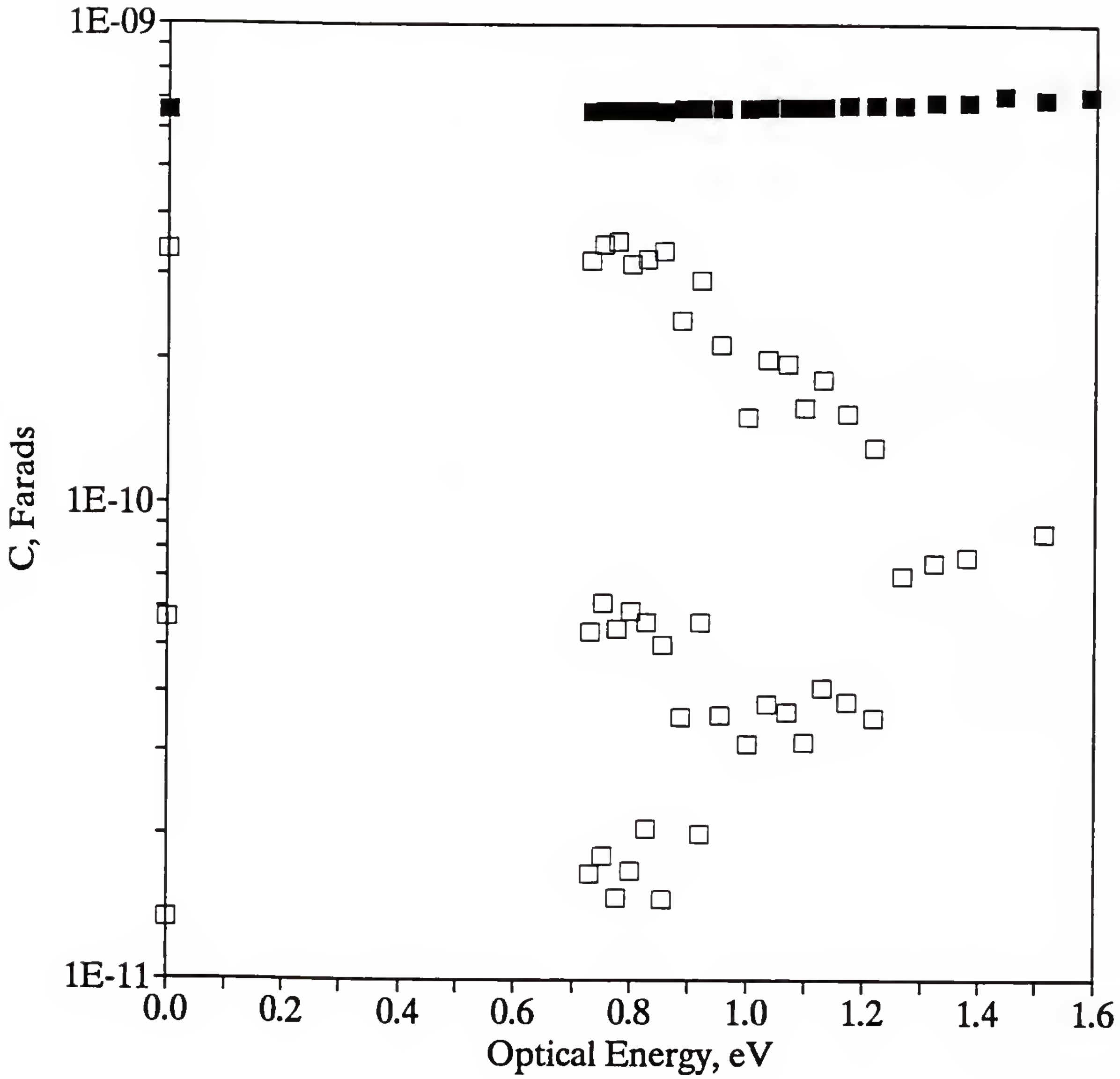

Figure 6.21: Capacitances from regression of impedance data to equivalent circuit as a function of optical energy for n–type GaAs with Schottky contact.

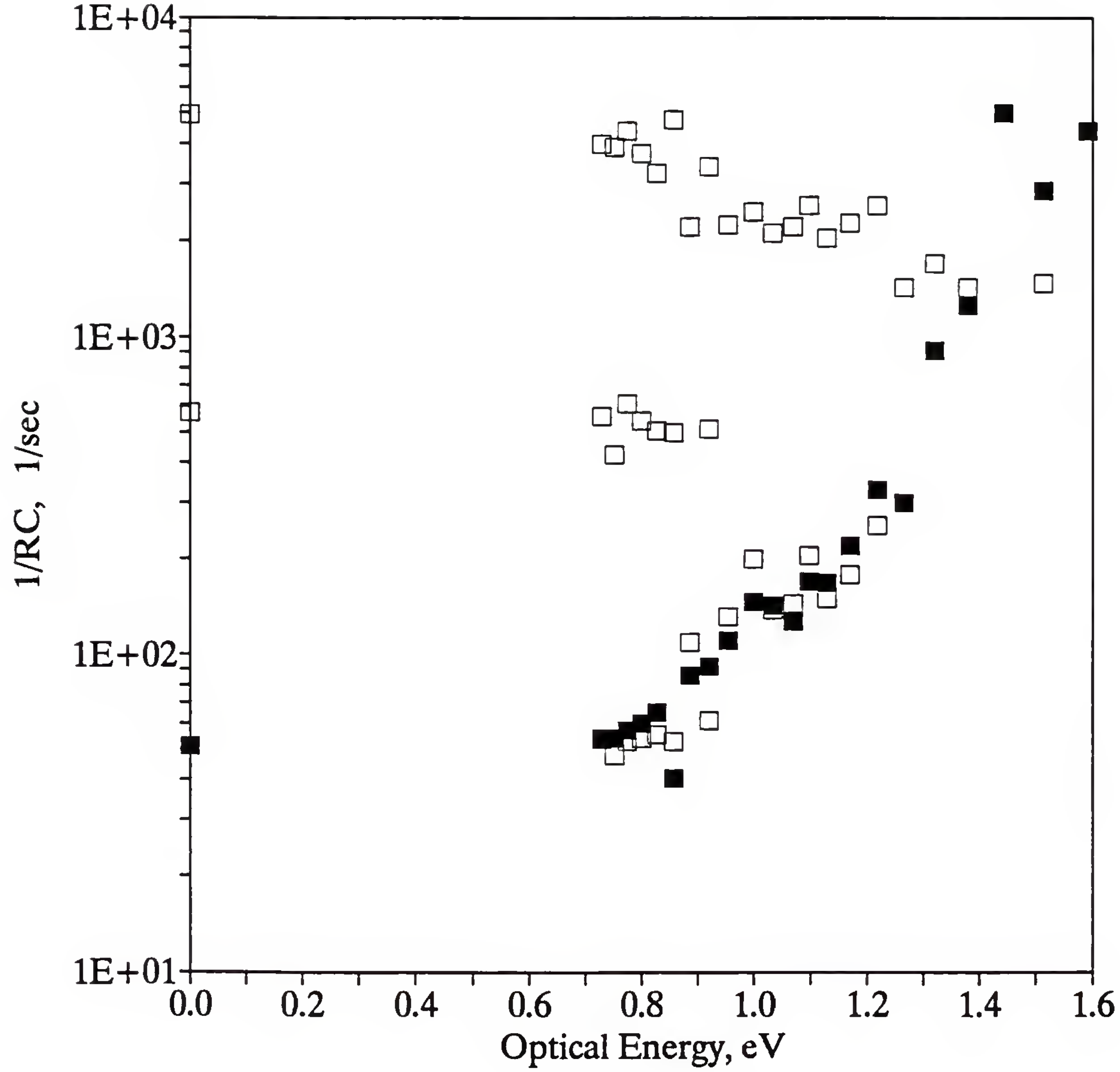

Figure 6.22: Characteristic frequencies from regression of impedance data to equivalent circuit as a function of optical energy for n-type GaAs with Schottky contact.

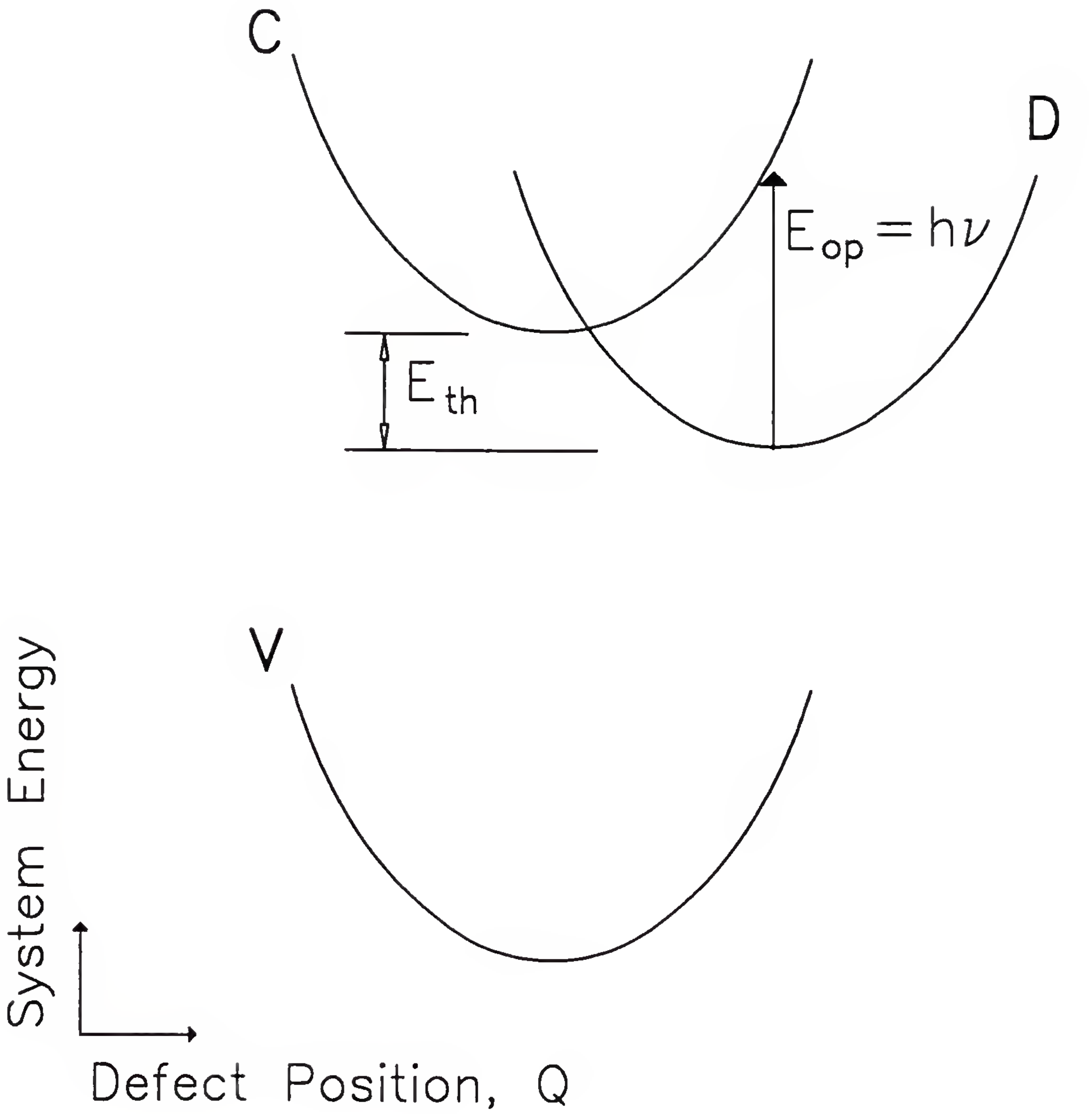

Figure 6.23: Curve C is for an unoccupied defect with its electron delocalized in conduction band, Curve V is for an unoccupied defect with its electron delocalized in valence band, and Curve D is for an occupied defect.

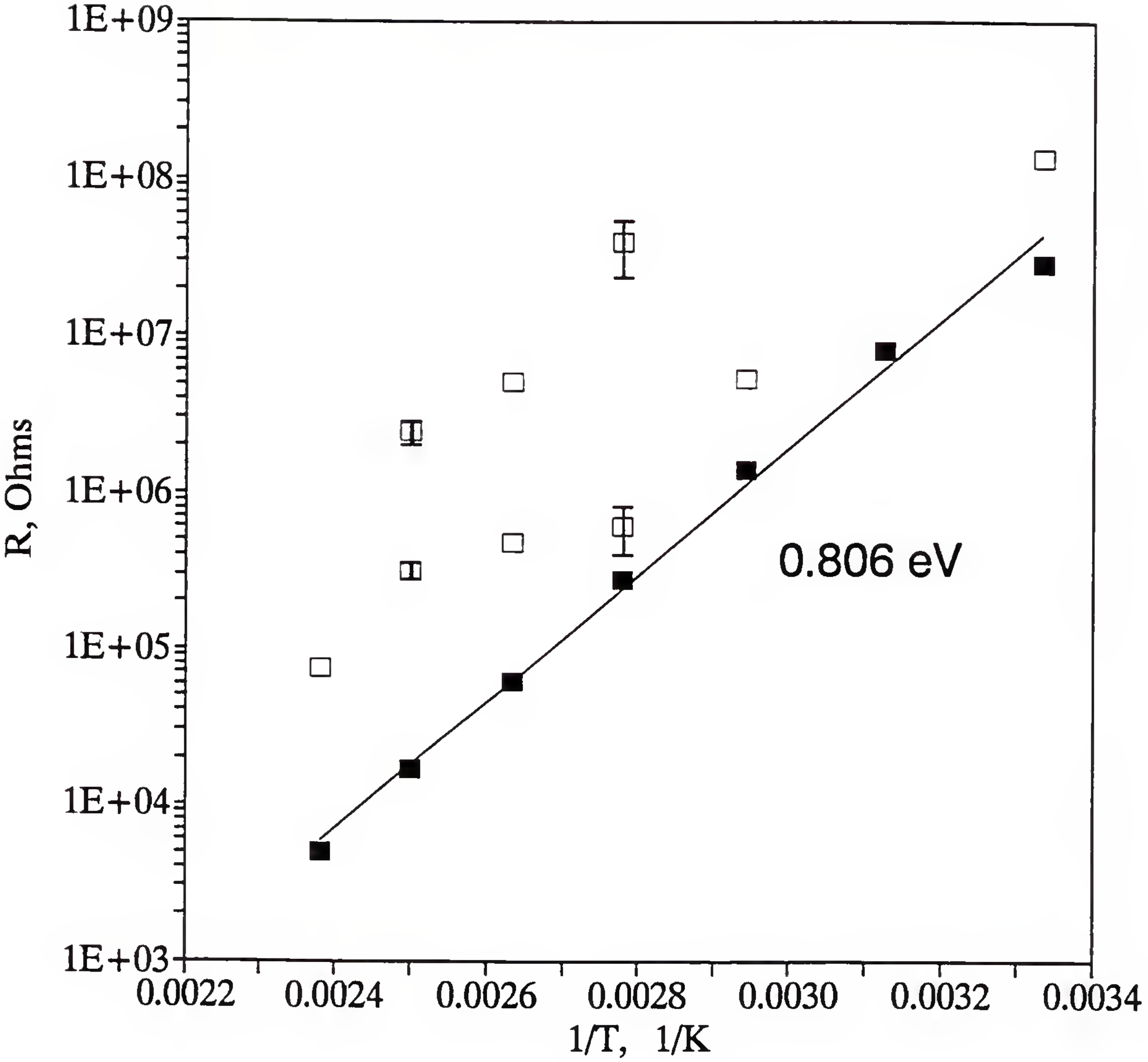

Figure 6.24: Resistances from regression of impedance data to equivalent circuit with no weighting as a function of optical energy for n-type GaAs with Schottky contact.

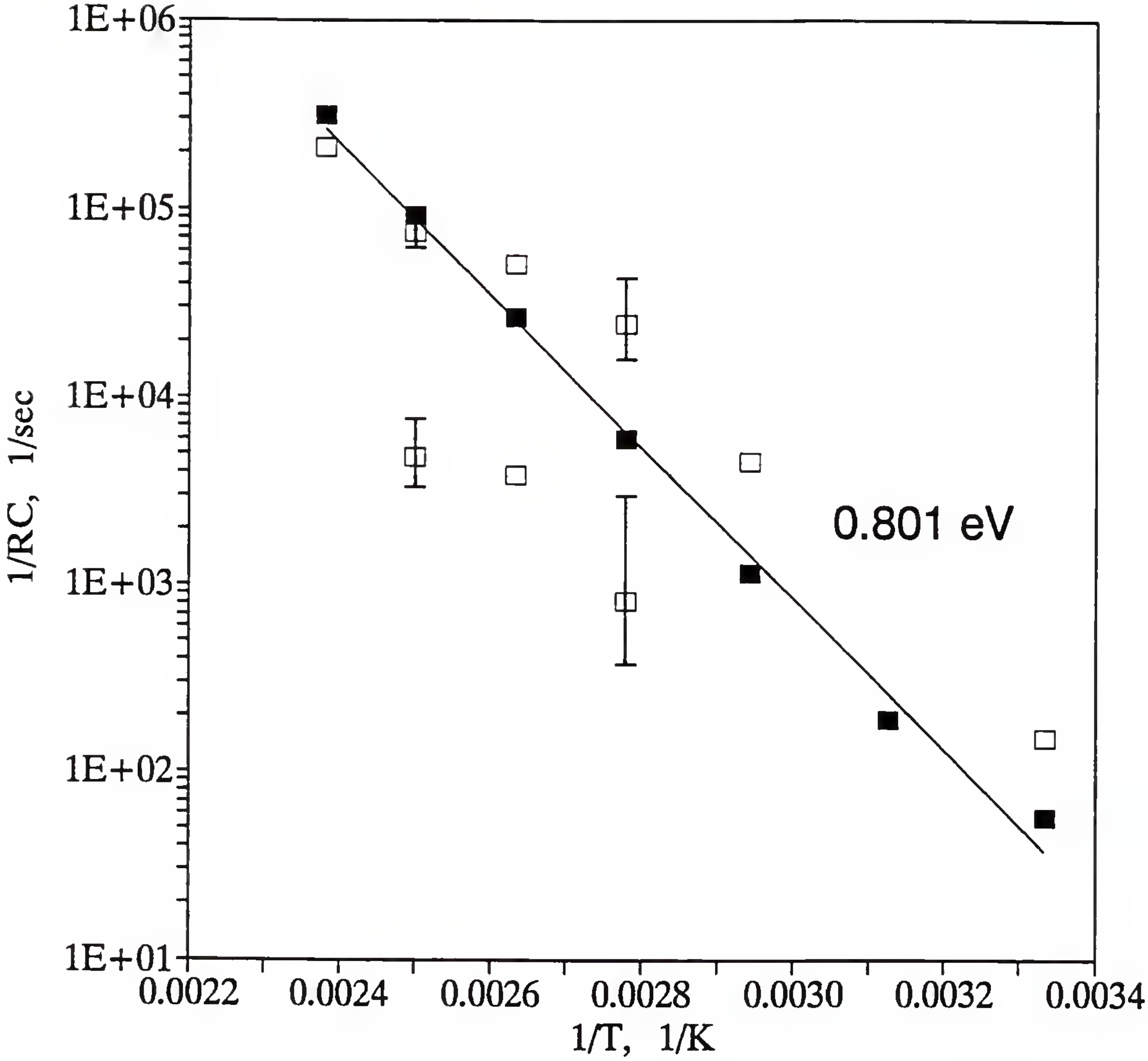

Figure 6.25: Characteristic frequencies from regression of impedance data to equivalent circuit with no weighting as a function of optical energy for n-type GaAs with Schottky contact.

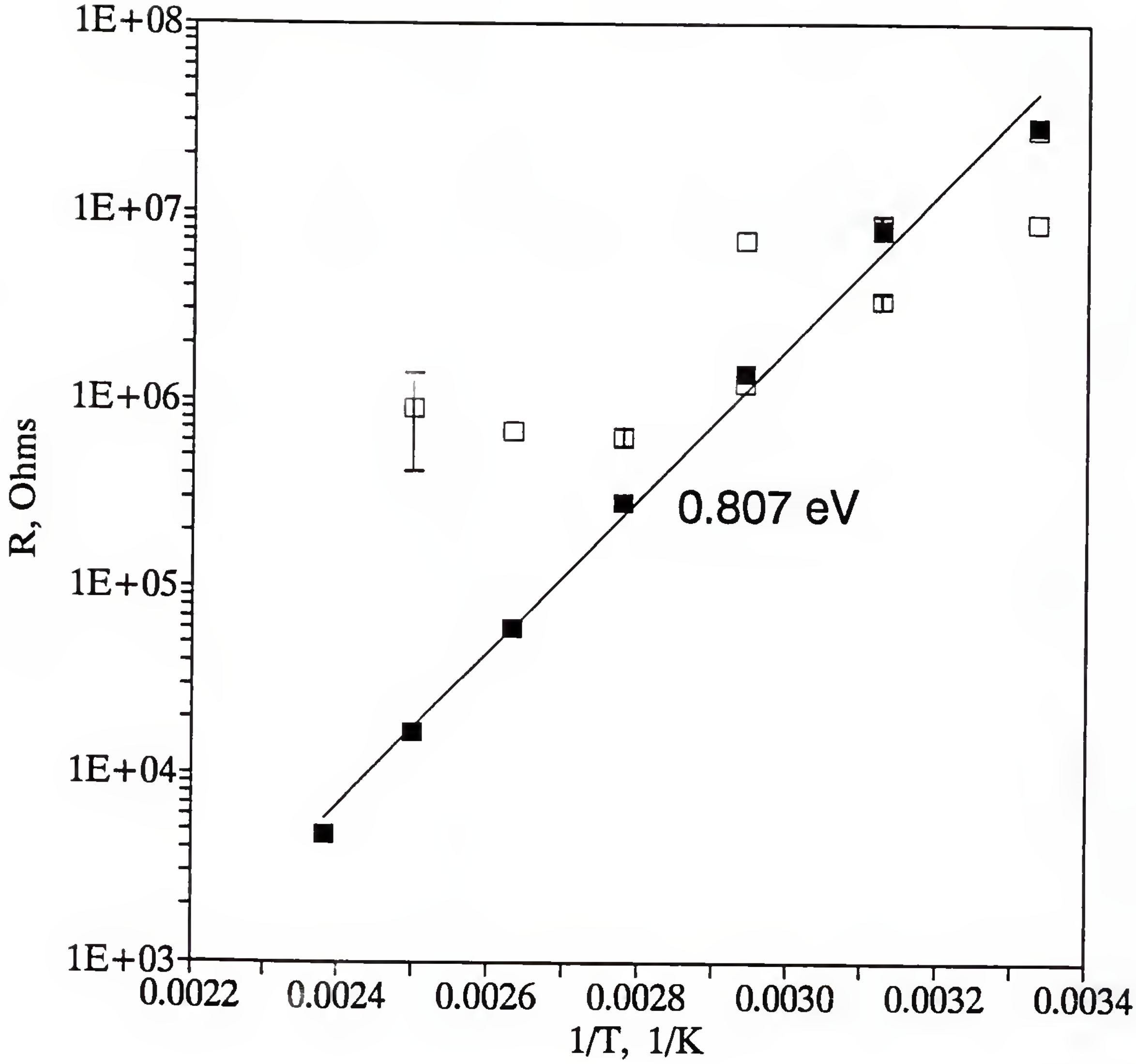

Figure 6.26: Resistances from regression of impedance data to equivalent circuit with proportional weighting as a function of optical energy for n–type GaAs with Schottky contact.

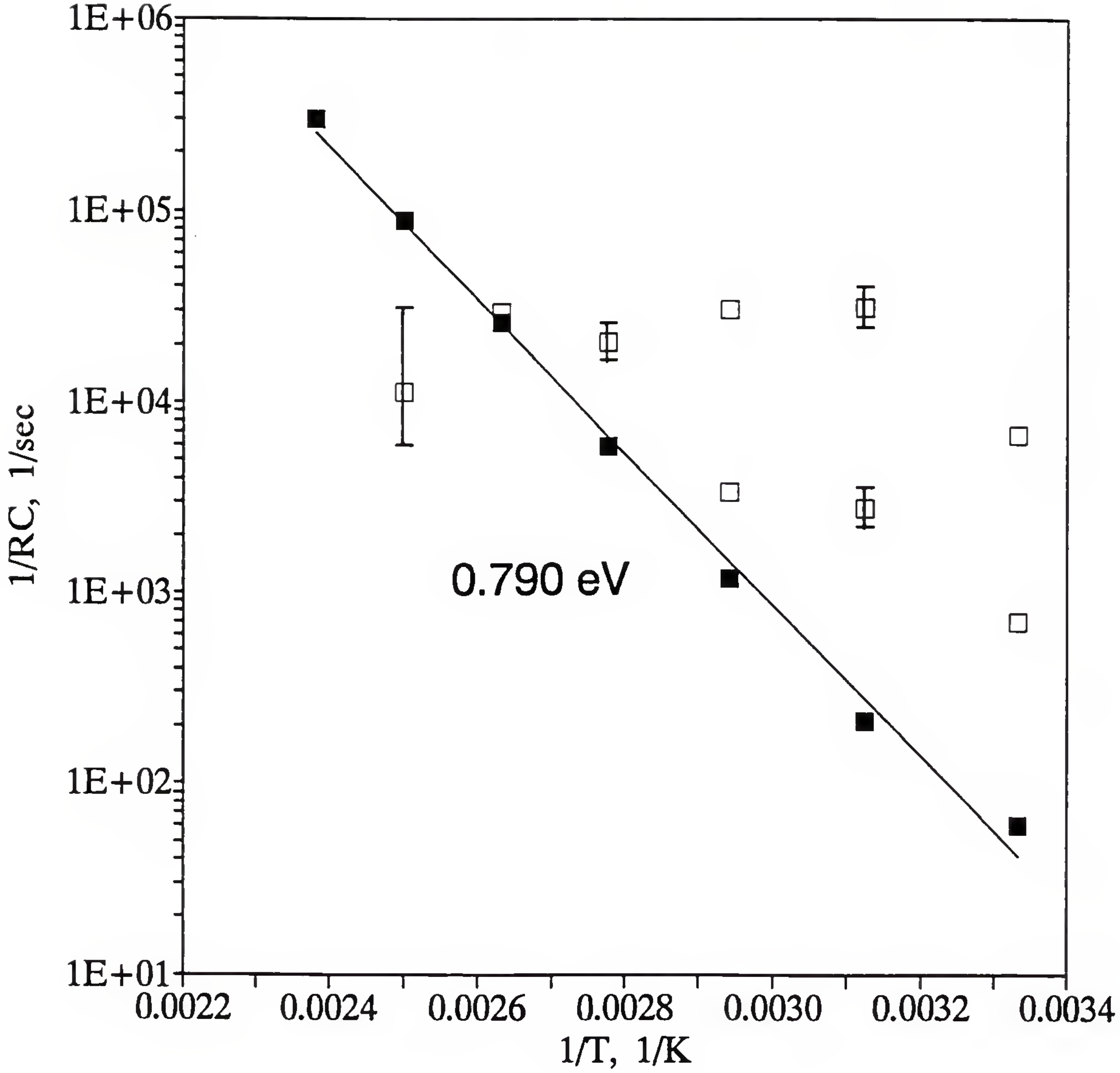

Figure 6.27: Characteristic frequencies from regression of impedance data to equivalent circuit with proportional weighting as a function of optical energy for n-type GaAs with Schottky contact.

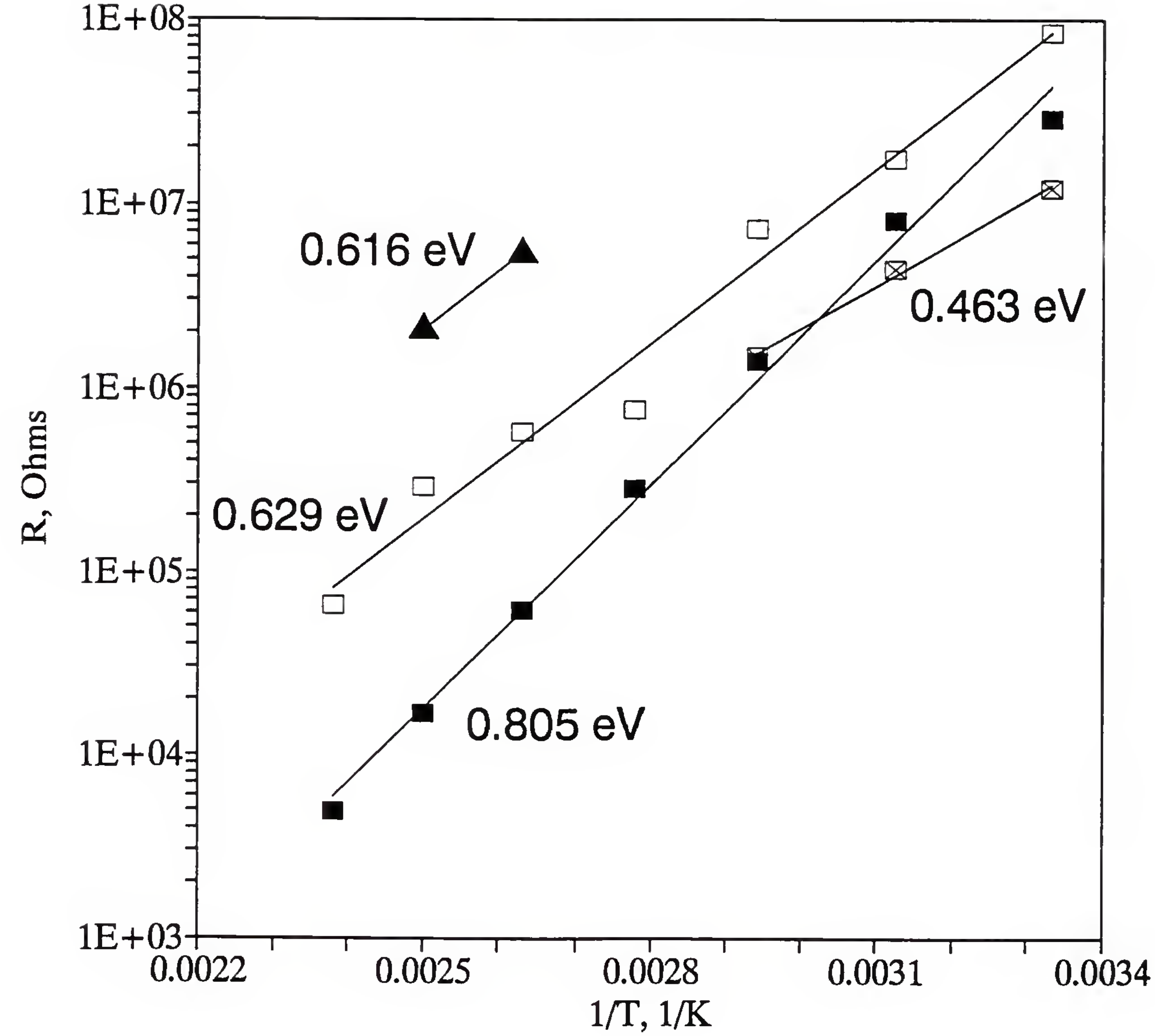

Figure 6.28: Resistances from regression of impedance data to equivalent circuit with modulus weighting as a function of optical energy for n–type GaAs with Schottky contact.

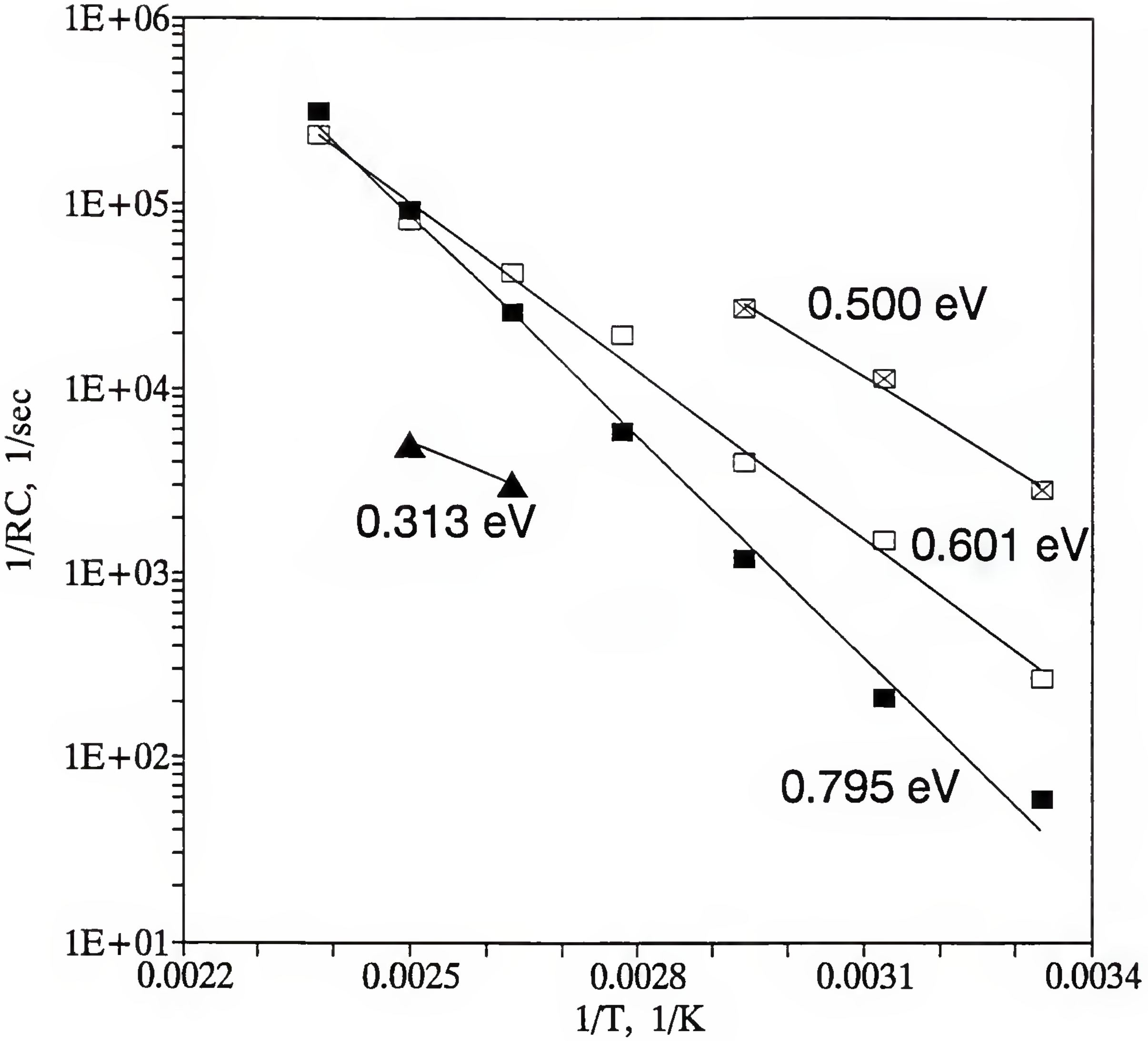

Figure 6.29: Characteristic frequencies from regression of impedance data to equivalent circuit with modulus weighting as a function of optical energy for n–type GaAs with Schottky contact.

Parameter	Value	System
α	3.29×10^{-4}	Solartron 1286 Electrochemical and Solid State
β	1.20×10^{-3}	
γ	2.83×10^{-4}	
α	2.75×10^{-2}	PAR 273 Electrochemical
β	0	
γ	2.76×10^{-3}	
α	0	PAR 273 Solid State
β	9.05×10^{-3}	
γ	0	

Table 6.2: Model variance weighting parameters used in regression of impedance data. Values were determined by Pankaj Agarwal.

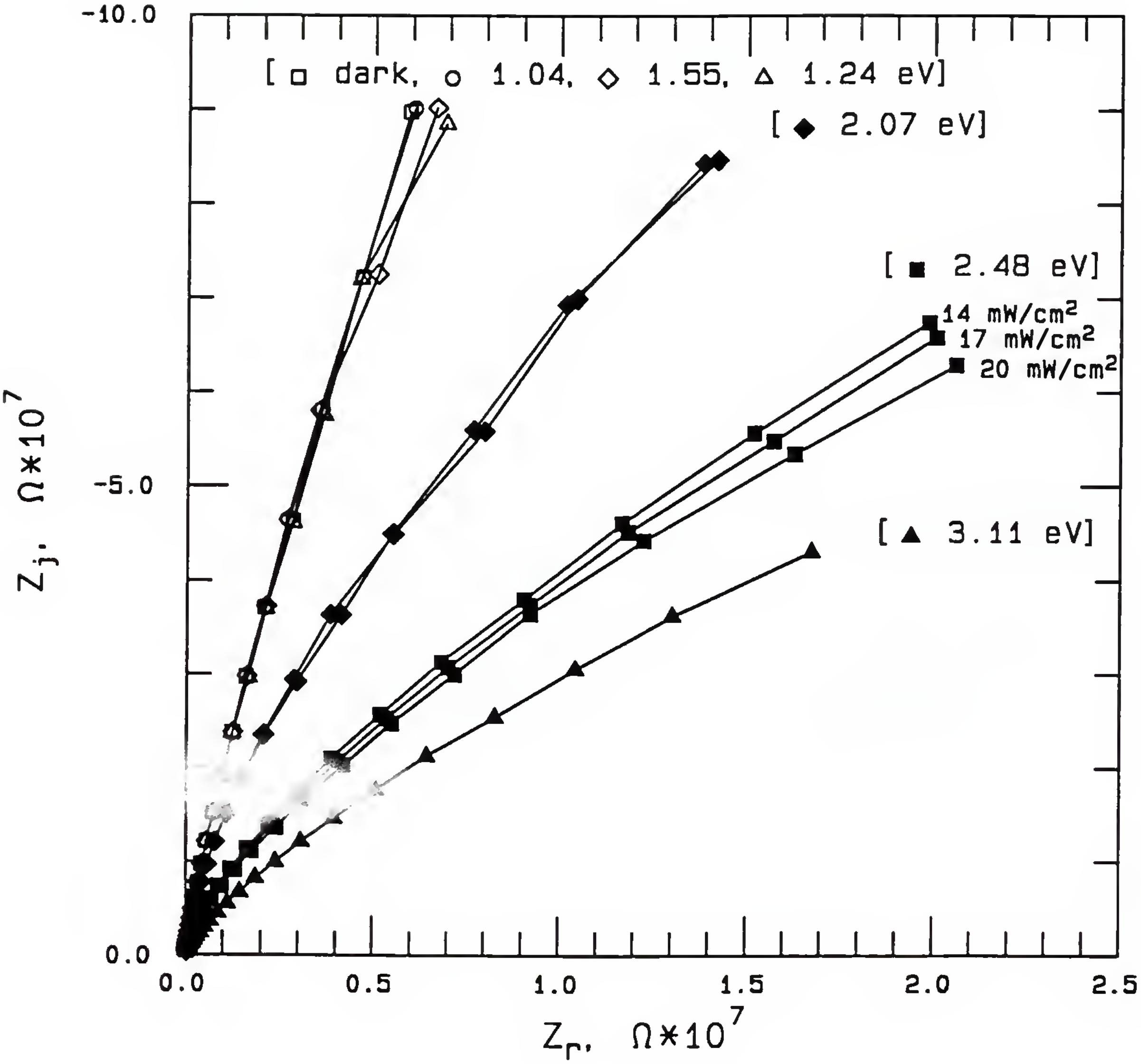

Figure 6.30: Imaginary component of the impedance as a function of the real component of the impedance for frequencies ranging from 0.2 to 100 Hz and with optical energy as a parameter for the ZnS:Mn TFEL panel.

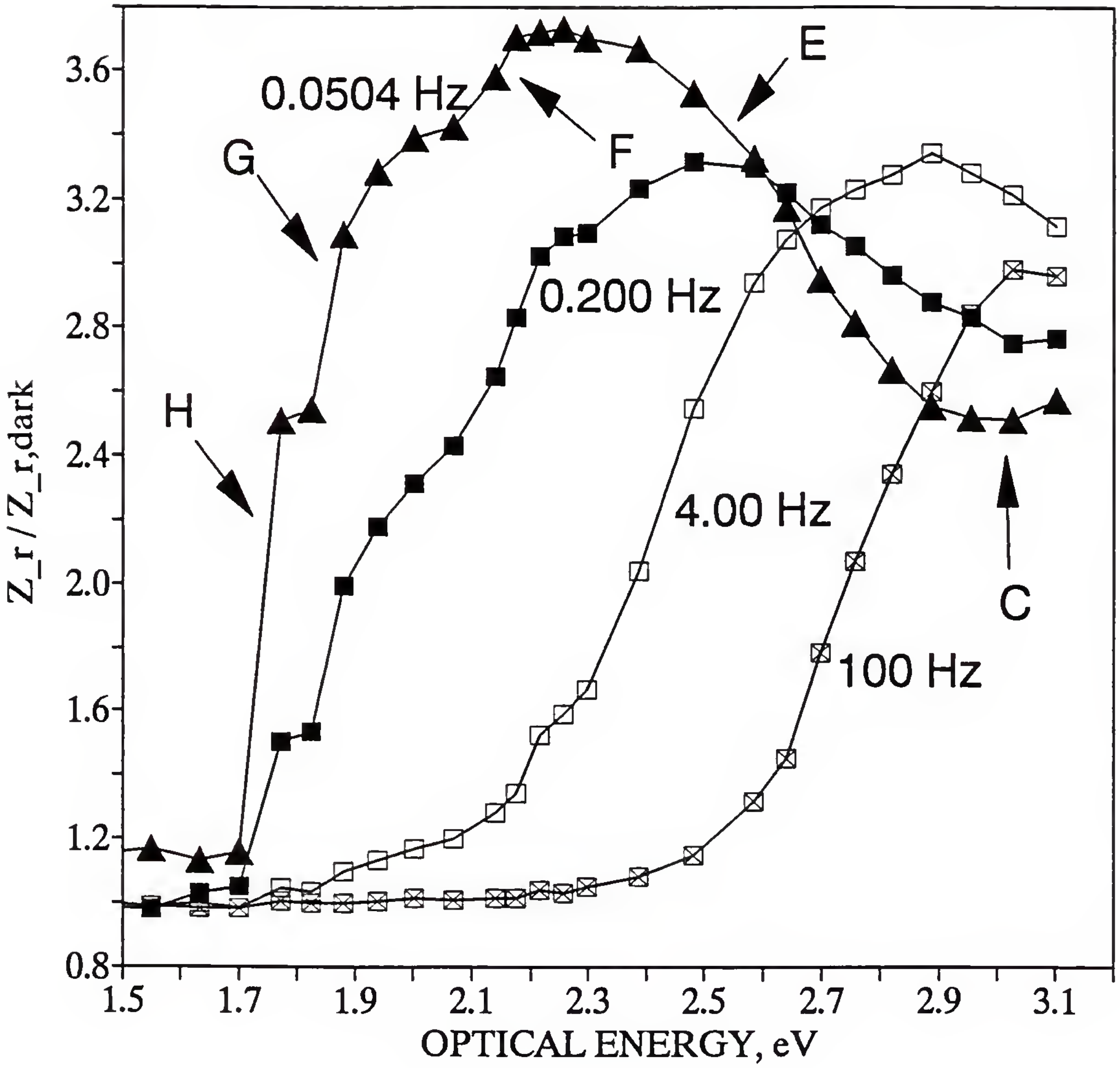

Figure 6.31: Dimensionless real component of the impedance as a function of optical energy with electrical frequency as a parameter for the ZnS:MN TFEL panel.

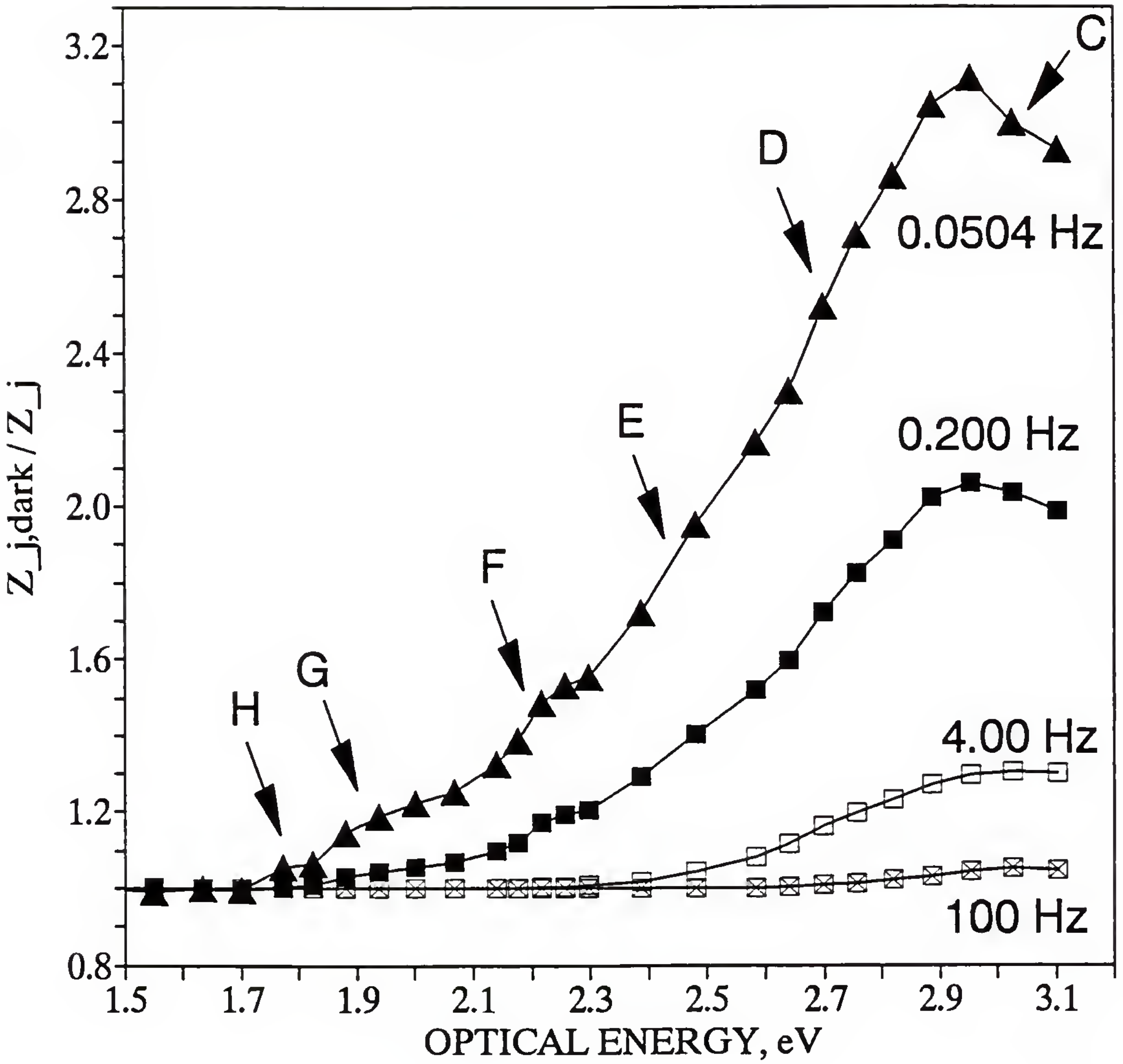

Figure 6.32: Dimensionless imaginary component of the impedance as a function of optical energy with electrical frequency as a parameter for the ZnS:Mn TFEL panel.

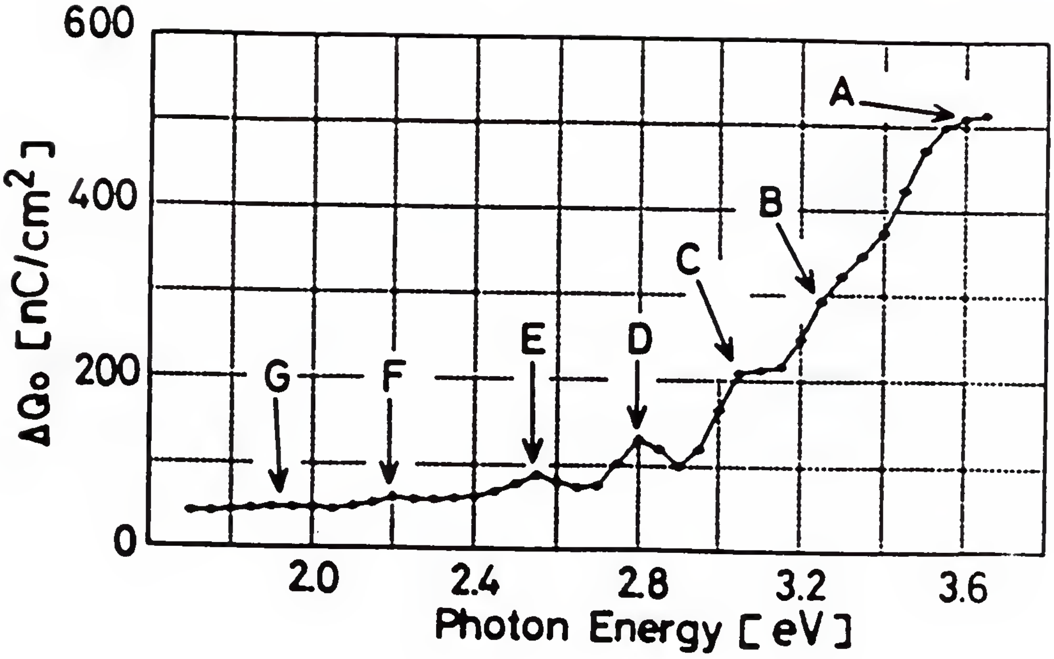

Figure 6.33: Change in photon–released residual charge as a function of photon energy for a ZnS:Mn TFEL panel from reference [108].

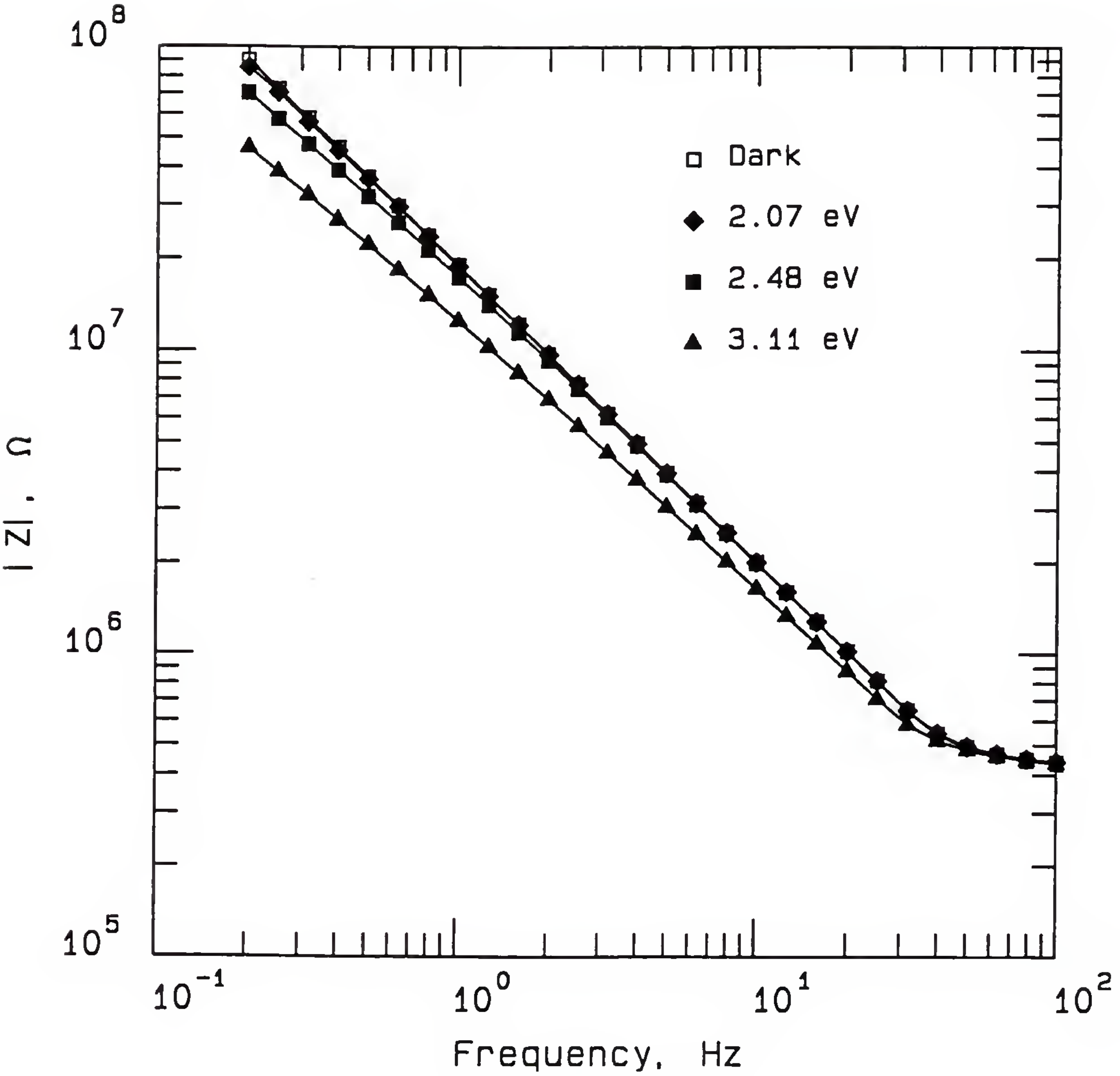

Figure 6.34: Total impedance as a function of frequency with optical energy as a parameter for the ZnS:Mn TFEL panel.

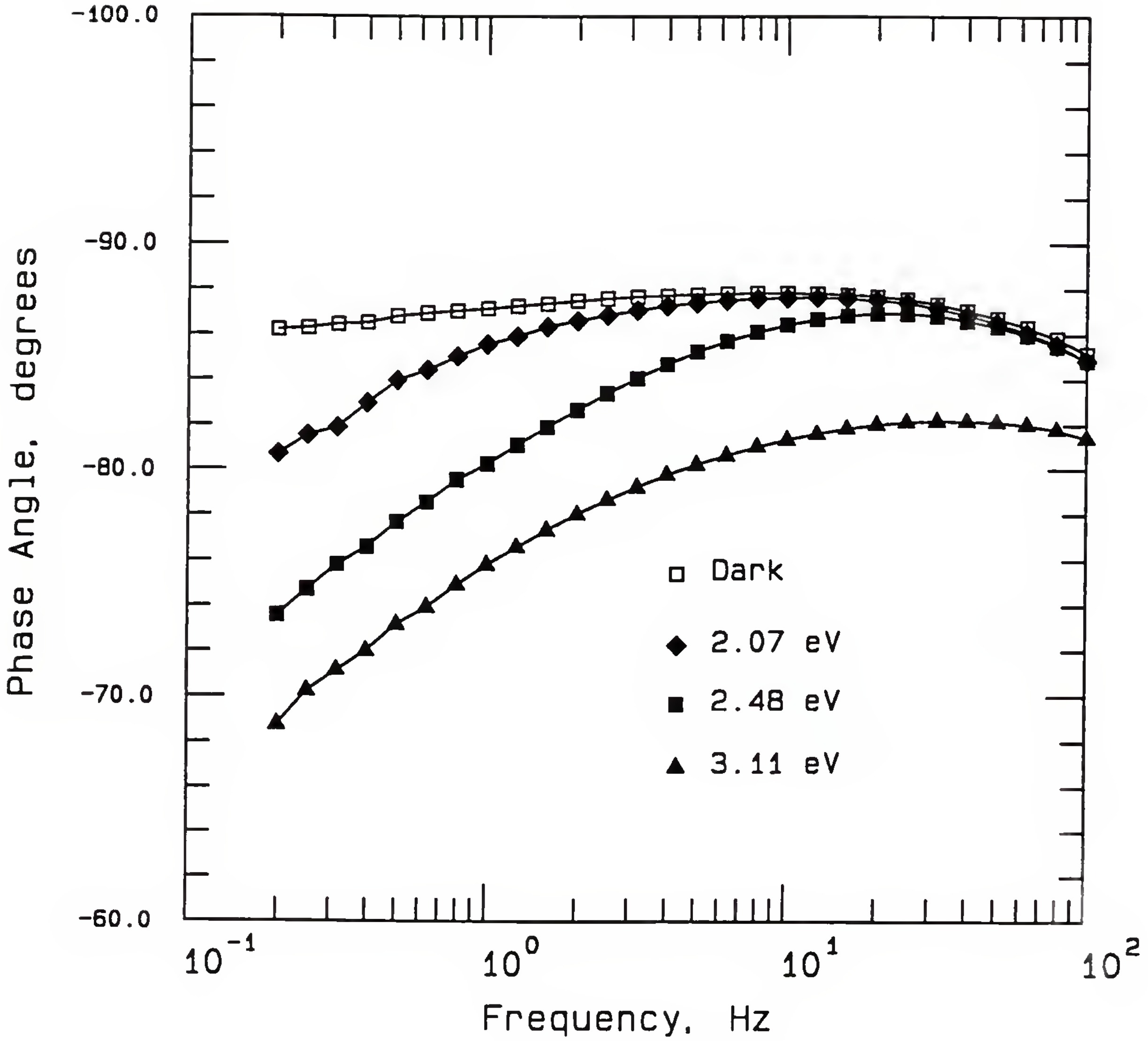

Figure 6.35: Phase angle as a function of frequency with optical energy as a parameter for the ZnS:Mn TFEL panel.

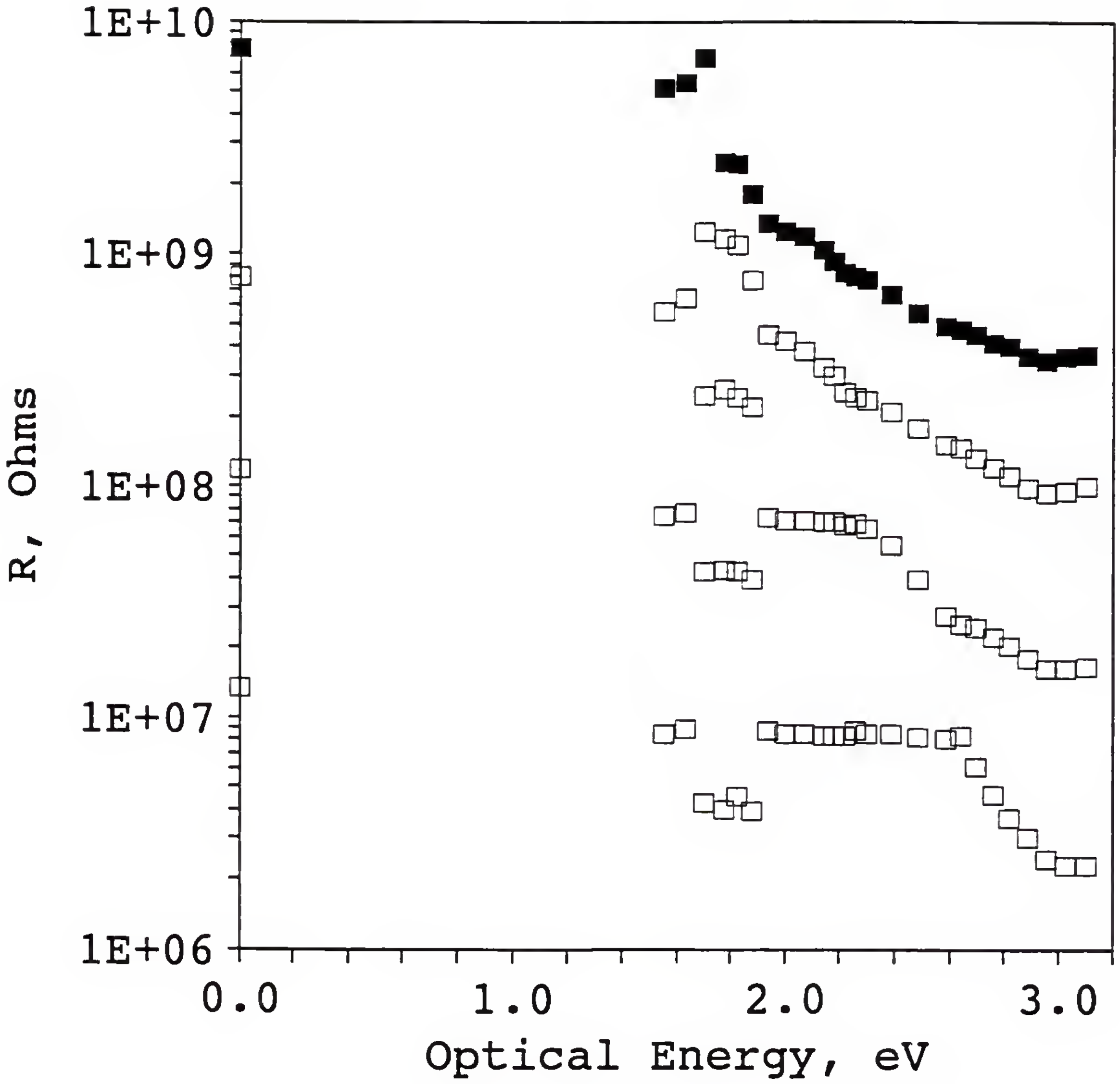

Figure 6.36: Resistances from regression of simplified equivalent circuit to impedance data as a function of inverse temperature for the ZnS:Mn TFEL panel.

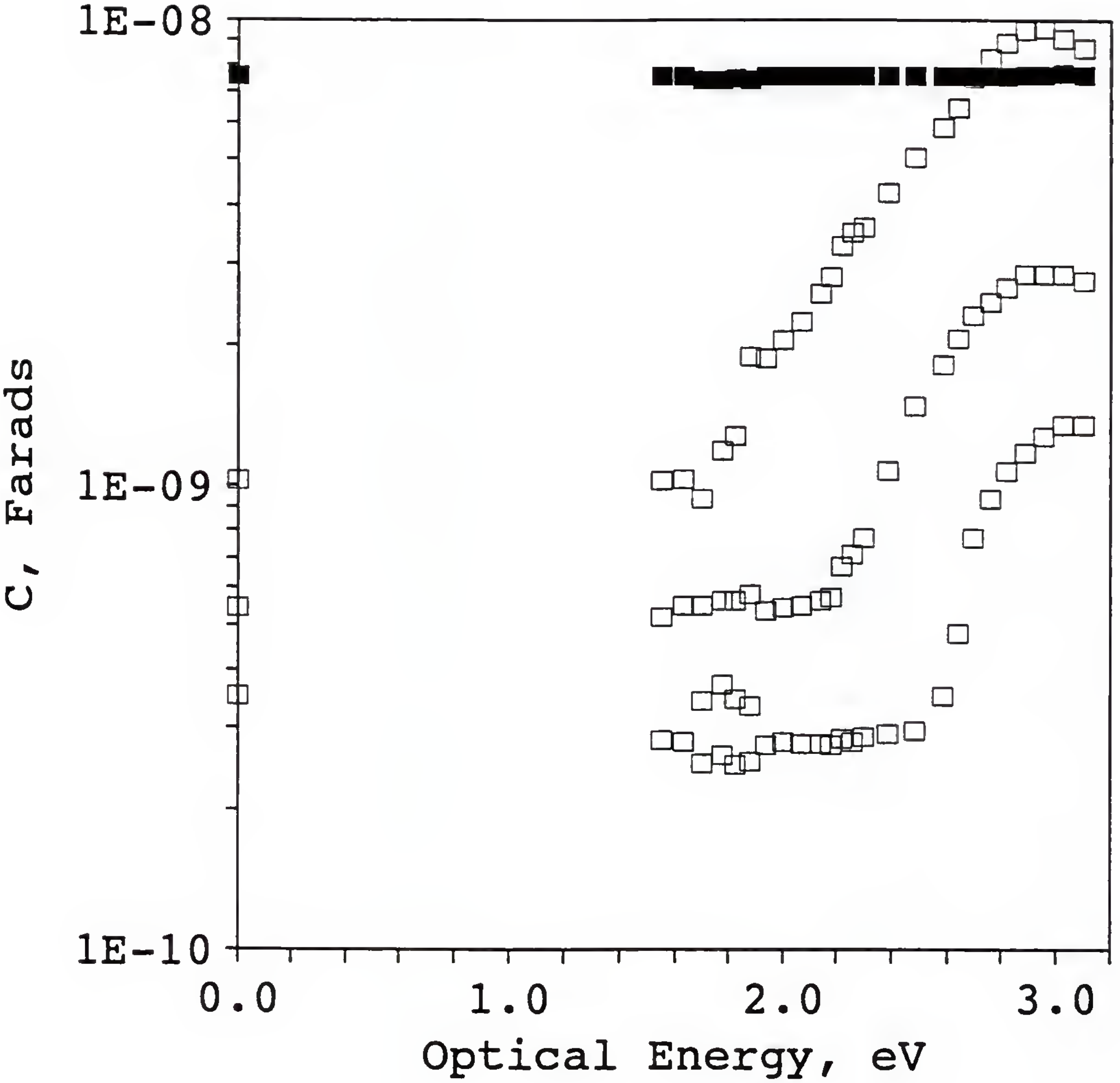

Figure 6.37: Capacitances from regression of simplified equivalent circuit to impedance data as a function of inverse temperature for the ZnS:Mn TFEL panel.

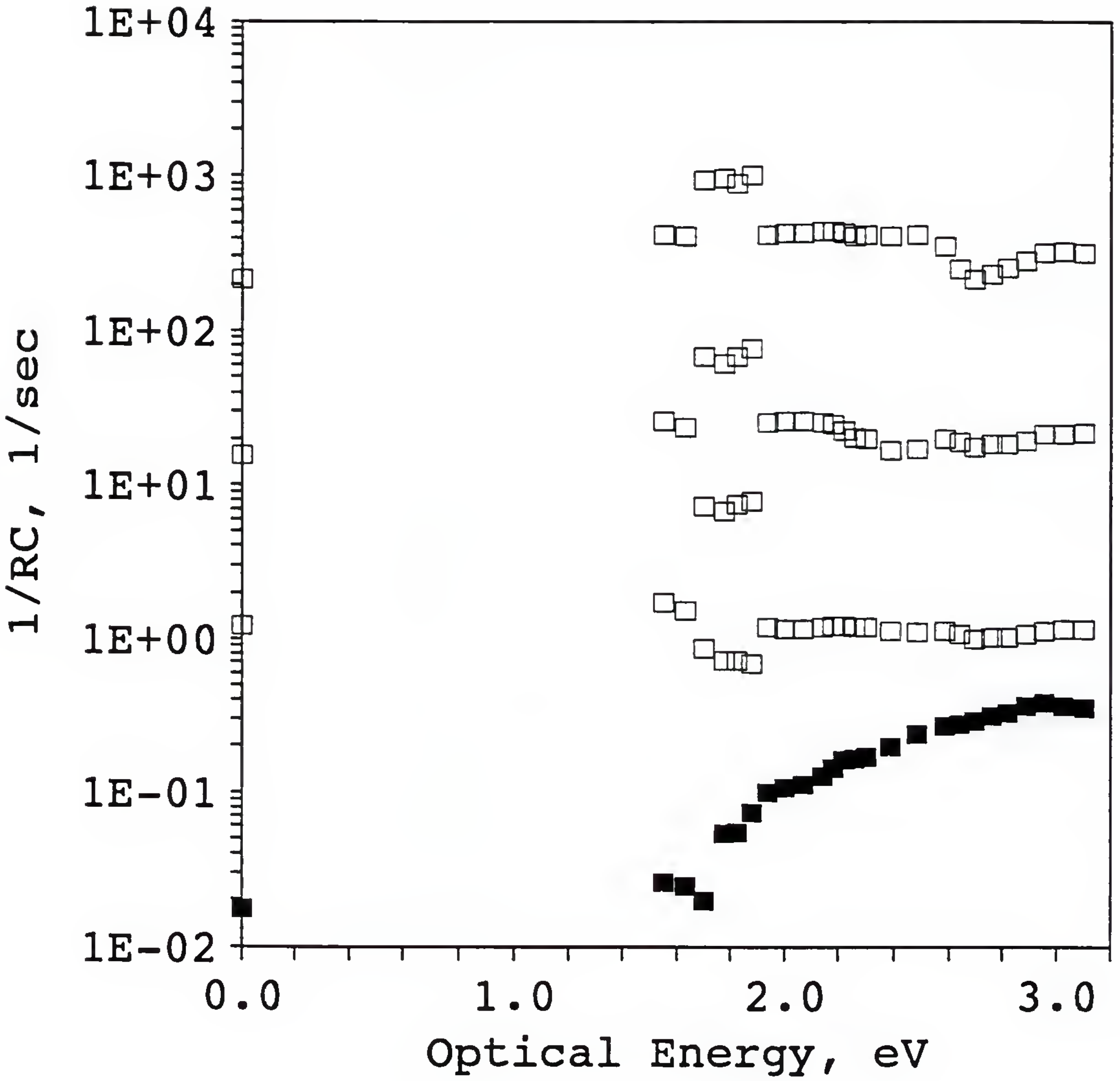

Figure 6.38: Equivalent circuit characteristic frequencies from regression of simplified equivalent circuit to impedance data as a function of inverse temperature for the ZnS:Mn TFEL panel.

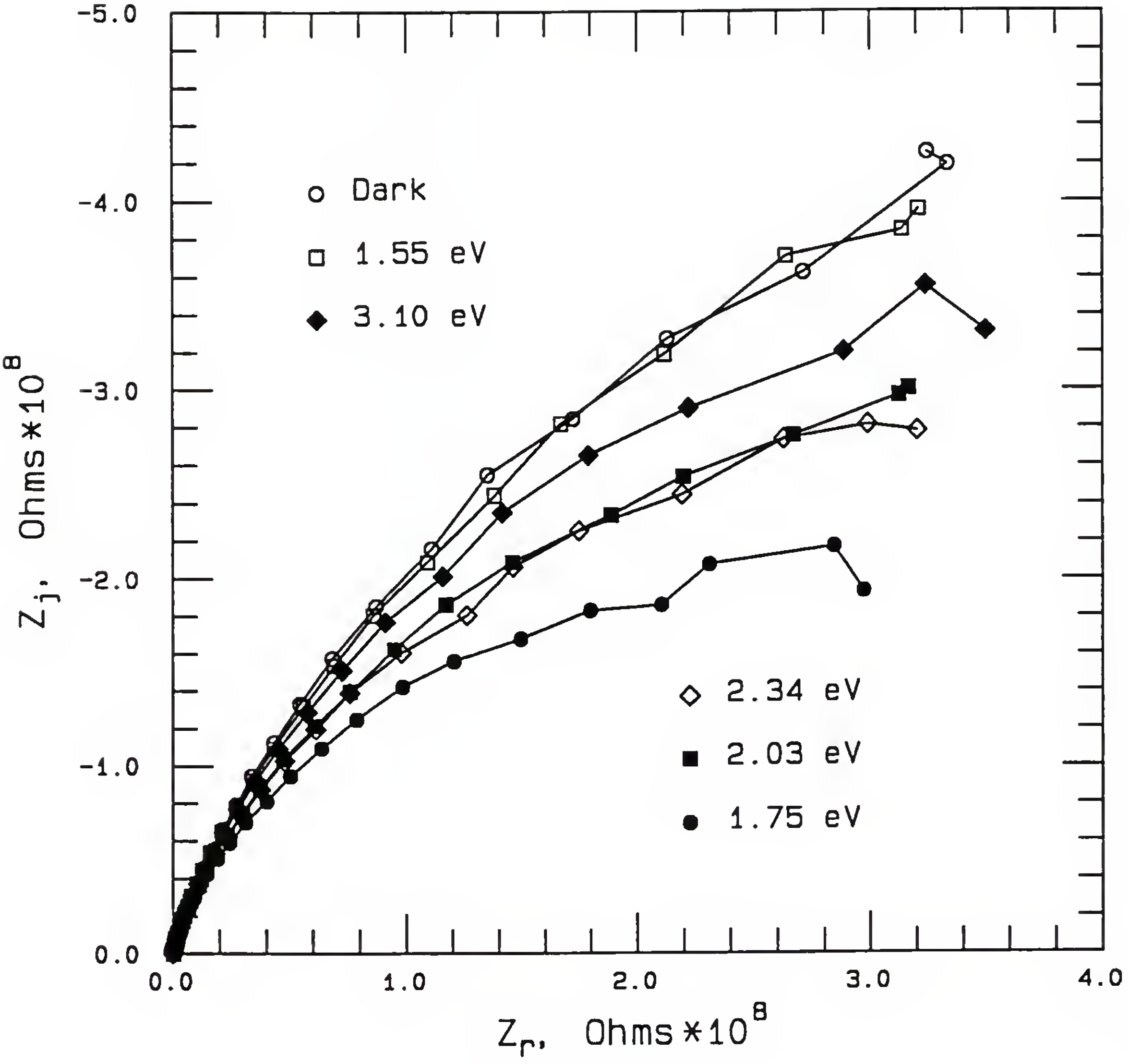

Figure 6.39: Imaginary component of the impedance as a function of the real component of the impedance for frequencies ranging from 20000 to 0.05 Hz with optical energy as a parameter for the unaged ZnO varistor.

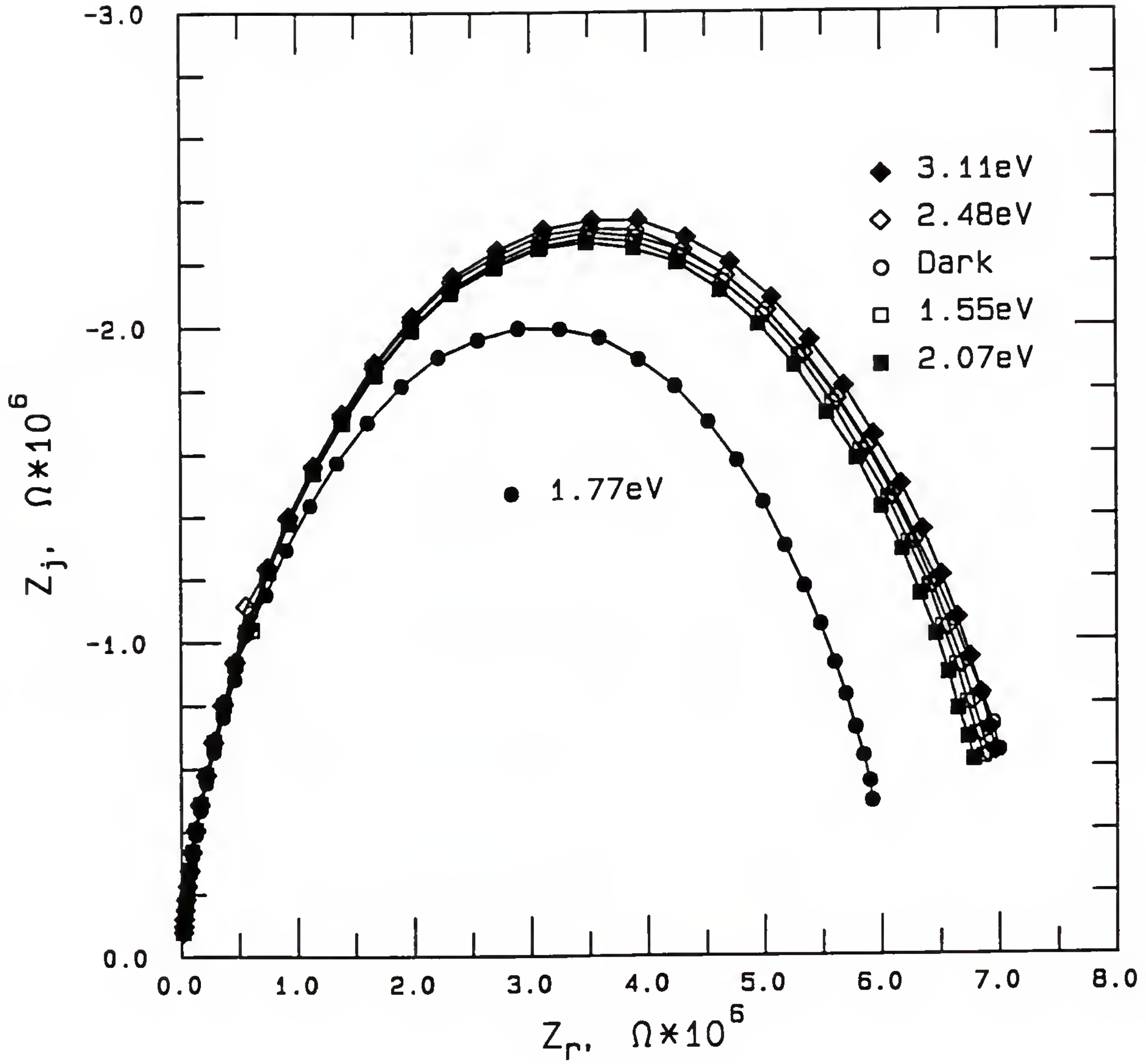

Figure 6.40: Imaginary component of the impedance as a function of the real component of the impedance for frequencies ranging from 1500 to 0.2 Hz with optical energy as a parameter for the aged ZnO varistor.

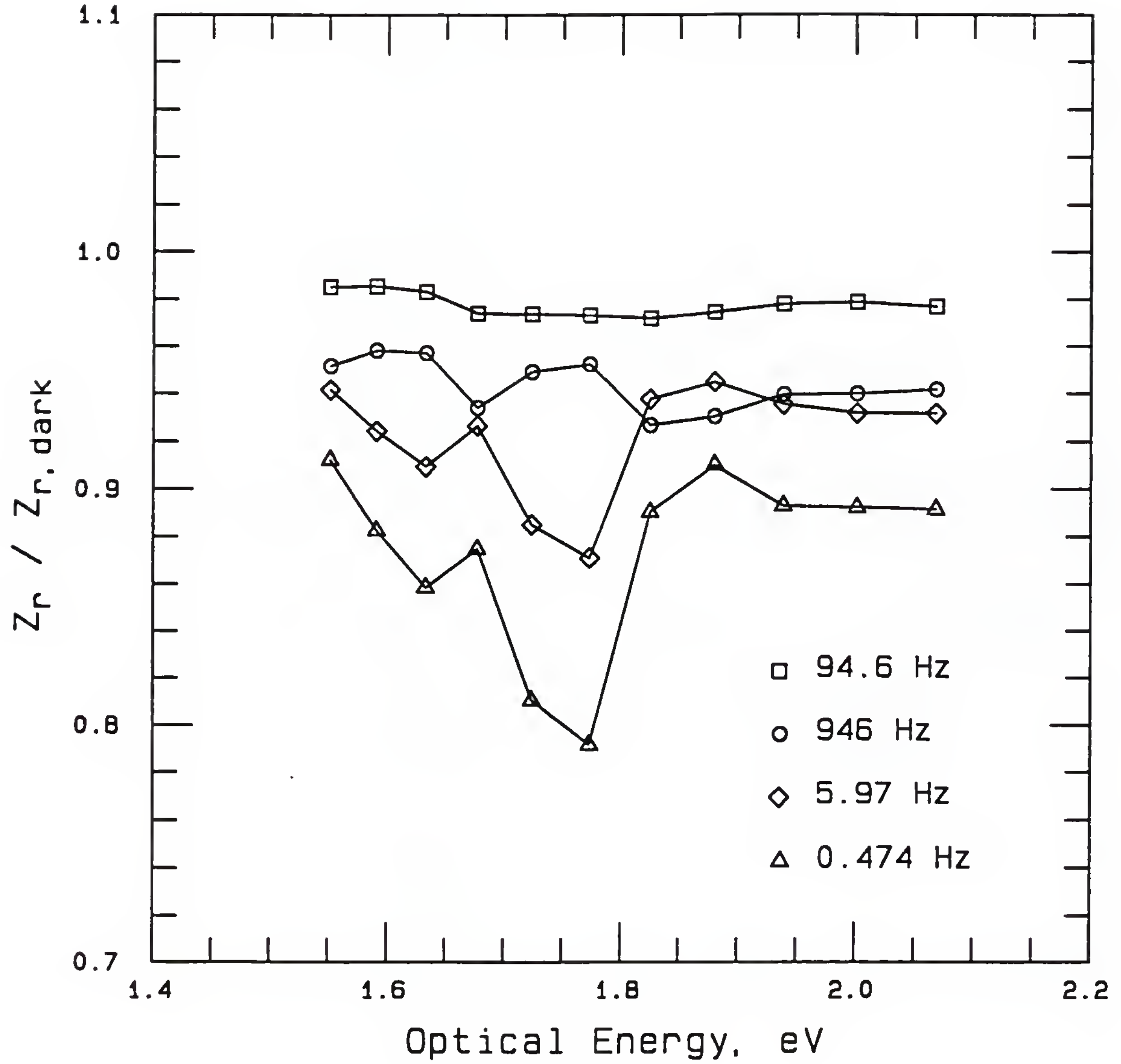

Figure 6.41: Dimensionless real component of the impedance as a function of optical energy with electrical frequency as a parameter for the aged ZnO varistor.

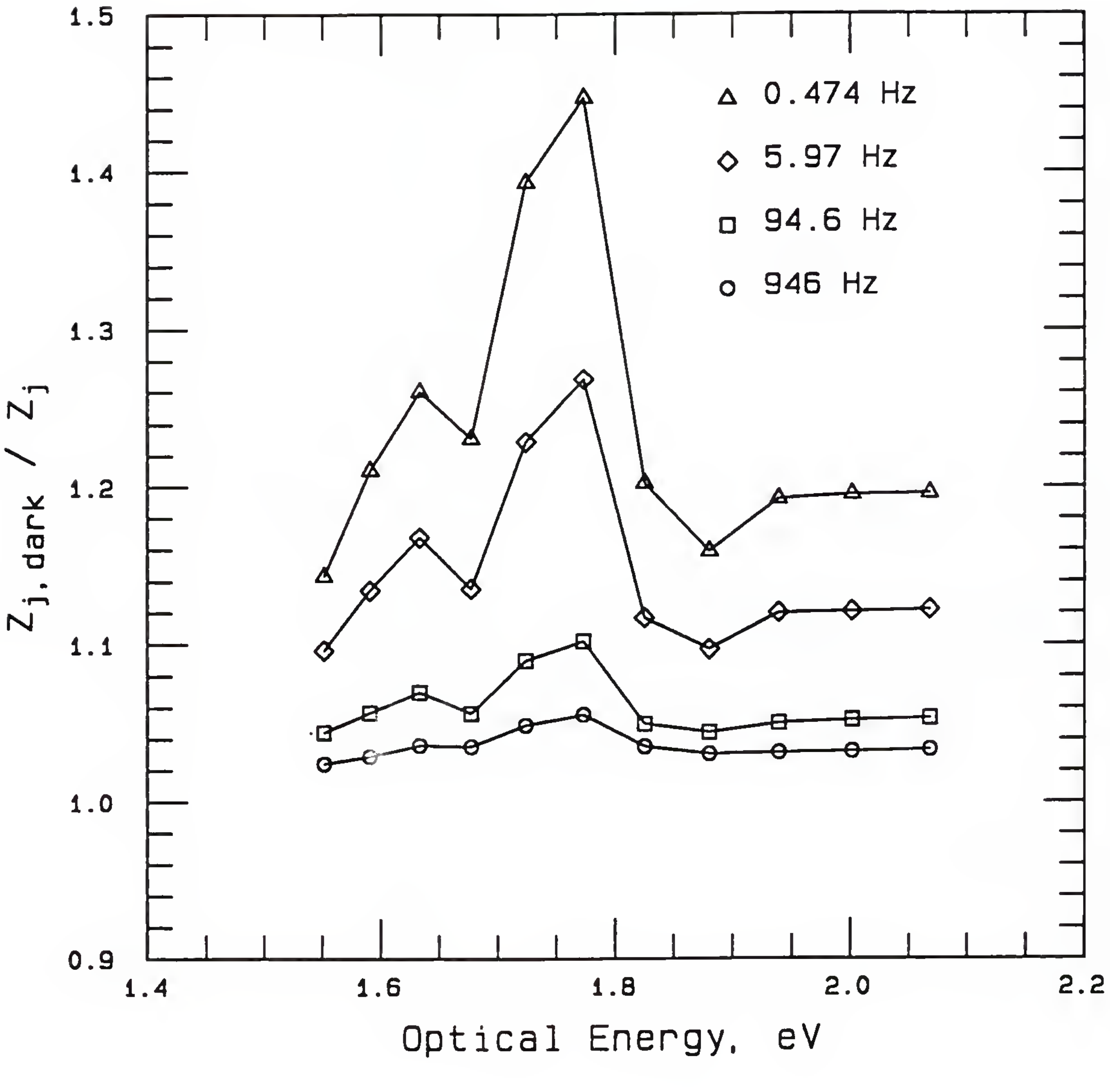

Figure 6.42: Dimensionless imaginary component of the impedance as a function of optical energy with electrical frequency as a parameter for the aged ZnO varistor.

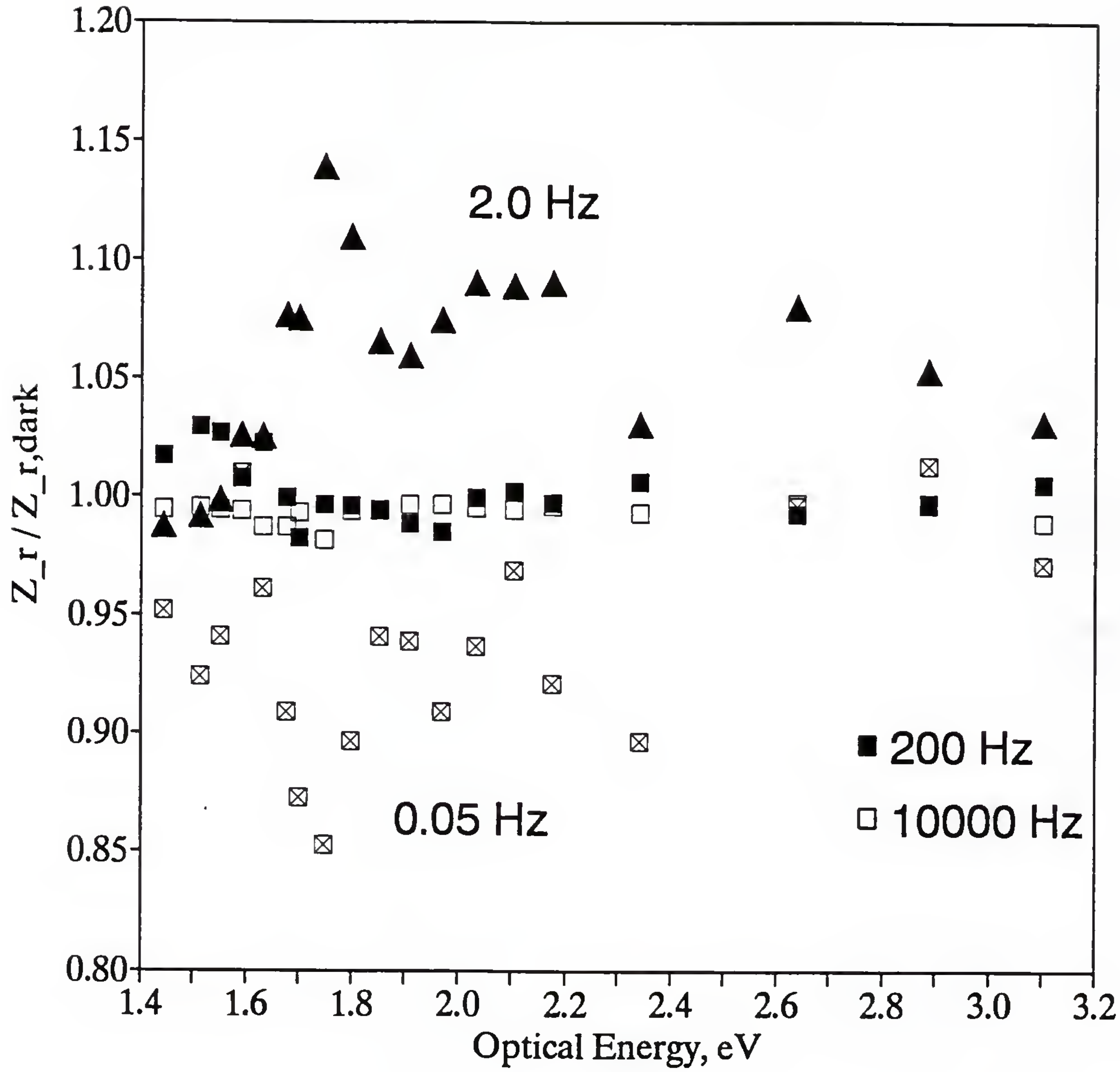

Figure 6.43: Dimensionless real component of the impedance as a function of optical energy with electrical frequency as a parameter for the unaged ZnO varistor.

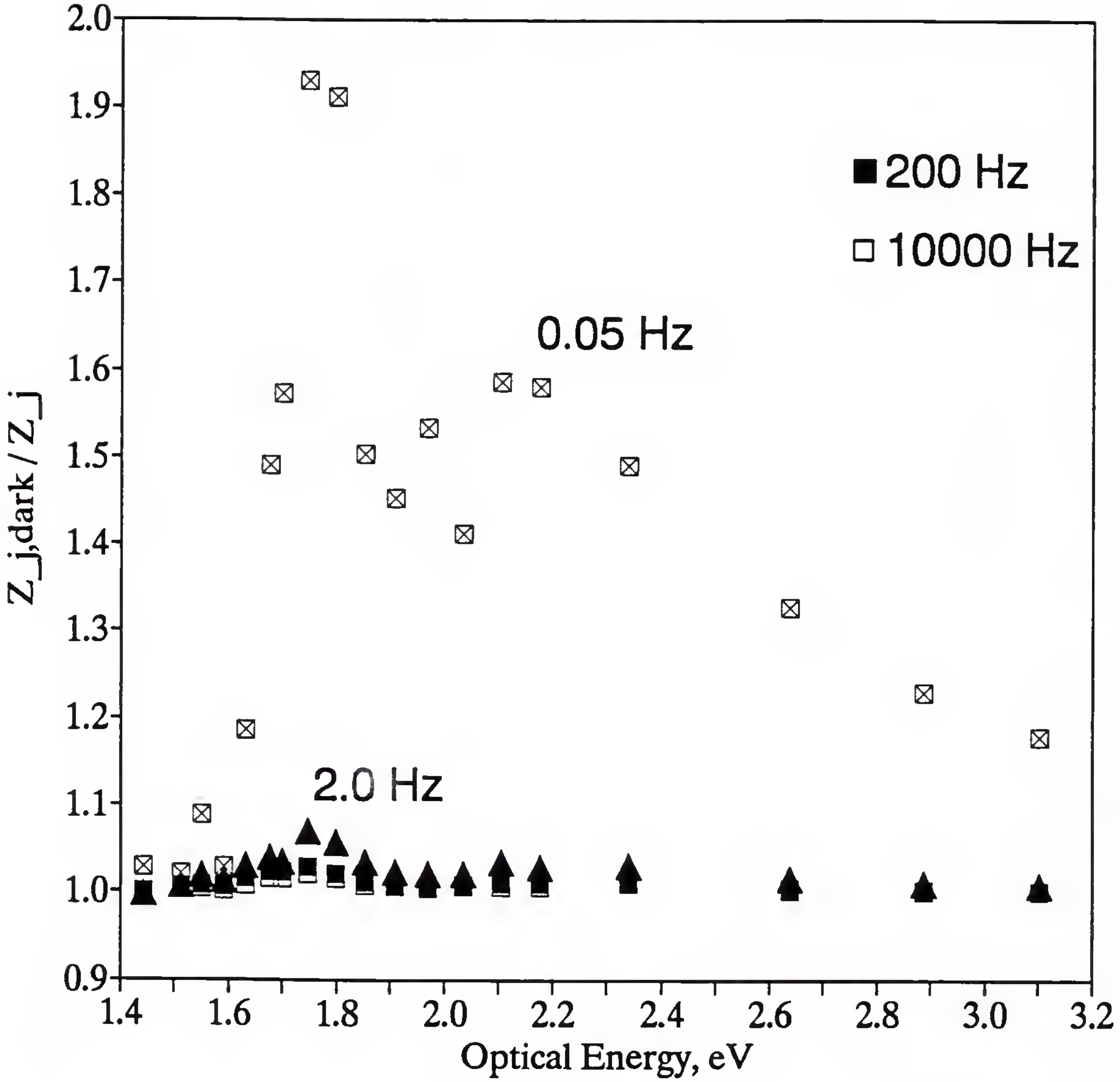

Figure 6.44: Dimensionless imaginary component of the impedance as a function of optical energy with electrical frequency as a parameter for the unaged ZnO varistor.

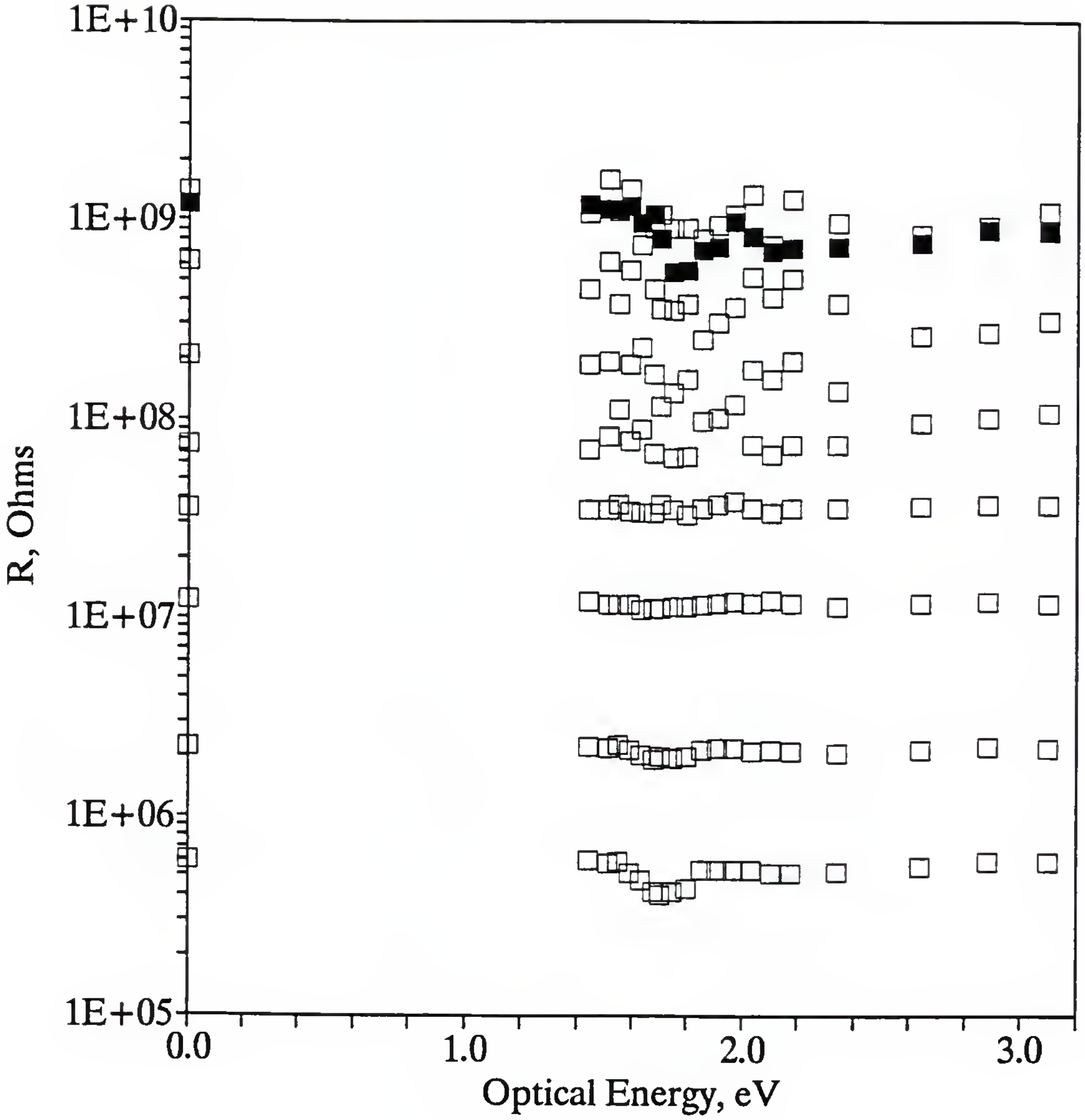

Figure 6.45: Resistances from regression of simplified equivalent circuit to impedance data as a function of inverse temperature for the unaged ZnO varistor.

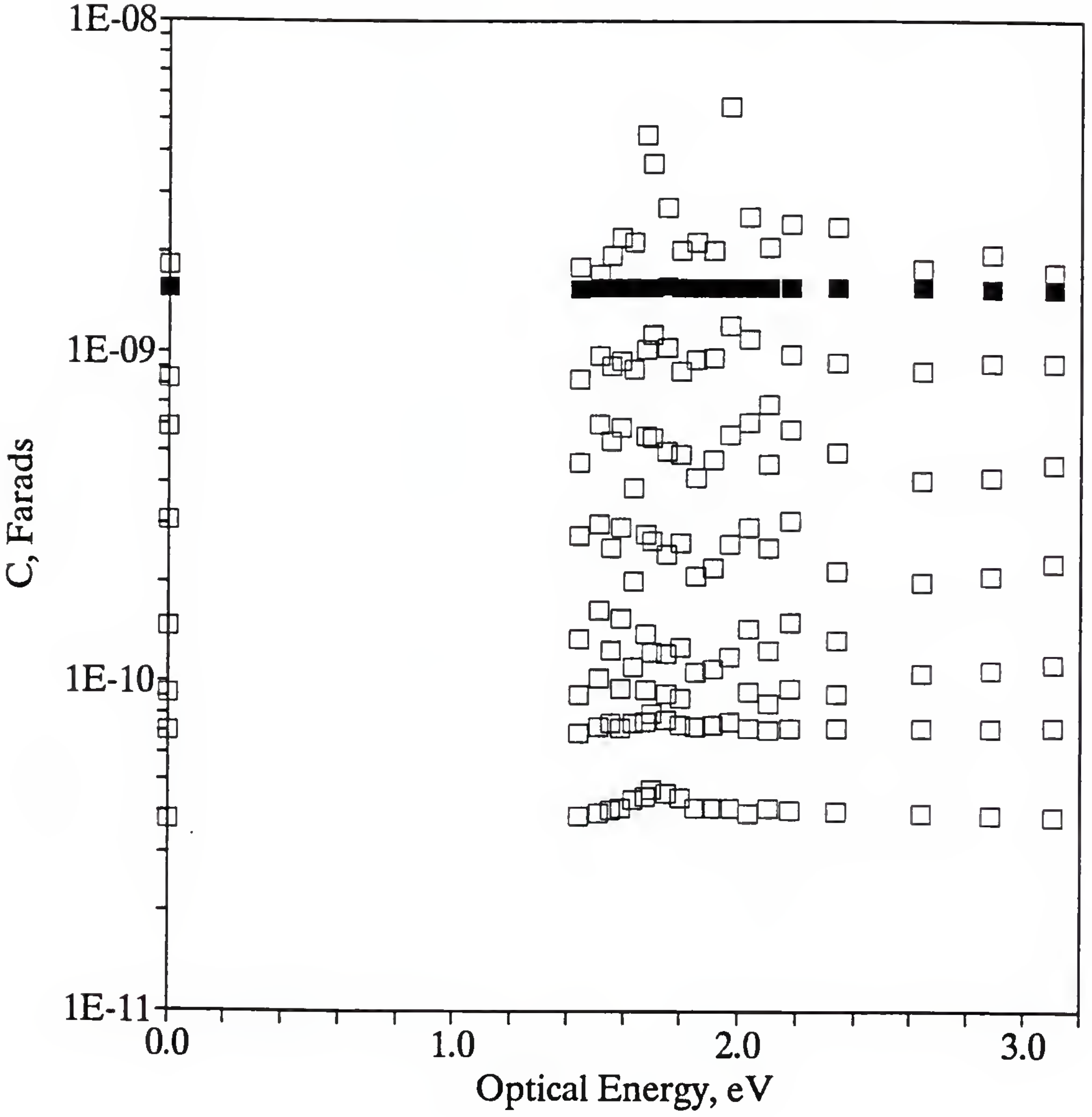

Figure 6.46: Capacitances from regression of simplified equivalent circuit to impedance data as a function of inverse temperature for the unaged ZnO varistor.

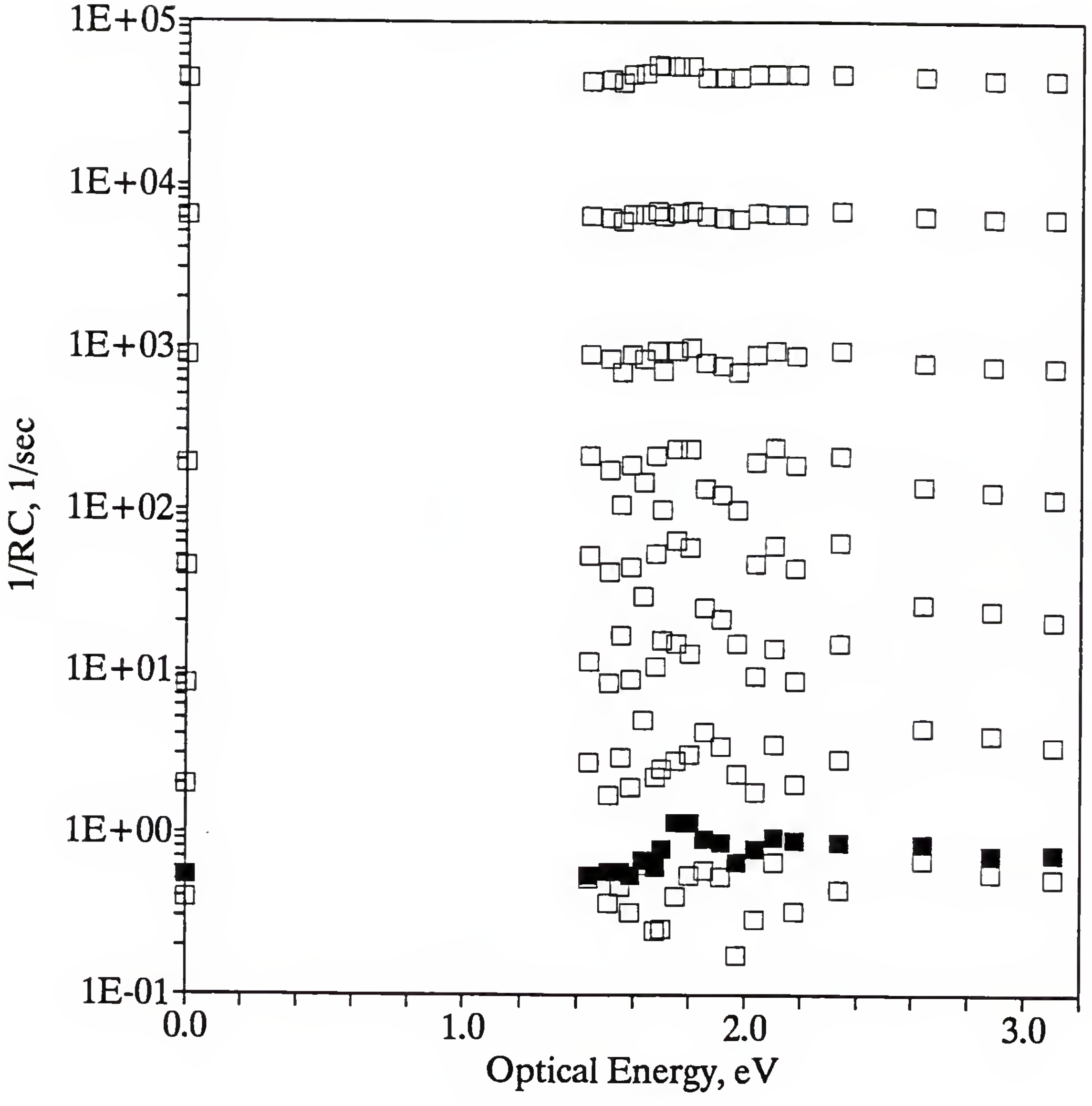

Figure 6.47: Equivalent circuit characteristic frequencies from regression of simplified equivalent circuit to impedance data as a function of inverse temperature for the unaged ZnO varistor.

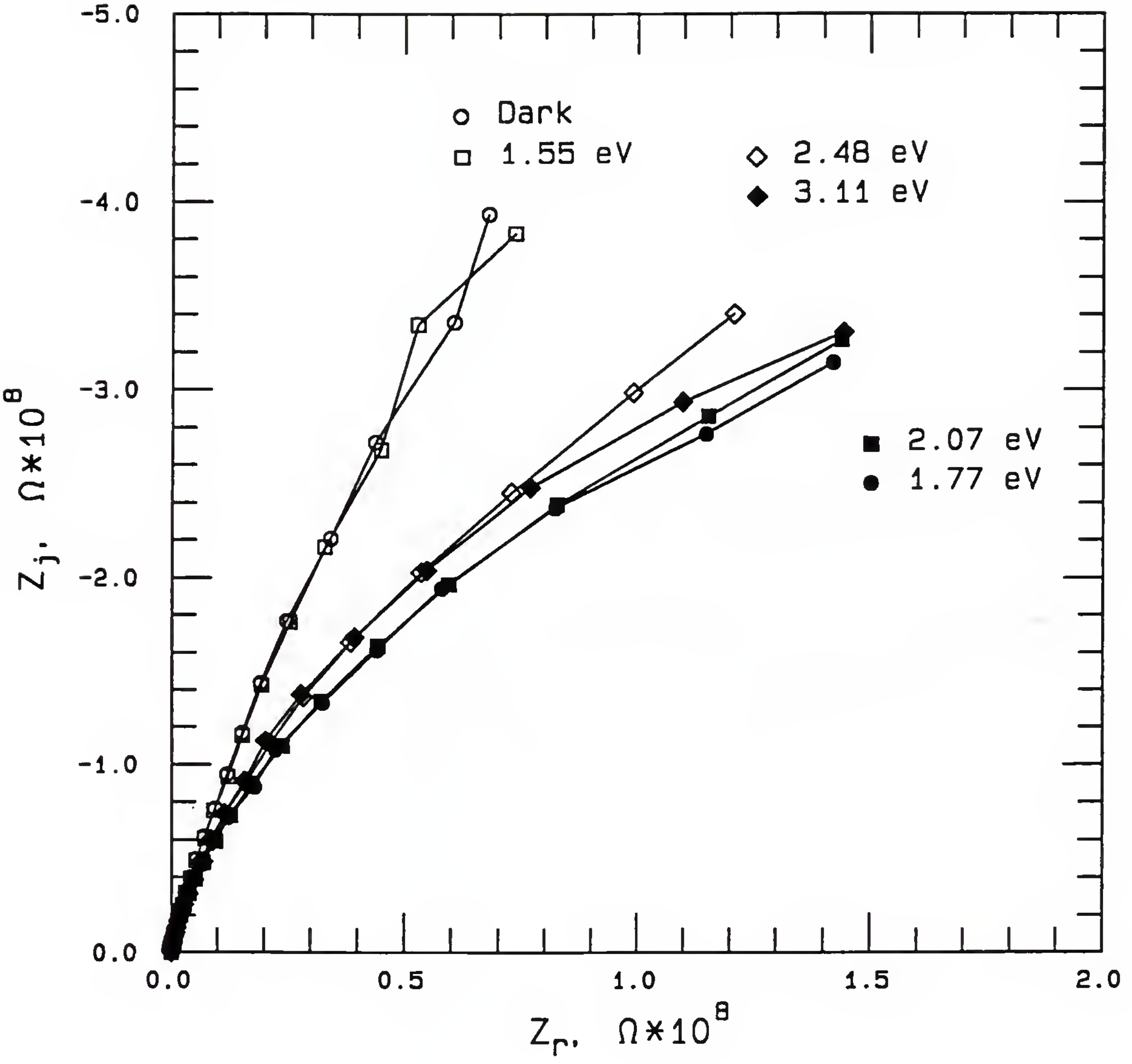

Figure 6.48: Imaginary component of the impedance as a function of the real component of the impedance for frequencies ranging from 1500 to 0.2 Hz with optical energy as a parameter for the unaged ZnO varistor annealed at 600°C.

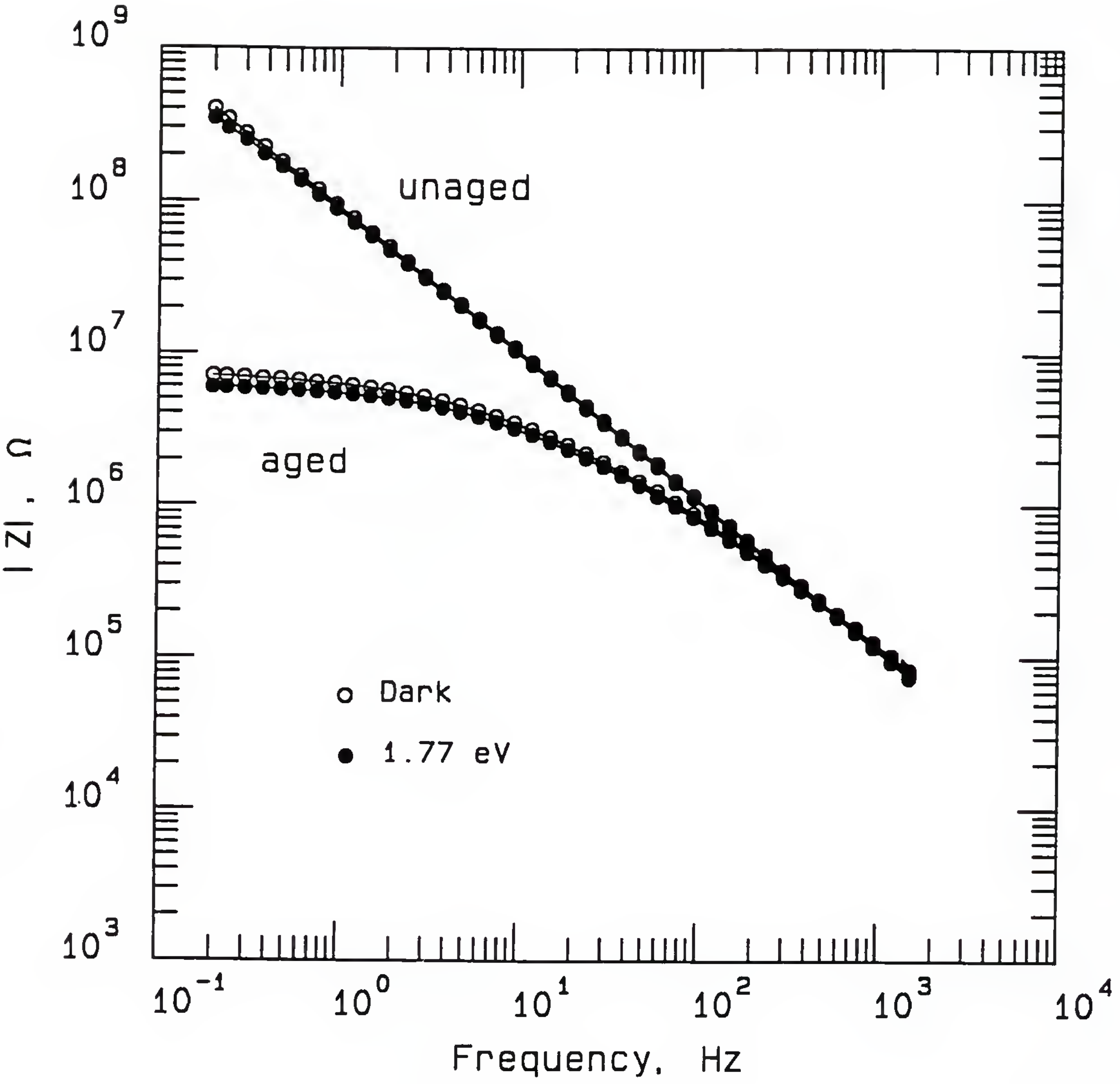

Figure 6.49: Total impedance as a function of frequency under no illumination and illumination of 1.77 eV for the aged and unaged ZnO varistors annealed at 600°C.

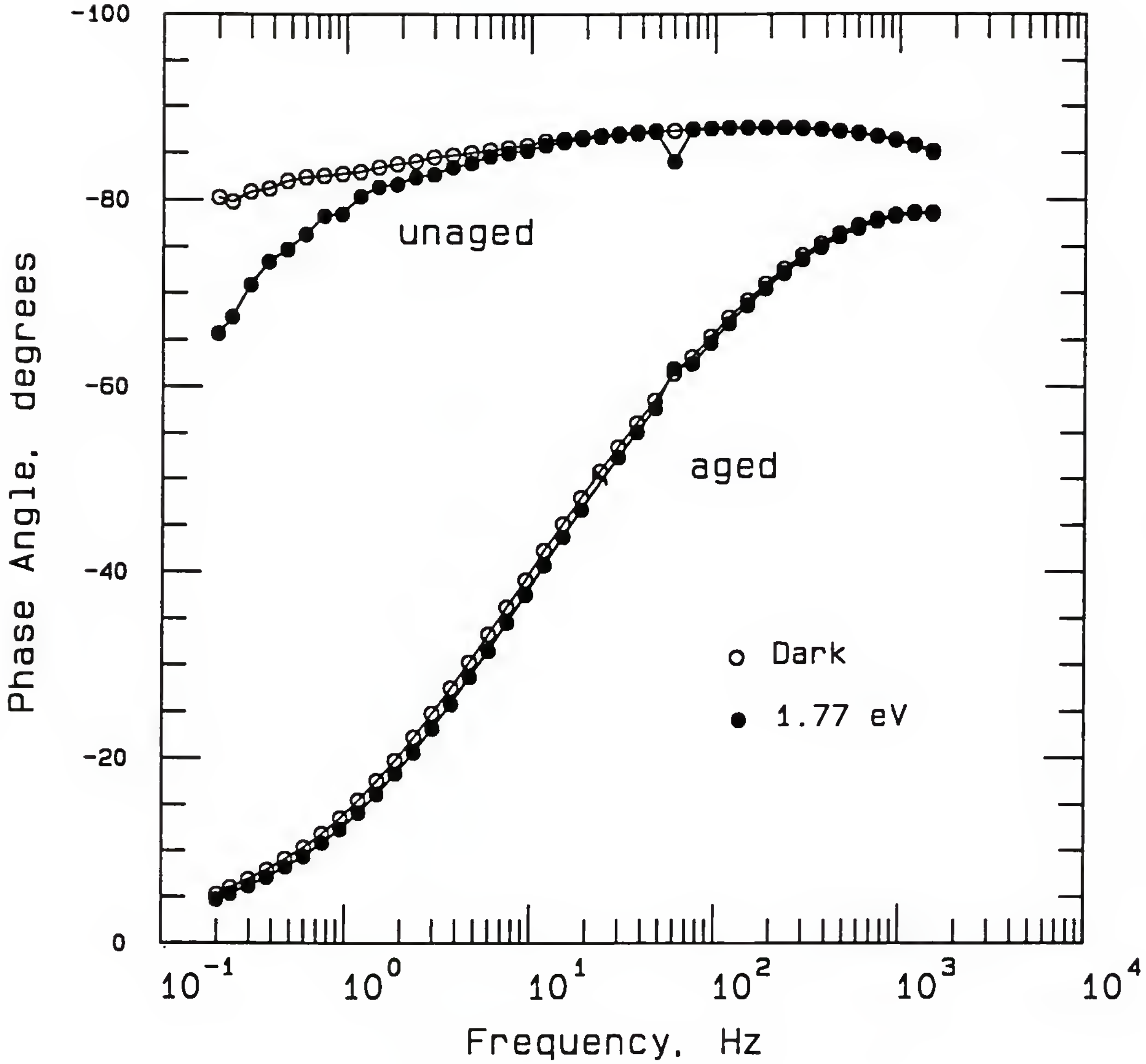

Figure 6.50: Phase angle as a function of frequency under no illumination and illumination of 1.77 eV for the aged and unaged ZnO varistors annealed at 600°C.

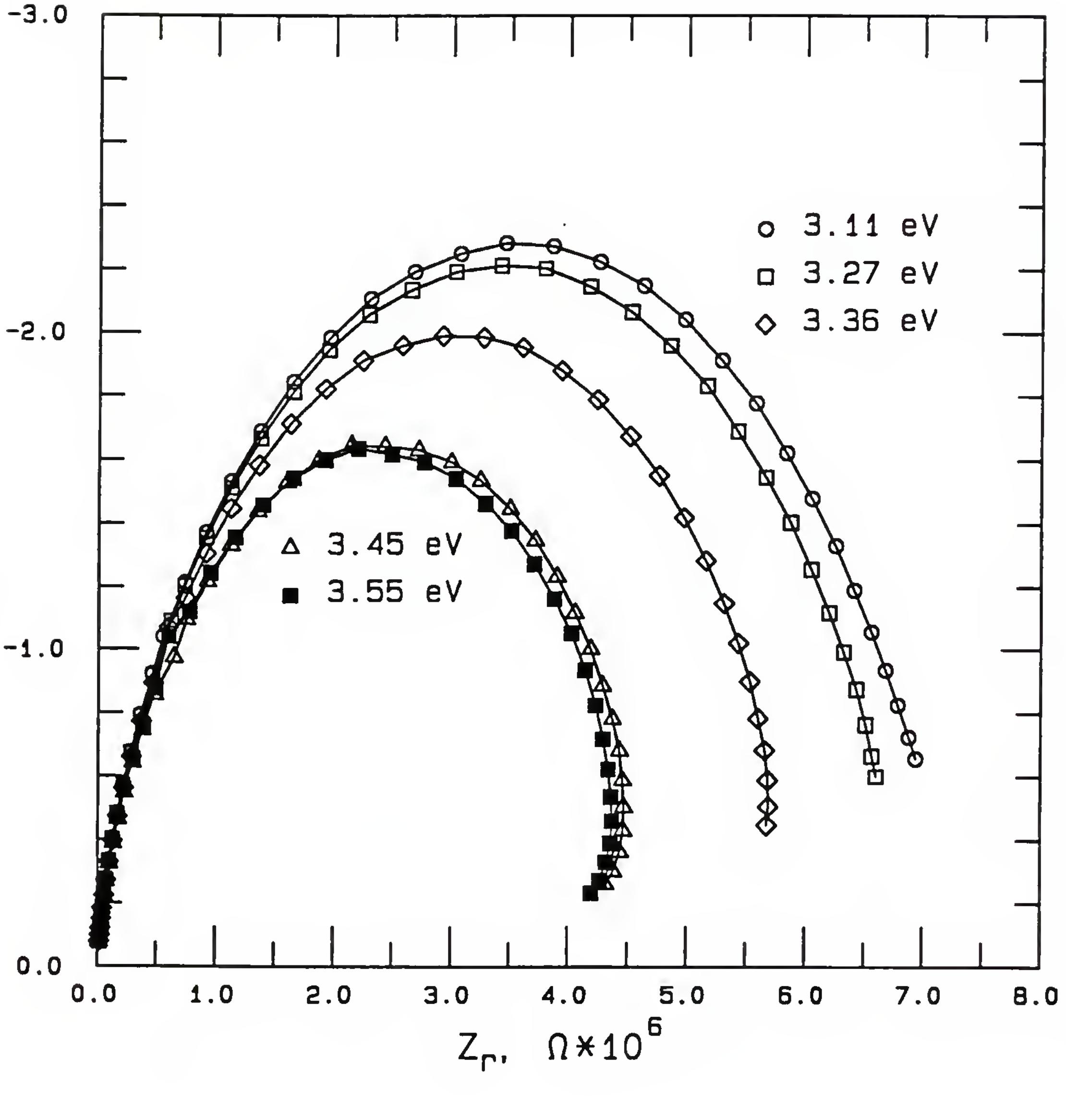

Figure 6.51: Imaginary component of the impedance as a function of the real component of the impedance for frequencies ranging from 1500 to 0.2 Hz with optical energy near the bandgap as a parameter for the aged ZnO varistor.

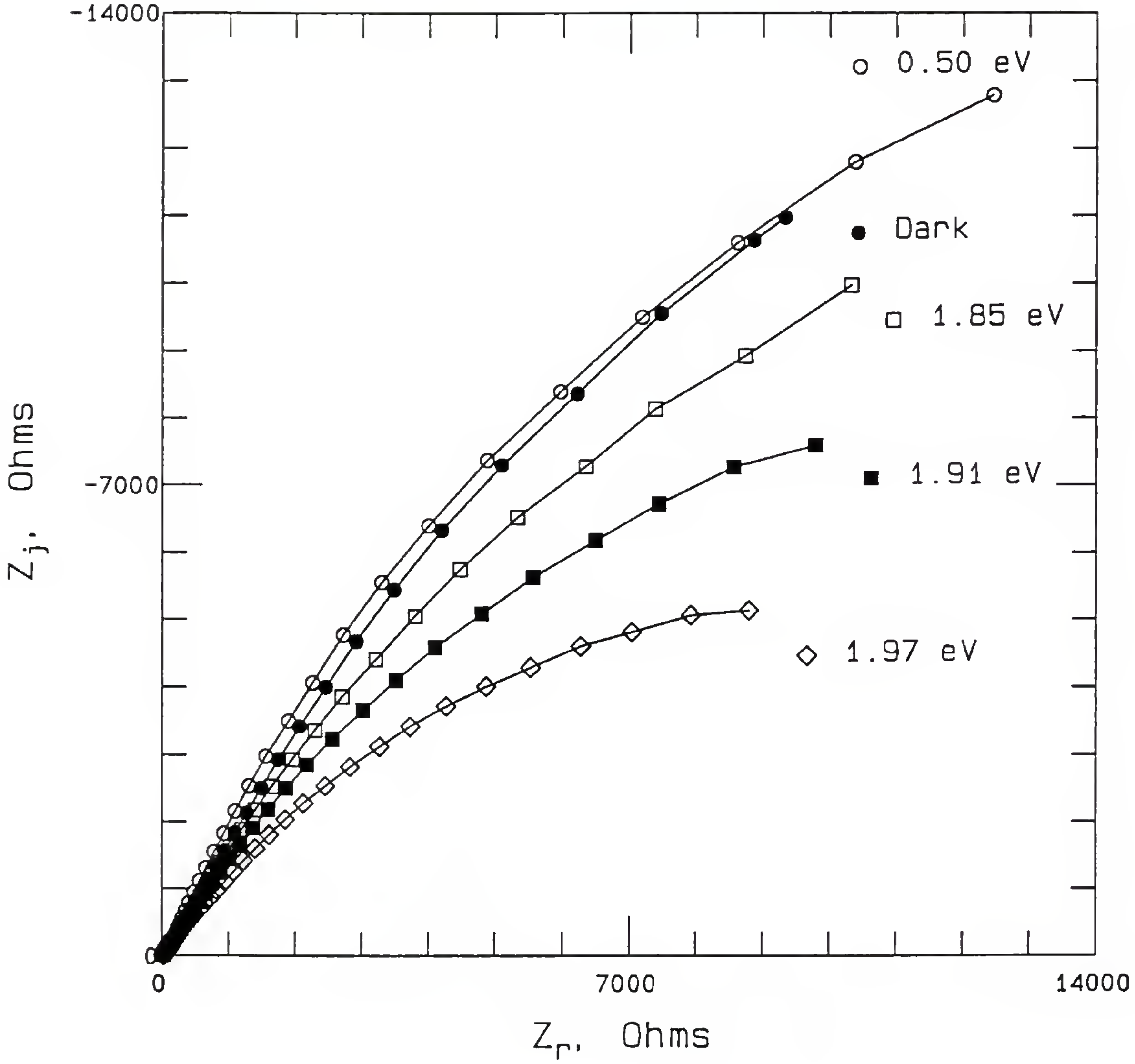

Figure 6.52: Imaginary component of the impedance as a function of the real component of the impedance for frequencies ranging from 65000 to 0.1 Hz with optical energy as a parameter for cuprous oxide (aged in light) in alkaline–chloride solution.

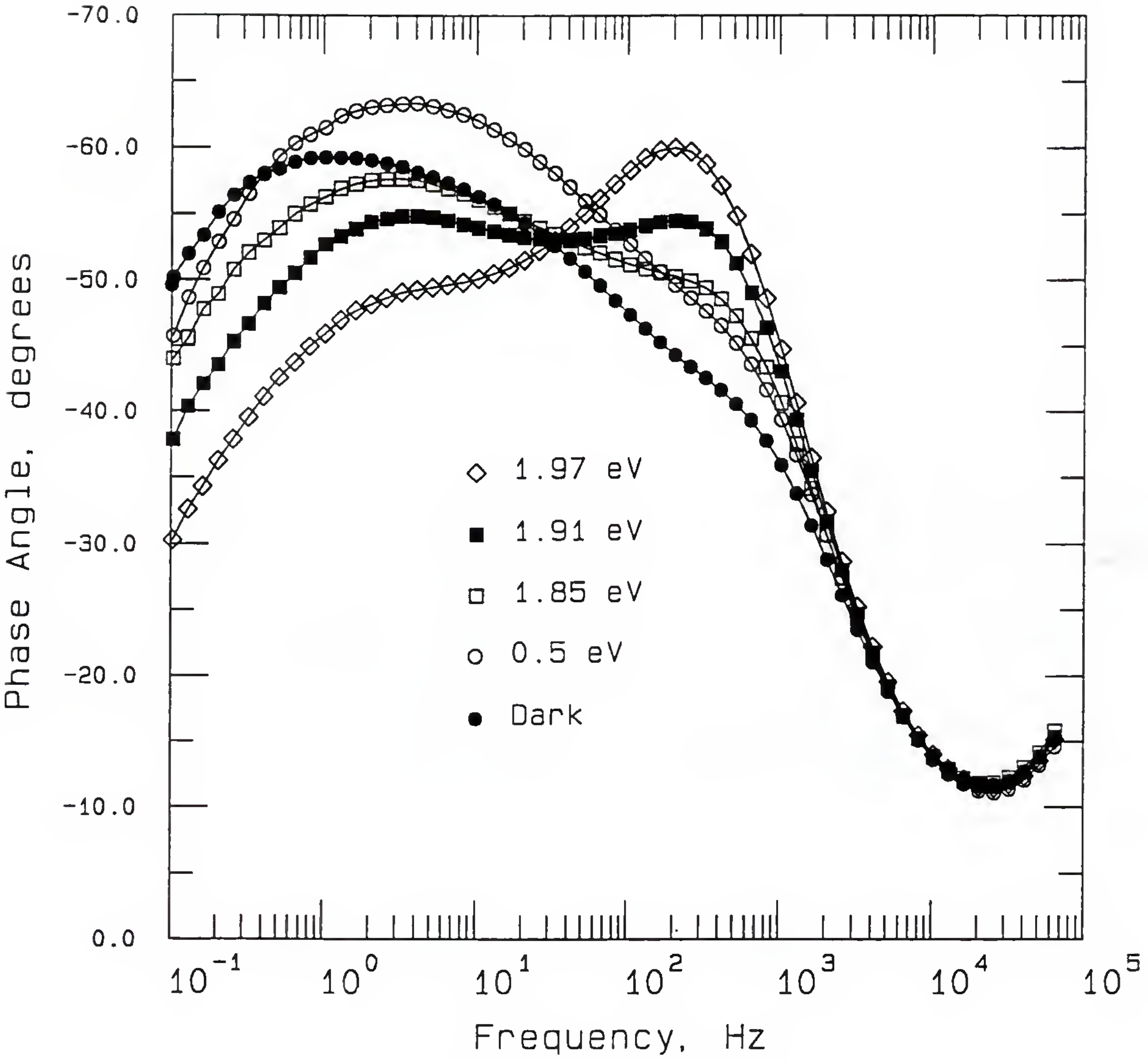

Figure 6.53: Phase angle as a function of frequency with optical energy as a parameter for cuprous oxide (aged in light) in alkaline–chloride solution.

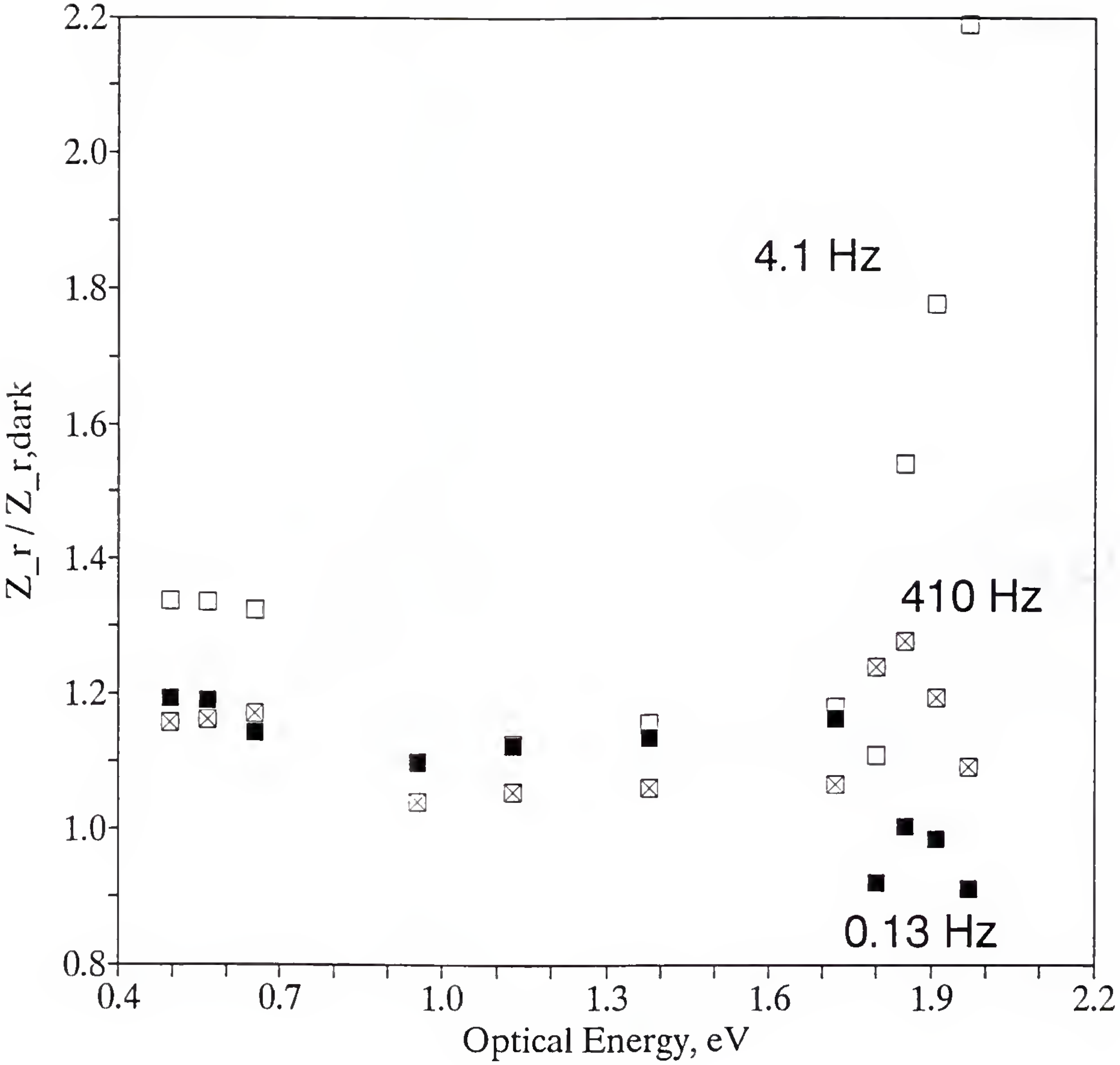

Figure 6.54: Dimensionless real component of the impedance as a function of optical energy with electrical frequency as a parameter for cuprous oxide (aged in light) in alkaline-chloride solution.

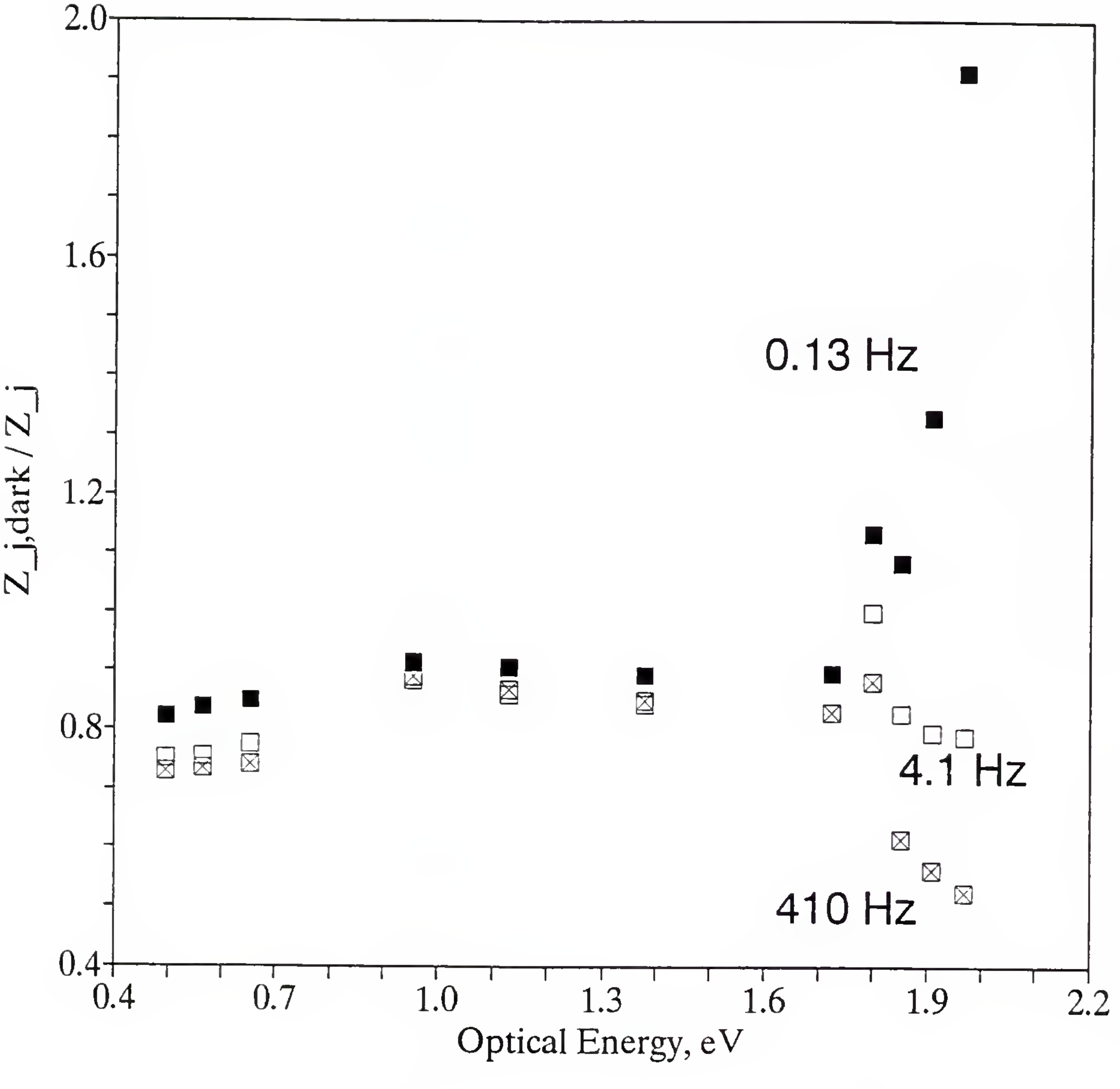

Figure 6.55: Dimensionless imaginary component of the impedance as a function of optical energy with electrical frequency as a parameter for cuprous oxide (aged in light) in alkaline–chloride solution.

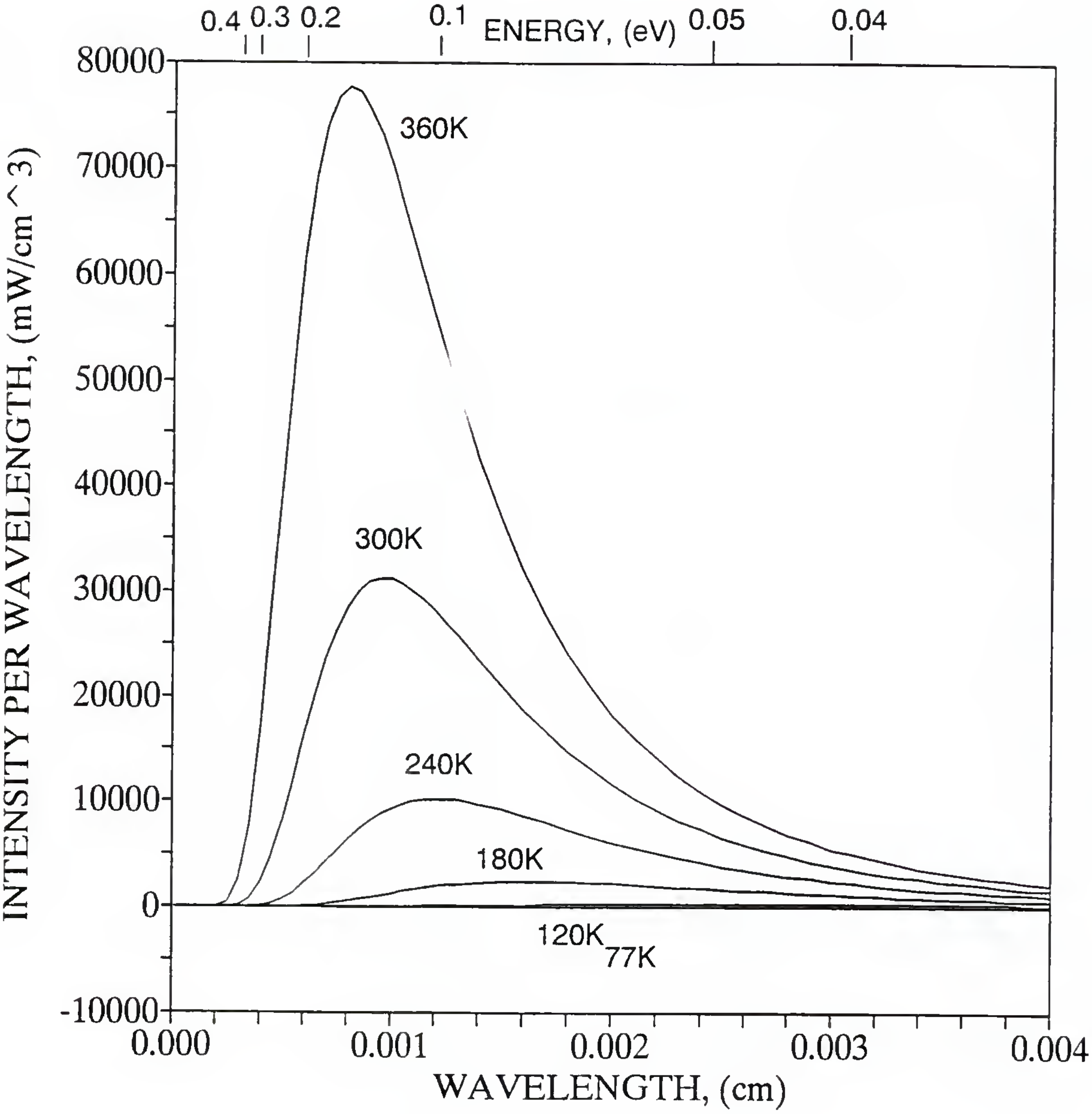

Figure 6.56: Black body radiation intensity per wavelength as a function of wavelength with temperature as a parameter, from Planck distribution law.

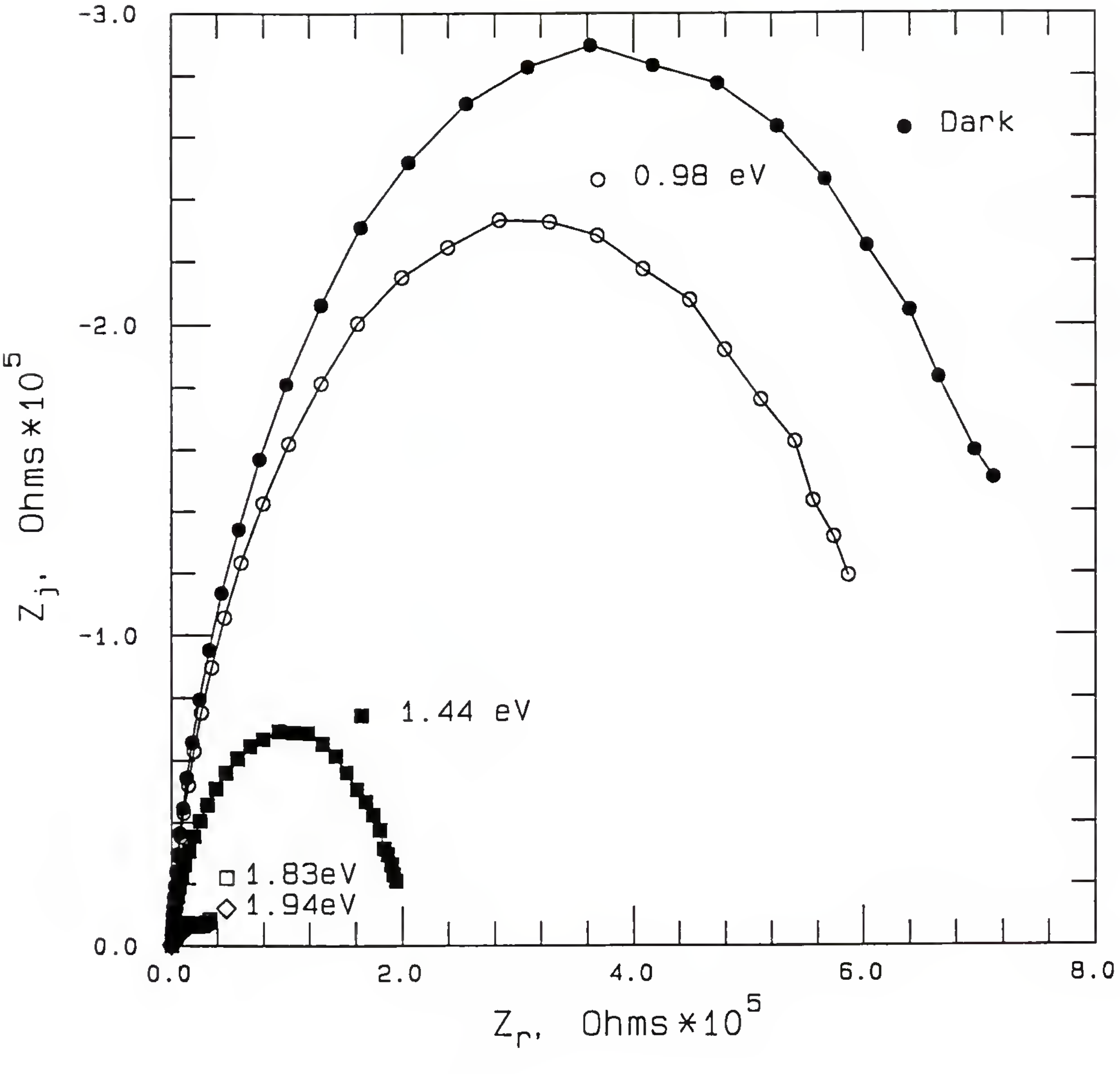

Figure 6.57: Imaginary component of the impedance as a function of the real component of the impedance for frequencies ranging from 10000 to 0.2 Hz with optical energy as a parameter for cuprous oxide (aged in dark) in alkaline–chloride solution.

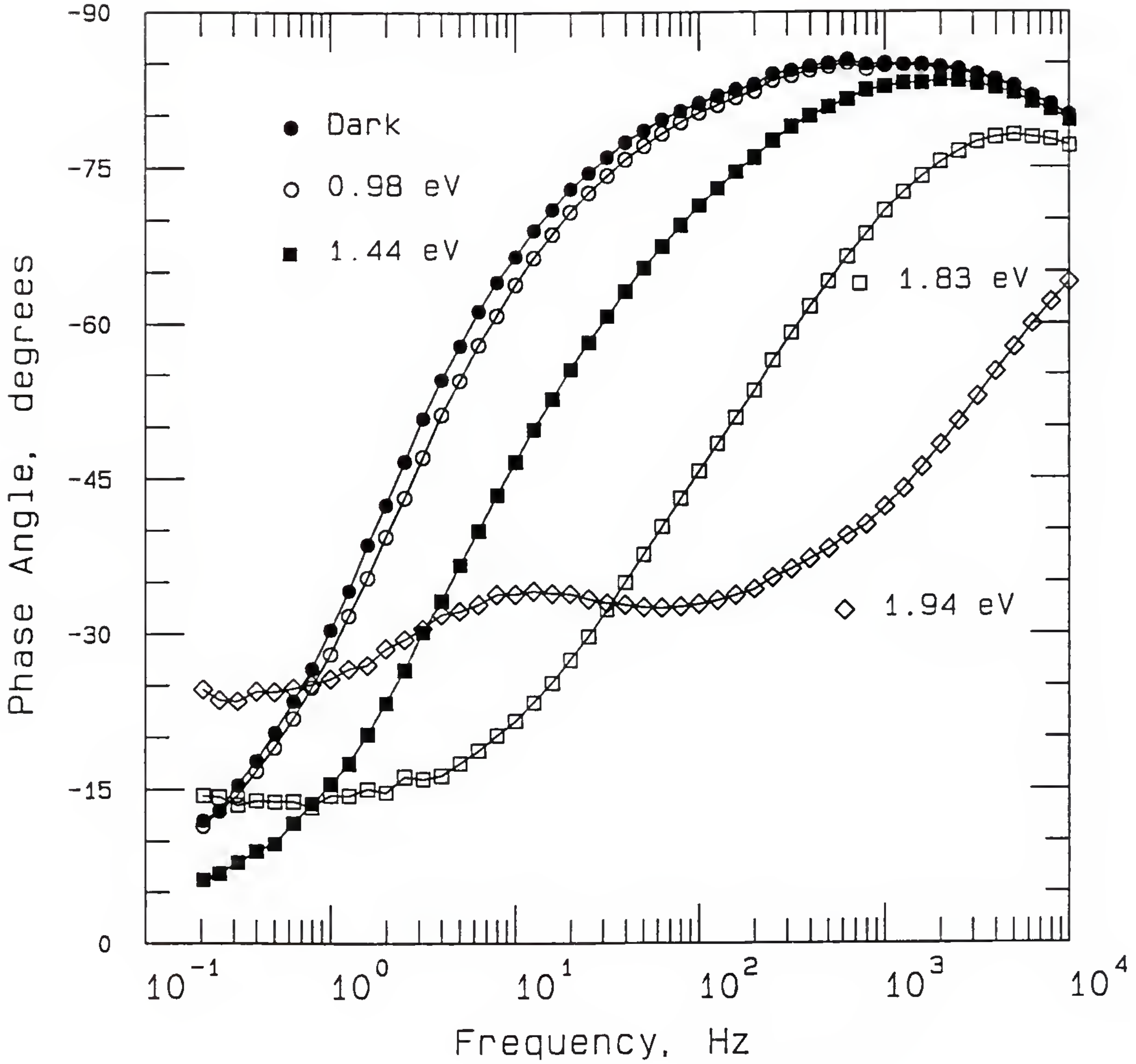

Figure 6.58: Phase angle as a function of frequency with optical energy as a parameter for cuprous oxide (aged in dark) in alkaline–chloride solution.

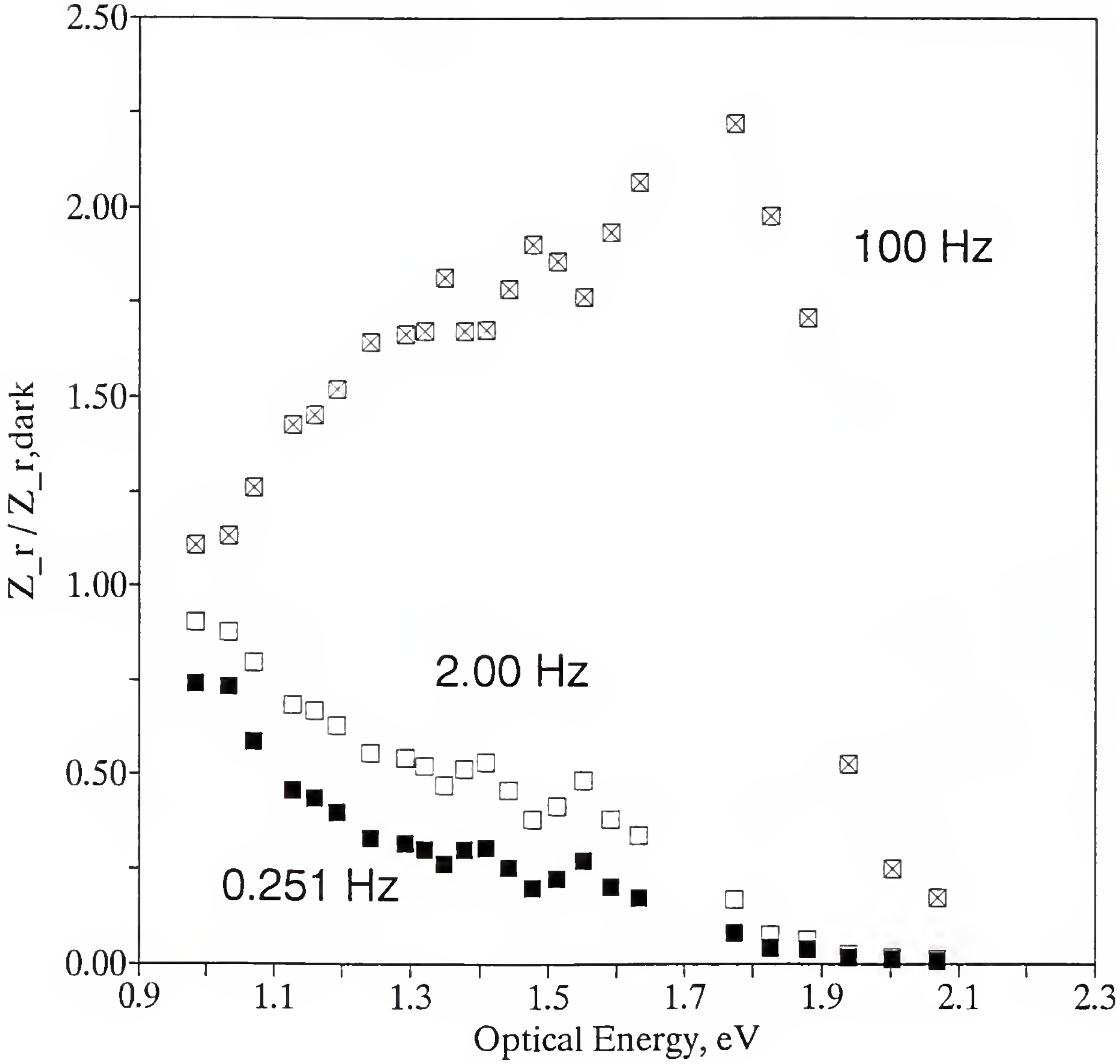

Figure 6.59: Dimensionless real component of the impedance as a function of optical energy with electrical frequency as a parameter for cuprous oxide (aged in dark) in alkaline–chloride solution.

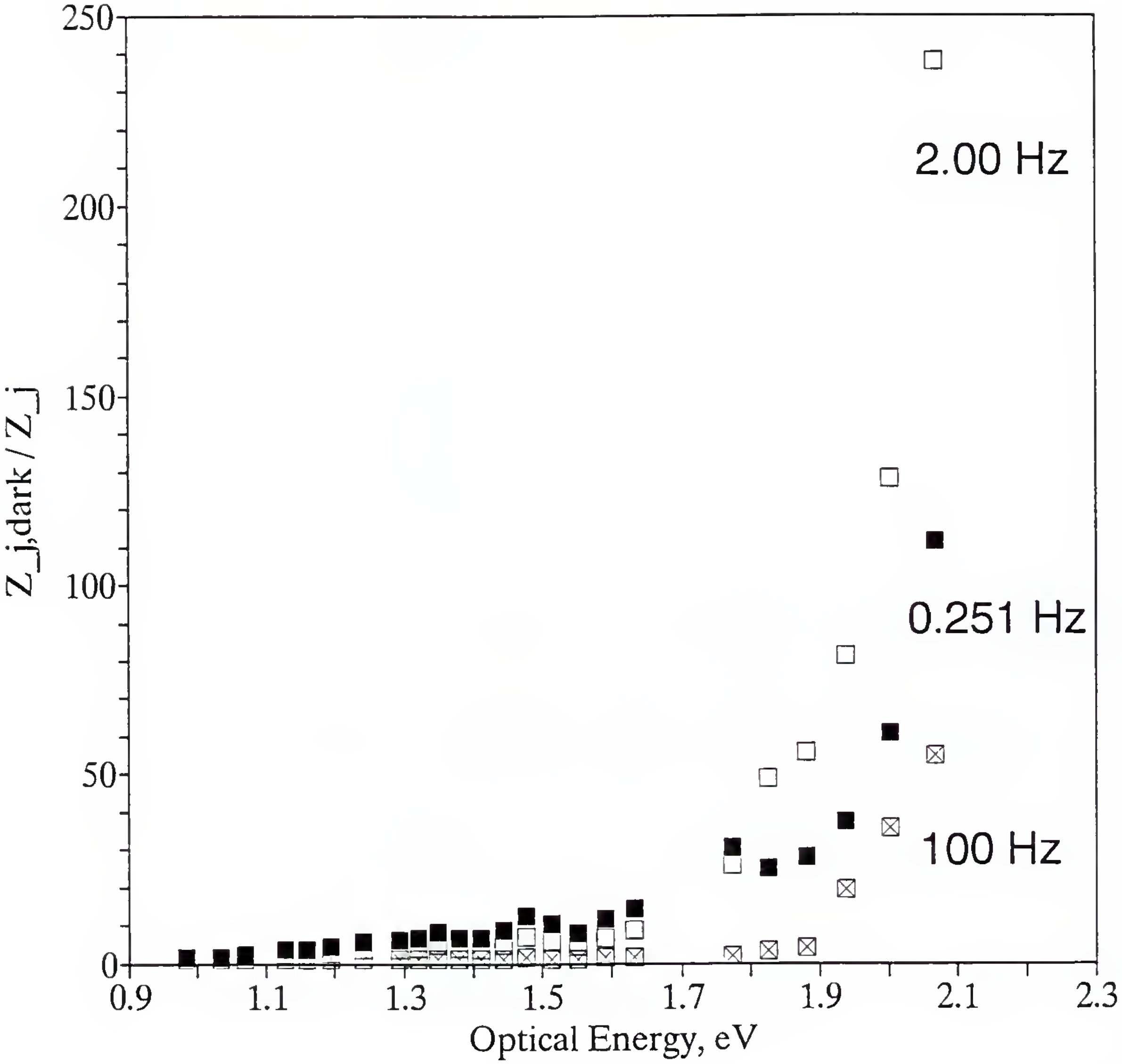

Figure 6.60: Dimensionless imaginary component of the impedance as a function of optical energy with electrical frequency as a parameter for cuprous oxide (aged in dark) in alkaline–chloride solution.

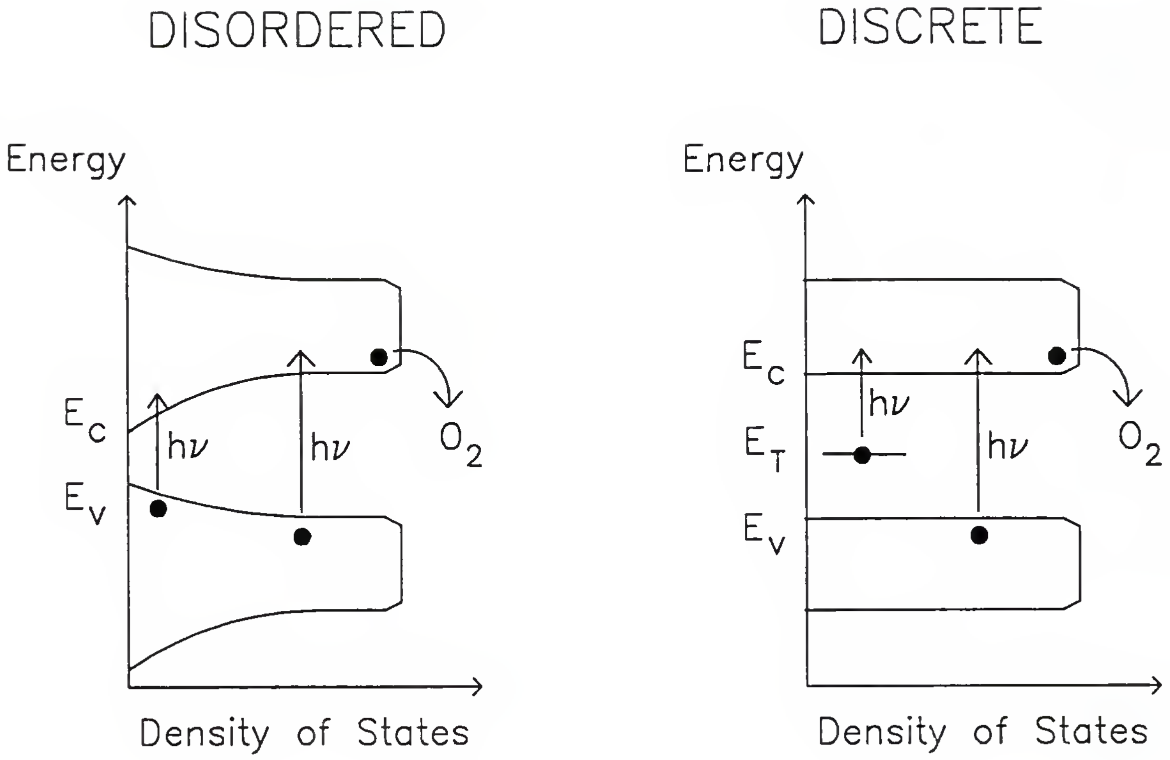

Figure 6.61: Density of states as a function of energy for a disordered semiconductor (left) and a crystalline semiconductor with a discrete state (right).

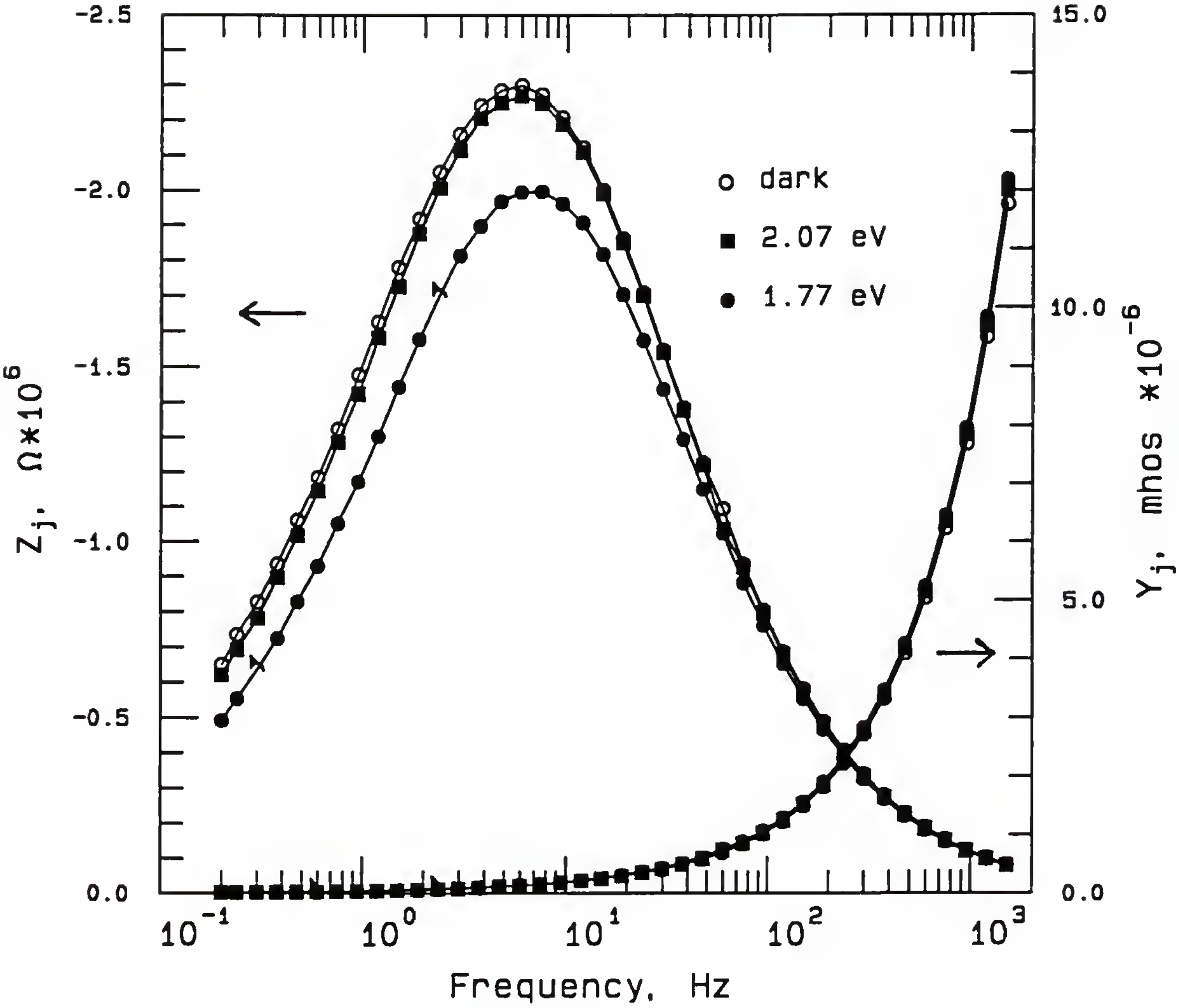

Figure 6.62: Imaginary component of the impedance and of the admittance as a function of electrical frequency with optical energy as a parameter for the aged ZnO varistor.

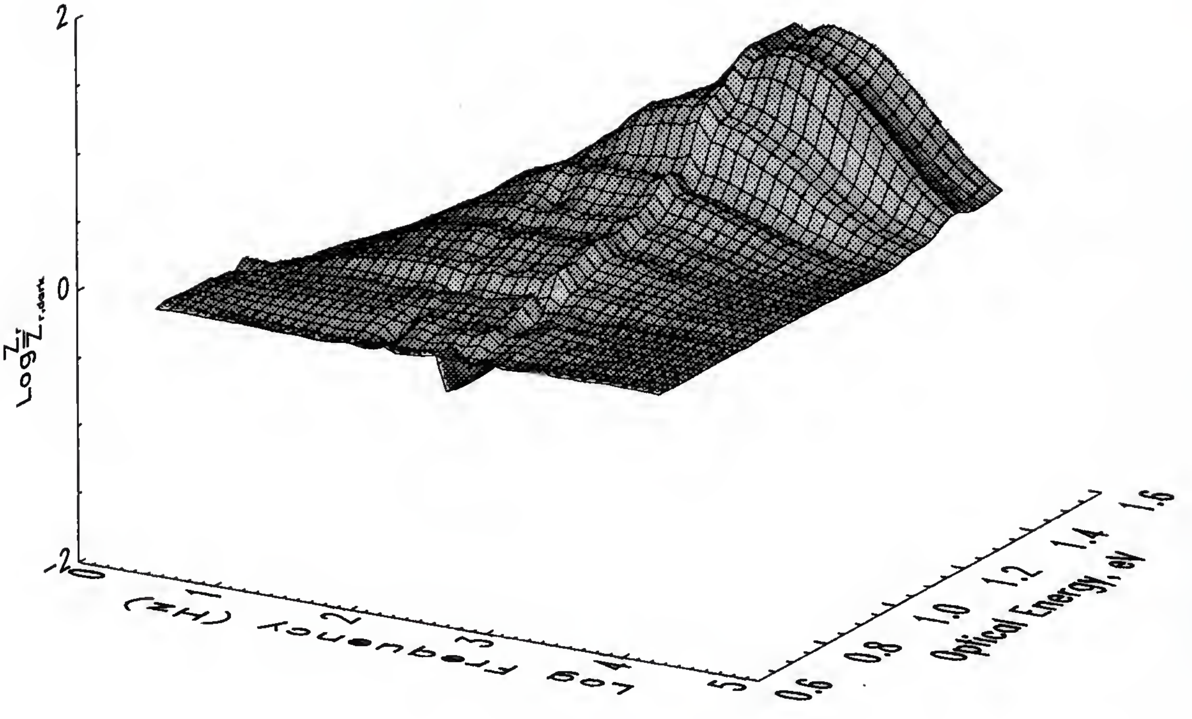

Figure 6.63: Dimensionless real component of the impedance as a function of optical energy and electrical frequency for n–type GaAs with Schottky contact.

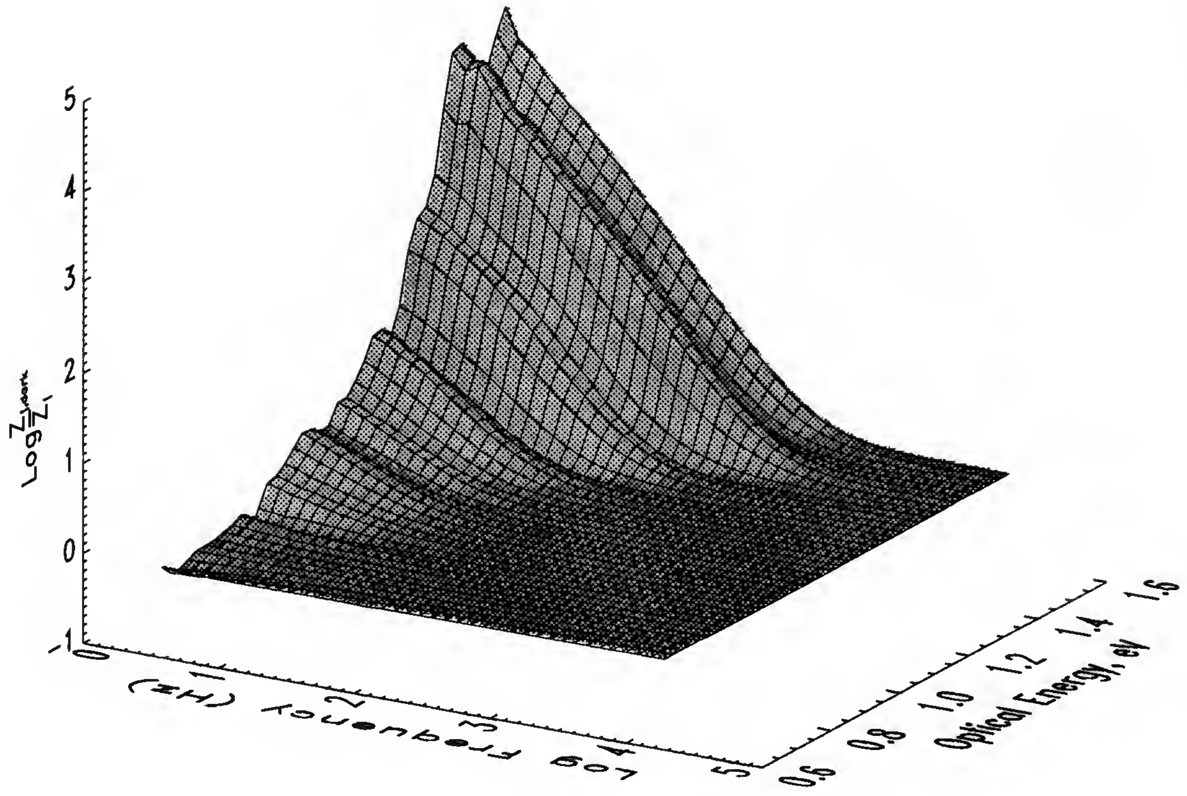

Figure 6.64: Dimensionless imaginary component of the impedance as a function of optical energy and electrical frequency for n–type GaAs with Schottky contact.

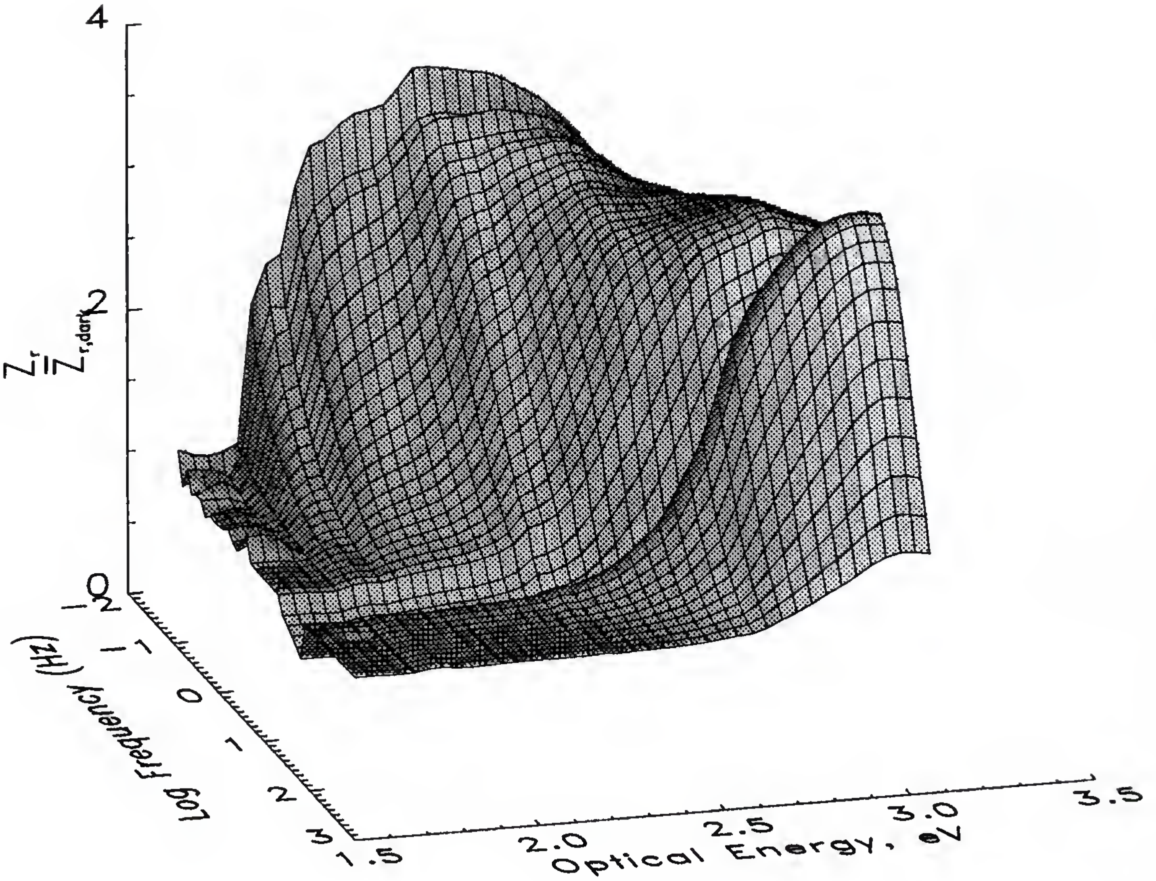

Figure 6.65: Dimensionless real component of the impedance as a function of optical energy and electrical frequency for the ZnS:Mn electroluminescent panel.

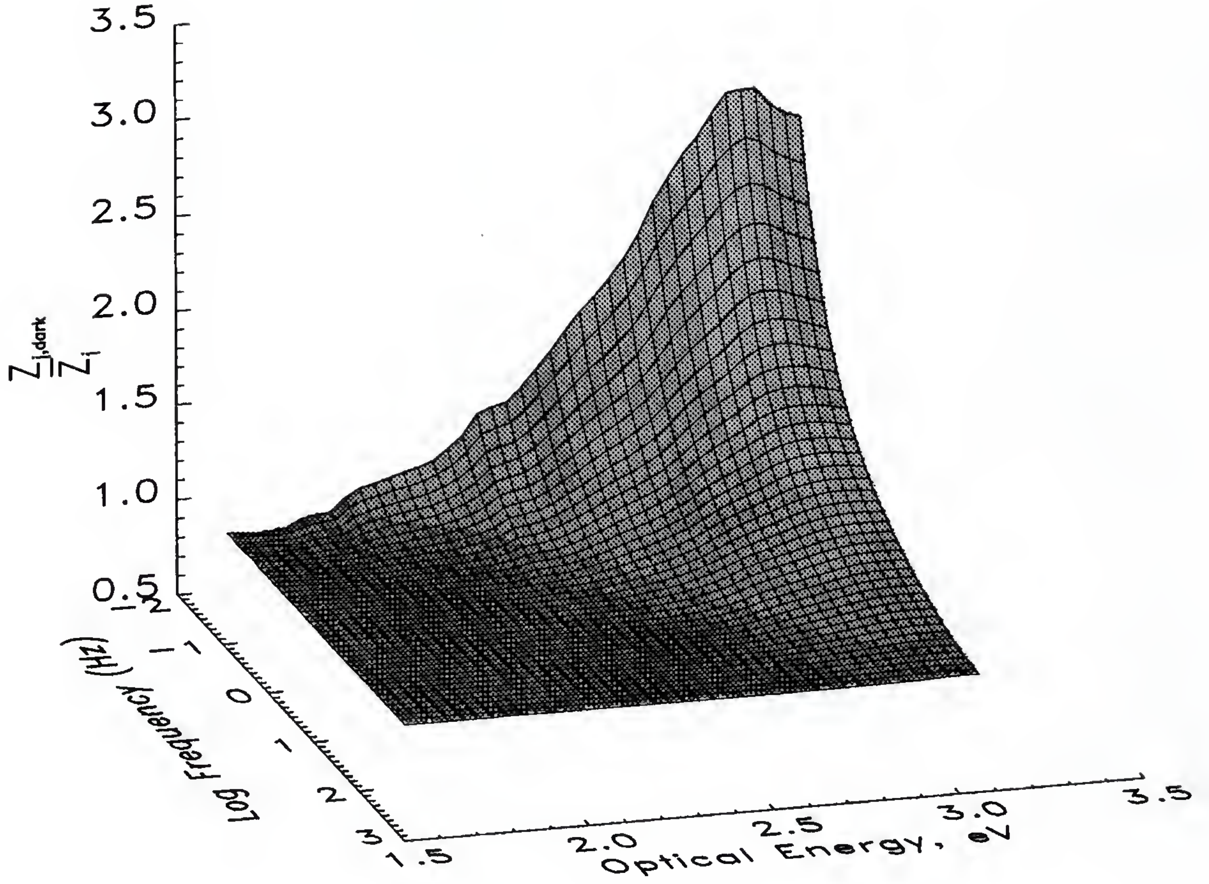

Figure 6.66: Dimensionless imaginary component of the impedance as a function of optical energy and electrical frequency for the ZnS:Mn electroluminescent panel.

CHAPTER 7
CONCLUSIONS

Optically Stimulated Deep–Level Impedance Spectroscopy (OS–DLZS) can be a useful technique to analyze deep–level electronic transitions in semiconductors. This technique can be performed at room temperatures and at low applied potentials even if the device is highly capacitive. Electronic transitions were more clearly observed with this technique at low electrical frequencies than at high frequencies typical of most impedance techniques. Thermally Stimulated Deep–Level Impedance Spectroscopy (TS–DLZS) was also shown to be a powerful tool in the analysis of deep–level transitions. This technique is ideal for determining thermal activation energies. Its advantage over the more common DLTS technique is the use of a wide range of continuous electrical frequencies.

An equivalent circuit derived from the governing equations for electrons, holes, and deep–level states was proven to be valid. The equivalent circuit was regressed to the thermal impedance data and also to the optical impedance data. Valuable information was extracted from regression of the impedance data such as activation energies and concentrations. A comparison was made to DLTS results.

The EL2 state in single–crystal gallium arsenide was observed in both OS–DLZS and TS–DLZS techniques. The thermal activation energy and the optical energy were found to be approximately the same with a value around 0.8 eV below the conduction band. It was found that ZnS:Mn thin film electroluminescent panels were highly capacitive in nature and exhibited the presence of at least six distinct electronic transitions. These transitions were pronounced in the resistances and capacitances from the nonlinear regression. Unaged ZnO varistors were also highly capacitive and exhibited an electronic state near the middle of the bandgap. When the ZnO varistor was aged, the impedance decreased by two orders of magnitude and the electronic state near the middle of the bandgap underwent a redistribution.

CHAPTER 8

SUGGESTIONS FOR FUTURE WORK

Improvements in this work can be divided into three categories: equipment, samples, and model. An upgrade in impedance equipment is needed to analyze high resistivity semiconductors. In almost all of semiconductor samples studied, the impedance was in the range of several hundred million ohms. This value is much greater than the measuring resistances of either potentiostat. Solartron Instruments (division of Schlumberger) is now selling the 1260 Impedance/Gain–Phase Analyser. This analyser is capable of applying a potential bias and perturbation, and most importantly, current measurements are made within the analyser. A potentiostat is no longer required to measure the voltage and current signals. The 1260 can also be used in a two electrode cell configuration; ideal for solid state analysis. It can measure resistances greater than 100 MΩ and apply frequencies up to 32 MHz.

A higher impedance range will enable low temperature analysis of the GaAs sample. Low temperature experiments were not feasible with the present equipment and GaAs sample because of a poor signal to noise ratio. The effects of higher energy states can be 'frozen out' by going to lower temperatures as is done is DLTS and AS. For instance, a plot of the peak imaginary impedance for the GaAs data as a function of inverse temperature (300K to 420K) results in an activation energy of 0.85 eV. This is the energy of the EL2 state. It would be interesting to see if this activation energy becomes 0.3 eV and 0.5 eV in lower temperature ranges corresponding to the two lower energy states found in DLTS. Admittance Spectroscopy (AS) suggests they would.

The optical section of the equipment setup could also be improved. A beam splitter is needed so that intensity measurements of the applied light beam can be measured before each experiment. It was estimated through experiments that the error in light intensity was 22 percent. It should also be determined if the intensity is uniform over the illuminated area. Improvements in the resolution of the wavelength could be made with smaller slit widths, however, the intensity would decrease. A laser system would provide high resolution, but would operate in narrow regions of the optical spectrum.

A bulk grown GaAs sample was used in this work because it was expected to have an EL2 state (0.83 eV). This state could be excited with the present optical equipment. However, this state is a defect state, not a chemical species in which the concentration can be controlled. A semiconductor sample should be found with a dopant species that lies deep within the bandgap. Changes in the concentration can be related to changes in the impedance response. A good candidate for this is gold doped silicon which has a donor level at 0.35 eV above the valence band. Note that silicon is an indirect semiconductor. Gold doped silicon was studied in the literature [118–121].

The concentration of shallow level dopant species should be kept low enough that the assumption of non–degeneracy holds. The Fermi level should be approximately 4kT below the conduction band (for n–type semiconductor) which is 0.1 eV at room temperature. The GaAs sample used in this work is only 1.5kT below the conduction band. However, the impedance increases as the concentration of free carriers decreases. The higher impedance might be out of the impedance range of the present equipment.

The observation that the leakage resistance has a thermal activation energy close to the EL2 energy for the GaAs sample should be better explained. Experiments should be tried with a large reverse bias. Hopefully, this will reduce the influence of the leakage resistance in the data. Impedance scans as a function of biasing can also be used to identify surface states from bulk states.

The mathematical model could be improved by relaxing some of the assumptions made in its development. For instance, the equivalent circuit in Figure 4.5 could be tried. Allowing the capture and emission of the minority carrier species could also be included. These transitions are included in the complete equivalent circuit, but not in the reduced circuits. It was assumed that the current generator terms could be ignored due to the equilibrium assumption. This assumption might not hold for the impedance data taken under optical excitation.

APPENDIX
PROGRAM FOR DLTS INTERFACE

```
TYPE REGTYPE
  AX AS INTEGER
  BX AS INTEGER
  CX AS INTEGER
  DX AS INTEGER
  BP AS INTEGER
  SI AS INTEGER
  DI AS INTEGER
  FLAGS AS INTEGER
  DS AS INTEGER
  ES AS INTEGER
END TYPE
DECLARE SUB INTERRUPT (INTM AS INTEGER, INREGS AS REGTYPE,
          OUTREGS AS REGTYPE)
DIM INREGS AS REGTYPE, OUTREGS AS REGTYPE
DIM VALUE!(4800, 2)
CONST FALSE = 0, TRUE = NOT FALSE
COMMON SHARED IBSTA%, IBERR%, IBCNT%
SAVDT = FALSE
L = 1
XLABEL$ = "TEMPERATURE, K"
YLABEL$ = "DEL CAPACITANCE|pf"
```

```
'Input temperature controller parameters
INPUT "SELECT CONTROL MODE (0-LOCAL 1-REMOTE 2-REMOTE
W/LLK)[1]",M$
IF M$ = "" THEN B$ = B$ + "M1" ELSE B$ = B$ + "M" + M$
INPUT "SELECT DISPLAY SENSOR: A OR B [B] ", F1$
IF F1$ = "" THEN B$ = B$ + "F1B" ELSE B$ = B$ + "F1" + F1$
INPUT "SELECT SET POINT (0 TO 799.9) [300] ", S$
IF S$ = "" THEN B$ = B$ + "S300" ELSE B$ = B$ + "S" + S$
INPUT "SELECT PROPORTIONAL GAIN (0.1 TO 99.0) [2] ", P$
IF P$ = "" THEN B$ = B$ + "P2" ELSE B$ = B$ + "P" + P$
INPUT "SELECT INTEGRAL RESET (0.0 TO 99.0) [2.0] ", I$
IF I$ = "" THEN B$ = B$ + "I2.0" ELSE B$ = B$ + "I" + I$
INPUT "SELECT HEATER RANGE (2-OFF 3-100mA 4-330mA 5-1A) [2] ", R$
IF R$ = "" THEN B$ = B$ + "R2" ELSE B$ = B$ + "R" + R$
INPUT "WHAT IS THE MINIMUM TEMPERATURE [80] ", MIN$
IF MIN$ = "" THEN
MIN$ = "80"
END IF
INPUT "WHAT IS THE MAXIMUM TEMPERATURE [300] ", MAX$
IF MAX$ = "" THEN
MAX$ = "300"
END IF
'Input deep-level spectrometer parameters
INPUT "ENTER CAPACITANCE METER RANGE (10,30,100,300,1000) ", RANGE!
INPUT "ENTER PRE-AMP GAIN (1, 3, 10, 30, 100, 300, 1000) ", PREAMP!
INPUT "DO YOU WANT TO SAVE THIS DATA (Y OR N)? [N] ", SAV$
```

```
IF UCASE$(SAV$) = "Y" THEN
 INPUT "ENTER DATA FILE NAME WITHOUT SUFFIX [TEMP.DLT] ", DATA$
   IF DATA$ = "" THEN DATA$ = "TEMP"
 SAVDT = TRUE
END IF
'Initialize IEEE address for HP7090A Measurement Plotting System
HEWPK$ = "DEV5"
CALL IBFIND(HEWPK$, HEWPK%)
'Initialize IEEE address for the LakeShore Temperature Controller
TEMP$ = "DEV12"
CALL IBFIND(TEMP$, TEMP%)
'Setup Graph
SCREEN 4
CLS
X1! = VAL(MIN$)
Y1! = -RANGE! / PREAMP!
X2! = VAL(MAX$)
Y2! = RANGE! / PREAMP!
VIEW (50, 10)-(590, 340), 0, 1
WINDOW (X1!, Y1!)-(X2!, Y2!)
LINE (X1!, Y1!)-(X1!, Y2!)
LINE (X1!, 0)-(X2!, 0), , , &H8888
DELY! = (Y2! - Y1!) / 10!
DELX! = (X2! - X1!) / 10!
FOR I% = 0 TO 10
LINE (X1!, Y1! + I% * DELY!)-(X1! + .1 * DELX!, Y1! + I% * DELY!)
LINE (X1! + I% * DELX!, Y1!)-(X1! + I% * DELX!, Y1! + .1 * DELY!)
NEXT I%
LOCATE 24, 30
PRINT XLABEL$;
LOCATE 3, 1
FOR I% = 1 TO 18
  PRINT MID$(YLABEL$, I%, 1)
  LOCATE 3 + I%, 1
NEXT I%
LOCATE 1, 1
PRINT Y2!;
LOCATE 22, 1
PRINT Y1!;
LOCATE 23, 6
PRINT X1!;
LOCATE 23, 73
PRINT X2!;
'Collect Data
B$ = B$ + CHR$(13) + CHR$(10)
H$ = "D01,1,0,0;SD0.05;IR10.0;QD;" + CHR$(13) + CHR$(10)
CALL IBWRT(TEMP%, B$)
A$ = SPACE$(100)
LOCATE 24, 2
PRINT "PRESS ANY KEY TO ABORT";
DO WHILE INKEY$ = ""
'Collect data from the temperature controller
```

```
        TMP$ = ""
        B$ = "WS" + CHR$(13) + CHR$(10)
        CALL IBWRT(TEMP%, B$)
        CALL IBRD(TEMP%, A$)
          FOR I = 1 TO 100
          T$ = MID$(A$, I, 1)
          IF T$ = CHR$(13) THEN EXIT FOR
          TMP$ = TMP$ + T$
          NEXT I
        A$ = SPACE$(100)
'Collect data from the HP7090A
    CAPVOL$ = SPACE$(40)
    CALL IBWRT(HEWPK%, H$)
    CALL IBRD(HEWPK%, CAPVOL$)
    YVOLT! = VAL(CAPVOL$)
    DELC! = .2 * YVOLT! * RANGE! / PREAMP!
'Plot data on screen and save if so desired
 PSET (VAL(TMP$), DELC!)
 IF SAVDT THEN
    VALUE(L, 1) = VAL(TMP$)
    VALUE(L, 2) = DELC!
    L = L + 1
 END IF
'Pause for 0.5 seconds
' TMEPAS = FALSE
' INREGS.AX = &H2C00
' CALL INTERRUPT(&H21, INREGS, OUTREGS)
' TME = (OUTREGS.DX AND &HFF)
' DO
'   INREGS.AX = &H2C00
'   CALL INTERRUPT(&H21, INREGS, OUTREGS)
'   TMENEW = (OUTREGS.DX AND &HFF)
'   TMEDIF = TMENEW - TME
'   TMEPAS = (TMEDIF > 50) OR (TMEDIF < -50)
' LOOP UNTIL TMEPAS
'
'Pause for 1 second
 SLEEP 1
LOOP
  B$ = "M0" + "R2" + CHR$(13) + CHR$(10)
  CALL IBWRT(TEMP%, B$)
  LOCATE 24, 2
  PRINT "PRESS ANY KEY TO CONTINUE";
  DO UNTIL INKEY$ <> ""
  LOOP
'
'Store data to chosen file name
'
 IF SAVDT THEN
  FILNUM$ = DATA$ + ".DLT"
  OPEN FILNUM$ FOR OUTPUT AS #1
   FOR I = 1 TO L - 1
```

```
     PRINT #1, VALUE(I, 1), VALUE(I, 2)
   NEXT I
  CLOSE #1
 END IF
END
```

REFERENCES

[1] G. Nagasubramanian, B. L. Wheeler, G. A. Hope, and A. J. Bard, "Semiconductor Electrodes XLVII. A–C Impedance Techniques for Evaluating Surface–State Properties of n–$MoTe_2$ in Acetonitrile Solutions Containing Various Redox Couples," *J. Electrochemical Society,* **130** (1983), 385–391.

[2] G. Nagasubramanian, B. L. Wheeler, and A. J. Bard, "Semiconductor Electrodes XLIX. Evidence for Fermi Level Pinning and Surface–State Distributions from Impedance Measurements in Acetonitrile Solutions with Various Redox Couples," *J. Electrochemical Society,* **130** (1983), 1680-1688.

[3] R. Haak, C. Ogden, and D. Tench, "Electrochemical Photocapacitance Spectroscopy: A New Method for Characterization of Deep Levels in Semiconductors," *J. Electrochemical Society,* **129** (1982), 891–893.

[4] R. Haak and D. Tench, "Electrochemical Photocapacitance Spectroscopy Method for Characterization of Deep Level and Interface States in Semiconductor Materials," *J. Electrochemical Society,* **131** (1984), 275–283.

[5] P. Allongue and H. Cachet, "Photocapacitance Study of n–GaAs/Electrolyte Interfaces," *Ber. Bunsenges. Phys. Chem.,* **91** (1987), 386–390.

[6] M. Cocivera, W. M. Sears, and S. R. Morrison, "Photocapacitance Spectrography of Thin Film Cadmium Selenide Electrodes," *J. Electroanal. Chem.,* **216** (1987), 41–52.

[7] D. B. Bonham and M. E. Orazem, "A Mathematical Model for the AC Impedance of Semiconducting Electrodes," *AICHE Journal,* **34** (1988), 465–473.

[8] D. B. Bonham and M. E. Orazem, "A Mathematical Model for the Influence of Deep–Level Electronic States on Photoelectrochemical Impedance Spectroscopy: 2. Assessment of Characterization Methods Based on Mott–Schottky Theory," *J. Electrochemical Society,* **139** (1992), 127–131.

[9] D. B. Bonham and M. E. Orazem, "A Mathematical Model for the Influence of Deep–Level Electronic States on Photoelectrochemical Impedance Spectroscopy: 1. Theoretical Development," *J. Electrochemical Society,* **139** (1992), 118–126.

[10] M. E. Orazem, "The Impedance Response of Semiconductors: An Electrochemical Engineering Perspective," *Chemical Engineering Education,* **W** (1990), 48–55.

[11] E. Escalante and J. Kruger, "Stress Corrosion Cracking of Pure Copper," *J. Electrochemical Society*, **118** (1971), 1062–1066.

[12] J. Joffe, "Schottky's Theories of Dry Solid Rectifiers," *Electrical Communication,* **22** (1945), 217–225.

[13] R. DeGryse, W. P. Gomes, F. Cardon, and J. Vennik, "On the Interpretation of Mott–Schottky Plots Determined at Semiconductor/Electrolyte Systems," *J. Electrochemical Society,* **122** (1975), 711–712.

[14] J. D. Cohen and D. V. Lang, "Calculation of the Dynamic Response of Schottky Barriers with a Continuous Distribution of Gap States," *Physical Review,* **B25** (1982), 5321–5350.

[15] M. Derdouri, L. Mahdjoubi, and M. Benmalek, "Analysis of Admittance Spectroscopy Method for the Study of Deep–Levels," *Solid–State Electronics,* **25** (1982), 925–931.

[16] M. R. H. Khan and M. Saji, "Comparative Study of Admittance Spectroscopy and DLTS in Determining Trap Levels of CdTe–ZnTe Heterojunctions," *Solid–State Electronics,* **29** (1986), 253–256.

[17] L. C. Isett, "Characterization of CdS/CdTe Thin–Film Solar Cells by Admittance Spectroscopy and Deep–Level Transient Spectroscopy," *J. Applied Physics,* **56** (1984), 3508–3517.

[18] S. M. So, W. Hwang, P. V. Meyers, and C. H. Liu, "Defect Levels in Electrodeposited n–type CdTe Thin–Films," *J. Applied Physics,* **61** (1987), 2234–2243.

[19] D. V. Lang, "Deep–level Transient Spectroscopy: A New Method to Characterize Traps in Semiconductors," *J. Applied Physics,* **45** (1974), 3023–3032.

[20] S. Dueñas, M. Jaraiz, J. Vicente, E. Rubio, L. Bailón, and J. Barbolla, "Optical Admittance Spectroscopy: A New Method for Deep Level Characterization," *J. Applied Physics,* **61** (1987), 2541–2545.

[21] S. Dueñas, E. Castán, A. de Dios, L. Bailón, J. Barbolla, and A. Pérez, "Characterization of the EL2 center in GaAs by Optical Admittance Spectroscopy," *J. Applied Physics,* **67** (1990), 6309–6314.

[22] C. Gabrielli, "Identification of Electrochemical Processes by Frequency Response Analysis," Technical Report Number 004/83, *Solartron Instruments, Division of Schlumberger Technologies*, 829 Middlesex Turnpike, P.O. Box 7004, Billerica, MA 01821–7004, 1–800–225–5765 (1983).

[23] N. D. Cogger, "The Measurement of Signals From Electrochemical Phenomena," Technical Report Number 014/84, *Solartron Instruments, Division of Schlumberger Electronics (UK) Ltd.*, Victoria Road, Farnborough, Hampshire GU14 7PW England, Telephone: Farnborough (0252) 544433 (1984).

[24] R. Haberman, *Elementary Applied Partial Differential Equations*, Second Edition, Prentice–Hall, Inc., Englewood Cliffs, NJ (1987).

[25] R. J. Smith, *Circuits, Devices, and Sytems*, Fourth Edition, John Wiley & Sons, New York (1984).

[26] ZPLOT Electrochemical Impedance Software, Version 1.60, Scribner Associates, Inc., 1415 West Leigh Drive, Charlottesville, VA 22901, (804) 977–5521 (1991).

[27] 1286 Electrochemical Interface Operating Manual (1985), Solartron Instruments, Division of Schlumberger Technologies, 829 Middlesex Turnpike, P.O. Box 7004, Billerica, MA 01821–7004, 1–800–225–5765.

[28] Model 273 Potentiostat/Galvanostat Operating Manual (1985), EG&G Princeton Applied Research, P.O. Box 2565, Princeton, NJ 08540, (609) 452–2111.

[29] 1250 Frequency Response Analyzer Operating Manual (1985), Solartron Instruments, Division of Schlumberger Technologies, 829 Middlesex Turnpike, P.O. Box 7004, Billerica, MA 01821–7004, 1–800–225–5765.

[30] A. P. Malvino, *Electronic Principles*, Third Edition, McGraw–Hill, New York, 1984.

[31] ZFIT–A Shell For The CNLS Modeling Program, Scribner Associates, Inc., 1415 West Leigh Drive, Charlottesville, VA 22901, (804) 977–5521. CNLS program developed and owned by Dr. J. Ross MacDonald, Chapel Hill, North Carolina (1990).

[32] 1250 series Frequency Response Analyzer brochure, SI/DYN/031/Issue6/1.84, *Solartron Instruments, Division of Schlumberger Electronics (UK) Ltd.*, Victoria Road, Farnborough, Hampshire GU14 7PW England, Telephone: Farnborough (0252) 544433 (1984).

[33] V. Marrello, W. Rühle, and A. Onton, "The Memory Effect of ZnS:Mn AC Thin–Film Electroluminescence," *Applied Physics Letters*, **31** (1977), 452–454.

[34] V. Marrello and A. Onton, "Dependence of Electroluminescence Efficiency and Memory Effect on Mn Concentration in ZnS:Mn ACTEL Devices," *IEEE Transactions on Electron Devices*, **ED-27** (1980), 1767–1770.

[35] W. E. Howard, "Memory in Thin–Film Electroluminescent Devices," *J. Luminescence*, **23** (1981), 155–173.

[36] S. M. Sze, *Physics of Semiconductor Devices*, 2nd Edition, John Wiley & Sons, Inc., New York, 1981.

[37] B. L. Wheeler, G. Nagasubramanian, and A. J. Bard, "Semiconductor Electrodes LVII. Differential Photocurrent and Second Harmonic Techniques for in situ Monitoring of Surface States on n–MoSe$_2$ in Aqueous Solutions," *J. Electrochemical Society,* **131** (1984), 2289–2294.

[38] G. Nogami, "Some Aspects of Large Frequency Dispersion of Mott–Schottky Plots in TiO_2 Electrodes," *J. Electrochemical Society*, **132** (1985), 76–81.

[39] G. Nogami, R. Shiratsuchi, H. Nakamura, and H. Taniguchi, "The Influence of an Electrolyte on Impedance Characteristics in n–GaP Electrodes," *J. Electrochemical Society*, **132** (1985), 1663–1666.

[40] L. D. Yau and C. T. Sah, "Thermal Ionization Rates and Energies of Electrons and Holes at Silver Centers in Silicon," *Physica Status Solidi A*, **6** (1971), 561–573.

[41] D. V. Lang, "Fast Capacitance Transient Apparatus: Application to ZnO and O centers in GaP p–n Junctions," *J. of Applied Physics*, **45** (1974), 3014–3022.

[42] Hewlett–Packard 7090A Measurement Plotting System, Interfacing and Programming Manual (1984), HEWLETT–PACKARD, 16399 West Bernardo Drive, San Diego, CA 92127–1899.

[43] Remote Operation, Section IV of Operations Manual for Model 805 Temperature Controller, Lake Shore Cryotronics, Inc., 64 East Walnut Street, Westerville, OH 43081, (614) 891–2243.

[44] Short Form DLTS Operating Manual, Sula Technologies, P.O. Box 60903, Palo Alto, CA 94306, *Inquiries to:* Darwin Thusius (415) 694–7881 or (415) 284–2110.

[45] Operation & Maintenance Instructions, SPEX Industries, Inc., 3880 Park Avenue, Edison, NJ 08820, (201) 549–7144.

[46] W. Shockley and W. T. Read, Jr. "Statistics of the Recombination of Holes and Electrons," *Physical Review* **87** (1952), 835–842.

[47] R. N. Hall, "Electron–Hole Recombination in Germanium," *Physical Review* **87** (1952), 387.

[48] J. S. Blakemore, *Semiconductor Statistics*, Dover Publications, Inc., New York (1987).

[49] A. S. Grove, *Physics and Technology of Semiconductor Devices*, John Wiley and Sons, Inc. (1967), 131.

[50] W. Shockley, "Electrons, Holes, and Traps," *Proceedings of the IRE* **46** (1958), 973–990.

[51] C. T. Sah, "The Equivalent Circuit Model in Solid–State Electronics—Part I: The Single Energy Level Defect Centers," *Proceedings of the IEEE*, **55** (1967), 654–671.

[52] C. T. Sah, "The Equivalent Circuit Model in Solid–State Electronics—III: Conduction and Displacement Currents," *Solid–State Electronics*, **13** (1970), 1547–1575.

[53] C. T. Sah, *Fundamentals of Solid–State Electronics*, World Scientific Publishing Co., Singapore (1991), 276.

[54] C. T. Sah, "Theory of the Metal Oxide Semiconductor Capacitor," *Solid State Electronics Laboratory*, Technical Report No. **1**, *University of Illinois at Urbana–Champaign* (1964).

[55] E. H. Nicollian and A. Goetzberger, "The Si–SiO_2 Interface–Electrical Properties as Determined by the Metal-Insulator-Silicon Conductance Technique," *The Bell System Technical Journal*, **XLVI** (1967), 1055–1133.

[56] D. B. Bonham, Ph. D. Dissertation, Department of Chemical Engineering, University of Virginia, Charlottesville, VA (1988).

[57] M. Kazeminy and M. E. Orazem, "The Influence of Electrolytic Mass Transfer on the Performance of Photoelectrochemical Cells," *Chemical Engineering Communications*, **57** (1987), 335–349.

[58] C. T. Sah, "The Equivalent Circuit Model in Solid–State Electronics—Part II: The Multiple Energy Level Impurity Center," *Proceedings of the IEEE*, **55** (1967), 672–685.

[59] F. Hennig, "Emission and Capture of Electrons and Holes at Gold Centers in Silicon at Thermal Equilibrium," *Solid State Electronics Laboratory*, Technical Report No. **27**, *University of Illinois at Urbana–Champaign* (1974).

[60] C. T. Sah, R. N. Noyce, and W. Shockley, "Carrier Generation and Recombination in P–N Junctions and P–N Junction Characteristics," *Proceedings of the Institute of Radio Engineers*, **45** (1957), 1228–1243.

[61] T. Dickinson and R. Whitfield, "Some Experimental Factors Which Affect the Analysis of Impedance Measurements," *Electrochimica Acta*, **22** (1977), 385–389.

[62] A. van der Ziel, *Fluctuation Phenomena in Semi–Conductors*, Academic Press Incorporated, New York (1959), 22–45.

[63] A. van der Ziel, *Noise in Solid State Devices and Circuits*, John Wiley & Sons, New York (1986), 122–123.

[64] M. P. Dare–Edwards, A. Hamnett, and P. R. Trevellick, "Alternating–Current Techniques in Semiconductor Electrochemistry," *J. Chemical Society, Faraday Transactions*, **79** (1983), 2111–2124.

[65] L. H. Garcia–Rubio, Report in progress, Center for Materials Development, University of South Florida, Tampa, FL 33620.

[66] P. Agarwal, M. E. Orazem, and L. H. Garcia–Rubio, "Measurement Models for Electrochemical Impedance Spectroscopy–I. Demonstration of Applicability," *J. Electrochemical Society* **139** (1992), 1917–1927.

[67] J. J. Moré, "The Levenberg–Marquardt Algorithm: Implementation and Theory," in *Numerical Analysis*, G. A. Watson, editor, Lecture Notes in Math. 630, Springer–Verlag Berlin (1977), 105–116.

[68] J. R. Macdonald, "Complex Nonlinear Least Squares Immittance Fitting Program: LOMFP," University of North Carolina, Chapel Hill, NC (1988).

[69] J. S. Blakemore (editor), "Key Papers in Physics: Gallium Arsenide," Published by *American Institute of Physics*, Number **1**, New York (1987).

[70] G. M. Martin, A. Mitonneau, and A. Mircea, "Electron Traps in Bulk and Epitaxial GaAs Crystals," *Electronics Letters*, **13** (1977), 191-192.

[71] S. S. Li and R. Y. Loo, "Deep–level Defects and Numerical Simulation of Radiation Damage in GaAs Solar Cells," *Solar Cells*, **31** (1991), 349–377.

[72] E. R. Weber, K. Khachaturyan, M. Hoinkis, and M. Kaminska, "Point Defects in GaAs," *Point and Extended Defects in Semiconductors,* G. Benedek, A. Cavallini, and W. Schröter (editors), Plenum Press, New York (1989), 39–50.

[73] H. Uchiike, "Review of Flat Panel Displays: Electroluminescent Displays, Liquid Crystal Displays, Plasma Displays, etc.," *Electroluminescence,* Springer Proceedings in Physics, Volume **38**, Springer–Verlag Berlin, Heidelberg (1989), 238–245.

[74] A. G. Fischer, "Electroluminescent Lines in ZnS Powder Particles II. Models and Comparison with Experience," *J. Electrochemical Society*, **110** (1963), 733–748.

[75] D. H. Smith, "Modeling A.C. Thin–Film Electroluminescent Devices," *J. Luminescence*, **23** (1981), 209–235.

[76] W. E. Howard, "Electroluminescent Display Technologies and Their Characteristics," *Proceedings of the Society for Information Display*, **22** (1981), 47–56.

[77] D. Langer and S. Ibuki, "Zero–Phonon Lines and Phonon Coupling in ZnS:Mn," *Physical Review*, **A138** (1965), 809–815.

[78] U. W. Pohl and H.-E. Gumlich, "Long Range Mn Ion Pairs and Other Mn Related Centers in ZnS Detected by Site–Selected Spectroscopy," *J. Crystal Growth*, **101** (1990), 521–524.

[79] J. Dreyhsig, U. Stutenbäumer, H.-E. Gumlich, and J. W. Allen, "Excited State Absorption (ESA) of Mn in ZnS and ZnSe," *J. Crystal Growth*, **101** (1990), 443–448.

[80] G. O. Müller, J. Neugebauer, R. Mach, and U. Reinsperger, "Excited State Interaction in the Dopant System in ZnS:Mn Electroluminescence Devices," *J. Crystal Growth*, **86** (1988), 890–894.

[81] R. C. Buchanan (editor), *Ceramic Materials for Electronics: Processing, Properties, and Applications*, Marcel Dekker, Inc., New York (1986).

[82] F. Greuter and G. Blatter, "Current Control by Electrically Active Grain Boundaries," in *Polycrystalline Semiconductors*, Springer Proceedings in Physics, Volume 35, Springer Verlag Berlin, Heidelberg, 1989, 302-314.

[83] T. K. Gupta, "Application of Zinc Oxide Varistors," *J. American Ceramic Society,* **73** (1990), 1817–1840.

[84] Richard Einzinger, "Metal Oxide Varistors," *Ann. Rev. Mat. Sci.* **17** (1987), 299–321.

[85] P. Becker, C. Powers, and M. S. Thompson, "Metal Oxide Varistors and Methods Therefor," *U.S. Application Number:* 07–447748 (Dec. 8, 1989) patent application allowed.

[86] H. H. Uhlig, *The Corrosion Handbook*, Sponsored by *The Electrochemical Society, Inc.*, John Wiley & Sons, Inc., New York (1948).

[87] H. H. Uhlig, "Initial Oxidation Rate of Metals and the Logarithmic Equation," *Acta Metallurgica*, **4** (1956), 541–554.

[88] A. T. Fromhold, Jr., "Analysis of the Uhlig Defect Model of Oxidation Kinetics," *J. Electrochemical Society*, **115** (1968), 882–890.

[89] N. F. Mott, "The Theory of Crystal Rectifiers," *Proceedings of the Royal Society of London*, 171 A (1939) 27–38.

[90] D. J. G. Ives and A. E. Rawson, "Copper Corrosion IV. The Effects of Saline Additions," *J. Electrochemical Society*, **109** (1962), 462–466.

[91] G. Nagasubramanian, A. S. Gioda, and A. J. Bard, "Semiconductor Electrodes–XXXVII. Photoelectrochemical Behavior of p–Type Cu_2O in Acetonitrile Solutions," *J. Electrochemical Society*, **128** (1981), 2158–2164.

[92] U. Collisi and H.-H. Strehblow, "A Photoelectrochemical Study of Passive Copper in Alkaline Solutions," *J. Electroanalytical Chemistry*, **210** (1986), 213–227.

[93] U. Bertocci, "Photopotentials on Copper and Copper Alloy Electrodes," *J. Electrochemical Society*, **125** (1978), 1598–1602.

[94] J. Kruger and J. P. Calvert, "The Oxide Films Formed on Copper Single Crystal Surfaces in Water–III. Effect of Light," *J. Electrochemical Society*, **111** (1964), 1038–1041.

[95] N. F. Mott, "Notes on Copper–Cuprous Oxide Photocells," *Proceedings of the Royal Society of London*, **171 A** (1939) 281–285.

[96] *Metals Handbook, 8th Edition, Volume 2; Heat Treating, Cleaning and Finishing*, by *ASM Handbook Committee,* ASM, Metals Park, Ohio (1964), 284–292.

[97] R. E. Kremer, M. C. Arikan, J. C. Abele, and J. S. Blakemore, "Transient Photoconductivity Measurements in Semi–insulating GaAs. I. An Analog Approach," *J. Applied Physics*, **62** (1987), 2424–2431.

[98] A. Chantre, G. Vincent, and D. Bois, "Deep–Level Optical Spectroscopy in GaAs," *Physical Review*, **B23** (1981), 5335–5359.

[99] G. M. Martin and S. Makram–Ebeid, "The Mid–Gap Donor Level EL2 in GaAs," *Deep Centers in Semiconductors*, S. T. Pantelides (editor), Gordon and Breach Science Publishers, New York (1986), 455–473.

[100] M. D. Sturge, "Optical Absorption of Gallium Arsenide between 0.6 and 2.75 eV," *Physical Review*, **127** (1962), 768–773.

[101] M. Lax, "The Franck–Condon Principle and Its Application to Crystals," *J. Chemical Physics*, **20** (1952), 1752–1760.

[102] J. I. Pankove, *Optical Processes in Semiconductors*, Dover Publications, Inc., New York (1987), 113.

[103] D. V. Lang and R. A. Logan, "Large–Lattice–Relaxation Model for Persistent Photoconductivity in Compound Semiconductors," *Physical Review Letters*, **39** (1977), 635–639.

[104] D. V. Lang, R. A. Logan, and M. Jaros, "Trapping Characteristics and a Donor–Complex (DX) Model for the Persistent–Photoconductivity Trapping Center in Te–doped $Al_xGa_{1-x}As$," *Physical Review*, **B19** (1979), 1015–1030.

[105] D. V. Lang, "DX Centers in III–V Alloys," *Deep Centers in Semiconductors*, S. T. Pantelides (editor), Gordon and Breach Science Publishers, New York (1986), 492–504.

[106] G. Vincent, D. Bois, and A. Chantre, "Photoelectric Memory Effect in GaAs," *J. Applied Physics*, **53** (1982), 3643–3649.

[107] M. E. Orazem, P. Agarwal, A. N. Jansen, P. T. Wojcik, and L. H. Garcia–Rubio, "Development of Physico–Chemical Models for Electrochemical Impedance Spectroscopy," submitted to *Electrochimica Acta* (1992).

[108] H. Uchiike, M. Noborio, T. Tatsumi, S. Hirao, and Y. Fukushima, "Measurement of Trap Levels in Electroluminescent Devices by Photon–Released Residual Charges," *Springer Proceedings in Physics*, **38** (1989), 81–84.

[109] A. Cornet, A. Miralles, O. Ruiz, and J. R. Morante, "Near Infrared Photoluminescence of ZnO:Co Varistors," *Physica Status Solidi A*, **120** (1990), K105–K110.

[110] A. Pöppl and G. Völkel, "ESR and Photo–ESR Investigations of Zinc Vacancies and Interstitial Oxygen Ions in Undoped ZnO Ceramics," *Physica Status Solidi A*, **125** (1991), 571–581.

[111] J. C. Simpson and J. F. Cordaro, "Photocapacitance and Photoconductance of Bi–doped ZnO," *J. Applied Physics*, **69** (1991), 4011–4016.

[112] A. Rohatgi, S. K. Pang, T. K. Gupta, and W. D. Straub, "The Deep Level Transient Spectroscopy Studies of a ZnO Varistor as a Function of Annealing," *J. Applied Physics*, **63** (1988), 5375–5379.

[113] J. C. Simpson and J. F. Cordaro, "Defect Clusters in Zinc Oxide," *J. Applied Physics*, **67** (1990), 6760–6763.

[114] P. Gaucher, R. L. Perrier, and J. P. Ganne, "Prebreakdown in Low Voltage Varistors and Its Relation with Deep Levels," *Revue de Physique Appliquée*, **25** (1990), 823–830.

[115] J. Tanaka, S.-I. Hishita, and H. Okushi, "Deep Levels Near Grain Boundary in a Zinc Oxide Varistor: Energy Change Due to Electrical Degradation," *J. American Ceramic Society*, **73** (1990), 1425–1428.

[116] R. B. Bird, W. E. Stewart, and E. N. Lightfoot, *Transport Phenomena*, John Wiley & Sons, New York (1960), 433–437.

[117] B. Danzfuss and U. Stimming, "Iron(III)–Titanium(IV)–Oxide Electrodes: Their Structural, Electrochemical and Photoelectrochemical Properties," *J. Electroanalytical Chemistry*, **164** (1984), 89–119.

[118] C. T. Sah, L. Forbes, L. I. Rosier, A. F. Tasch, Jr. , and A. B. Tole, "Thermal Emission Rates of Carriers at Gold Centers in Silicon," *Applied Physics Letters*, **15** (1969), 145–148.

[119] A. F. Tasch, Jr. , and C. T. Sah, "Recombination–Generation and Optical Properties of Gold Acceptors in Silicon," *Physical Review*, **B1** (1970), 800–809.

[120] L. S. Lu and C. T. Sah, "Electron Recombination Rates at the Gold Acceptor Level in High–Resistivity Silicon," *J. Applied Physics*, **59** (1986), 173–176.

[121] L. S. Lu, T. Nishida, and C. T. Sah, "Thermal Emission and Capture Rates of Holes at the Gold Donor Level in Silicon," *J. Applied Physics*, **62** (1987), 4773–4780.

BIOGRAPHICAL SKETCH

Andrew Norbert Jansen was born on November 2, 1964, to Charles David and Shirley Ann (Kage) Jansen. He was raised in the small city of Marathon, Wisconsin. His father worked at Wausau Paper Mills as a millwright. Around 1979 his parents started to grow ginseng as a part time business which eventually became full time.

He graduated from Marathon High School in 1983. He then worked at Wausau Paper Mills under the title of Student Summer Help during the summers and Christmas semester breaks from 1983 thru 1986. Andrew enrolled at the University of Wisconsin–Marathon County Extension in Wausau, Wisconsin, in the fall of 1983. This permitted him to live at home while attending the first two years of college. He was accepted as a junior level chemical engineer at the University of Wisconsin–Madison in the fall of 1985.

Andrew graduated with his bachelor's degree in chemical engineering in December, 1987 with high honors. In January, 1988, he joined the electrochemical research group at the University of Virginia under the advisement of Dr. Mark E. Orazem. In August of the same year, his advisor transferred to the Chemical Engineering Department at the University of Florida–Gainesville. On April 22, 1989, Andrew married Rosalie L. Wozniak from Athens, WI. Andrew finished his masters degree at the University of Virginia in August, 1989 while still under the advisement of Dr. Orazem. He then moved to Florida to continue his studies with Dr. Orazem. Andrew finished his doctorate in chemical engineering in December, 1992.

I certify that I have read this study and that in my opinion it conforms to acceptable standards of scholarly presentation and is fully adequate, in scope and quality, as a dissertation for the degree of Doctor of Philosophy.

Mark E. Orazem, Chairman
Professor of Chemical
Engineering

I certify that I have read this study and that in my opinion it conforms to acceptable standards of scholarly presentation and is fully adequate, in scope and quality, as a dissertation for the degree of Doctor of Philosophy.

Timothy J. Anderson

Timothy J. Anderson
Professor of Chemical
Engineering

I certify that I have read this study and that in my opinion it conforms to acceptable standards of scholarly presentation and is fully adequate, in scope and quality, as a dissertation for the degree of Doctor of Philosophy.

Oscar D. Crisalle

Oscar D. Crisalle
Assistant Professor of
Chemical Engineering

I certify that I have read this study and that in my opinion it conforms to acceptable standards of scholarly presentation and is fully adequate, in scope and quality, as a dissertation for the degree of Doctor of Philosophy.

Chih-Tang Sah

Chih-Tang Sah
Eminent Scholar of Electrical
Engineering

I certify that I have read this study and that in my opinion it conforms to acceptable standards of scholarly presentation and is fully adequate, in scope and quality, as a dissertation for the degree of Doctor of Philosophy.

Kevin S. Jones
Associate Professor of Materials
Science and Engineering

This dissertation was submitted to the Graduate Faculty of the College of Engineering and to the Graduate School and was accepted as partial fulfillment of the requirements for the degree of Doctor of Philosophy.

December, 1992

for Winfred M. Phillips
Dean, College of Engineering

Madelyn M. Lockhart
Dean, Graduate School

UNIVERSITY OF FLORIDA
3 1262 08556 8136